Master Thesis

Development of a quasi-static simulation methodology for a damage tolerance assessment of impact damage in bonded CFRP structures

Michał Skarka

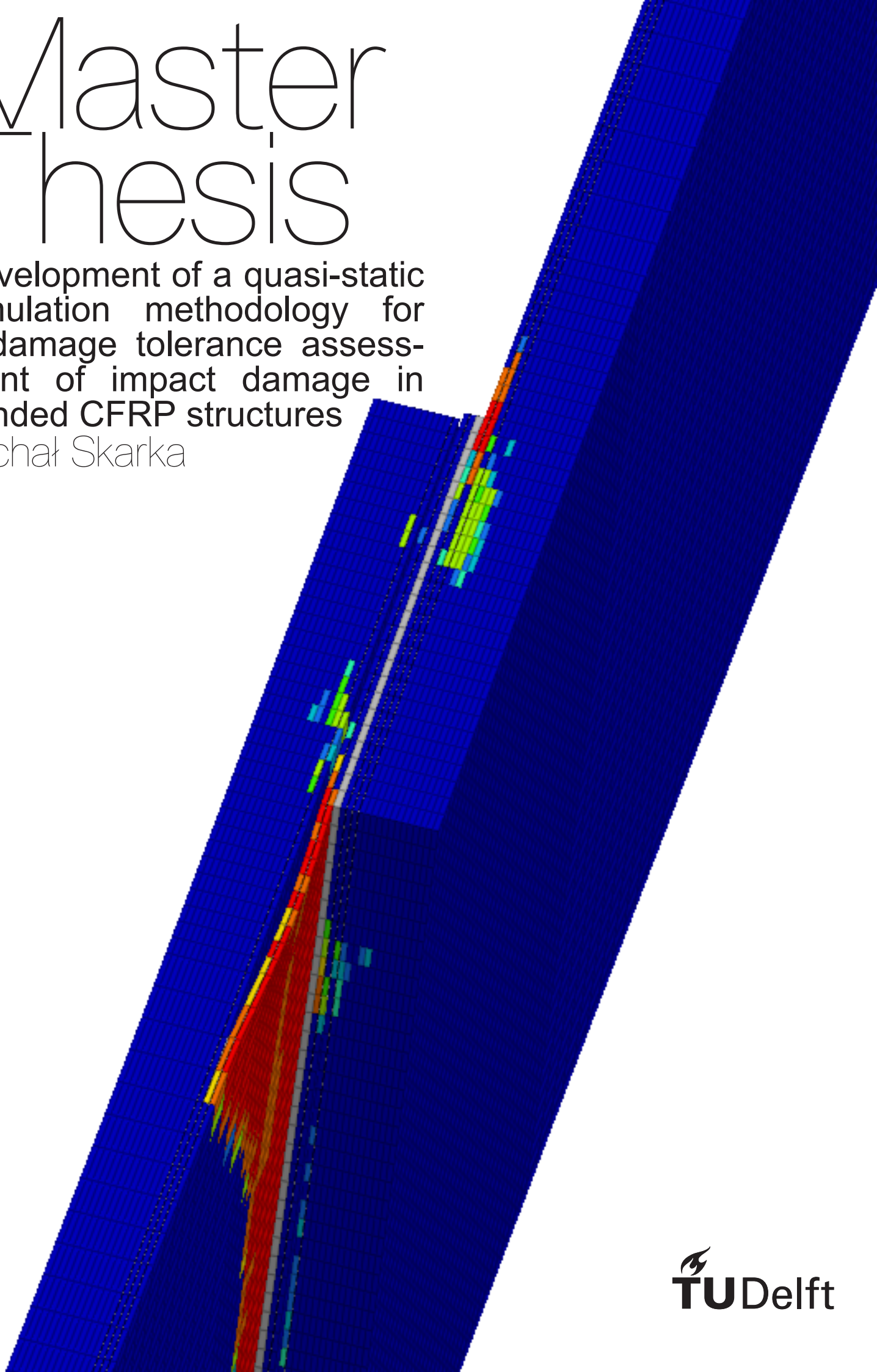

Technische Universiteit Delft

TU Delft

Master Thesis

on

Development of a quasi-static simulation methodology for a damage tolerance assessment of impact damage in bonded CFRP structures

by

Michał Skarka

Student number:	5621879	
Project duration:	January 2023 - July 2023	
Supervisor:	Dr. Sofia Teixeira de Freitas	Associate Professor, TU Delft
Co-supervisor:	Dr.-Ing. Saullo G.P. Castro	Associate Professor, TU Delft
Industrial supervisor:	Dr.-Ing. Ronny Sachse	Airbus Defence and Space GmbH
Industrial supervisor:	Dr.-Ing. Marco Hoffmann	Airbus Defence and Space GmbH

Cover page: Finite element simulation of static strength of SLS45 specimen. The contour of the intralaminar damage in the composite adherend.

TU Delft

Delft University of Technology
Faculty of Aerospace Engineering
Department of Aerospace Structures and Materials

GRADUATION COMMITTEE

Dated: 11.07.2023

Chair holder:

Dr. S. Teixeira de Freitas

Committee members:

Dr.-Ing. S.G.P. Castro

Dr.ir. J.A. Pascoe

Dr.ir. D.M.J. Peeters

TU Delft

Preface

The presented master thesis report is the final step in fulfilling the requirements to be awarded the title of Master of Science in Aerospace Engineering at Delft University of Technology. This thesis project was carried out at Airbus Defence and Space in Manching within the Structural Integrity and Structural Health Monitoring Department as part of the publicly funded research project ”JoinDT - Joining with predictable Damage Tolerance ”.

The product of my work is shown on the following pages and wouldn’t be possible without a big group of people surrounding it. First, I would like to thank the people supervising my day-to-day work at Airbus, Ronny Sachse and Marco Hoffmann. Thank you for our insightful weekly discussions. Immense gratitude goes to Sofia Teixeira de Freitas and Saullo Castro, my supervisors from TU Delft. I’m very grateful to you for challenging me with hard questions during our discussions and proposing ideas to tackle any issues encountered. Working with such knowledgeable and talented researchers and engineers sparked a gleam of curiosity in me. I hope that I will be able to develop myself as a researcher in the future.

The JoinDT project involves various partners from which the University of the Stuttgart and German Aerospace Center Braunschweig were engaged in testing and providing the validation data for this thesis project. I want to thank Mirijam Bastek, Oliver Völkerink and Thomas Körwien for the collaboration and for providing the data to validate the simulation methodology developed in this thesis.

This thesis wouldn’t be possible without my friends, who helped me in difficult times during the first-year courses and who supported me both during my internship and thesis. I would like to thank my dream team, Nico Gheorghe, Nikita Poliakov and Martino Giobbio.

Last, I want to thank my family, especially my parents, for their support and help during my studies.

Manching, July 2023 *Michał Skarka*

Abstract

The concept of lightweight design is driving future aircraft to exploit all the available strength of materials and further reduce the weight of an aircraft leading to lower fuel consumption and more sustainable aviation. Current designs introduce rivets and bolts to join the structure and simultaneously create holes in the pristine material, which is not wanted due to the local stress concentration. If the design wants to exploit all the strength of the material, stress concentration should be avoided using suitable joining technologies that don't require holes in the structure. This is possible with the adhesive bonding technology. However, many factors, such as the effects of manufacturing and impact-induced damage are still not fully understood. Thus, the damage tolerance of the design cannot be guaranteed. This results in conservatory safety factors being prescribed in the design process, which possibly reduces the exploitation of all available material strength.

The occurrence of barely visible impact damage (BVID) in aircraft composite structures, especially in adhesive joints, is a serious issue that can jeopardise an aircraft's structural safety during operation. However, virtual testing and numerous numerical approaches allow high-fidelity simulation of damage initiation and propagation in adhesives and composite adherends to predict the residual strength of the bonding accurately. Although the development is fast, accurate impact simulation is still computationally very expensive and thus not applicable in industrial cases where behaviour needs to be analysed to assess the structures' design, maintenance and repair.

This thesis investigated two topics that allow robust and accurate simulation methods to assess the effect of manufacturing and impact damage on the residual strength of bonded joints. The first topic is related to the development of the composite material damage model, where the multiscale material model is created by the use of a representative volume element (RVE). The second topic of simulation methodology is the development of the quasi-static simulation approach for the damage tolerance assessment of bonded joints. Modelling approaches to simulate residual strength are investigated through the finite element modelling of three groups (i) pristine, (ii) artificially damaged during manufacturing, and (iii) impacted bonded joints. In the numerical models, an approach based on the observation of the fracture surface of single-lap joints in different geometry and layup configuration is proposed in which the damage assessment focuses on the bondline area up to the first 0° ply. For the modelling of the damage in joints, two modelling techniques were studied, first removing elements in the damaged area and second detachment of the elements. Utilising those techniques, simplified approaches to model damage resulting from the impact were studied, with the modelling of impact damage as a hole, where all through-thickness elements are deleted and as delamination, where interlaminar cohesive zone elements are deleted.

The developed multiscale material model allowed for an accurate representation of failure modes occurring in the composite material by the characterisation of elastic, damage and plasticity parameters of the fibre and matrix constituents in the homogenisation and inverse characterisation process. The results showed that the deletion of the elements can be used to represent defects and damage of different kinds in the composite bonded joints, both in the adhesive and adherend. The comparison of different representations of the impact damage in the single lap joint configuration revealed that the best prediction in terms of the ultimate load, failure mode and size of the model is obtained with the simplified representation as a single delamination positioned before the first 0° ply in the layup and in the studied adherend configuration that was between the first (45°) and second (0°) ply in the layup. The study ends with the conclusion that in different geometries of single lap joints and different damage types studied, a numerical analysis should focus on the region of the overlap edge and in the thickness direction from the bondline up to the first 0° ply in the lay-up. The results and numerical method developed during this thesis create a base for the further investigation of a variety of impact cases on bonded joints.

Contents

Nomenclature

Abbreviations

$ASTM$	American Society for Testing and Materials
BK	Benzeggagh and Kenane
$BOPACS$	Boltless Assembling Of Primary Aerospace Composite Structures
$BVID$	Barely Visible Impact Damage
CAI	Compression After Impact
CDM	Continuum Damage Model
$CFRP$	Carbon Fibre Reinforced Plastics
CLS	Cracked-Lap Shear
CZE	Cohesive Zone Element
CZM	Cohesive Zone Model
DCB	Double-Cantilever Beam
DIC	Digital Image Correlation
DLJ	Double Lap Joint
DLR	Deutsches Zentrum für Luft- und Raumfahrt
DOF	Degrees of Freedom
ENF	End-Notched Flexure
FE	Finite Element
FEA	Finite Element Analysis
FEM	Finite Element Method
FNM	Floating Node Method
$JoinDT$	Joining with predictable Damage Tolerance
MMB	Mixed-Mode Bending
MMF	Mixed-Mode Flexure
MMR	Mixed-Mode Ratio
$NASA$	National Aeronautics and Space Administration
NDI	Nondestructive Inspection
PDA	Progressive Damage Analysis
$QUADS$	Quadratic nominal stress criterion
ROM	Reduced Order Model
RVE	Representative Volume Element
SLJ	Single Lap Joint
SLS	Single Lap Shear
$SLTAI$	Single Lap Tension After Impact
TAI	Tension After Impact
UC	Unit Cell
UD	Unidirectional
VED	Viscous Energy Dissipation
$WSLS$	Wide Single Lap Shear

Greek symbols

α	Coefficient of thermal expansion
β	Term for increase in yield strength
δ	Exponent for the damage evolution law

ϵ_{1C}	Strain at zero stress in compression
ϵ_1	Strain at zero stress
ϵ_{p0}	Equivalent plastic strain at which damage begins
ϵ_{p1}	Equivalent plastic strain at zero stress
η_{BK}	Fitting parameter in BK model
ν_{12}, ν_{13}	In-plane Poisson's ratio
ν_{23}	Transverse Poisson's ratio
ρ	Density
σ_0	Failure stress in tension
σ_y	Yield stress
σ_{0C}	Failure stress in compression
σ_{mean}	Mean stress at damage initiation
θ	Balance factor for kinematic and isotropic hardening

Latin symbols

C	Compression factor
D	Damage tensor
d	Damage variable
E	Young's modulus
E_{11C}	Longitudinal compressive modulus
E_{11T}	Longitudinal tensile modulus
E_{22T}, E_{33T}	Transverse tensile modulus
G_c	Critical strain energy release rate
G_{12}	In-plane shear modulus
G_{13}, G_{23}	Transverse shear modulus
H	Linear term for hardening law
$J1$	Volumetric strain to failure
K	Bulk modulus
K	Stiffness
l_{cz}	Cohesive zone length
m	Mass
S_U	Shear strength
T	Traction
v	Velocity
w	Damage variable
w_{max}	Maximum allowed damage variable
X_C	Longitudinal compressive strength
X_T	Longitudinal tensile strength
Y_C	Transverse compressive strength
Y_T	Transverse tensile strength

List of Figures

List of Tables

1 Introduction

This chapter describes the relevance of the chosen research topic, the motivation behind it and previous research work conducted at Airbus in the topic of damage tolerance of bonded joints. The definition of the main research objectives as well as the thesis outline is presented.

1.1. Relevance and motivation

Composite materials are increasingly used in the aerospace industry due to their excellent strength-to-weight, stiffness-to-weight ratio and outstanding formability. The application of composite materials is seen extensively both in commercial and military aircraft. For example, around 80 % of the Eurofighter Typhoon's external structure by weight is built from carbon fibre reinforced plastics (CFRP) [1]. A similar trend is seen in commercial applications, where 53 % of an Airbus A350 XWB structure by weight was designed with CFRP, which reduced operational aircraft costs up to 25 % [2].

Every designed aircraft structure, whether it is metallic or composite, needs to be divided into components and parts due to the shape complexity, manufacturing and cost reasons. An aircraft can consist of as many as 6 million parts that have to be connected with joints that guarantee structural integrity during the lifetime of an aircraft [3]. The current bottleneck of the aircraft design is that in the traditional joining technologies where rivets and bolts are used, holes are needed in the aircraft structure, creating local stress concentration points. This doesn't comply with the idea of the lightweight and damage-tolerant design, where one wants to exploit the full strength of the material as significantly higher stresses occur around the holes leading to fast crack initiation. Stress concentration is especially unwanted for the composite material because this material doesn't undergo plastic deformation as metallic materials. The same goes for the damage tolerance philosophy, where points around the holes are especially crucial for crack initiation in the structure. In addition, riveted and bolted connections add additional weight to the structure and a large number of points that must be regularly monitored during the inspection, which is undesirable.

The preferred and most suitable way in terms of weight and mechanical performance to join composite parts is with adhesives due to the more uniform stress distribution compared to the riveted connection where stress concentration occurs around the holes [4]. Due to certification requirements, bonding technology's use for primary aircraft structures is currently restricted. State-of-the-art is an additional application of rivets on top of bondline, limiting the advantages of bonded joining technology [5]. The potential sudden and brittle failure, the limited crack-arresting capability of bonded joints, as well as the inability of nondestructive tests to detect interface failure, such as kissing bonds, limit the application of adhesive bonding in load-bearing structures. Furthermore, the failure modes of adhesive joints are complex, as failure can occur in both the adherend and the adhesive. The scatter of material properties, the variability of environmental effects, and damage, which are important factors in composite structure design, also come into play for bonded joints with composite laminates as adherends.

Damage to composite bonded joints can be associated with manufacturing processes, handling and impact during service resulting in defects that reduce the strength of the bond. Composite materials are prone to impact damage due to their weak transverse properties and brittle nature [6]. Random impacts during handling or operations are inevitable and can significantly reduce a joint's mechanical performance, especially in compression [7]. Barely visible impact damage (BVID) is not detectable with the accuracy of standard nondestructive inspections (NDI) and thus poses a threat. To accurately predict the behaviour of damaged composite structures and bonded joints, it is necessary to develop accurate simulation methods that can include the preexisting damage in both the composite adherends and the bondline.

The complex nature of bonded joints highlights the need to develop predictive tools for the efficient and global implementation of adhesive joining in the aerospace industry. Mechanical testing and numerical simulation are the two most popular ways to prove that bonded joints can sustain certain loads. Mechanical testing can be very costly and time-consuming. Virtual testing is developing very rapidly and is seen as the way to answer the needs of the industry to validate its designs [8]. Additionally, simulation provides valuable information on structural failure's likelihood, causes, and consequences. This is especially useful in the presence of defects and damage, where one can observe the defect's effect on the stress field around it.

1.2. Background on JoinDT project and previous work at Airbus

Airbus Defence and Space is one of the leading partners in the publicly funded project "JoinDT - Joining with predictable Damage Tolerance ". The project aims to develop a certifiable method for the damage-tolerant design and assessment of bonded connections of fibre composite components. The focus is on predicting and managing the growth of cracks in joints situated in the primary load paths when subjected to fatigue loading, along with considering potential impact scenarios that can result in damage to the structure and assessing the residual strength of a connection. The method allowing the damage tolerance verification is to be provided within the scope of the project using finite element (FE) simulation. This can enable the certification of adhesive connections in main load paths with reduced testing effort. According to the Advisory Circular AC20-107B [9], the method to show compliance with damage tolerance is not regulatory in nature. Thus, the project partner can propose different methods and tools for the approval of structural bonding. Preceding this thesis project, two other researchers have been working on the topic of static and fatigue numerical simulation on composite bonded joints at Airbus Defence and Space in Manching. The work in this thesis project should be treated as a continuation of the work based on the previous experience in JoinDT project.

The work of Volle [10] focused on static strength and fatigue crack growth assessment. For the static strength, the implementation of the cohesive zone element in the Optistruct solver was verified and calibrated by replication of Double-Cantilever Beam (DCB) and End-Notched Flexure (ENF) tests. A generic multiscale material model of CFRP provided by Altair was used to model damage in the composite adherend. The joint modelled in this thesis was a T-joint using the prior knowledge of the failure mode from mechanical testing. The critical areas were identified with a simulation on a simplified 2D model. Refining this model into a 3D full-scale model and applying the developed modelling approaches identified a failure load which differed approximately 20% from the experiment. The developed modelling strategy couldn't replicate the failure mode of a delamination failure. However, the critical area was identified accurately. For the fatigue assessment, a methodology of Sachse [11] was used where the cohesive zone elements allowed to evaluate the strain energy released in the crack front to calculate the local crack propagation rate by applying Paris' law. This crack propagation rate was used to address the requirements for the fatigue crack no-growth and arrested crack growth. The conclusions of this work suggested that modelling of damage in the composite adherend, especially matrix damage and delamination, should be investigated in much more detail to predict the failure load and failure mode of composite bonded joints.

The work of Donelli [12] focused on the scarf repair joint (EN6066), single-lap shear (SLS) and cracked-lap shear (CLS) samples. The composite adherend modelling was realised with the implementation of

a stacked and hybrid meshing approaches. The comparison of the hybrid meshing, where one element can be used to model a few composite plies, and the stacked meshing approach, where each ply is modelled with an individual element, suggested that in the future, the stacked mesh should be used to guarantee good predictability of the simulation. The material model used was a generic model for a similar CFRP material and not a specifically generated one base on the coupon data and target values for the IM7/8852 unidirectional (UD) prepreg used in the JoinDT project. Additionally, new modelling feature was tested. The introduction of interlaminar cohesive zone elements allowed to account for delamination, improving the predictability of the failure modes. The topic of the fatigue simulation was explored with the same methodology as Volle [10] with a focus on crack-arresting features such as holes with rivets in CLS sample.

In order to create a holistic simulation approach for the damage tolerance assessment of bonded joining technology in accordance with the goals of the JoinDT project, the next steps proposed in the conclusions of the work of Volle [10] and Donelli [12] were to:

- Create a universal modelling strategy for pristine joints to capture accurately failure modes of joints, especially the delamination failure in the composite adherend.
- Create a multiscale material model using the Altair Multiscale Designer tool based on the coupon tests of IM7/8552 CFRP and material parameters from the JoinDT project.
- Extend the static simulation methodology to samples containing the effects of defects from manufacturing and damage resulting from impact.
- Extend the modelling strategy to element scale structures to confirm the general applicability on a wide range of sizes and geometries.

In the scope of this thesis, the first three were targeted for the work. The focus lies in providing the accurate prediction of the quasi-static scenarios in the static and residual strength simulation.

1.3. Research objectives

Despite the number of successful numerical studies conducted on bonded joints, the accurate and robust simulation is still limited due to the complex nature of the failure in composite bonded joints. This thesis explored the numerical methodologies and modelling approaches to simulate the mechanics of bonded joints with artificially introduced defects and damage resulting from low-energy impact. The objective of this thesis can be defined as to

> *Develop a simulation approach for an efficient and accurate prediction of the failure of composite bonded joints with defects resulting from manufacturing, and damage resulting from low-energy and low-velocity impact.*

To tackle the research objective, the main research questions were formulated to serve as a guide throughout the progress of the study. Two main research questions were established. First, tackling the issue of the composite material model characterisation was defined as

> *How can the multiscale material model be generated using the representative volume element and used on macro level to predict damage in the composite material during static and residual strength simulations of bonded joints?*

The second research question was established, seeking tools and ways to implement damage resulting from an impact in the numerical model in a simplified manner and was formulated as

How can damage resulting from low-velocity and low-energy impact be included in the Finite Element Model without running an explicit impact simulation?

The subsequent subquestions for the research questions were derived after conducting a literature review in order to explore current trends, tools, methods and approaches in the relevant literature and are presented in Section 2.7.

1.4. Thesis outline

The following thesis is divided into seven chapters and thesis structure presented in Figure 1.1. Chapter 2 presents the overview of the theoretical background of the main concepts necessary for the development of the simulation methodology for the damage tolerant assessment of bonded joining. The scope of the thesis is broken down into specific research subquestions after this theoretical framework. In Chapter 3, the specimens and testing campaign used for the validation of the simulation methodology are presented. Chapter 4 introduces the concept of the multiscale material model characterised using RVE in Multiscale Designer software from Altair. Chapter 5 presents the methodology for the modelling approach for the (i) pristine, (ii) artificially damaged during manufacturing, and (iii) impacted bonded joints. The modelling approach for adhesive and composite laminate is discussed, as also simulation settings and results are presented. Three different measures are compared with tests, namely (i) ultimate load, (ii) stiffness and (iii) failure modes. Chapter 6 discusses the results and assesses the proposed approaches and methods. Finally, In Chapter 7, a thorough assessment is conducted to determine if the research questions have been adequately addressed. Furthermore, several recommendations for future research in this field and a proposal for upcoming tests are provided.

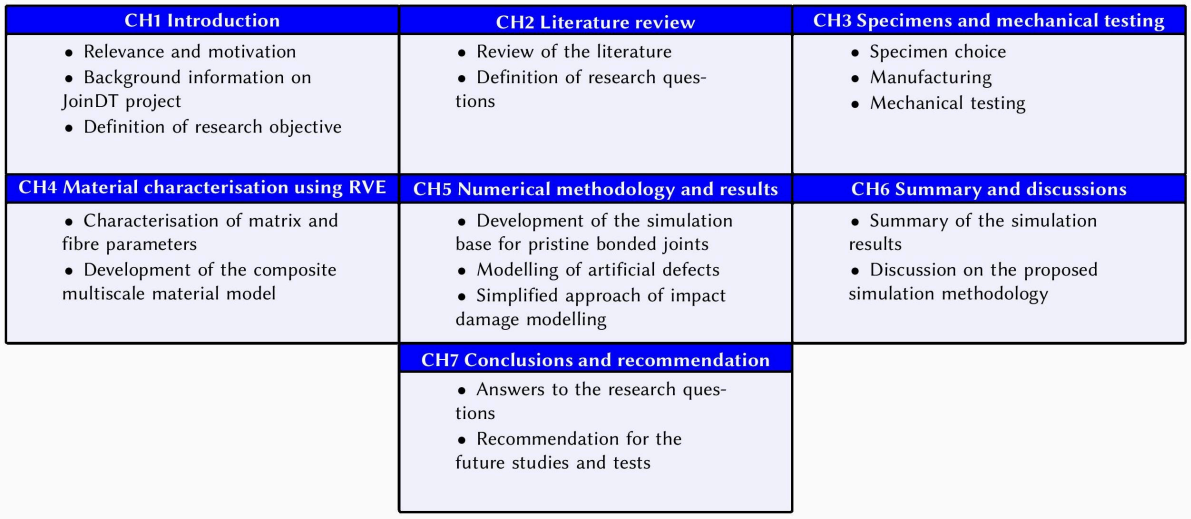

Figure 1.1: Graphical outline of the thesis.

2

Literature review

In order to understand the challenges involved in the design and analysis of bonded joints in fibre composite aircraft structures, this chapter covers the aspects of the damage-tolerant analysis of composite bonded joints. Possible methodologies of analysis, state of the art in the topic of static and impact simulation of bonded joints as well as alternative solutions for modelling defects and damage in numerical models are presented. Based on this overview, the limitations of available state-of-the-art analysis approaches that could support the damage tolerance analysis process are pointed out, and possible solutions to overcome them are identified. The chapter is finalised with the specification of the research subquestions.

2.1. Damage tolerant design and analysis of bonded joints

Damage tolerance, also referred to as safety by inspection, is a third-generation design philosophy currently used for designing and analysing aircraft structures. Damage tolerance as defined by the Federal Aviation Administration (FAA) [13] means that the structure has been evaluated to ensure that the damage resulting from fatigue, corrosion, or accidental impact occurring within the operational life of the airplane allows the remaining structure to withstand reasonable loads without failure or excessive structural deformation until the damage is detected. Once detected, a damaged component can be repaired or in some critical cases replaced, and the strength of the structure needs to return to its pristine strength. The following section presents the significance of this approach in the design and analysis of the bonded joints and how the virtual testing method based on the test pyramid supported by mechanical testing for validation can be used in the damage-tolerant design of aircraft structures.

2.1.1. Significance of damage tolerance

The structure designed in the philosophy of damage tolerance can perform its design function in the presence of a defect or damage. As learned from previous aircraft accidents such as the famous accidents of De Havilland DH-106 Comet 1 [14] or Boeing 737-200 during Aloha Airlines Flight 243 [15], damage such as in the form of fatigue, corrosion or impact can be present in the structure and grow quickly to a significant size. The design should guarantee that damage growth should be slow or arrested so that the flaw can be detected and repaired in the damage detection period. After the repair, the structure should restore its initial ultimate load. Additionally, the strength assessment has to assume imperfections and manufacturing flaws present in the pristine structure from Day 1, which implies more emphasis on damage growth analysis rather than structural life. The keywords related to this approach can be described as well-understood effects and controlled damage growth. Damage tolerance analysis should demonstrate through a calculation that some assumed pre-existing defect would not propagate to failure between two inspections, the first being assumed to be made at a time when the defect was at the threshold of detectability. In practice, this means that every aircraft manufacturer should demonstrate damage tolerance through analysis supported by tests. This starts at the

bottom of the test pyramid with the coupon tests used to generate the material data. The more detail added to the test, and the more the tested structure represents the final structure, the more complex and expensive tests are. Because of that, tests mostly serve the validation of numerical analyses, fewer tests are needed [16].

Dilger *et al.* [1] demonstrated the significance of damage tolerance in the design of aircraft structures using the Eurofighter as an example. Analysis of the Eurofighter used the design principles based on the safe life concept but was supplemented with some damage tolerance aspects. As later discovered during the design phase, an analysis of a significant portion of the aircraft's fatigue-critical sections was not identified. This emphasises the need for a simulation-driven detailed structural design and is ascribed to inadequate stress analyses caused by inadequately detailed or inaccurate finite element method (FEM) calculations as well as poor detail design. It is important to conduct a detailed FEM analysis of the critical point where stress concentration is identified during global FEM analysis, as demonstrated in this example. Such analysis can identify the critical points where cracks could initiate in the structure and which should be monitored with special attention.

Another important topic in terms of damage tolerance is random impacts that can occur during manufacturing and operations. Acceptable impact energy values were established as a design criterion because composite materials are impact sensitive. The adverse effects of barely visible impact damages and manufacturing flaws on strength and fatigue were determined to be covered by the design allowables. As a result of the effects of impact damage still not being fully understood for the composite materials, the allowed values were taken as very conservative, far lower than the theoretical material allowables. This emphasises research in the direction of understanding the effects of the random impacts on the composite structure.

2.1.2. Virtual testing of bonded joints

In recent years, virtual testing of composite structures expanded due to the developments in computational efficiency and power available, allowing analysts to test larger and/or more complicated models. FE simulation can be used to analyse the stress and strain distribution, deformation, damage initiation, and failure modes of the bonded joint and other structural elements under various loading scenarios. This can help engineers design optimal adhesive joints that can withstand the intended loads, identify the locations and causes of failure, and develop repair and maintenance strategies.

The term multiscale analysis refers to the process of coupling different FE analyses at different scales [17]. The traditionally used approach in the multiscale analysis of aerospace structures is called the top-down approach. Different levels of methodology are presented in Figure 2.1.

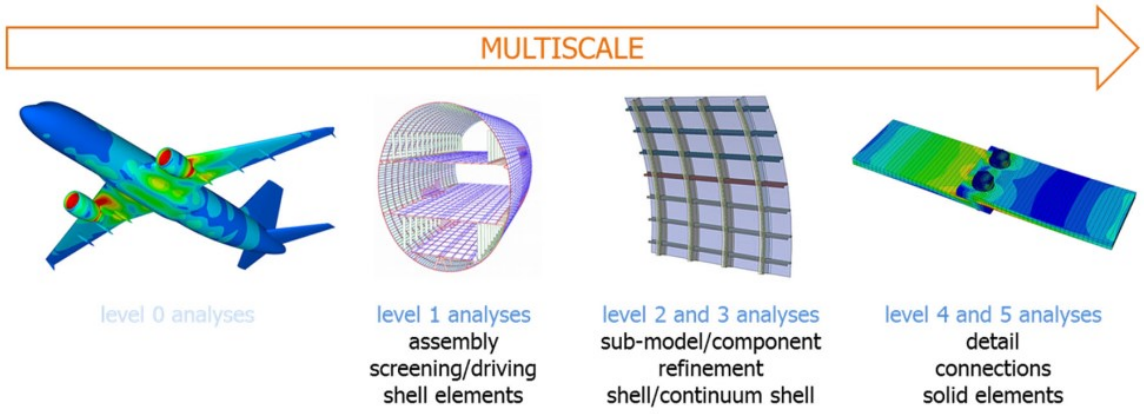

Figure 2.1: Traditional top-down multiscale strategy adopted at the aerospace industry. From Lopes et al. [17].

This approach necessitates predicting the behaviour of an entire structure using mostly linear but also nonlinear FE models. This is then used to define the driving boundary conditions for the subsequent models at lower modelling scales. The underlying principle is to keep the interface and link between the various modelling scales consistent. However, in this approach, the simulation stops at level 4 or 5 and thus does not consider the underlying physics of the damage in the composite material that lies on the lower levels/smaller scales of the test pyramid. To stop the simulation chain at this level, conservatory safety factors are prescribed to consider the unknowns lying on the smaller scales. The reason to end the top-down approach at the detail level can be associated with the high number of possibilities that each level yields at a correspondingly lower level. Each level of the simulation pyramid creates various design possibilities and high-stress locations that should be tested in more detail. When one reaches levels 4 and 5, the number of simulation cases increases significantly. Testing levels below would yield a huge number of simulations which would not be feasible to test and analyse in a reasonable amount of time.

To overcome the limitation of top-down strategy and adapt the multiscale approach with the development of composite structures, Llorca *et al.* [18] proposed a novel strategy for the virtual testing of composite structures using a bottom-up approach, where computational micromechanics, mesomechanics, and macromechanics form the basis for the testing of coupons, elements, sub-components, components, and complete structures. In Figure 2.2, different levels of simulation and strategy are presented. The smallest scale in the top-down approach, described as detail level 4/5, lies between the laminate and subcomponent levels presented in the bottom-up approach. This is the scale at which the link and transfer of information between the two approaches can be created.

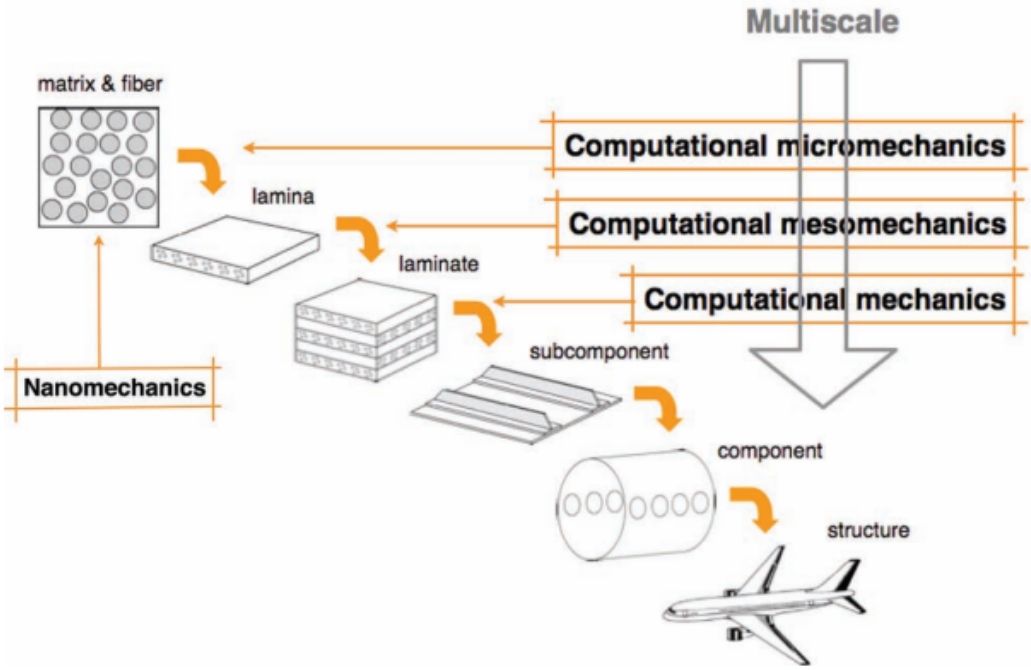

Figure 2.2: Bottom-up simulation strategy to conduct virtual composite structure tests. From Llorca et al. [18].

The main advantage of the bottom-up approach is that it's similar to the manufacturing and assembly levels of the structures and allows to consider the deformation and failure mechanisms at different length scales relevant to individual plies, laminates and components. Therefore, multiscale modelling is performed by transferring information between three different length scales instead of coupling different simulation techniques as in the top-down approach. In this approach, the transfer of information from mechanical testing is very straightforward and can be coupled with the appropriate computational scale.

The mechanical behaviour of the composite structures can be described on different levels. First of all, three different modelling levels related to the composite manufacturing can determine the modelling base. The first level approach separately describes properties of the constituents of composite material (fibres and matrix) in a micromechanical fashion, the second level describes the individual properties of each homogenised ply using mesomechanics as the base, and in the third level properties of laminates built from individual plies are described with a macromechanical approach. These physical scales emphasise the underlying physics of the damage in the composite material, where the damage can occur at different levels.

In a multiscale strategy for virtual testing of the composite structure, bonded joints are usually placed at the detail or subcomponent level. This results in the use of the levels below as a modelling base for the representation of the adhesive joints, where a bottom-up approach can be used for high-fidelity prediction of static strength.

The top-down approach allows one to identify critical components of the aircraft structure. The bottom-up approach allows one to consider different levels at which damage occurs in the composite material. Ultimately the combination of both approaches is needed to fully analyse full aircraft structures with the link between the two strategies on a subcomponent or detail level.

2.2. Numerical theories

There are different approaches to evaluating adhesive joints' static strength and failure mode. In the numerical methods, the most commonly used one is FEM. When assessing adhesive joint failure using FEM, several approaches can be taken: continuum mechanics, fracture mechanics and damage mechanics [19]. These approaches are used in numerical methods such as cohesive zone model (CZM), progressive damage analysis (PDA) and damage modelling using representative volume element (RVE) [20]. These can be used to model damage and failure in bonded joints with composite adherends on different scales.

2.2.1. Continuum mechanics

Continuum mechanics criteria are used, in conjunction with FEM analysis, to study the distribution of stresses along the length and width of the adhesive layer. In the continuum mechanics approach, the adhesive layer is modelled with a continuum shell or solid elements. Traditionally, failure criteria, such as determining failure based on the maximum stress or strain in the adhesive, are used to determine failure. However, in bonded joining, they are rather obsolete due to the stress singularities in the bondline. The locations of singularities in the single lap joint (SLJ) are presented in Figure 2.3. This results in a problem where the stress value rises with mesh refinement and prevents convergence of the solution, which makes the solution of the analysis using continuum mechanics heavily mesh dependent. There were rather unsuccessful numerical trials conducted by Chaves *et al.* [21] to remove singularities by adding the filet to the adhesive. Other studies showed that in these cases, the maximal stress value depends on the fillet radius, which is also unwanted [4].

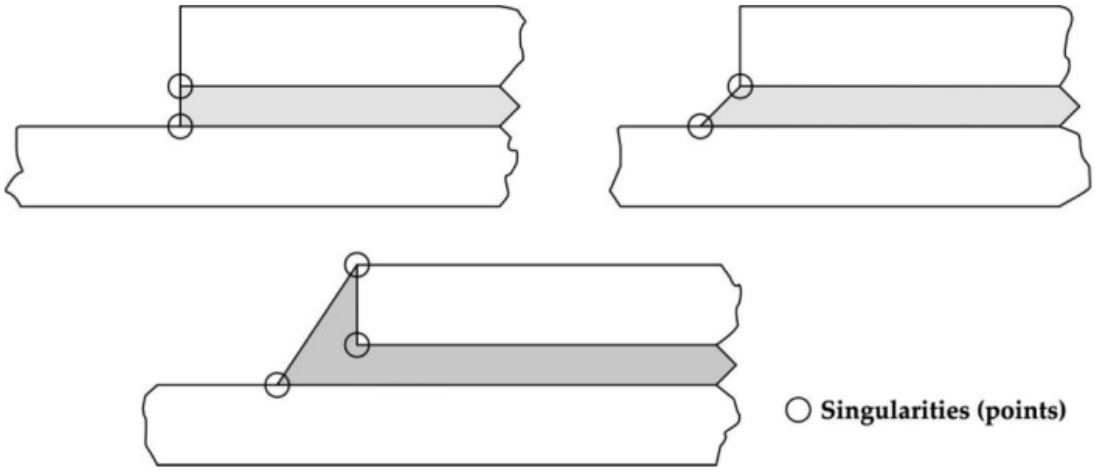

Figure 2.3: Stress singularities in adhesive joints. From Chaves et al. [21].

The continuum mechanics approach was studied by Díaz *et al.* [22]. The authors concluded that, with the currently available computational power, three-dimensional models should be used to model SLJ. These models in contrary to two-dimensional models, can be used in the bigger global models which correspond to the bottom-up approach. The continuum mechanics approach allowed researchers to study the distributions of peel and shear stresses but could not predict damage and its evolution in the joints.

Additionally, this approach applies to the continuous structure and is found to have similar convergence problems in structures with defects or when there are more than two different materials and a stiffness mismatch occurs [21]. Due to identified problems related to the approach and the fact that a variety of other methods is available, the study of the failure of bonded joints results in disregarding the plain continuum mechanics methods to be used in this research. The fact that in this research, damaged and defective joints are to be studied only highlights the further search for more suitable methods.

2.2.2. Fracture mechanics

Fracture mechanics is a method for improving the predictive capabilities of models with irregularities over continuum mechanics simulation methods. This approach is used to study the propagation of cracks or discontinuities in materials while avoiding conventional stress methods of continuum mechanics due to the sharp edges of crack fronts, which are characterised by infinitely small tip radii, resulting in nonphysical stress concentration factors. Delaminations, debonding, cracks, and voids are stress concentration points in the bonded joints where failure initiates.

Three different crack opening modes presented in Figure 2.4 have been identified and studied in the literature. They can be classified as

- **Mode I** associated with peel forces.
- **Mode II** resulting from longitudinal shear forces.
- **Mode III** induced by transverse shear forces.

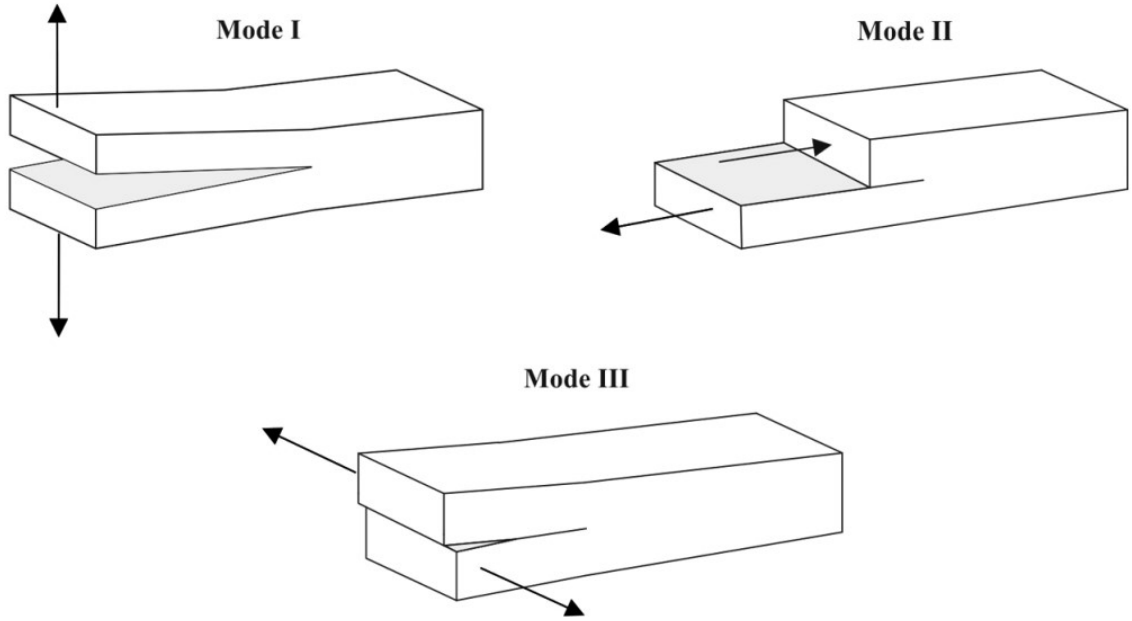

Figure 2.4: Fracture modes of bonded joints. From Chaves et al. [21].

Fracture mechanics uses a measure of the strain energy release rate G to evaluate fracture processes. This energy measure expresses the decrease in total potential energy per increase in fracture surface area. When the energy release rate exceeds a critical value G_c, crack growth begins.

Strain energy release rate is mode dependent and can be summed to total energy release rate G_{tot}. As a mixed-mode loading scenario occurs in most cases, the mixed-mode ratio (MMR) can be defined to represent a fraction of energy related to shear modes as

$$MMR = \frac{G_{II} + G_{III}}{G_I + G_{II} + G_{III}}. \tag{2.1}$$

Shear modes are often regrouped, and their sum is referred to under the same index II. The following designation is used in this work.

During the operations of the structures, loading occurs mostly under the mixed mode scenarios. To calculate a critical strain energy release rate for any possible MMR, fracture criteria combining modes were established in the literature. Several models are used to compute the critical energy release of mixed-mode fractures from pure-mode values. They have been established to reduce the number of mechanical tests under different MMR and rather fit the curve from which the critical energy release rate can be calculated for any MMR. The two most known mixed-mode fracture criteria are the Benzeggagh and Kenane (BK) model and the power law model due to the simple relations used in the formulas and good curve fit with the experimental data [23]. BK law can is defined as

$$G_c = G_{Ic} + (G_{IIc} - G_{Ic}) \left(\frac{G_{II}}{G_I + G_{II}} \right)^{\eta_{BK}}, \tag{2.2}$$

where η_{BK} is a parameter determined by a curve fit to the critical energy release rate data plotted as a function of MMR. The fitting parameter is an exponent defining the power relation between the critical energy release rate and MMR. Curve fitting in the BK mixed-mode fracture criterion is presented in Figure 2.5.

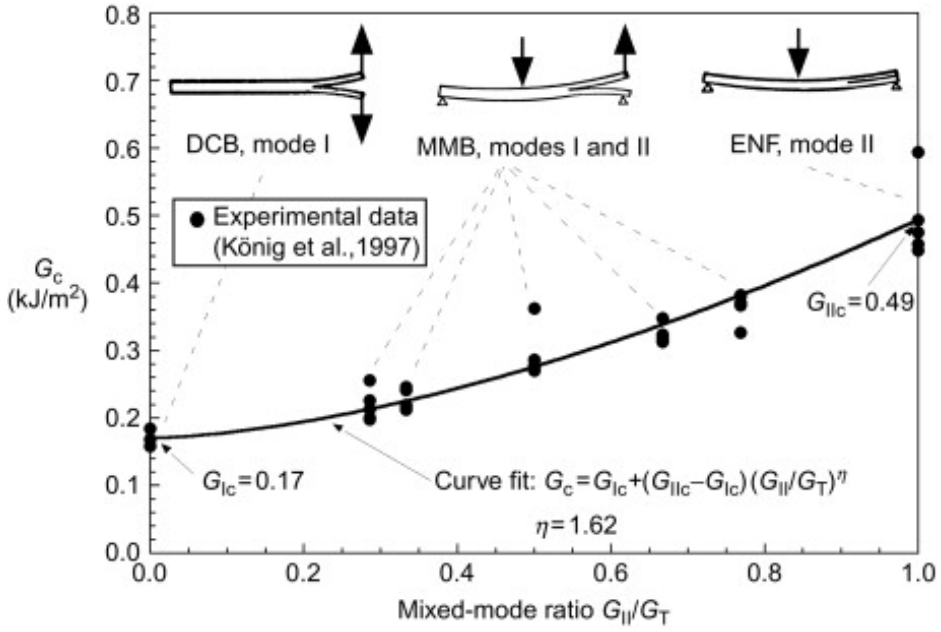

Figure 2.5: Ilustration of BK mixed-mode fracture criterion. From Krueger [24].

For the power law, mixed-mode fracture criteria is defined as

$$\left(\frac{G_I}{G_{Ic}}\right)^{\alpha}+\left(\frac{G_{II}}{G_{IIc}}\right)^{\beta}=1. \tag{2.3}$$

In the power law relation, α and β are used to fit the curve to the pairs of the data points G_I and G_{II} for which crack propagation occurs under different loading scenarios. The α parameter fits the power of the peel mode release energy rate relation, and β fits the power of the shear mode release energy rate relation. As illustrated in Figure 2.6, for $\alpha=\beta=1$, this criterion becomes the linear interaction criterion, where the G_I component of the experimental data is plotted versus G_{II} component. In other cases, a linear relation can be presented on the graph where G_I^{α} is plotted versus G_{II}^{β}.

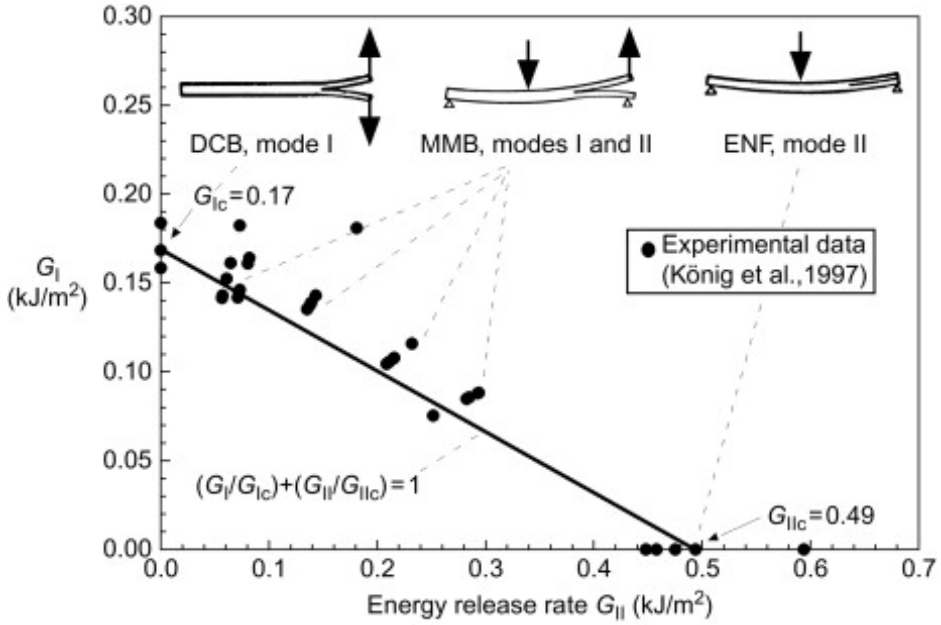

Figure 2.6: Illustration of linear mixed-mode fracture criterion. From Krueger [24].

The crucial limitation of these mixed-mode fracture criteria is that the underlying physics of the fracture process is put aside, and the most accurate fit based on a few data points is ruling the process. Comparing different criteria, one might see that researchers just propose different curve fit relations to get the best curve fitting and don't consider the process's physics.

Standard tests to characterise the mixed-mode fracture criteria are conducted on double-cantilever beam (DCB), end-notched-flexure (ENF) and on mixed-mode tests, i.e. in mixed-mode bending (MMB) or mixed-mode flexure (MMF). DCB is the most widely used test method for measuring mode I energy release rate. In this test, one side of the specimen is cracked, and a load is applied to a specimen with an embedded insert. In the experiment, different ways are used by researchers to create cracks of known lengths in samples. Release film insert can be used for that reason, or a sharp razor blade to cut through the pristine sample. In the DCB test, cracked faces are pulled apart, which creates a pure peel scenario. ENF uses a specimen similar to DCB, but the loading and boundary conditions differ. Samples are loaded in a three-point bending configuration, where loading is placed in the middle of the sample and roller supports are on both ends of the sample. MMB test combines the ideas of DCB and ENF. Two types of loading are applied to the sample, force through the insert at the end of the sample as in the DCB test and in the middle of the specimen as in the ENF test. The loading ratio between the two forces creates different MMR scenarios used to characterise the mixed-mode fracture laws. The MMB test configurations offer several advantages, such as ability to generate various mixed-mode ratios with a test specimen being a simple coupon geometry. This is not seen in the MMF test, where different ratios of arm thicknesses need to be manufactured to produce different MMR. In MMB, only one specimen geometry needs to be manufactured.

However, testing is not as straightforward as it may look. Several limitations need to be taken into account. The critical strain energy release rate is not straightforward to be calculated. It will depend on the definition of the crack initiation and the accuracy of the measurement of the load and crack length. Additionally, curve fitting depends on the test data and especially the number of tests conducted. An optimal number of different MMRs tested to produce accurate results with a low number of tests was found to be 3 in the National Aeronautics and Space Administration (NASA) report [25].

Considering that fracture mechanics allows for accurate damage initiation and propagation modelling based on released strain energy, it makes it a very useful tool for simulating the mechanics of the bonded joints with preexisting damage. Cracks and defects are the base of the fracture mechanics approach. In fracture mechanics, defects are usually modelled as pre-cracks artificially placed to simulate the damage initiation. The energy-based approach is best suited for damage propagation, and thus it is usually combined with different approaches for the initiation of the damage. This is where the next assessment comes in, namely the damage mechanics approach.

2.2.3. Damage mechanics

Traditional failure prediction tools are insufficient to capture a complex sequence of multiple failure mechanics of composite structures. Thus, the damage mechanics approaches have been explored by the researchers. Damage mechanics describes the evolution of degradation phenomena on the microscale from the initiation state up to the creation of a crack on the mesoscale. The damage mechanics approach can simulate progressive material degradation in the adherend and adhesive, which means that it will gradually lose its stiffness and load-bearing capability until the failure point [19]. Either a fracture energy criterion or softening governs a relaxation process. In the softening approach, the scalar variable of damage d is used to represent the effect of damage on the stiffness. Its values vary from 0 in undamaged material to 1 in failed material. The damage variable is related to the decrease in the material's stiffness. When the value of $d = 1$ is reached, the element is either deleted from the simulation or its stiffness is set to zero. Similar to fracture mechanics, the ability of damage mechanics to model damage in bonded joints makes it a usable and appealing technique.

2.3. Numerical methods

Different approaches have been studied using the concept of continuum, fracture and damage mechanics to assess the failure of bonded joints. The most popular are the CZM, continuum damage model (CDM) implemented in PDA and the micromechanical RVE approach.

2.3.1. Cohesive zone model

CZM has been widely used to study damage and crack propagation in adhesive joints in recent years. This method is commonly used in conjunction with the FEM, where predefined node pairs behave according to the established, cohesive law. Within the FEM, CZM is implemented in the form of cohesive zone elements (CZE), which can depict the plastic response of the material during failure by introducing a mechanical spring response to the relative displacement of the upper and lower elemental surfaces. Three areas of the cohesive model can be differentiated: a cracked zone, a fracture zone, and an intact material. The zone of interest is the fracture zone, where the fracture process occurs. A physical representation of the cohesive zone is presented in Figure 2.7. This model is typically based on empirical relationships from mechanical tests and is used to predict the onset and evolution of damage within the cohesive zone as the structure is subjected to external loads.

The cohesive law of CZE can be illustrated with a traction-separation curve. The traction-separation curve is typically plotted on a stress-displacement plane, with the normal stress (traction) on the y-axis and the separation displacement on the x-axis. The curve represents the relationship between the normal stress applied to the material and the corresponding separation displacement within the cohesive zone and is presented in Figure 2.8.

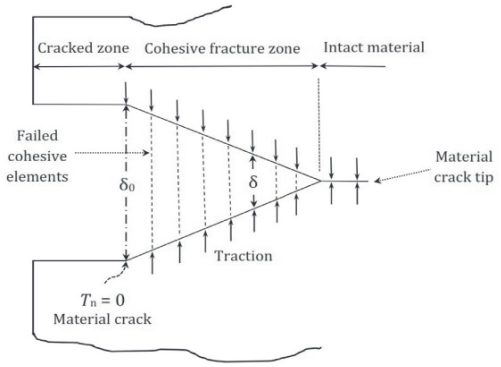

Figure 2.7: Schematic of cohesive zone model. From Naghdinasab et al. [26].

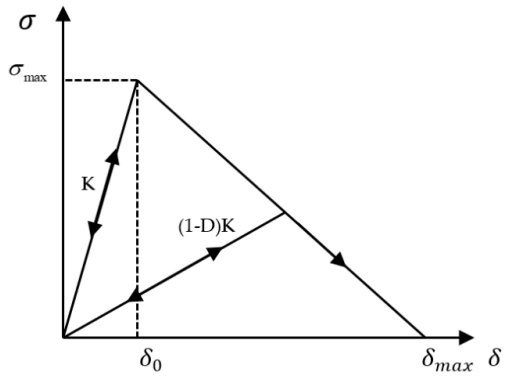

Figure 2.8: Traction-separation law of CZM. From Hu et al. [27].

The shape of the traction-separation curve can differ depending on the type of adhesive. Depending on the behaviour of the material represented within the cohesive zone, different constitutive models will produce different shapes for the curve. Typical shapes include bi-linear (triangular), tri-linear (trapezoidal), parabolic and exponential. Due to the simplicity and implementation in each commercial software, the triangular law is the most commonly used [19]. Different forms of traction-separation law are presented in Figure 2.9. The use of a traction-separation curve is usually defined with the specification of the critical strain energy release rate (G_c), maximum traction (T^0), stiffness (K) and form of the law for three fracture modes.

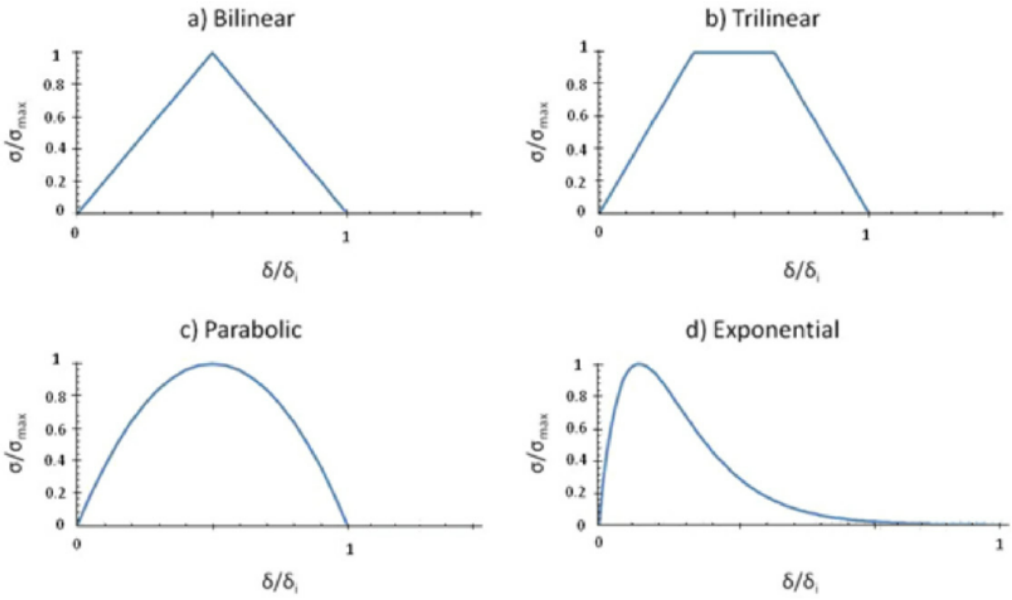

Figure 2.9: Different types of traction-separation cohesive law. From Dogan et al. [28].

In CZM, damage initiation is defined by a stress criterion and crack propagation by a fracture law. In most relevant research work summarised by Ribeiro *et al.* [23], damage initiation is defined with a quadratic nominal stress criterion (QUADS). Damage is assumed to initiate when a quadratic interaction function involving the nominal stress ratios reaches a value of one, defined as

$$\left(\frac{T_I}{T_I^0}\right)^2 + \left(\frac{T_{II}}{T_{II}^0}\right)^2 + \left(\frac{T_{III}}{T_{III}^0}\right)^2 = 1, \tag{2.4}$$

where t_i is traction, t_i^0 is maximum traction and subscript i represents one of the three crack opening modes. The propagation of damage is defined with the damage variable. In the bilinear model, the definition is as follows

$$d = \frac{\delta_f}{\delta_{max}} \frac{(\delta_{max} - \delta_0)}{(\delta_f - \delta_0)}, \tag{2.5}$$

where δ_0 is the separation at the beginning of damage, δ_f is the separation at failure, and δ_{max} is the maximum separation ever reached in the loading history that represents the irreversibility of the process. The softening of the material is defined with the damage variable, and, in the case of damage, the traction t is calculated as

$$T = (1 - d)K\delta. \tag{2.6}$$

where K is a stiffness tensor of the undamaged material.

There are two different approaches to the application of CZM in the FE modelling of bonded composite joints. These approaches can be used both for modelling the adhesive layer and in the case of composite interlaminar layers. Most commonly, cohesive elements are used to simulate the entire adhesive bond, which has a finite thickness and connects the two adherends. The second approach employs cohesive elements to connect superimposed nodes of elements, resulting in a zero-thickness interface, which is also known as cohesive contacts. In the finite element analysis (FEA) of composite bonded

joints, common applications of CZM is to represent the behaviour of the adhesive layer that bonds the two composite components together. In Figure 2.10, a model of a SLJ, with the adhesive embedded with cohesive elements is presented.

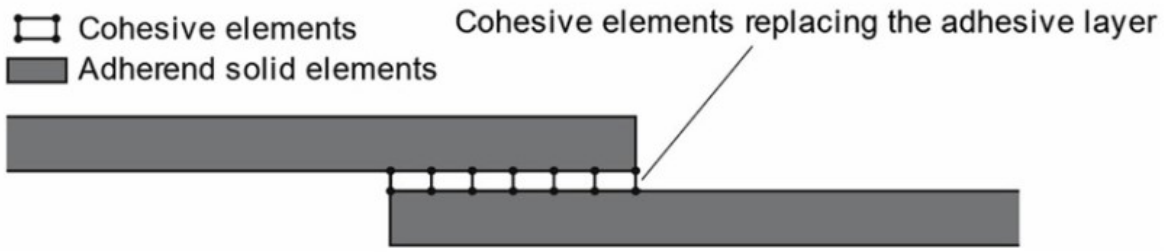

Figure 2.10: Cohesive zone modelling of the adhesive layer in SLJ. From Ramalho et al. [19].

CZM was applied to different types of joints, such as SLJ, double-lap joint, scarfed joint, stepped-lap joint, and T-joint, allowing for an accurate prediction of the failure strength and failure mode [23]. Additionally, CZM is widely used to simulate delamination between the plies in composite laminates, where a CZE layer is inserted between the mesh of two-ply layers.

The main challenge in the current state of the art is the characterisation of the adhesive properties that are geometrically dependent. However, the mixed formulation that includes continuum mechanics principles for the initiation of damage and fracture mechanics principles for the crack propagation method has been extensively studied in academia and has been proven to provide accurate strength prediction for a wide range of joint geometries. This method seems to be an approach that can be particularly used in the content of the research due to the ability to model defects and damage. Its usability is widely seen in the modelling of adhesives and in the modelling of interlaminar layers in adherends.

2.3.2. Progressive damage analysis using continuum damage model

The continuum damage model is a progressive damage modelling approach that predicts damage initiation and evolution without modifying the original finite element mesh of the structure being analysed. CDM approaches represent the effects of cracks by softening certain components of the constitutive stiffness tensor rather than modelling cracks by discrete insertion of discontinuities into the original finite element mesh. A set of scalar damage state variables accounts for various damage modes. This set is called the phenomenological damage tensor D [29]. Following the onset of damage, the affected stiffness terms are degraded according to the defined law.

This approach resulted from the stiffness degradation seen in composite laminates under complex continuous or cyclic loading [29]. It is a physical and mechanical response of the composite laminate to the evolution of damage and failure. In contrast, to the CZM, this approach is applied rather to represent damage in composite adherends than to adhesives.

This approach uses a range of well-established composite failure criteria to model the damage initiation. Two categories of criteria can be separated. The first ones are theories proposed by Tsai-Hill and Tsai-Wu that do not identify failure modes. Later developed theories of Puck and Hashin are the most popular ones used in current research due to the identification of different failure modes of composite material.

The typical implementation of the CDM in progressive failure analysis is presented in Figure 2.11. The most important part is highlighted with the dashed light-blue line. To apply the progressive stiffness degradation laws, the failure initiation criterion is checked in elements, and if it is reached the degradation rules are applied to the elements. Finally, the stress field is recalculated with the softened elements.

The PDA was used in the work of Völkerink and Hühne [8] to model damage in composite adherends. This allowed for an accurate static strength prediction of a double lap joint with a relative error of around 5% between simulation and test results. Another successful application of CDM is seen in the work of Leone *et al.* [30], where the authors simulated the strength of the composite sandwich panels and captured a correct failure mode.

The approach is very well developed in the current state of the art. However, its implementation is mostly done in the form of customised user-written subroutines. Additionally, in the classical PDA, the physics of the material softening behaviour is highly omitted because, in most of the cases, linear softening in the stiffness tensor is applied and damage is assessed on the homogenised lamina scale. To better understand the physics of composite damage, micromechanical approaches have been developed and are presented in the next subsection.

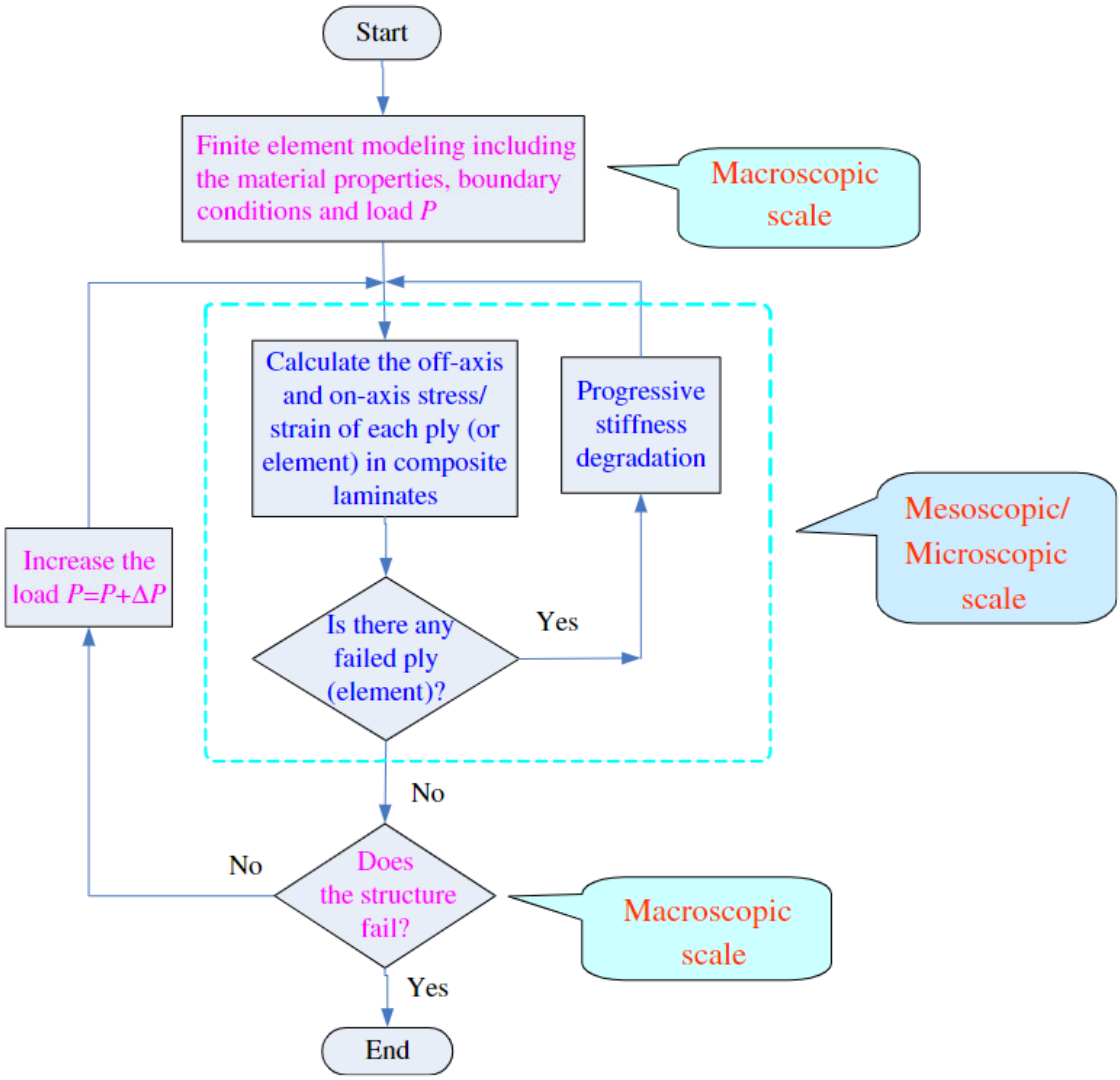

Figure 2.11: Flowchart of progressive failure analysis of composite laminates. From Liu et al. [31].

2.3.3. Micromechanical damage model using representative volume element

On a microscale, a composite material can be represented in RVE also referred to as unit cell (UC). At first, RVE was used to model composite material properties such as stiffness and strength. In recent years, researchers found that RVE can also be used to simulate the onset and growth of damage and

its impact on material behaviour on a micromechanical scale.

The RVE of the composite material must be defined as sufficiently small to distinguish heterogeneity but sufficiently large to predict the general homogenised properties of the medium [32]. Researchers developed different types of RVEs, the most crucial in the aspect of this research are representations of unidirectional (UD) carbon fibre fabric presented in Figure 2.12. The square RVE is referred to as the most unitary approach to represent constituents of composite material. In this representation, a single fibre is surrounded by the matrix. The hexagonal approach extends the unit cell to five fibres, where the middle fibre is modelled as a full cylinder and four others as quarters of the cylinder in the corners of RVE. This model, in principle, allows capturing in more detail the interaction between the matrix and surrounding fibres.

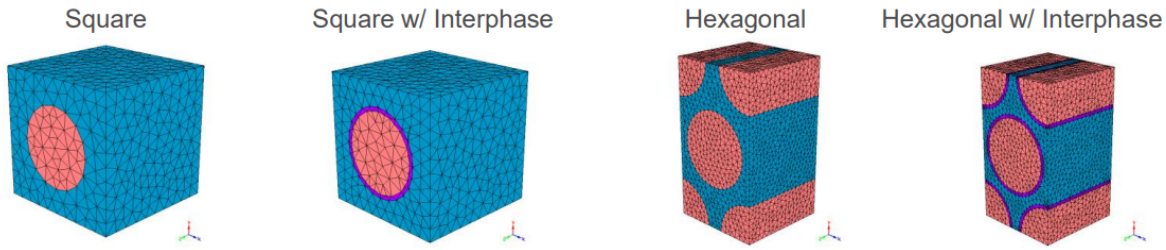

Figure 2.12: RVE models of UD composites. From Altair [33].

Models of RVE can additionally include the interface between fibre and matrix. The interface between the fibre and matrix is used to model the sizing present on fibres. Sizing is a homogeneous coating applied to the surface of fibres during the manufacturing process. Commercially produced fibres come with a thin polymeric film which protects the fibre from damage due to friction between adjacent fibres during handling, transportation and textile processing. Additionally, it improves adhesion between the fibre and the matrix, which was found to be crucial for the glass fibres because they don't bond easily with some matrix systems. As mentioned by Thomason [34], fibre sizing is the most critical component involved in the manufacturing of glass fibres. For the CFRP materials, the sizing influence was found to be less critical. The disadvantage of modelling the interface is related to the fact that the properties of the interface phase can't be measured with a specific test. One can omit modelling of the interphase and assume perfect bonding that can be modelled using contact properties.

The study of different RVE representations of UD composites was carried out by Huang [35]. In the work of the author, it was shown that to attain the best accuracy of the strength and stiffness prediction, single fibre UC gives much more accurate predictions compared to random fibre models with tens of fibres that tried to capture the variability and randomness. This confirms the applicability of the square and hexagonal RVEs. However, in this research, the damage wasn't studied, revealing one of the research gaps herein identified.

RVE is typically modelled within FE software. The FE model of RVE can be created based on the volume fraction of composite constituents. To model the properties of composite material, a characterisation campaign is required to obtain the properties of homogenised composite material and matrix. The characterisation can be based on coupon tests such as: 0^o tension, 0^o compression, 90^o tension, 90^o compression and $\pm 45^o$ tension. Additional off-axis or open-hole tests can be used for the verification. Stress-strain curves from coupon tests are used to calculate material properties.

Integration of the multiscale design capabilities in a FEM allows for the efficient design and testing representing physical scales of composite materials. Only one relevant study by Yuan *et al.* [36] assessed the usability of the RVE to model damage on a microscale and its usage in the simulation of composite structures, which reveals next research gap.

2.4. Finite element modelling of bonded joints

Bonded structures can be modelled using FEM utilising different approaches for the composite laminate and adhesive. In order to provide a modelling scheme specially adapted to the bonded joints the observation of the researches of the failure of single lap joints are presented with the modelling approaches for the composite laminates and adhesives.

2.4.1. Experimental observation of the failure of single lap joints

Purimpat *et al.* [37] tested single lap joints, all with the same quasi-isotropic (QI) properties, but with different ply layups. The adherends were made from carbon fibre epoxy prepreg composite and the specimens were bonded with an epoxy paste adhesive. Researchers reported damage initiation at the adhesive edges where the highest peel and shear stresses are located. Then the cracks followed a more or less complex path into the adherends depending on the individual stacking sequence. Different layup stacking sequences were tested by researchers and the further away from the adhesive the 0°-ply was positioned, the deeper the cracks extend into the adherends thickness direction was observed .

The effect of the composite layup on the occurring damage mechanisms was also investigated by Kupski *et al.* [38]. As in the previously reviewed study, single lap joints were examined, but in this case, they were made from a thermoset carbon fibre composite combined with an epoxy film adhesive. As can be seen in Figure 2.13 for specimens with 0° plies adjacent to the bondline, damage was observed predominately in the bondline accompanied by some intralaminar damage in the 0° plies. In the laminates with a 45° adjacent layer, a mix between damage in the bondline near the interface and damage inside the composite adherend occurred. By turning the orientation of the layer adjacent to the bond line even further away from 0° to 90° the damage leading to joint failure was entirely located inside the composite adherends. The similarity of the fracture surfaces shows that in all samples the damage extends up to the first 0° ply, which acts like a crack redirecting feature changing cracks propagating in the thickness direction to the delamination propagating above the 0° layer.

Very similar observations were made in the work of Völkerink [16]. In this case, the composite adherends were manufactured from a thermoset carbon fibre composite combined with an epoxy film adhesive. Similarly as previous researchers observation was made that the damaged area in the single lap joint extends in the adherend up to the first 0° ply in a layup.

In the testing campaign of Galliot *et al.* [39], where thermoset composite single lap joints were tested, researchers observed a similar pattern where failure in the joint was limited to the area close to the bondline. The boundary of the area was set by the first 0° layer in the composite layup. In Figure 2.13 schematics of the observed crack propagation are presented.

The observations made by the researchers create an area of focus on the damage initiation and propagation in the single lap joint configuration. The area of interest lies in the adhesive edges region and extends from the adhesive up to the first 0° ply in the layup. This observation was used in the thesis for the meshing approach and for the modelling of interlaminar damage.

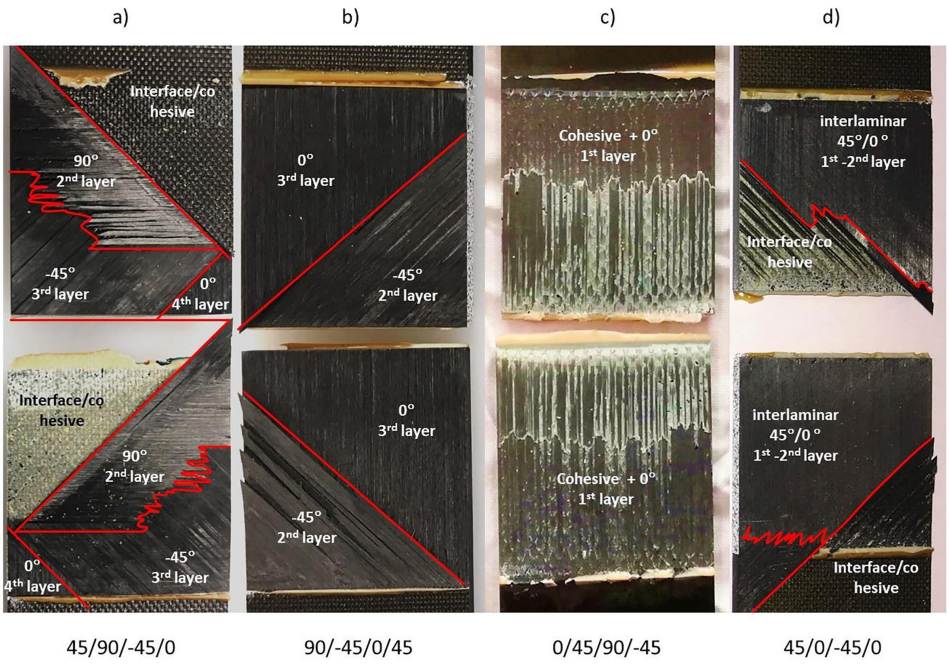

Figure 2.13: Typical fracture surfaces for different layup configurations in single lap joints. From Kupski et al. [38].

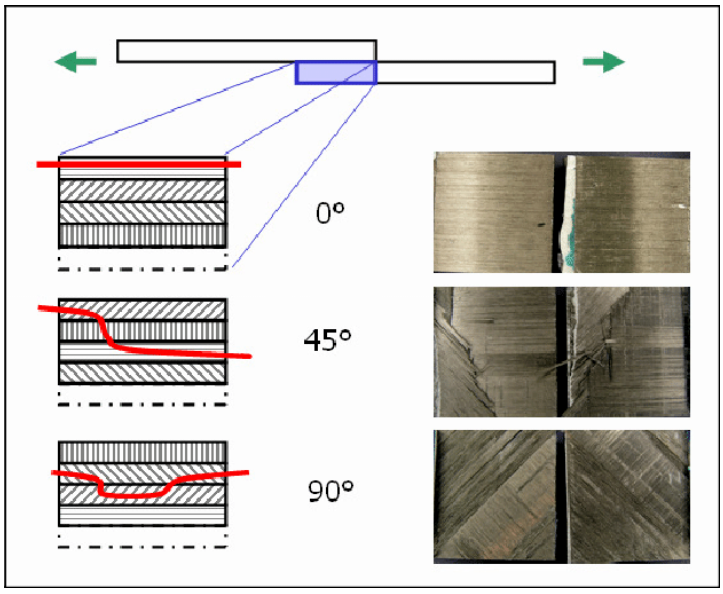

Figure 2.14: Schematics of through-thickness crack propagation in single lap joints with different stacking sequence. From Galliot et al. [39].

2.4.2. Modelling of composite laminate

FE modelling approaches for bonded joints vary from lower fidelity models, where properties of multiple composite layers are homogenised as laminate properties, to higher fidelity methods, where each layer is modelled individually. Similarly, meshing approaches for bonded joint models range from the layered shell, stacked shell, stacked continuum shell to stacked solid approaches. In the layered approach, the composite is meshed with one through-thickness element with a defined laminate lay-up. On the other hand, the stacked approach represents each ply or subset of plies with one layer of elements. Additionally, in the stacked approach, each layer can be separated with interlaminar CZE to explicitly model delamination. Different meshing approaches summarised in the literature are presented in Figure 2.15.

The stacked approach was found to be state of the art in the simulation by Sachse *et al.* [40]. Especially, the stacked continuum shell that offers a good compromise between accuracy and computational efficiency.

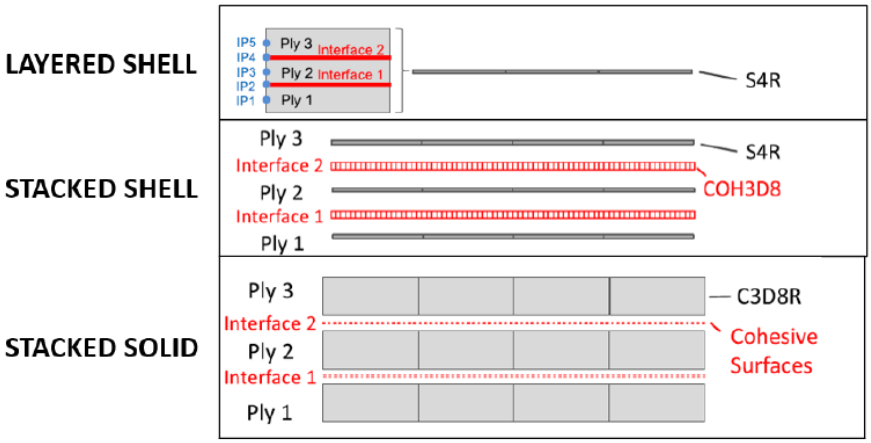

Figure 2.15: Adherend modelling approaches. Edited from Bogenfeld et al. [41].

For the modelling of damage in the composite adherends, several approaches are found in the state of the art. The first is used in the joints where the failure occurs cohesively in the adhesive, and the composite is modelled as elastic-orthotropic material. However, in most cases, damage occurs simultaneously in the adherend and adhesive. The second approach is preferred with PDA applied using user-defined material models, using the UMAT or VUMAT subroutines, respectively, for the implicit or explicit solvers.

2.4.3. Modelling of adhesive

CZM represents state of the art in the modelling of bonds, where the adhesive layer is modelled with one thorough thickness layer of CZE. The state of the art in damage modelling is the bi-linear traction-separation law of damage initiation and propagation. This is especially applicable to brittle types of adhesives. The characterisation of an elastic region up to full strength, followed by a softening region until a complete nodal pair separation at zero traction, is easy to implement and to be used in the calculation. Ease is related to only three parameters that need to be provided in the model, namely (i) critical strain energy release rate, (ii) maximum traction and (iii) stiffness for three crack opening modes. Only the first parameter represents the physics of the adhesive behaviour, and two others can be adjusted based on the numerical convergence. On the other hand, a tri-linear law can be important to model the plastic behaviour in ductile adhesives. However, the fact that it is often not implemented in commercial software forces researchers to use a bi-linear model.

2.5. Impact on composite laminates and composite bonded joints

Continuous efforts are being made to reduce the weight of composite aircraft structures while improving their energy absorption and load-bearing capabilities. CFRP composites widely used in aircraft structures are vulnerable to low-energy transverse impact. Generally, BVID does not require repair of the structure because the reduction of the strength associated with BVID is incorporated into the design allowables. However, these allowables are conservative due to the not fully understood implications of BVID. This motivates a large amount of research trying to understand the effect of such damages on the composite residual strength. Scientists investigate the capabilities of the currently existing tools and methodologies both in mechanical testing and numerical simulation. The following section summarises the current state of the art on impact damage, focusing on the numerical simulation field.

2.5.1. Low-velocity and low-energy impact

Most of the relevant research concerning the impact on composite bonded joints is referred to as a low-energy and low-velocity impact. The low-energy impact can be defined as an impact that causes subsurface damage without significant deformation or penetration into the structure but leaves a large damaged area within the composite material [42]. Low-velocity impact events are particularly dangerous because they can leave BVID to the structure. This can dramatically reduce structure strength, even up to 50 % in compression [7]. The danger in the cases of BVID comes from the fact that this damage is not detectable with the standard NDI, such as visible inspection conducted before each flight, because the damage is not obviously seen from the exterior surface of the composite structure. The main criterion to classify damage resulting from impact as BVID can be defined as an impact that produces internal damage without leaving any visible marks on the structure's surface. Kassapoglou [43] defined a BVID event as an impact resulting in an indentation depth less than 1 mm seen from approximately 1 m away after three days from impact event so that most of the relaxation process already took place.

Localised craters of damage and plastic deformation in bonded joints were found to be present in the composite layers of the top adherend and extended until the bondline interface [44]. The composite laminate is an adherend in the adhesive joining technology, making it more prone to damage than the bondline. However, damage in the bondline shouldn't be disregarded as it can also be significant depending on the joint's geometry and impact energy [45]. During the literature review, it was found that very extensive research concerning BVID has been conducted on composite laminates, and significantly fewer studies have been conducted on the bonded joints with composites as adherends. Knowledge from the studies on composite laminates can be reused in bonded joint studies because composite laminate is an external part of the joint which has direct contact with the impactor. Many researchers have studied the damage resulting from impact in composite laminates but also the effect of impact damage on the residual strength of composite laminates and composite bonded joints. These studies are summarised to identify the state of the art and gaps in the current research.

2.5.2. Type of damage resulting from low-energy and low-velocity impact

Various types of damage are observed in low-energy or low-velocity impact, such as matrix cracks, delamination, fibre breakage, fibre-matrix debonding, and fibre pull-out [46]. In studies of Wang *et al.* [42], Verma *et al.* [44], and Bieniaś *et al.* [46], main and crucial types of damage were identified as delamination and matrix damage in the form of cracking and splitting.

Delamination is regarded as one of the critical failure mechanisms that can significantly reduce the residual strength of a composite, particularly in compression. The presence of cracks in the matrix reduces the material's properties and alters how loads are transferred. Fibre damage generally occurs with a higher energy of impact and is not a primary concern in low-energy impact cases [47]. To fully analyse the case, the impact damage and the behaviour of damage propagation in the joint loaded after impact must be considered. Soto *et al.* [48] in their research on compression after impact concluded that matrix cracking is negligible and fibre breakage has a primary effect on structural failure. Hoseinlaghab *et al.* [49] studied damage types occurring in glass fibre-reinforced polymer (GFRP) during tensile loading after impact. Using acoustics emissions authors classified the main damage types occurring during tensile loading after impact as as (i) matrix cracking, (ii) fibre–matrix debonding, (iii) fibre breakage, and (iv) fibre pull-out in the order of the most to least dominating. The above can conclude that all three damage types, namely fibre damage, matrix damage, and interlaminar damage, need to be considered to fully analyse the effect of impact damage on the residual properties of a structure.

It is important to mention how the surface shape and the in-depth damage pattern look in impacted composite structures. The pattern presented in Figure 2.16 was found to resemble a truncated cone, commonly called pine tree distribution damage, as it looks like the branches of a pine tree [45].

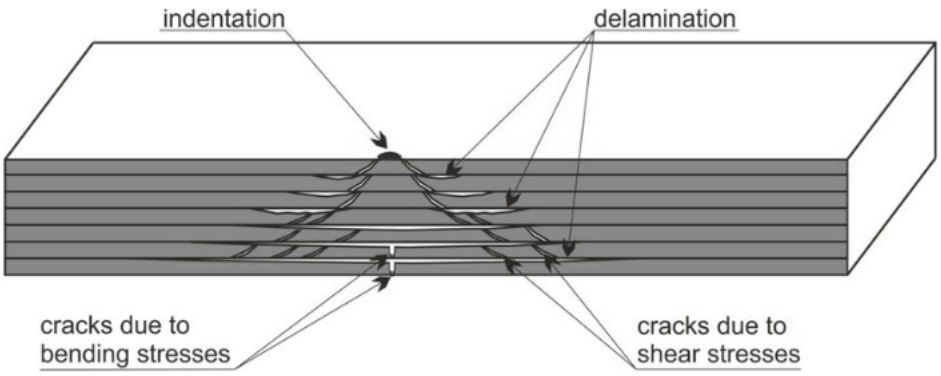

Figure 2.16: Through thickness characteristic pine tree shape of BVID in composite laminates. From Wronkowicz-Katunin et al. [45].

The pine tree shape can be attributed to the simultaneous action of tensile, compressive and shear forces acting on a composite during impact. This characteristic damage pattern can be associated with the local bending of the composite laminate. The bending behaviour results in compressive loading on the impacted surface and tensile loading on the opposite surface of the laminate. Additionally, impact force results in a transverse shear loading of the composite laminate, which leads to matrix cracking. Delamination was found to occur between layers of different fibre orientations. Between different orientation layers mismatch in bending stiffness occurs, which results in high localised interlaminar shear force [50]. The action of delamination and matrix cracking was found to influence each other, resulting in a damage pattern where delaminations are connected with matrix cracks between the layers [45]. The typical round shape of the impact crater and the damaged area in the composite bonded joints after impact in the top view is presented in Figure 2.17. This impacted region usually extends near the back wall of laminate and in bonded joints can be present in the adhesive layer and bottom adherend too [51]. Zone presented in cross-sectional view in Figure 2.18 was found to cause mechanical interlocking that affects bonding between the composite and the adhesive [27]. However, to effectively assess whether the joint needs to be repaired, besides identification of the damage type, a quantification of the damage size and its effect on the ultimate strength of the joint must be performed.

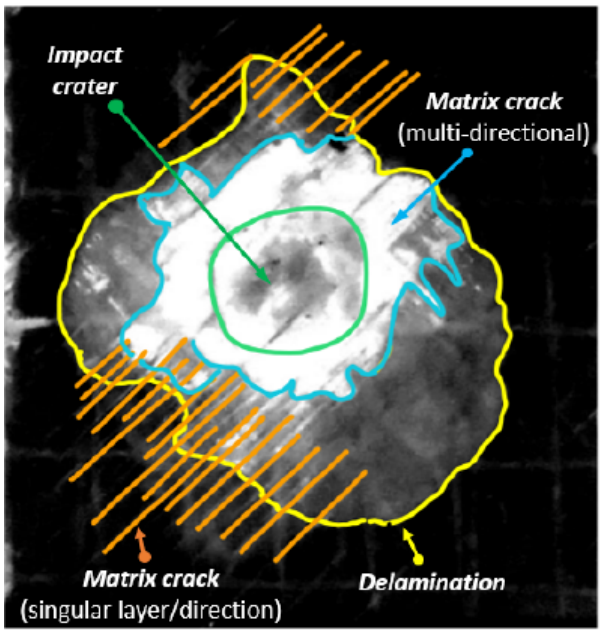

Figure 2.17: Top view of the damaged area in the bonded joint resulting from impact. From Verma et al. [44].

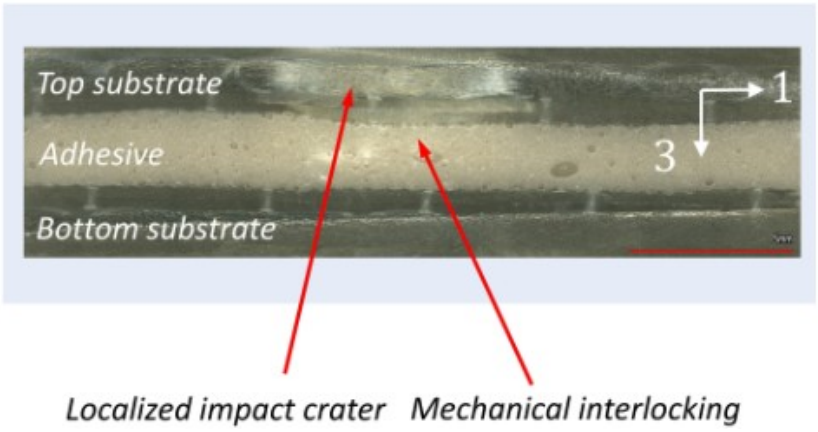

Figure 2.18: Cross-sectional view of the damaged area in the bonded joint resulting from impact. From Verma et al. [44].

2.5.3. Quantification of the damage

The impact is defined and quantified in the measure of energy with the standard unit of joules (J). Depending on the scientist, different impact energy values used in their experiments and/or simulations can be found in the literature. Impact energy is a function of the mass m and velocity v of the impactor. The following equation is used to calculate the impact energy

$$E = \frac{mv^2}{2}. \tag{2.7}$$

As one can see in the above equation, the same energy value can be generated with different combinations of mass and velocity. However, the damaged pattern generated with different combinations can be very different. The impactor of very small mass and high velocity can penetrate the structure and leave a small but long in-depth damage area. On the other hand, an impactor of high mass and low energy would rather result in a greater but short in-depth damage area.

Similar variability is seen in the impact resulting from the different shapes of an impactor. Kassapoglou [43] described the most probable tools to be dropped on composite structures during manufacturing and service. Examples of mentioned equipment are the ruler, callipers, hammer, screwdriver, rivet gun and power equipment. Objects like rivet guns produce a blunt impact that is better distributed over the area, and some, like screwdrivers a sharp impact that results in a deeper damage pattern.

To limit the number of possible tests due to the high variability of the impact cases that can occur, a standard test D7136/D7136M has been proposed by ASTM [52]. In this test, the standard impactor mass was defined as 5.5 ± 0.25 kg. The tip of the impactor is standardised as a smooth hemispherical surface of 16 ± 0.1 mm. Additionally, the hardness of the impactor material was standardised to the range of 60 to 62 HRC. This type of test results in a rather blunt impact. Testing and virtual replication of this test are widely seen in the literature. All of the presented below work utilised the ASTM test standards in their work unless explicitly mentioned in the text.

Huang *et al.* [53] used energies under 3 J to simulate the low-energy impact on adhesively bonded joints. Shi and Soutis [54], and Zhou *et al.* [47] used energy under 15 J in their tests and simulations of impact on composite laminates. Verma *et al.* [44] studied the damage in SLJ with different bondline thicknesses subjected to localised impact damage with energies ranging from 5 to 15 J. Li *et al.* [31] simulated impact with different environmental effects up to 16 J of impact energy. Sayman *et al.* [55] tested the tensile strength of the bonded joints after impact with energies up to 20 J. Wang *et al.* [42] studied the impact on thicker composite plates, where the impact energy ranged from 15 to 45 J. All of the above work presents damage that has characteristics of a low-energy impact. However, the

authors cannot identify a universal energy value that results in the BVID, which can be used in the design process as a critical sizing case.

Different authors use different threshold levels to quantify the boundary of low-energy impact. Huang *et al.* [53] suggested that the boundary is defined as 3.7 J. On the contrary, Wang *et al.* [42] set the boundary for 20J. However, as seen in the work of other authors, even energies up to 45 J can result in a damage pattern characteristic of a low-energy impact. This all depends on the laminate or joint used in the test and their parameters, such as thickness or layup.

In their investigation, Shi and Soutis [54] measured the delamination area after impact in the SLJ and compared their test results with FE explicit simulation. The area of delamination was compared with the impact energy in two different measures, the first defined the smaller area where the CZE completely failed between the plies ($d = 1$), and the second measure defined the larger area measured by the number of CZEs where damage was initiated but, the complete failure was not yet reached ($0 < d \leq 1$). The delaminated area measured in the mechanical testing was compared to the area of the damaged CZEs. This area in all test cases was between both numerical measures proposed, closer to the area of fully damaged CZEs. This study quantified the delamination area as primary damage resulting from impact, and other types of damage have not been considered.

In the conclusions of the experimental test campaign conducted by Huang *et al.* [53], it was suggested that the specific impact energy, which is the ratio of the impact energy to the mass of the impacted structure, could be used to quantify the effects of impact in the SLJ. The measure of the specific impact energy is defined in units of joules per kilogram (J/kg) and can take the effects of the variability of the impacted structures into account. This is very important as a simple measure of energy cannot quantify the effect of the variability of structures that are impacted. The impact energy of, i.e. 15 J will result in much different damage extended in a 1 mm thick composite laminate compared to a 20 mm thick bonded joint. This measure can allow for better quantification of the structural resistance and a better understanding of the effect of variability of structural parts. However, this was suggested as a conclusion and hasn't been applied in any relevant research yet, which showcases a research gap.

Impact energy is used as a universal parameter to compare different cases and the effect of impact on composite structures. By comparing different studies, the lack of a universal measure that would consider the parameters of the impacted structure is seen. Only one relevant work was found on the coupled effect of laminate thickness and impact energy on composite strength. In this work, Morais *et al.* [56] concluded that under 3.7 J impact energy, the resistance to repeated impacts increases only with laminate thickness, regardless of fibre reinforcement. The increase in resistance also depends on the fibre used and the spatial distribution of the fibres for the higher energy level analysed in this work. However, no measure to quantify or analyse the coupled effect of laminate thickness and impact energy was given by the authors.

2.5.4. Impact simulation

In the topic of numerical simulation, a variety of explicit FE simulations were conducted by researchers. In their study, Shi and Soutis [54] evaluated stress-based and fracture mechanics criteria to predict the onset and development of damage in the FE simulation for low-impact damage in composite laminates. The authors used the PDA approach testing Hashin and Puck failure criterion for damage initiation, combined with the linear stiffness degradation model where the damage variable is used to describe a gradual degradation of material stiffness. A study conducted in the paper was to investigate the modelling of the interfaces between the composite plies with interlaminar cohesive zone elements that allowed for capturing the delamination resulting from the impact. In the CZE modelling, damage initiation was defined with a quadratic stress-based criterion combining mixed failure modes. Damage was implemented as a traction-separation curve, where failure modes are combined with a fracture-based BK criterion. Furthermore, the authors took the initiative to model matrix splitting by inserting cohesive elements between neighbouring finite elements with predetermined crack spacing inside every single ply, which significantly increased the computational time. The recently developed Floating Node Method (FNM) proposed by Chen *et al.* [57] for modelling multiple discontinuities in a FE, can also

be used to model the model matrix cracking and capture the interaction between matrix cracking and delamination. However, the application of this method has not been seen in the impact simulations. It can be related to the high computational time of the simulation.

The methodology of Shi and Soutis [54] was investigated in the FE explicit simulation, where the composite was meshed with eight-node linear brick elements with CZE between each ply. The impactor was modelled as a rigid body with a prescribed initial velocity. This approach allowed the authors to predict the absorbed energy, the area and the shape of the delamination with a relative error of approximately 10 % by recreating an ASTM D7136/D7136M-15 standardised test [52]. However, there are a few points that need to be addressed for future improvement, being most important the combination of sample size, number of elements, and computational time. The simulated composite laminate was a circular plate of 75 mm diameter, meshed with 34500 solid elements for which the explicit impact simulation took 50 hours of computational time. However, the authors did not include any information about the computational power, such as the number of cores and memory required, making it hard to evaluate the method's applicability for larger coupons.

Very similar research on progressive damage modelling for composite laminates under low-energy damage was conducted by Zhou *et al.* [47]. The author used the same modelling strategy where the modified progressive damage of the composite was implemented in the VUMAT subroutine. The composite was modelled with interlaminar CZE to simulate delaminations between composite plies.

Li *et al.* [31] modelled impact on SLJ using data for CZM from the DCB and ENF experiments. The modelling approach utilised CZEs for the adhesive, with the mixed-mode bi-linear cohesive law. However, this simulation did not include interlaminar and composite damage, leading to differences between the simulation and testing results.

Soto *et al.* [48] simulated the impact on thick composite laminates, which is a very challenging numerical procedure due to the high number of solid elements across the thickness. Interlaminar layers were modelled with zero-thickness CZE. The continuum damage model was used for the damage in the composite solid elements, with bilinear traction separation law defined to describe the CZM of interlaminar layers. Researchers devoted attention to computational efficiency in their work by applying double-symmetry boundary conditions, nevertheless resulting in the omission of asymmetric modes that the authors found to affect the strength after impact predictions. Furthermore, the authors encountered another numerical issue concerning the simulation's convergence. Despite overall good predictions, it was not possible to converge an impact simulation after a few days of simulation. This was attributed to a large number of modelled plies and interfaces, which caused numerical contact issues. The problem was partially avoided by not deleting the elements once the damage variable reached 1, but instead leaving them with a very low stiffness value (i.e. 1 MPa).

The work of Soto *et al.* [48] greatly summarises the current state of the art and problems seen in the impact simulation. Among the other researchers, similar schemes are used. Explicit FE simulation utilising solid mesh with interlaminar CZE is seen. Modelling the interlaminar CZE is crucial to capture a delamination failure mode that was found to be of primary importance in the impact cases. Damage in adhesives is modelled with bilinear traction-separation curves and in adherends with the PDA. Coarse meshes, small coupons, and high computational time dominate the field of impact simulation. Researchers tried to reduce the simulation time without much success. To counteract this problem, a novel approach should be involved that will allow for the reduction of the time of the simulation.

2.5.5. Residual strength simulation

In the current state of the art, two types of simulation are coupled to assess the residual strength after impact. Two tests are conducted after impact, tension after impact (TAI) or compression after impact (CAI). The experimental method used to test composite plates is standardised and described in the ASTM D7137/D7137M-17 standards [58] for the residual strength. Virtual replications of these tests are extensively seen in the literature.

The first similarity of research work is that to evaluate strength after impact, two steps of experimental testing or simulation have to be conducted. The FE simulation consists of two analysis steps: the dynamic low-velocity impact step and the quasi-static tension or compression step. A workflow of the simulation is presented in Figure 2.19. This approach is seen in the work of Soto *et al.* [48], Wang *et al.* [42], Huang *et al.* [53] and Li *et al.* [31]. The specifics of the application differ as authors use different software packages. Nevertheless, the similarities in the setup involve geometry, material non-linearity, contact, dynamic structural behaviour and loading.

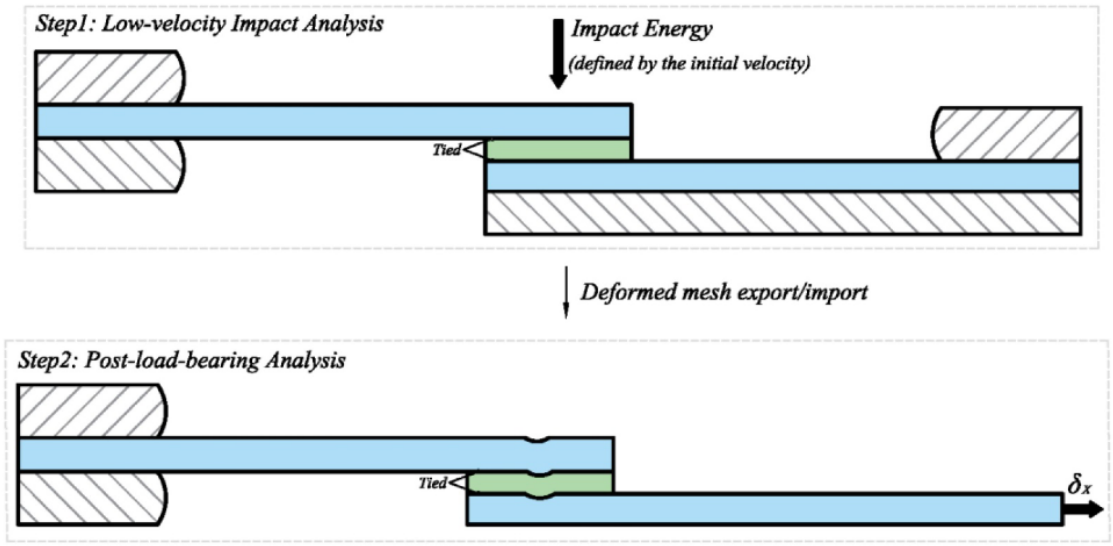

Figure 2.19: Typical two-step workflow for simulating residual strength after impact. From Li et al. [31].

Soto *et al.* [48] tested and simulated the residual strength of the composite laminate under compression. Researchers noticed that fibre breakage, although less common during impact, is ruling the failure of the impacted laminate in compression. On top of that, compression after impact is characterised by very brittle behaviour, which doesn't comply with the damage tolerance design of the composite structures. Thus the criticality of the evaluation of impacted composite laminates is emphasised.

Wang *et al.* [42] investigated the residual tensile strength of composite laminates. The researchers tested the stacking sequence's effect on the laminate's residual tensile strength. However, only two different lay-ups have been tested. The cross-ply lay-up $[0/90/90/0]$ resulted in much higher degradation of tensile strength after impact compared to the second angle-ply lay-up $[45/-45/-45/45]$, which suffered from lower degradation. This allowed researchers to conclude that ±45 layers allow for better energy dissipation from the transverse impact. However, as only two different lay-ups were investigated, further research should follow to confirm the effect of lay-ups on residual properties. Another part of the research investigated the effect of different impact energy levels on the residual tensile strength. The energy threshold was found to be around 20 J, after which the residual properties dropped drastically, suggesting that a low energy impact boundary for these specific laminates is around 20 J. Both variables and their effect on residual strength are presented in Figure 2.20.

The graph shows the important effects of energy values found by the authors. The first is the lower-impact energy degradation stage. The matrix shear cracking was found to be present in the outer surface of composite laminate even under a very small energy impact (less than 3 J). Matrix cracks in the impacted area cause stress concentration during the tension process, lowering the laminate's residual strength. The second plateau stage represents the cases where the main damage modes are matrix cracking and delamination, and fibres do not fail. Even though the damaged area is increasing, undamaged fibre can carry most of the load in the tensile case, which results in a quite constant residual strength over the wide energy range. In the high-impact energy degradation stage, fibre damage was

found to have a critical effect. Tensile residual strength was found to be drastically lower with increased impact energy, where a larger area of fibre damage occurs due to the impact. Findings of Wang *et al.* [42] allow to confirm that in low-energy impact, the damage is seen in the form of matrix cracking and delamination, and cases, where fibres are damaged should be treated as high-energy impact.

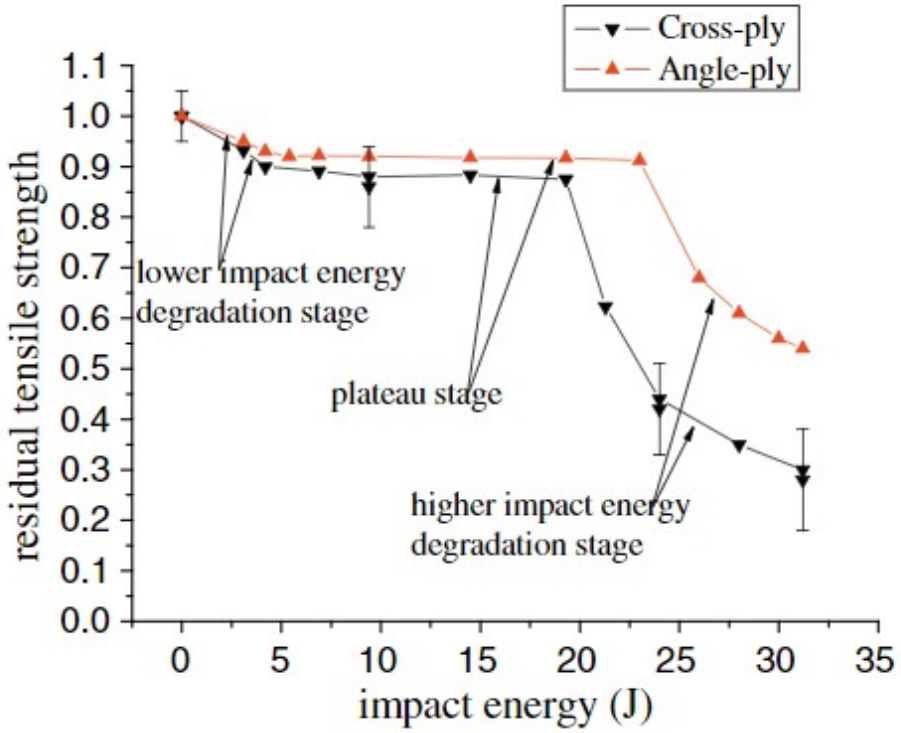

Figure 2.20: Degradation of residual tensile strength for two different stacking sequences. From Wang et al. [42].

Research by Chen *et al.* [59] investigated CAI in CFRP laminates manufactured by resin transfer moulding (RTM) using progressive damage methodology. Authors claim that, unlike prepreg material, the RTM technology laminate does not own a physical bonding interface between two adjacent layers. So correspondingly, from the assumption, the authors derived that no interlaminar CZE modelling is necessary. However, delamination results from in-plane and out-plane shear stresses between the plies, meaning that the change of stiffness (ply orientation) is a primary inducer of delamination. In addition, in many cases, delamination is induced by matrix cracking when the crack changes the direction of propagation when encountering the ply boundary. No other relevant research was found to disregard delamination in the impacted plates due to the manufacturing technology, thus this questions the methodology and conclusions drawn by the authors.

Some studies investigated the coupled effect of low energy impact and temperature difference on the residual properties of the bonded joints. These two factors are well-known as a source of variability for composite properties. Two research groups: Li *et al.* [31] and Huang *et al.* [53] investigated the topic of residual properties of adhesively bonded joints with impact damage at different temperatures. The results of experimental testing showed that the test temperature, impact energy, and various adherend combinations all have a significant impact on the residual tensile properties of composite SLJs.

In their work, Li *et al.* [31] concluded that the post-load-bearing capacity of the bonded joints decreased as the impact energies increased. The second one was that the failure loads of specimens subjected to impact loading did not decrease significantly at -30°C or 50°C. However, the failure load of the specimens clearly decreased at 80 °C.

Investigation of the criticality of the location of impact on the residual strength in SLJ was conducted by Farrow *et al.* [60]. Four different cases were investigated and are presented in Figure 2.21. The authors concluded their experimental research with the fact that impact case 2 is less critical, and the damage created during impact in the middle of the overlap area doesn't superpose with the stress concentration on the edges of adhesive in the SLJ configuration. For cases 1,2, and 4, similar results were obtained. This was associated with the stress concentration effect occurring at the edges of the adhesive layer which, superimposed with the stress concentration in the impact-damaged area, reduces residual strength significantly.

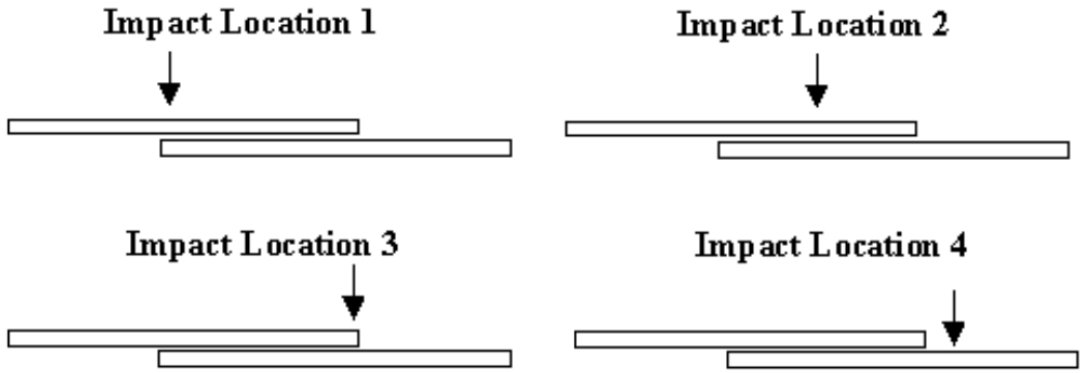

Figure 2.21: Different locations of impact on SLJ. From Farrow et al. [60].

A common factor found in the current state of the art in the simulation of behaviour after impact is that the meshes used are rather coarser due to the long computational time related to the two-step simulation scheme, which results in the application of the methodology on small in size composite coupons. Even though the authors emphasise this problem, no data concerning computational time, the number of cores or solver settings could be found, making it difficult to evaluate the scale of the problem accurately. However, as identified in the research of Soto *et al.* [48], the most challenging computational part of the simulation is the explicit impact simulation. This was attributed to convergence issues encountered during damage propagation in the interlaminar layers of composite laminate. Another point found for large models was that the simulation was found to be very computationally expensive due to the additional damping step between the impact and post-bearing simulation and due to the restart of the simulation engine between the steps. This is also related to the convergence issues following impact simulation and finding a suitable time increment to start residual strength simulation.

2.6. Methods for the modelling of damage resulting from impact

Different methods and approaches for the modelling of the damage were explored by researchers. Two different categories can be differentiated here, firstly the method of damage and defects modelling in the FE model and the second approach for reduced modelling of damage resulting from impact. This section covers studies by the researchers on the models with defects and damage either artificially introduced to the sample, coming from the manufacturing error or from the impact.

2.6.1. Finite element modelling of defects in bonded joints

The researchers have particularly taken one approach to represent a defect in FE models. Llorca *et al.* [18] investigated numerically the effect of imperfect bonding, caused by a partial lack of adhesive, on the strength of double-lap joints (DLJ) with adherends from non-crimp fabric. The joint was modelled with a 3D solid mesh on all parts, utilising the damage mechanics. The pristine model of the DLJ is presented

in Figure 2.22a. For the model, part of the solid elements that represented the area of the disbonded adhesive layer was deleted. Case C1 represents perfect bonding between the substrates and two different disbond cases presented in Figure 2.22b as cases C2 and C3 were tested. A comparison of numerical simulations of failure initiation and progression in the DLJ with testing results revealed that the applied methodology can predict the strength and failure mechanisms of imperfect bonded joints. A maximum relative error between the numerical results and mechanical tests of around 20 % was obtained by the authors.

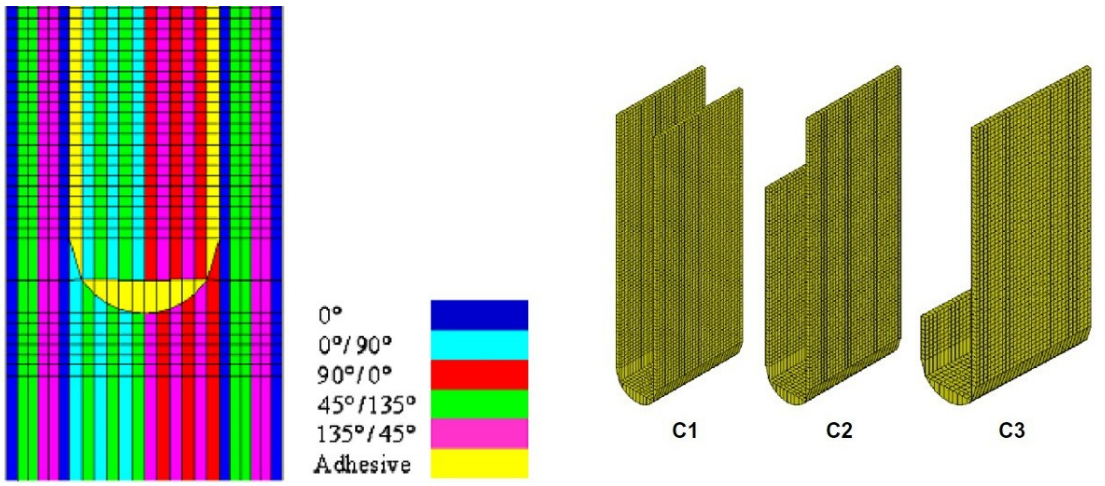

(a) FE mesh of the double lap shear joint.

(b) FE meshes of the adhesives representing different disbond areas.

Figure 2.22: Finite element model of double lap shear joint with imperfect bonding. From Llopart et al. [61].

An experimental and numerical study of SLJ with defects centred in the adhesive layer was conducted by Ribeiro *et al.* [23]. The numerical analysis incorporated a cohesive zone model for the adhesive and an elastic-orthotropic model for adherends due to the assumed absence of plastic effects by the authors. This assumption is considered to not be exactly true as due to the stress concentration in the defective joints. Damage can also occur in the composite areas, especially close to the bondline. The simulation results showed stress peaks on the boundaries of the defective area and at the edges of the bondline, which drove the failure of the joint. Similarly, here the methodology of deletion of elements resulted in strength values compared to the experimental testing. However, the defect size simulated by the authors ranged from 25 % to 75% of the bondline length, with is quite an unrealistic proportion for the bonded joints in the realistic structures.

2.6.2. Simplified approaches to models effects of impact

Besides the modelling of the defects in the finite element models, authors have proposed a method that could represent impact damage in both analytical, semi-analytical and numerical models. In the work of Kassapoglou [43] three simplified approaches to model damage resulting from impact as (i) hole, (ii) delamination or (iii) region of reduced stiffness are proposed.

Modelling impact damage as hole

In cases where the impact energy is very high, the impactor can completely penetrate the laminate. In low-velocity and low-energy impacts, there is no actual penetration and hole in the structure. However, this approach might be used in order to achieve the same residual strength as given impact damage. This approach takes a very conservatory approach, especially in the cases of BVID, where the damaged region is still capable of carrying some load. The underlying question of the approach is what diameter should the representative hole have.

Modelling impact damage as delamination

In this approach, the damage is represented in the form of one of the most seen damage types in the laminate after impact, the delamination. As the approximation of the random damage pattern, one may model a single or few critical delaminations of equivalent size instead of modelling all delamination created in the composite laminate.

The unknowns related to this approach are what should be the equivalent size and shape of this delamination, how many layers should be represented as delaminated and where through the thickness that delamination should be located.

Modelling impact damage as a region of reduced stiffness

In the composite laminate during impact matrix cracking, delamination and fibre breakage can occur. The above phenomena change the in-plane stiffness of the laminate. This change is not uniform and depends on the shape and extent of the damage. One can assume that it increases from the lowest value in the indentation point to the undamaged value at the boundary of the affected field. This approach neglects complete buckling and delamination of sub-laminates which can result in inaccurate prediction, especially for the compressive loading. The underlying question is how to incorporate the gradual change of the stiffness around the impact point to the FE model and what should be the size of this area.

2.7. Summary of literature review

The above literature review allowed to identify some research gaps that gave the directions to pursue in this thesis project. Established methods, tools and trends define the subquestions to the two main research questions defined in the introduction of this thesis.

It was identified in the literature review that the novel approach of modelling damage utilising the multiscale material model generated using FE simulation of the RVE applied in the commercial software Multiscale Designer from Altair has not yet been evaluated either on the composite structures or the composite bonded joint models. This approach allows for the characterisation of the damage occurring on a microscale using the FE model of a RVE. Furthermore, coupled with the bottom-up approach for testing, the physics of the underlying damage initiation and propagation could be captured and explained in more detail, motivating the formulation of research question RQ1: ***How can the multiscale material model be generated using the representative volume element and used on macro level to predict damage in the composite material during static and residual strength simulations of bonded joints?***. The research in this thesis investigated the application of this approach to simulate the damage in the composite material in the static and residual strength simulation.

To characterise the CFRP material behaviour, data from coupon testing needs to be collected and post-processed. Stress-strain curves from coupon testing allow to model an accurate damage initiation and propagation in the composite material. However, what is the link between the coupon data and damage models is unknown. The interest of this thesis project lies in identifying crucial material parameters for a RVE characterisation and how unknown constituent parameters can be found using homogenization and inverse characterisation loop. This motivated the formulation of research subquestions RQ1.1: ***How can the damage initiation and propagation in composite be accurately modelled using the experimental data from coupon tests?***

In order to capture softening of the material and damage propagation in any material, very small time steps are usually required to reach a convergence in a numerical simulation. The work in this project is realised in the implicit solver thus the investigation focuses on the applicability of such material model in implicit solvers and if there are any additional steps or settings required for the application. This motivated the formulation of the second subquestion of the first research question RQ1.2: ***What is the applicability of the multiscale damage model generated with Multiscale Designer in the implicit***

Finite Element solver?

The material characterisation using RVE is based on the material models on the constituent scale. This allows to model damage on a micro-scale, however the damage in the composite bonded joints can occur also on a macro-scale. Thus the research subquestion RQ1.3: ***How to model a bonded joint using RVE generated multiscale material model to take into account all possible failure modes?*** was established in order to investigate what additional modelling features are needed to capture failure modes of bonded joints.

Evaluation of state of the art in the subject of impact on composite bonded joints allowed identifying current research gaps. The main research gap is related to the two-step simulation of the impact. The current bottleneck of the simulation is that models include relatively coarse meshes, the simulation takes a very long time, and the model are limited to very narrow coupons with the typical width of 25mm. As identified, the most computationally costly is the first step consisting of an explicit impact simulation. Thus, the second research question RQ2: ***How can damage resulting from low-velocity and low-energy impact be included in the Finite Element Model without running an explicit impact simulation?*** was established, aiming to reduce the simulation time by skipping the first step of the simulation. The investigation focused on whether impact damage can be included in the model without running an explicit impact simulation. This can contribute to the development of efficient virtual testing methods to assess the effects of BVID in CFRP structures.

A substantial gap in research is related to the applicability of the simplified modelling approaches of the impact damage in FE elements models. The approaches proposed by Kassapoglou [43], originally for the semi-analytical methods should also be evaluated in the FE models. This motivated the formulation of the first subquestion of the second research question RQ2.1: ***What is the applicability of the simplified modelling approaches, such as modelling impact damage as a hole, delamination and region of reduced stiffness in composite bonded joints?***

The methods used to model damaged areas in composite materials and adhesives should be further evaluated in terms of their ability to represent low-energy and low-velocity impact damage. Firstly the method of deleting elements in the damaged area as proposed by Llopart *et al.* [61], and secondly detaching solid elements representing plies for the modelling of the delamination. The two methods create a base for the formulation of the subquestions RQ2.2: ***What is the applicability of the modelling techniques, such as removing elements and detaching solid elements to represent impact damage in the form of delamination in composite bonded joints?***

Taking into account experimental observation in the work of Völkerink [16], Purimpat *et al.* [37], and Kupski *et al.* [38] where the researchers showed that damage initiates and propagates in the single lap configuration in the bondline region up to the first 0° ply, the research subquestion RQ2.3: ***Which interlaminar layers are critical for the representation of impact damage?*** was established in order to investigate if similar patterns about the criticality of the through-thickness position of delamination can be found in the impacted bonded joints. To provide a conservative representation of the impact damage, the critical delamination should be represented.

The predictability of the method in this project is evaluated in RQ2.4: ***How accurately and efficiently can ultimate load be predicted using the simplified impacted joint model?*** by taking into account two factors, the first one being the time of the simulation and the second one the accuracy of the results. The accuracy of the solution should underpredict the failure load ideally in the standard deviation range or with the relative error between simulation and test results not greater than 20 %. For the simulation time, due to this being one of the first proposals seen in the literature, a few days of simulation for the first applications will be satisfactory. Ideally, it should be reduced to the time of one day.

The summary of the research questions established based on the previous work at Airbus, goals of the JoinDT project and literature review is presented Figure 2.23.

Research Question RQ1

How can the multiscale material model be generated using the representative volume element and used on macro level to predict damage in the composite material during static and residual strength simulations of bonded joints?

Subquestion RQ1.1

How can the damage initiation and propagation in composite be accurately modelled using the experimental data from coupon tests?

Subquestion RQ1.2

What is the applicability of the multiscale damage model generated with Multiscale Designer in the implicit Finite Element solver?

Subquestion RQ1.3

How to model a bonded joint using RVE generated multiscale material model to take into account all possible failure modes?

Research Question RQ2

How can damage resulting from low-velocity and low-energy impact be included in the Finite Element Model without running an explicit impact simulation?

Subquestion RQ2.1

What is the applicability of the simplified modelling approaches, such as modelling impact damage as a hole, delamination and region of reduced stiffness in composite bonded joints?

Subquestion RQ2.2

What is the applicability of the modelling techniques, such as removing elements and detaching solid elements to represent impact damage in the form of delamination in composite bonded joints?

Subquestion RQ2.3

Which interlaminar layers are critical for the representation of impact damage?

Subquestion RQ2.4

How accurately and efficiently can ultimate load be predicted using the simplified impacted joint model?

Figure 2.23: Summary of the established research questions.

3

Specimens and mechanical testing

This chapter describes the background for the choice of the bonded joint samples and the mechanical tests that were conducted. The acquisition of the data from the tests is mentioned briefly. Samples used in the thesis project were manufactured and tested as a part of the JoinDT project by the University of Stuttgart, German Aerospace Center and Airbus Defence and Space. Data from mechanical testing was used to create a modelling approach for the impact damage in single lap configuration and to validate the results of numerical models developed for pristine, artificially damaged and impacted bonded joints. The manufacturing and mechanical testing was not performed within the scope of this thesis. The variety of the data from testing was used as an input data for the development of the simulation methodology and was post-processed in the scope of this thesis project.

3.1. Background on the specimen choice

The first experiences in the testing and simulation of single lap joints on a large scale were started at Airbus during the EU-funded project Boltless Assembling Of Primary Aerospace Composite Structures (BOPACS). During this project, the research in the direction of the composite adhesive joints for primary aircraft structures was conducted. Most of the relevant research investigated the fatigue behaviour of the joint with damage and defects coming either from manufacturing or impact.

To study the effects of defects and impact, a wide single-lap shear (WSLS) specimen was chosen. The WSLS specimen is a standard SLS specimen but significantly longer in the width direction. The initial studies were conducted on the specimen with a 500mm width. This gives enough space to test the effects of defects and damage without free edge effect which can interfere with the stress field around the damaged area. The initial overlap length has been set to 60 mm, chosen as a representation of large longitudinal adhesive joints that occur for example in fuselages. A great example of such an application can be a longitudinal connection of the fuselage parts in Airbus A350 XWB. A schematic of such a connection is presented in Figure 3.1. It was established that this specimen will allow research on the influence of manufacturing and impact damage on the realistic, bonded element.

The single-lap configuration is a simple joint configuration of two flat bodies but can also be used as the model for curved surfaces for which the curvature in the joint can be neglected if the radius of curvature is greater than 2000 mm. Otherwise, the curvature should be considered [62]. There is little knowledge on the subject of impact damage on bonded specimens of this size and the spread of damage. Therefore, it makes sense to keep the bond configuration as simple as possible at the beginning of an investigation to produce basic results. Furthermore, the results of the WSLS investigations were supposed to validate a simulation methodology. With this approach, it should be possible in the future to design adhesive joint structures in a damage-tolerant manner.

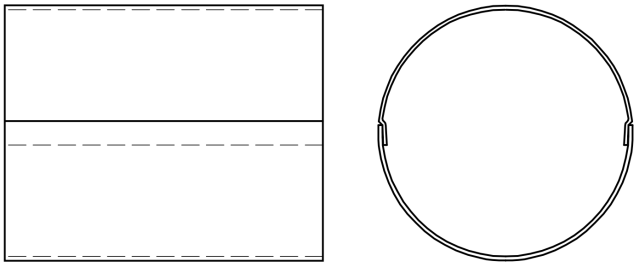

Figure 3.1: Longitudinal single-lap connection of fuselage sections. From Kim et al. [63].

However, experiences with simulations of the WSLS showed that with the current computational power and mesh size being limited to a size under 1mm, it's not possible to produce accurate and robust simulation results on such a large specimen [64]. In the JoinDT project, it was decided to decrease the width of the joint from 500mm to 100mm in the representative single-lap tension after impact (SLTAI) samples with artificial and impact damage. This allows to reproduce the model numerically with reasonable computational time, which wasn't possible for WSLS joint with the available resources, and still keep a reasonable width so that the edge effect won't significantly affect the stress field of the damaged area. For the pristine samples used as an initial validation of the modelling approach, a relatively small width of 25mm samples was used for the development of the simulation methodology on base models.

3.2. Samples

Samples manufactured and tested are different variations of the classical SLS coupons as defined in the ASTM D5868-01 standard [65]. Two coupons, SLS0 and SLS45 are relatively small specimens with a 25mm width and were used to validate the initial methodology, the material model for the CFRP and the adhesive material model with low computational time. Two different layups of coupons were studied to observe different coupon failure modes - one dominating in the adhesive and a second one dominantly in the composite adherend, taking into account conclusions from the work of Völkerink [16], Purimpat *et al.* [37], Kupski *et al.* [38], and Galliot *et al.* [39].

3.2.1. SLS0

The SLS coupons manufactured from laminates with a $[(0, 45, 90, -45)_2]_s$ layup are referred to as SLS0. The coupon's dimensions are presented in Figure 3.2 and the length of the sample presented is a free length between the two clamps in the testing machine.

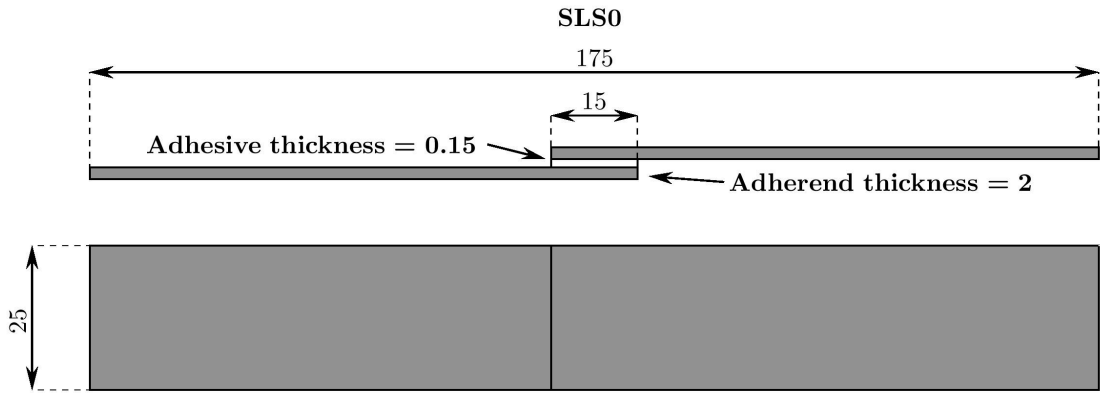

Figure 3.2: Geometry of SLS0 coupon.

3.2.2. SLS45

The SLS coupons manufactured from laminates with a $[(45, 90, -45, 0)_2]_s$ layup are referred to as SLS45. The coupon's geometry is presented in Figure 3.3.

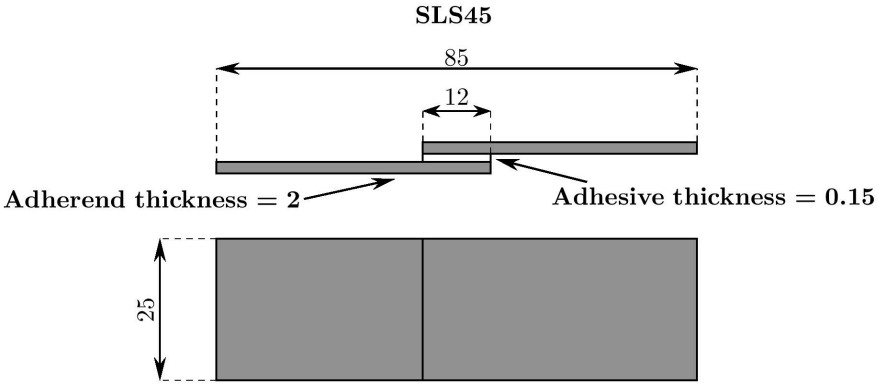

Figure 3.3: Geometry of SLS45 coupon.

3.2.3. SLTAI60

The wider version of SLS coupons manufactured from laminates with a $[(45, 90, -45, 0)_2]_s$ layup and overlap length of 60mm are referred to as SLTAI60. The coupon's dimensions are presented in Figure 3.4 and the length of the sample presented is a free length between the two clamps in the testing machine.

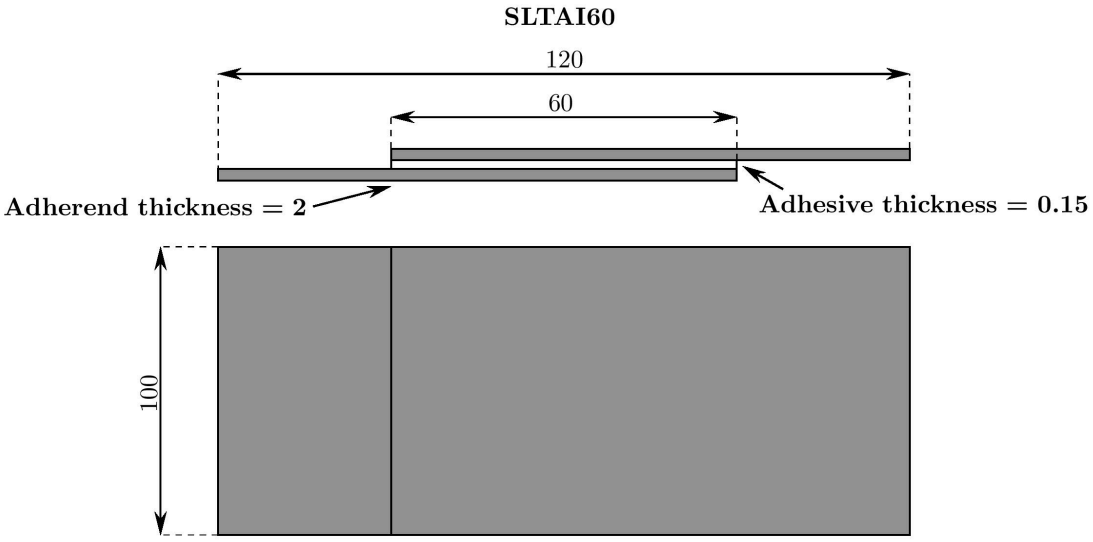

Figure 3.4: Geometry of SLTAI60 samples (not to scale).

Damage in bonded joints is assumed to originate mainly from two mechanisms, manufacturing defects and impacts. One of the most studied types of defects is a disbond or kissing bond, an adhesive bonding defect in which the adhesive and the substrate are in contact but the interface has a lack of adhesion. Disbonds can be caused in the manufacturing process by contamination or by various forms of environmental factors. They are especially dangerous because it's one of a very specific type of defect that cannot be detected with a standard NDI. To study the effects of manufacturing defects,

samples with artificially introduced defects to act like a disbond were introduced with the help of release film placed between the composite adherend and adhesive. The naming convention for the samples is SLTAI60 disbond and the geometry of defect presented in Figure 3.5.

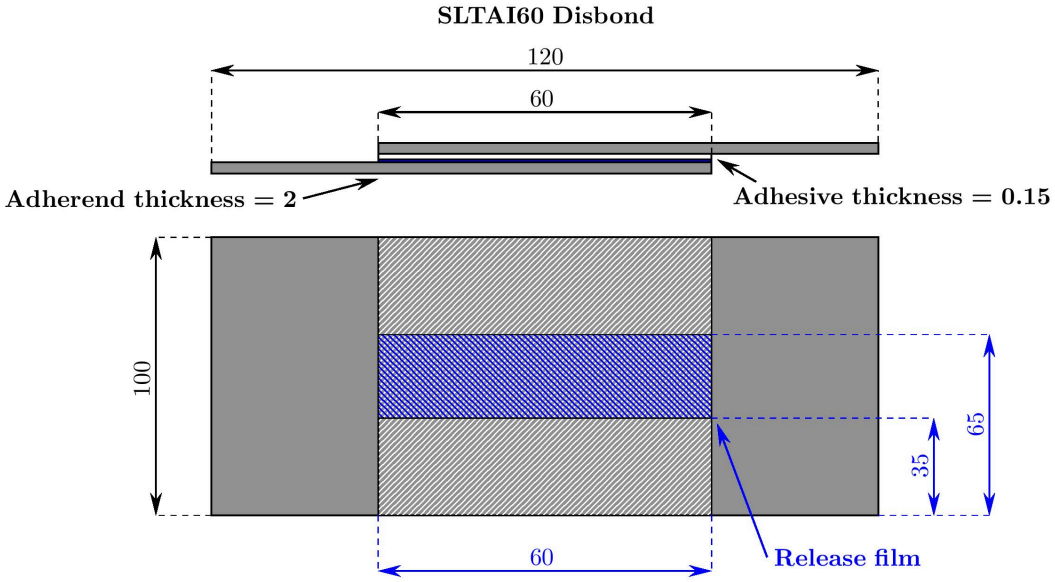

Figure 3.5: Geometry of SLTAI60 disbond samples (not to scale).

Delamination is a common failure mode and damage type that occurs during the impact in which cracks grow between the plies of the composite material. During manufacturing, a release film was inserted between the plies of the composite laminate to create artificial delamination in the adherend. The through-thickness application of release film is presented in Figure 3.6. The geometry of the SLTAI60 samples with artificially introduced delamination is presented in Figure 3.7.

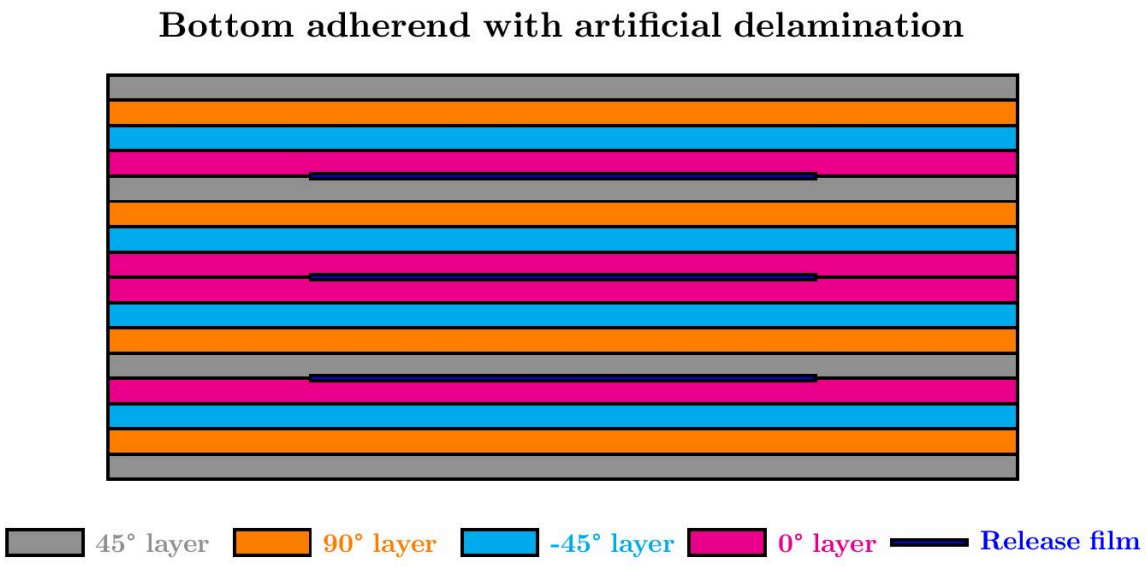

Figure 3.6: Through-thickness position of the artificial delamination in SLTAI60 specimen.

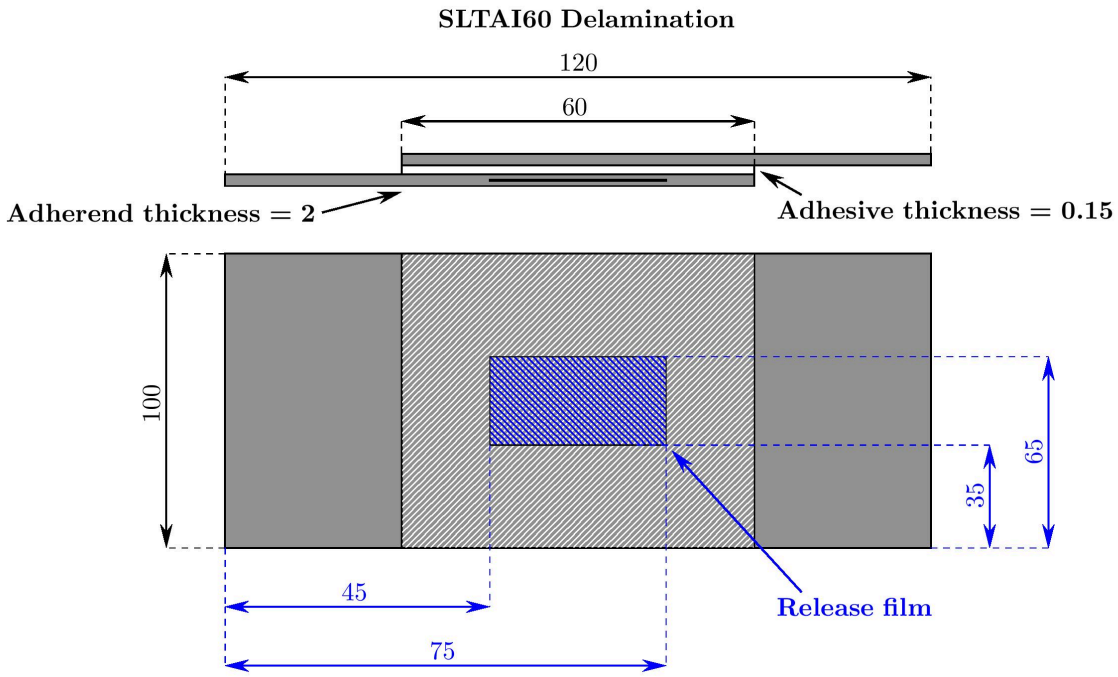

Figure 3.7: Geometry and dimensions of SLTAI60 delamination sample (not to scale).

3.2.4. SLTAI30

The wider version of SLS coupons manufactured from laminates with a $[(45, 0, -45, 90)_2]_s$ layup and overlap length of 30mm are referred to as SLTAI30. The coupon's dimensions are presented in Figure 3.8 and the length of the sample presented is a free length between the two clamps in the testing machine.

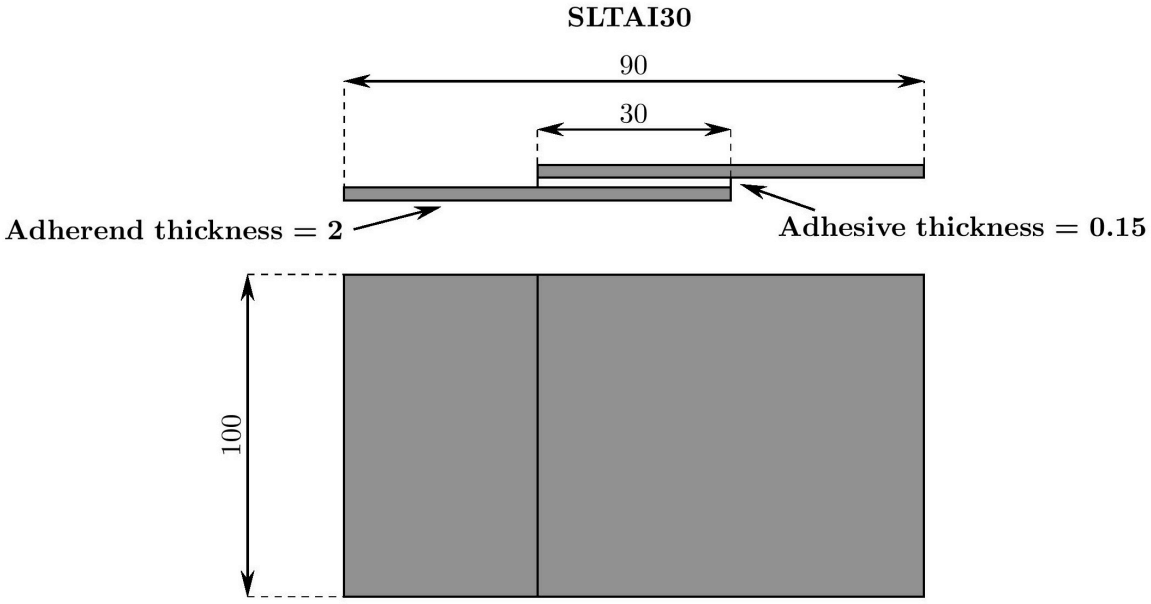

Figure 3.8: Geometry and dimensions of SLTAI30 sample (not to scale).

To study the effects of impact damage, SLTAI30 samples were impacted in the position close to the adhesive edge reported by Farrow *et al.* [60] as one of the critical impact positions for the single-lap configuration. Chosen impact position is in the middle of the joint's width with a 10mm offset from the overlapping centre. The geometry and position of impact are presented in Figure 3.9.

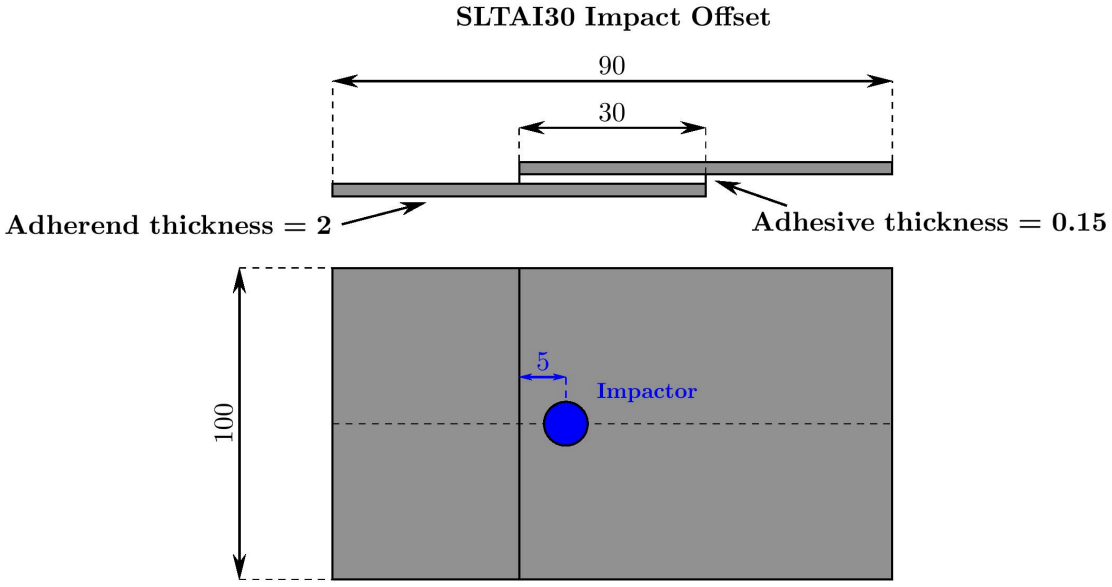

Figure 3.9: Geometry and dimensions of SLTAI30 impact samples (not to scale).

3.3. Manufacturing

All coupons in this study were manufactured using unidirectional Hexcel® HexPly® prepreg with IM7 fibre in 8552 resin as the material for adherend laminate and LOCTITE® EA 9695 AERO film adhesive. Film adhesives have the advantage of creating an uniform adhesive layer thickness throughout large areas in contrast to paste-like adhesives, which results in a more uniform thickness of a adhesive. The CFRP panels were manufactured from 16 layers of prepreg in different layup configurations resulting in a laminate thickness of 2mm. The plates were manufactured by a hand layup with a peel ply placed on the top of the panel, sealed in a vacuum bag, and cured in an autoclave with the curing cycle recommended by the manufacturer. After curing, the plates were demoulded and cut down into smaller sizes with diamond saw. The surface preparation of the samples before bonding was made with an isopropyl and an atmospheric pressure plasma treatment for samples manufactured at DLR - SLS0, SLS45 and SLTAI60 and with the isopropyl and manual grinding using Scotch-Brite™ Handpad 7447 for the samples manufactured at Airbus - SLTAI30. In an autoclave process, two composite plates were joined together while vacuum and temperature were applied for the duration recommended by the adhesive manufacturer. Finally, joints were cut to the width size of the specimen and were inspected by a technician visually and with an ultrasonic scan for the presence of any unwanted manufacturing defects.

3.4. Testing of specimens

To validate a numerical simulation, three indicators were used, namely (i) ultimate load - mean value and standard deviation, (ii) stiffness and (iii) failure mode. Those were measured during the testing campaign on SLJ specimens. Static strength, impact and residual strength tests were conducted during this project.

3.4.1. Static and residual strength

The norm for static testing of SLS specimens is ASTM D-5868-01 [65]. This test was designed to determine the shear strength of adhesives for bonding materials when tested on an SLS joint. The tests were performed following the standards, with the main difference in the geometry of the samples.

For the static tests, the Zwick 1494 servomechanical testing machine was utilised. To ensure the non-eccentric load introduction of the specimens, the hydraulic specimen grips were positioned with an offset in the sample thickness direction. End tabs were bonded to the specimens in the grip region to guarantee proper in-plane alignment and to increase the area of the loading region and hence lower local stress concentrations to protect the edge material from being damaged. The tests were conducted at an ambient temperature of 23°C, and samples were loaded at a steady cross-head speed of 1.0 mm/min until a load drop occurred.

3.4.2. Impact

The AITM1-0010 [66] standard describes the procedure for carrying out an impact test. AITM stands for Airbus Test Method, and the standard is specially designed for testing fibre composites. As there is no separate standard for the impact test of composite bonded joints, the the standard test composite plates was utilised. The standard impactor with a 16 mm diameter and 3.048 kg mass was used. The velocity was adjusted by changing the height of the initial impactor position to obtain different impact energies. For the representative 8J sample studied in this thesis, the impact velocity was 1.62 m/s. CEAST Instron® 9350 drop tower impact system presented in Figure 3.10 was used for tests.

Figure 3.10: Drop weight impact testing machine.

Before the test, the samples were examined for the presence of defects with visual inspection. Bonded joints of a total thickness of 4.15mm were impacted (similarly to the standard composite plate thickness of 4mm ± 2% as per AITM1-0010 [66]) The schematics of impact test set-up and clamping of the specimen is presented in Figure 3.11.

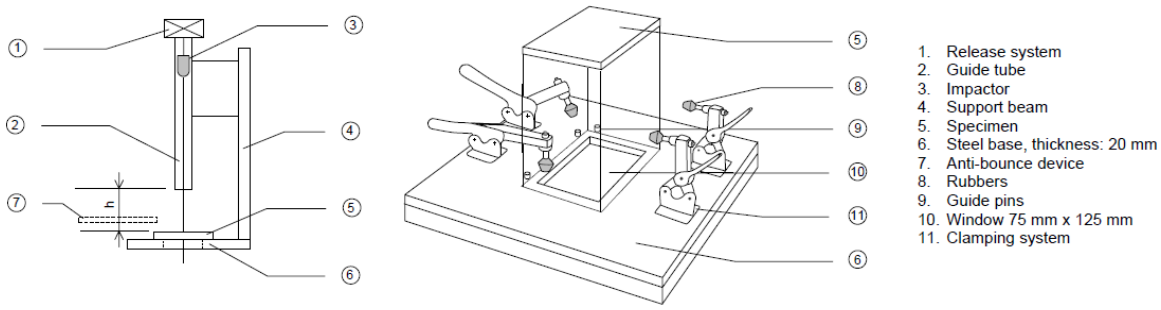

Figure 3.11: Set-up of impact test. Modified from Airbus [66].

The indentation measurement was conducted to assess if the impact can be classified as a low-energy impact on the specific structure. A Mitutoyo digital gauge was used to measure the indentation. This device measures indentation with an accuracy of 0.01mm. The measurement was conducted three days after the impact test for the relaxation of the material to take place. As defined in the Airbus standard, the indentation was measured from four points in different directions of the impact point and 20mm away from the impact point. The point of the measurement was the lowest point of the indentation. Due to the step present in the SLJ, one point lays on the surface at a different height. Thus only three points are used. The indentation was calculated as the mean of three measurements.

After the impact, a nondestructive inspection using ultrasonic B- and C-scans was conducted using 200 MHz ultrasonic imaging system USPC 3060 UHF. On some of the samples, a destructive inspection was conducted by cutting the area around the impact with a diamond blade to prevent any additional damage and conducting a microscopic inspection on the cross-section of the joint. After cutting, the specimens were cleaned from any excessive dust, cast in transparent epoxy and ground down on the cut edge side of the polish. These samples were analysed under a light microscope and evaluated. Between 20 and 100 photos with 50x magnification were taken for the microsection and assembled into a panorama image.

3.4.3. Displacement measurement

Force-displacement graphs were created based on the digital image correlation (DIC) analysis in the samples tested by DLR (SLS0, SLS45 and SLTAI60) and based on the laser extensometer measurements in the samples tested by Airbus (SLTAI30). To enable DIC measurements, speckles were painted on the side surface of the SLS0 and SLS45 specimens and to the top surface of SLTAI60 specimens. The points of relative displacement measurements are indicated for samples in the figures below, for SLS0 in Figure 3.12, for SLS45 in Figure 3.13, for SLTAI60 in Figure 3.14 and for SLTAI30 in Figure 3.15. The ARAMIS 12M system was utilised as a DIC system during the testing of one specimen from each series so that the displacement and strain of the specimen between the grips could be measured without being influenced by the stiffness of the testing machine. The displacement based on those specific points was used to compare with the simulation results, where displacement for nodes located in the same points was extracted.

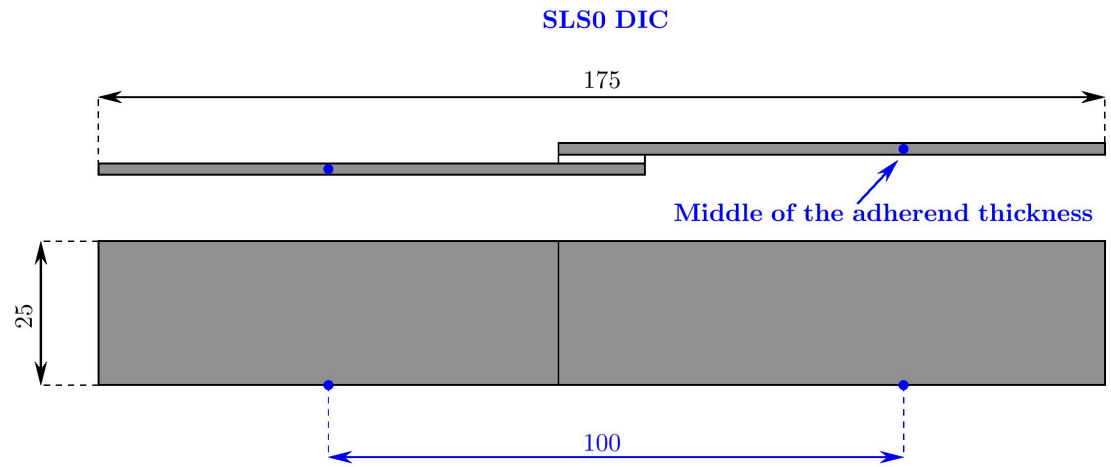

Figure 3.12: Points of displacement measurement with DIC on SLS0.

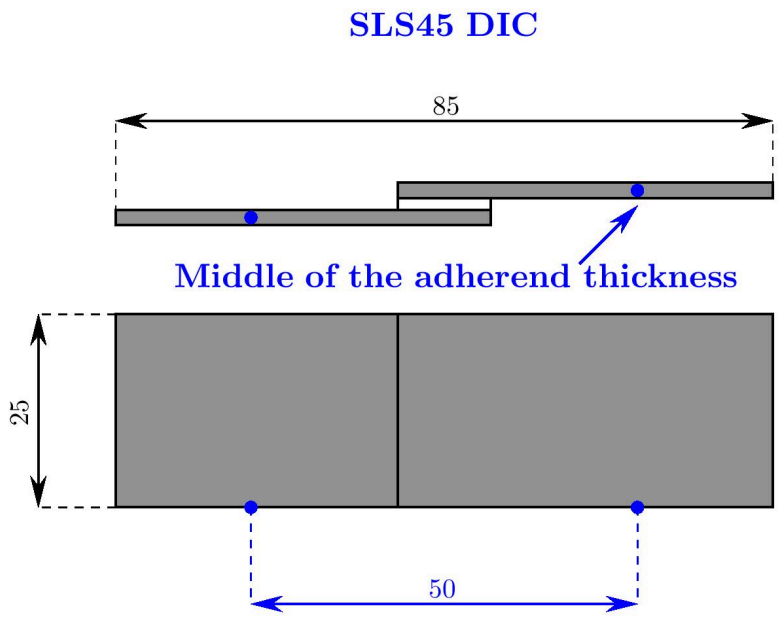

Figure 3.13: Points of displacement measurement with DIC on SLS45.

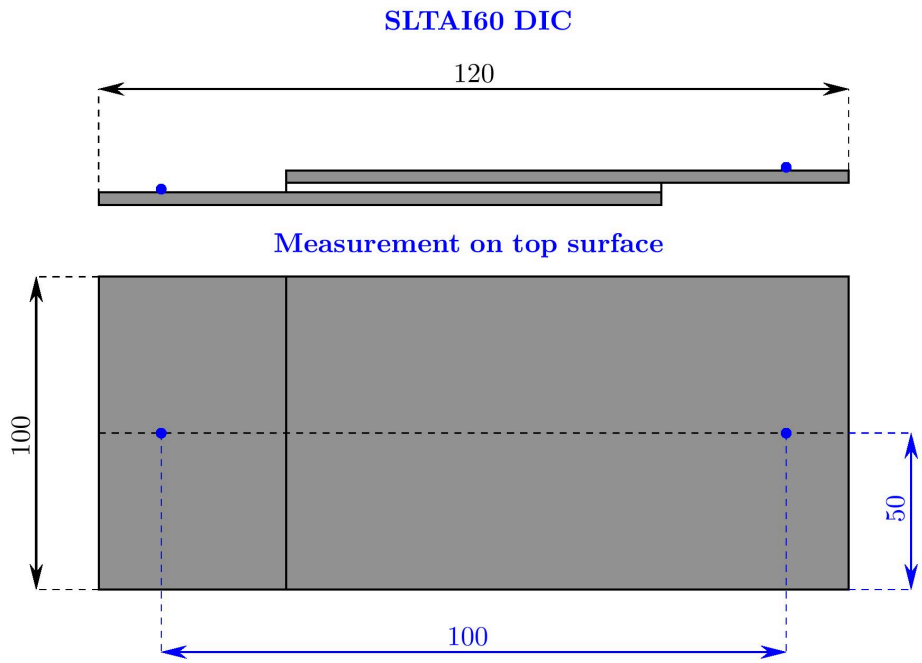

Figure 3.14: Points of displacement measurement with DIC on SLTAI60 (not to scale).

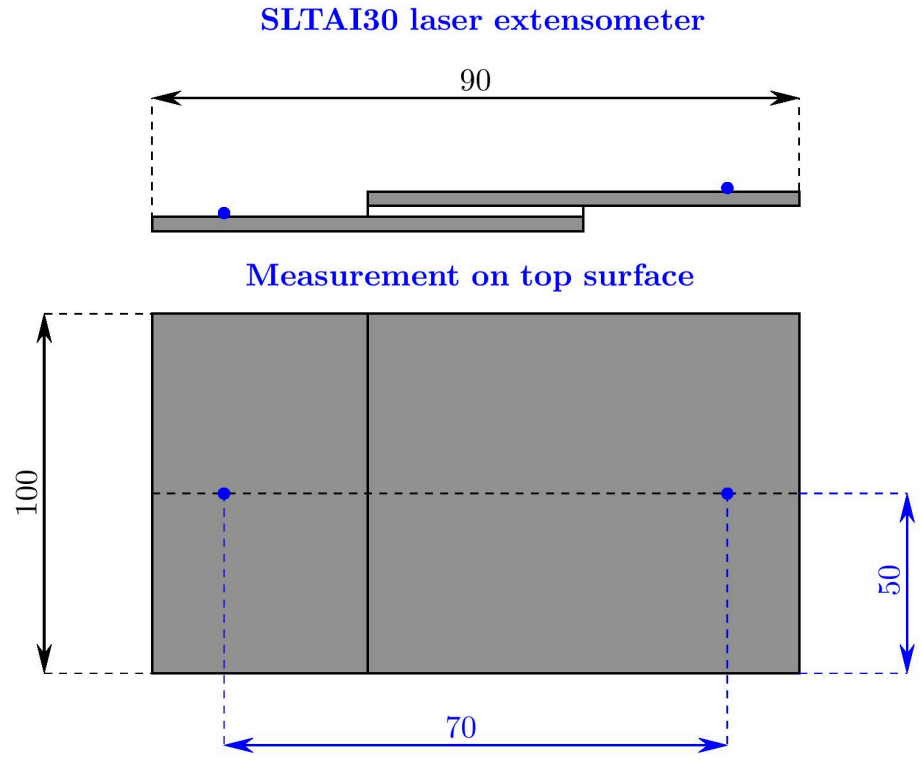

Figure 3.15: Points of displacement measurement with laser extensometer on SLTAI30 (not to scale).

4

Material characterisation using representative volume element

To characterise the mechanical behaviour of composite material, the virtual simulation of RVE was used to derive parameters of microphases needed to accurately simulate failure occurring in the composite adherends on the level of the constituents. The target composite material parameters used in the characterisation come from mechanical testing on a coupon scale and initial constituents parameters from the Altair material database. The characterisation of the phase parameters was based on homogenisation and inverse characterisation with the set homogenised target values. The numerical model was created with Multiscale Designer software from Altair, utilising existing material, damage and plasticity laws. The following chapter presents a multiscale material characterisation process using Multiscale Designer along with the methodology, guidelines for characterisation, a validation process, implementation to the solver and characterisation results. Generated material model in the scope of the thesis was used in the FE models of bonded joints to represent the behaviour of the composite laminate.

4.1. Material parameters of IM7/8552

In Table 4.1, the relevant material parameters that were utilised in the JoinDT project are presented. The indices have been assigned to differentiate between the various directions and loading conditions under which the properties were measured. Specifically, ”1,” ”2,” and ”3” correspond to the path along the in-plane longitudinal, in-plane transverse, and out-of-plane directions, respectively. Additionally, ”T” and ”C” indicate tensile and compressive loading conditions. These parameters were utilised as target values for the homogenised composite material in the RVE-based approach.

Table 4.1: Material properties of HexPly® IM7/8552 UD-prepreg. From JoinDT [67].

Property	Symbol	Value
Longitudinal tensile strength	X_T	2500 MPa
Longitudinal compressive strength	X_C	1200 MPa
Transverse tensile strength	Y_T	55 MPa
Transverse compressive strength	Y_C	253 MPa
Shear strength	S_U	91 MPa
Longitudinal tensile modulus	E_{11T}	171400 MPa
Longitudinal compressive modulus	E_{11C}	140600 MPa
Transverse tensile modulus	$E_{22T} = E_{33T}$	9100 MPa
In-plane shear modulus	$G_{12} = G_{13}$	4500 MPa
Transverse shear modulus	G_{23}	3140 MPa
In-plane Poisson ratio	$\nu_{12} = \nu_{13}$	0.32
Transverse Poisson ratio	ν_{23}	0.45

4.2. Material characterisation methodology

This work used the approach of material characterisation with RVE proposed by Altair [33] and Fish [68] in the Multiscale Designer tool version 2022.0. It consists of a few steps, where in the first step, the unit cell model is created and meshed.

Next, two steps of linear and non-linear material characterisation are needed to characterise the elastic and in-elastic material behaviour. This is needed to create a reduced order material model with the approach of Fish [68]. This separation of the characterisation into two steps allows for using a reduced order elastic model as a base for characterising the non-linear behaviour with damage and plasticity laws on macroscale virtual tests of composite coupons. The elastic material model represented in the form of the set of two stiffness matrices differentiating tensile and compressive loading scenarios and a set of matrices linking homogeneous strains to the constituent strains allows to derive further sets of matrices describing the non-linear homogenised behaviour, and its link to the constituent scale. This is described in more detail in subsection 4.2.6.

In the second step of the material characterisation process, the matrix and fibres' linear (elastic) material properties are calibrated, considering different directions and different behaviour in tension and compression based on the homogenised target values of the composite material. The target values are the material properties established in the JoinDT project presented in Table 4.1. Properties of fibres and matrix are found and optimised in a loop of homogenisation and inverse characterisation of composite material.

After that, in the third step, non-linear properties (damage and plasticity) are defined, and the same optimisation process is run for non-linear properties using stress-strain curves from coupon tests. In this process, the parameters defining the failure behaviour of the matrix and fibre can be found, and thus a failure occurring on the constituent scale can be characterised.

After the constituents parameters are derived, in the last fourth step, the reduced order model of the RVE is created in which matrices defining the link between the homogenised and constituent strains are saved. The process of material characterisation is presented in Figure 4.1.

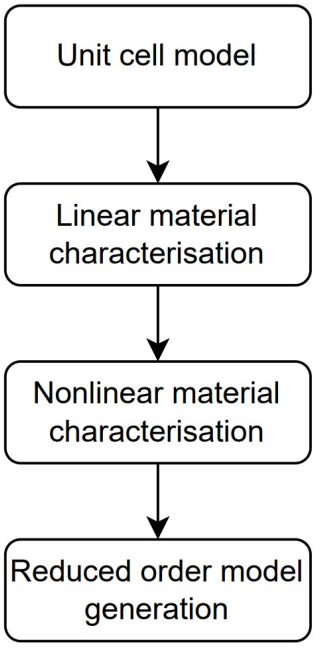

Figure 4.1: Flowchart of the material characterisation process.

The two techniques used to derive the parameters of the constituents used in the process are homogenisation and inverse characterisation. They are an essential part of this process as known material parameters are on the homogenised material behaviour scale, and in order to characterise the behaviour of constituents in the approach of Fish [68] both are needed. The failure of the fibre or matrix drives the failure modes of composite material. A micromechanical model can capture individual constituents degradation accurately, and information from that model can be coupled with a larger ply scale in the material's homogenisation process. However, composite material testing occurs on the ply level, and testing neat fibre is nearly impossible. Thus, inverse characterisation can be used to obtain properties of fibres and matrix when ply properties are known, and an initial guess for the constituent properties is provided. The process of the optimisation loop proposed by Altair [33] to calibrate properties of constituents based on the parameters of homogenised material is presented in Figure 4.2.

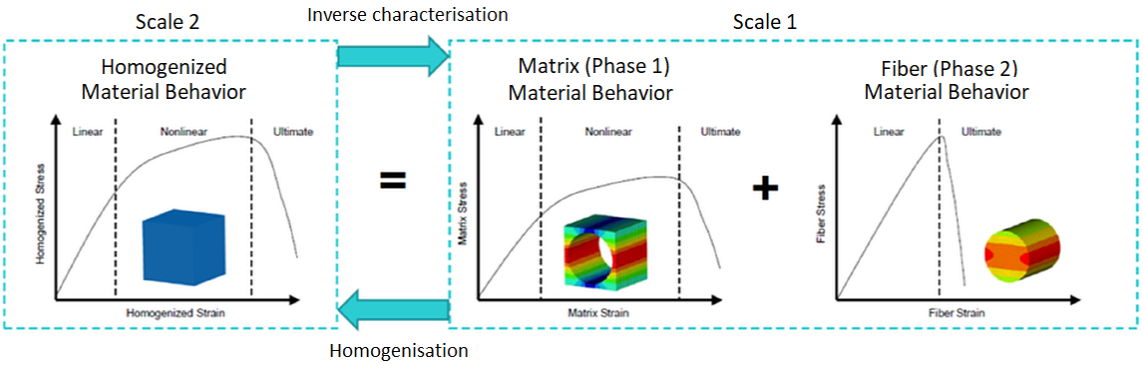

Figure 4.2: Optimisation loop of homogenisation and inverse characterisation of composite material. From Altair [33].

4.2.1. Forward homogenisation

In the forward homogenisation, the microphase properties are defined, and the matching macro properties of the heterogeneous unit cell are determined in the homogenisation simulation. It allows replacing the composite medium with an equivalent homogeneous medium to solve the global material simulation problem easily. The approach is that the material is considered as one homogeneous medium despite comprising two separate phases. The homogenised properties of the composite unit cell are calculated based on the theory of elasticity. The relation between the stress and strain of the material is described by the stiffness matrix and is defined for orthotropic material as

$$\begin{Bmatrix} \sigma_1 \\ \sigma_2 \\ \sigma_3 \\ \tau_{12} \\ \tau_{23} \\ \tau_{13} \end{Bmatrix} = \begin{bmatrix} C_{11} & C_{12} & C_{13} & 0 & 0 & 0 \\ C_{21} & C_{22} & C_{23} & 0 & 0 & 0 \\ C_{31} & C_{32} & C_{33} & 0 & 0 & 0 \\ 0 & 0 & 0 & C_{44} & 0 & 0 \\ 0 & 0 & 0 & 0 & C_{55} & 0 \\ 0 & 0 & 0 & 0 & 0 & C_{66} \end{bmatrix} \begin{Bmatrix} \epsilon_1 \\ \epsilon_2 \\ \epsilon_3 \\ \gamma_{12} \\ \gamma_{23} \\ \gamma_{13} \end{Bmatrix}. \tag{4.1}$$

In this approach, the stiffness response of the homogeneous material is measured by executing multiple FE simulations of the unit cell. This is a direct single-step process. The response of the homogenised medium is measured by the response of the unit cell to the unitary strains, three in the axial and three in the shear directions. This means that in total a scheme of six simulations is needed to characterise the full stiffness matrix. An example of the boundary condition for the unitary strain being applied in the x direction is

$$BC1 : \epsilon_1 = 1 \quad and \quad \epsilon_2 = \epsilon_3 = \gamma_{12} = \gamma_{23} = \gamma_{13} = 0. \tag{4.2}$$

The 3D stress state is simulated for each boundary condition due to the unitary strain in one direction. From this stress state, an average value over the volume can be measured as

$$\overline{\sigma_i} = \frac{\int \sigma_i dv}{\int dv}. \tag{4.3}$$

Due to the applied unitary strain, the measured stress is directly equal to the specific column values in the stiffness matrix. And for the BC1 can be measured as

$$C_{11} = \overline{\sigma_1},\ C_{21} = \overline{\sigma_2},\ C_{31} = \overline{\sigma_3}. \tag{4.4}$$

This is repeated for five other boundary conditions to assemble the whole stiffness matrix of homogenised material. After the stiffness matrix is calculated, the compliance matrix can be calculated as

$$[S] = [C]^{-1}. \tag{4.5}$$

From the compliance matrix, nine independent engineering constants can be calculated using the dependency

$$[S] = \begin{bmatrix} \frac{1}{E_1} & \frac{-\nu_{21}}{E_2} & \frac{-\nu_{31}}{E_3} & 0 & 0 & 0 \\ \frac{-\nu_{12}}{E_1} & \frac{1}{E_2} & \frac{-\nu_{32}}{E_3} & 0 & 0 & 0 \\ \frac{-\nu_{13}}{E_1} & \frac{-\nu_{23}}{E_2} & \frac{1}{E_3} & 0 & 0 & 0 \\ 0 & 0 & 0 & \frac{1}{G_{12}} & 0 & 0 \\ 0 & 0 & 0 & 0 & \frac{1}{G_{23}} & 0 \\ 0 & 0 & 0 & 0 & 0 & \frac{1}{G_{13}} \end{bmatrix}. \tag{4.6}$$

Those constants define the behaviour of the homogenised material based on the six unitary strain simulations of the RVE.

4.2.2. Inverse characterisation

The inverse characterisation requires an initial value of the micro- and macro-phase based on the optimisation loop. The task to be solved is determining the fibre and matrix constituent properties that will produce the homogenised objective parameters. This loop consists of two-step homogenisation from the level of the constituent to homogenised composite material and an update of the initial parameters based on the homogenised target values.

For the optimisation problem, selected macro properties of the unit cell are user-defined from experimental data, and the micro-phase material properties that would produce the material's macro homogeneous properties are determined. This allows calibration of the micro properties based on experimental macro data from different layups tested.

The material inverse characterisation problem is reduced to solving a nonlinear least squares problem. Additionally, the side restrictions are prescribed to the optimised parameters to prevent solutions far from the initial values during the inverse characterisation process. The selected set of target values are the macro material properties in the case of a linear characterisation (the engineering constant for a given linear elastic material law) and a set of stress-strain curves (points defining curves) for a nonlinear region. The optimisation problem is solved iteratively with a user-defined tolerance, maximum number of iterations and step bound.

Both active parameters (variables that can be altered) and objectives (responses that must be attained within tolerance constraints) are defined to complete an inverse characterisation issue. The initial value, the lower and upper bound of each active parameter must be given.

4.2.3. Unit cell model

A hexagonal fibre arrangement model was chosen to create a unit cell model of composite UD material. In principle, the hexagonal unit cell can capture the interaction between the matrix and fibre better compared to the square model [35]. Additionally, an interface between phases can be modelled. In this project, it was decided to proceed with the model without the interface. The use of the model with

the interface introduces additional unknowns to the material characterisation loop, which is unwanted. Having fibre and matrix parameters unknown is already a complex task to be solved. On top of that, in the last step of characterisation, a reduced order model is created, which spreads information back to the matrices defining the correlation between the homogenised material and constituents, thus it seems like a crucial part of the information about the interface could be lost in this process. For CFRP materials, it can be assumed that there is very good bonding between fibre and matrix because of a stable and high-quality production process. This led to the above choice of the unit cell model.

The geometry of the model, which is presented in Figure 4.3 was loaded from the unit cell library. The fibre radius and gap between fibres were calculated based on the fibre volume fraction. In the case of this characterisation, the fibre volume fraction was set to $V_f = 60\%$. For such a volume fraction, the values of the dimensionless geometrical parameters are presented in Table 4.2. With a chosen unit system of mm-t-s, the created unit cell's dimensions are in mm. The fibre volume fraction can differ in reality due to the production of the composite bonded joints by different project partners with different processes. However taking into account that fibre volume fraction wasn't measured on each manufactured sample, it was decided that one standard value will be used to represent adherend material. The value of 60% is standard for such material after curing, as also indicated by the Hexcel in material data sheets.

Table 4.2: Unit cell dimensionless parameters.

Parameter	Value
Unit cell length in x	1
Unit cell length in y	1
Unit cell length in z	1.7321
Fibre radius	0.4067
Fibre gap	0.0933
Fibre volume fraction	60%

The mesh on the RVE model was created automatically on the geometry using mesh control settings. For the chosen geometry, a real-time assistant in the software set the possible element size range between 0.05 and 0.1866. Adaptive meshing used quadratic tetrahedron elements (CTETRA10) with an element size of 0.1. Tetrahedron elements were chosen as the most suitable for meshing the curved geometries between the two constituents. The mesh size was chosen to guarantee good accuracy and computational time balance based on the recommended range. Additionally, a mesh study was conducted, and an influence of the mesh size in the recommended range was found to be insignificant. The details of the mesh study are presented in subsection 4.4. The mesh of the RVE model is presented in Figure 4.4.

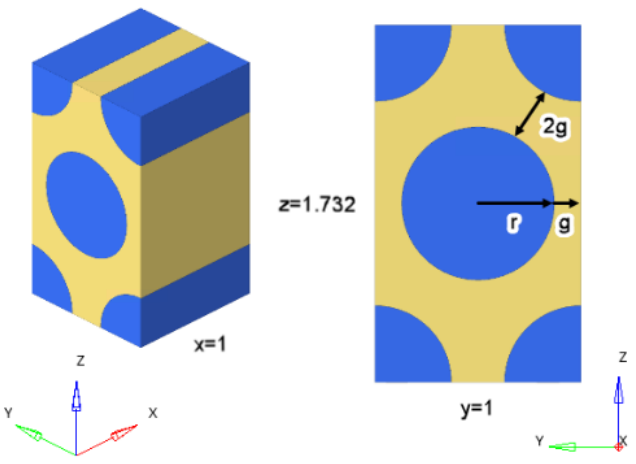

Figure 4.3: Geometry of RVE FE model.

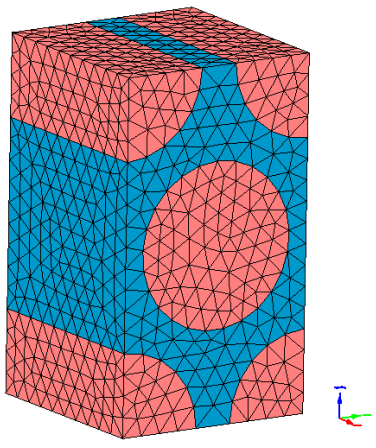

Figure 4.4: Mesh of RVE FE model.

4.2.4. Linear regime characterisation

The material characterisation process began with the identification of the initial constituent parameters. Linear material parameters for several physical fields must be defined for the general multi-physics analysis as material models can be used for implicit, explicit, and thermal analyses. Direct scalar fields (such as density), differential scalar fields (such as heat conductivity and diffusivity), and differential vector fields (such as elastic mechanical characteristics) are the three types of fields that can be characterised in a mathematical multiscale approach. To find the unit cell's micro and macro linear material features, forward homogenization and inverse characterisation can be applied for each field type. All micro phase parameters need to be prescribed a priori, and the matching macro unit cell homogenised properties are obtained by solving a forward homogenization problem. After the first homogenization is done, optimisation can be used to find the values of microphase based on the homogenised data set as a target of optimisation.

After the difference between the homogenised parameters of the unit cell and project values is acceptably small (under 1%), the linear reduced order model was derived automatically. The ROM of the linear part consists of the stiffness matrix of the homogenised RVE and amplification matrices which describe the relationship between the homogenised strains of the unit cell with the strains of the constituents in the linear regime. Figure 4.5 depicts the flowchart of the linear material characterisation process.

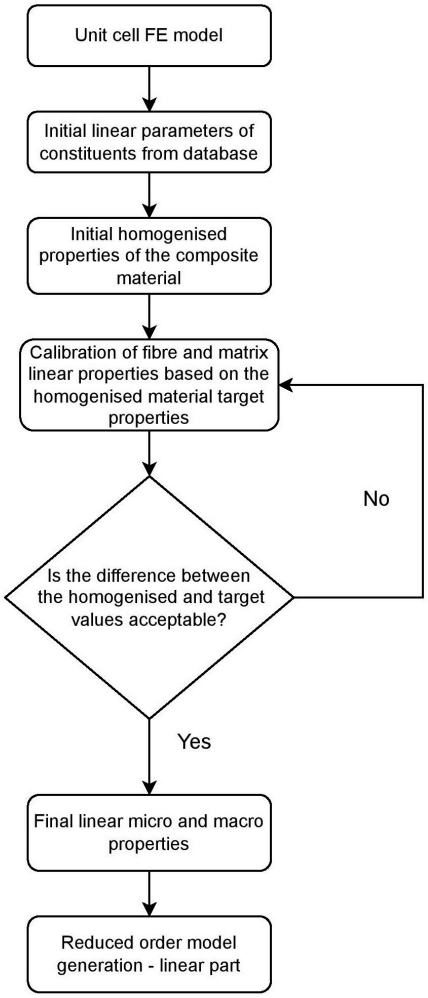

Figure 4.5: Flowchart of the linear material characterisation.

In practice, linear material characterisation started from the matrix and fibre data definition as an initial starting point for the loop of forward homogenization and inverse characterisation process. Due to the lack of data, it was chosen to start with generic parameters from the constituent material Altair database. To obtain the most accurate values, the initial properties of the IM7 carbon fibre were defined as the intermediate modulus carbon fibre from the database, and for the 8552 matrix, a high modulus epoxy was chosen. All parameters in the database were characterised at room temperature (23°C) in a dry environment. Different symmetry types characterise each microphase to reduce the number of material parameters describing an elastic response of the material. For the matrix, an isotropic symmetry and for the fibre, a transversely isotropic type was chosen. Next, the homogenization and inverse characterisation problems in the optimisation loop were solved. In Table 4.3, identified groups that can be used for the optimisation scheme are presented. First, the single parameters were targeted to obtain more accurate values based on single homogenised target properties. After that, final optimisations utilising a group of parameters was used. The number of active parameters must be less than or equal to the number of objectives. In this case, the equal number was always used. Identified groups were used one after another until the difference between the simulated homogenised properties and target values were under 1%.

Table 4.3: Groups of active variables and optimisation targets used for initial and final optimisation during linear material characterisation.

Active constituent parameter	Target homogenised property
Initial	
Fibre: E_{11T}	E_{11T}
Fibre: E_{22T}	E_{22T}
Fibre: ν_{12}	ν_{12}
Fibre: G_{12}	G_{12}
Fibre: E_{11C}	E_{11C}
Final	
Matrix: E_T Fibre: E_{11T}, E_{11C}, E_{22}	E_{11T}, E_{11C}, E_{22T}, E_{33T}
Matrix: E_C Fibre: E_{11T}, E_{11C}, E_{22}, G_{12}, ν_{12}	E_{11T}, E_{11C}, E_{22T}, E_{22C}, G_{12}, ν_{12}
Matrix: ν Fibre: ν_{12} and ν_{23}	ν_{12}, ν_{13}, ν_{23}
Matrix: E_T Fibre: G_{12}, E_{22}	G_{12}, G_{23}, G_{13}

4.2.5. Non-linear regime characterisation

As in the linear material characterisation step, both the forward homogenization and inverse characterisation approaches were used to characterise the nonlinear macro homogenised characteristics and the nonlinear micro properties. The nonlinear material models of constituents are based on the damage and plasticity models.

All nonlinear micro qualities are a priori-defined using a material database as the starting point, and in the forward homogenization approach, the nonlinear homogenised parameters are computed. At the same time, nonlinear macro features are characterised by executing multiple macro simulations on the coupon level. Nonlinear macro homogenised properties are determined based on experimentally observed test data from the coupon tests, and the unknown nonlinear micro properties are characterised by solving the optimisation problem. Macroscopic stress-strain test data from separate coupon tests can be included simultaneously in creating the optimisation objective function for an inverse characterisation of the mechanical solution sequence. Figure 4.6 depicts the flowchart of the nonlinear material characterisation process.

Similarly, a least squares problem with side restrictions is to be solved for the nonlinear characterisation. This is based on the data points on stress-strain curves. To efficiently run an optimisation scheme, a step of simulation and data spacing from the tests has to be unified to the same data spacing in the strain domain.

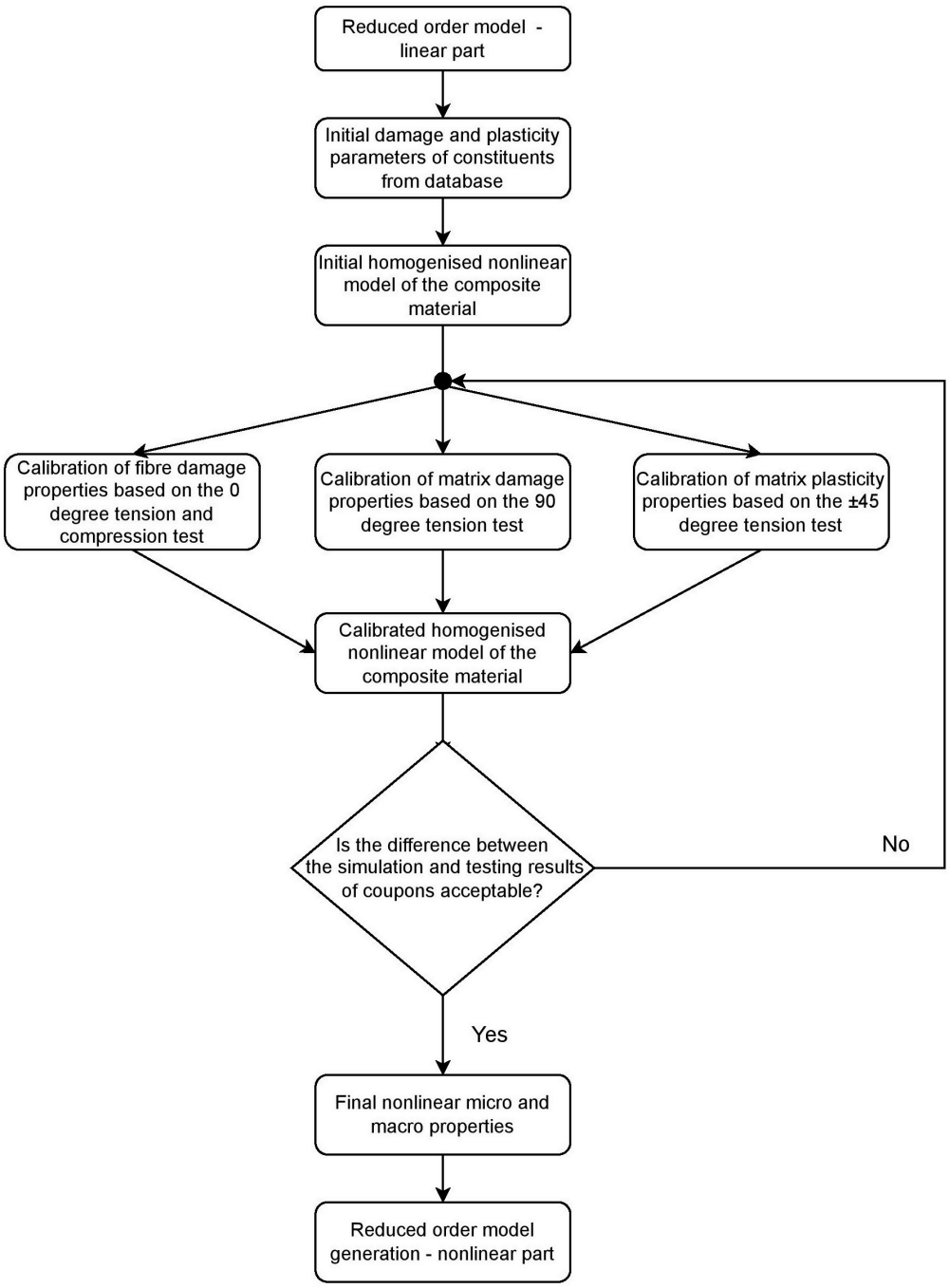

Figure 4.6: Flowchart of the nonlinear material characterisation.

Fibre damage model

Constituents of composite material show different behaviour during the damage initiation and propagation and thus have to be characterised by different damage laws. Fibre is known to suffer from brittle failure behaviour [68]. Under idealised conditions, fibre failure can be modelled with a shear or von Mises strain condition. Under realistic conditions inside composite materials, the shear limit can not be attained under axial loading. In tension, brittle failures occur, often aided by material imperfections, and cause fracture before the shear limit is reached [68].

Similarly, in compression, fibre instability is the intervening failure mode. Fibre instability is a complex process that involves interactions between local matrix failure near the fibre, which can accelerate fibre buckling. In practice, the damage of fibre is essential to model under axial load since matrix failure dominates in the transverse direction [32]. To accurately model fibre failure with a simple model, one can assume that fibre fails only under axial loading conditions and can be characterised with a simple bilinear continuum damage model described by the failure stress - σ_0 and strain at zero stress - ϵ_1 (representing complete degradation of a fibre). Figure 4.7 presents the damage law's visualisation. This is distinguished between the tensile and compressive loading conditions in the axial direction. Material degradation is formulated by degradation of the elastic stiffness tensor using one scalar damage state variable w.

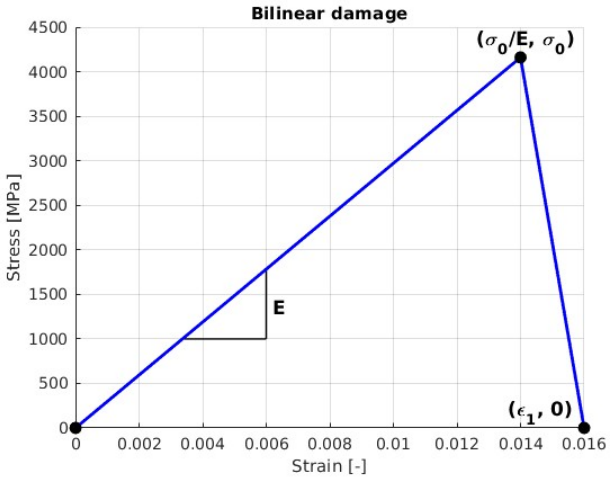

Figure 4.7: Bilinear continuum damage model of fibre.

The damage mechanics models often suffer from stability and convergence issues. To tackle this problem, a damage propagation process can be stretched in the time domain by increasing the strain difference between the damage initiation and final failure [33]. For the numerical stability reasons in the fibre model, the strain at full degradation can be assumed as

$$\epsilon_1 = 1.1\frac{\sigma_0}{E_{11}}, \tag{4.7}$$

where σ_0 is stress in a fibre at damage initiation and E_{11} is the longitudinal Young's modulus of fibre.

Matrix damage and plasticity model

Plastic materials show brittle and ductile behaviour depending on the loading conditions. The volumetric strain dominates the brittle behaviour, and the shear strain dominates the ductile behaviour [33]. Epoxies and other highly cross-linked polymers show low strain to failure under loading resulting in dilatation (change in volume without change in shape). Still, they can withstand very high strain to failure under loading resulting in distortion (change in form without volume change). Combining the damage model to represent a brittle behaviour with the volumetric strain-driven rate-independent plasticity model allows for the modelling of these materials [68]. It takes into account both the brittle and plastic behaviour of the polymer. The rate-independent model means that when a material experiences a certain stress level, it undergoes irreversible straining described by the plasticity law. The plastic strains are assumed to occur immediately and are not affected by time. The plasticity model incorporates a linear and a quadratic factor for pressure sensitivity in the yield surface to account for the pressure sensitivity of the yield point in polymers. For the linear and quadratic terms, there are two associated parameters, 1 and 2, respectively. The linear term by itself is often adequate for minor stacked volumetric strains. The matrix phase is tightly bound in a carbon fibre-polymer matrix composite and may undergo mild

volumetric strains. In this situation, the quadratic term can be added to the model because the linear term might not be adequate [33].

The chosen orthotropic damage law degrades the material's stiffness by three damage variables (w1, w2, w3) aligned with a local material coordinate system of three orthogonal axes. The orthotropic model accounts for the orthotropy introduced into the material by the directional nature of the stiffness lost during cracking. In contrast to the isotropic continuum damage model, which considers a norm of the principal strain vector, the orthotropic continuum damage model evolves damage in a two-step process. Depending on their orientation and the appropriate compression and shear factors, the main strain vectors are computed and modified in the first step. In the second step, the damage is evolved by requiring all three modified principal strain vectors to lie within an ellipsoidal surface. The visualisation of enforced damage law is presented in Figure 4.8 and the visualisation of the plasticity law in Figure 4.9.

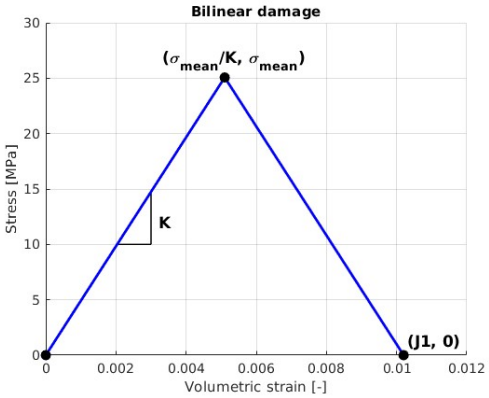

Figure 4.8: Bilinear damage law of matrix

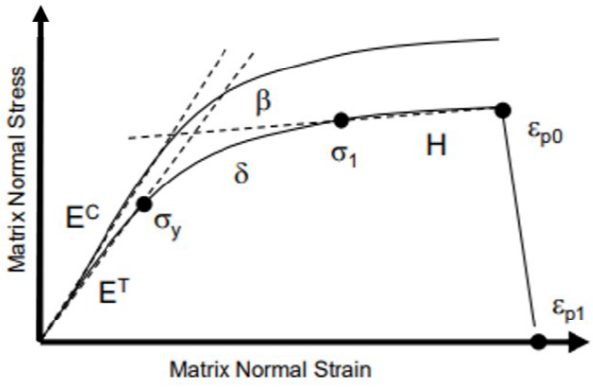

Figure 4.9: Plasticity law of matrix.

Similarly, the matrix volumetric strain region between the maximum mean stress and full degradation should be stretched [33]. For the numerical stability reasons in the matrix model, the volumetric strain at full degradation can be assumed in the range between

$$J1 = \ from\ 1.25\ to\ 1.5\frac{\sigma_{mean}}{K}, \tag{4.8}$$

where $J1$ is volumetric strain to failure, σ_{mean} is mean stress at damage initiation and $K = \frac{E}{3(1-2\nu)}$ is the bulk modulus of the matrix.

In practice, nonlinear material characterisation started from defining the matrix and fibre data as an initial starting point for the loop of forward homogenization and inverse characterisation process. Again parameters from the constituent material Altair database were used. To find constituents damage and plasticity properties, four coupon tests were used (i) 0° tension and (ii) 0°compression to calibrate fibre damage properties, (iii) 90° tension to calibrate matrix damage properties and (iv) ±45° tension to calibrate matrix plasticity properties. During the work with the Multiscale Designer, it was observed that it's more efficient to use the single coupons in the optimisation definition in the beginning and, in the end, define one global optimisation problem using all four stress-strain curves.

4.2.6. Reduced order model

The last step of the material characterisation process was to generate a material file based on the parameters defined in the previous steps. This is a model where the ROM represents the behaviour of the homogenised RVE that will be used directly in the FE model, and its correlation to the phase behaviour is saved. In the unit cell problem, the reduced order model technique is utilised to lower the total number of degrees of freedom of the original RVE mesh to the set of matrices.

The parameters are obtained from virtual tests where a strain is applied to measure the response of the unit cell. This can be differentiated for the tension and compression loading. Thus, two types of virtual tests based on the sign of strain are conducted. The matrices are saved either with the keyword tension mode or compression mode. This ROM can directly simulate the material's behaviour in finite element software. No linked connection to the Multiscale Designer software is needed if the input file with the material model is provided. Once generated, a file can be used in multiple simulations. However, a micromechanical solver, besides a macro solver, must be installed to degrade the damaged elements' properties accordingly based on the pristine state and constituents parameters saved in the material file. By keeping track of the phase states, the material model can determine whenever damage initiates in one of its phases. The homogeneous stiffness matrix is then degraded accordingly to account for plasticity and damage.

The generation of ROM entails solving a sequence of influence function problems, and the resulting coefficient tensors serve as the lower-order unit cell model's material database. In the reduced order model, three types of matrices are generated type Homo, type A and type P. The matrices type Homo describe the homogenised material's stiffness matrix [C] and are calculated using forward homogenisation. Type A matrices are amplification matrices describing the relationship between the composite's homogenised strains and the constituents' strains in the linear regime. The following equation presents the relation between the strains of the homogenised material and strains of one of the phase

$$\{\bar{\epsilon}\}^{phase} = [A]^{phase} \{\bar{\epsilon}\}^{homogenised}. \tag{4.9}$$

Type P matrices are the amplification matrices that describe the relationship between the composite's homogenised strains with the constituents' strains in the nonlinear regime while the plasticity or damage starts to occur. Using ROM, the total strain in the case of plasticity or damage can be calculated as

$$\{\bar{\epsilon}\}^{phase} = [A]^{phase} \{\bar{\epsilon}\}^{homogenised}_{elastic} + \sum_{m=1}^{k} [P]^{phase}_{m} \{\bar{\epsilon}\}^{homogenised}_{inelastic}, \tag{4.10}$$

where subscript m defines the number of subregion and k defines a total number of different sub-regions defined in the inelastic region. The number k of P-type matrices depends on the number of damage and plasticity laws chosen for the constituents. At the final step of model generation, the material model was saved as a text file containing those three types of matrices. This text file is referenced in the main FE model and works on a similar principle as UMAT or VUMAT user subroutines.

4.3. Results of the material characterisation

The methodology described above was applied to characterise the IM7/8552 material based on the targets of the JoinDT material model. The results of the characterisation process are presented below. Initial values taken as an initial guess of the constituent parameters are presented with the final values obtained after the optimisation.

4.3.1. Linear constituents parameters

Initial parameters from the database and optimised parameters are presented in Table 4.4. As clearly visible, the initial generic parameters differ from the values optimised for the 8552 matrix and IM7 fibre. The difference is within the ±15 % for the matrix and within the ±23 % for fibre, confirming the generic parameters' usability as the starting point in the optimisation loop. The most significant difference is between Young's modulus in compression for the matrix and in transverse Young's modulus for the fibre. Additionally, the density was optimised to match the homogenised material density of $1.58E-3$ g/mm^3 from the Hexcel data sheet for the possible application of the material model in the explicit solver. The thermal parameters were left as default values as they won't be used in this project. The role in the optimisation and influence of the parameters on the values of the homogenised material is discussed briefly in Appendix.

Table 4.4: Initial and after optimisation linear parameters of fibre and matrix constituents.

Parameter	Symbol	Initial value	Final value	Unit
Matrix - Isotropic				
Young's Modulus in Tension	E_T	4451	3904	MPa
Poisson Ratio	ν	0.34	0.4012	–
Young's Modulus in Compression	E_C	4896	4172	MPa
Coefficient of Thermal Expansion	α	5.40E-05	5.40E-05	$1/°C$
Density	ρ	1.25E-03	1.3E-03	g/mm^3
Fibre - Transversely Isotropic				
Longitudinal Young's Modulus in Tension	E_{11}	275250	283024	MPa
Transverse Young's Modulus	E_{22}	19850	15302	MPa
In-plane Poisson Ratio	ν_{12}	0.25	0.2683	–
Transverse Poisson Ratio	ν_{23}	0.2	0.2005	–
In-Plane Shear Modulus	G_{12}	24800	21045	MPa
Longitudinal Young's Modulus in Compression	E_{11C}	248200	231425	MPa
Coefficient of Thermal Expansion	α_1	-1.08E-06	-1.08E-06	$1/°C$
Coefficient of Thermal Expansion	α_2	1.08E-05	1.08E-05	$1/°C$
Density	ρ	1.78E-03	1.77E-03	g/mm^3

4.3.2. Nonlinear constituents parameters

The initial and final values of the damage and plasticity parameters for constituents are presented in Table 4.5. The difference between the initial and final values is significantly higher as for the linear part, especially for the parameters defining the shape of the stress-strain curve in the plastic region for the matrix (δ and H). The role in the parameters' optimisation and influence on the homogenised material's stress-strain curves is discussed briefly in Appendix.

Table 4.5: Initial and after optimisation damage and plasticity parameters of fibre and matrix constituents.

Parameter	Symbol	Initial value	Final value	Unit
Matrix - Orthotropic Damage and RI Plasticity				
Yield stress	σ_y	32.02	49.07	MPa
Ultimate stress	σ_1	102.63	90.75	MPa
Exponent for the evolution law	δ	311	110	–
Linear term for the hardening law	H	0	160	–
Linear term for increase in yield strength	β_1	0.15	0.24	–
Quadratic term for increase in yield strength	β_2	-1E-06	-1E-06	–
Equivalent plastic strain at which damage begins	ϵ_{p0}	0.1	0.1	–
Equivalent plastic strain at zero stress	ϵ_{p1}	0.11	0.11	–
Mean stress at damage initiation	σ_{mean}	32.46	25.07	MPa
Volumetric strain to failure	$J1$	0.0088	0.0102	–
Compression factor	C	0	0	–
Maximum allowed damage	w_{max}	1	1	–
Fibre - Axial Isotropic Damage - Bilinear				
Failure stress in tension	σ_0	5230	4160	MPa
Strain at zero stress in tension	ϵ_1	0.0209	0.01606	–
Failure stress in compression	σ_{0C}	4126	1909	MPa
Strain at zero stress in compression	ϵ_{1C}	0.01829	0.009075	–

The comparison of simulated and tested stress-strain curves of four coupons are presented in Figure 4.10. All four curves show a good overlap of the results besides minor differences in the yield region of the ±45 tension curve. Even though the difference between the initial and final value in the nonlinear region is higher, the optimised results overlap with test curves which confirm the usability of the initial generic values as starting point.

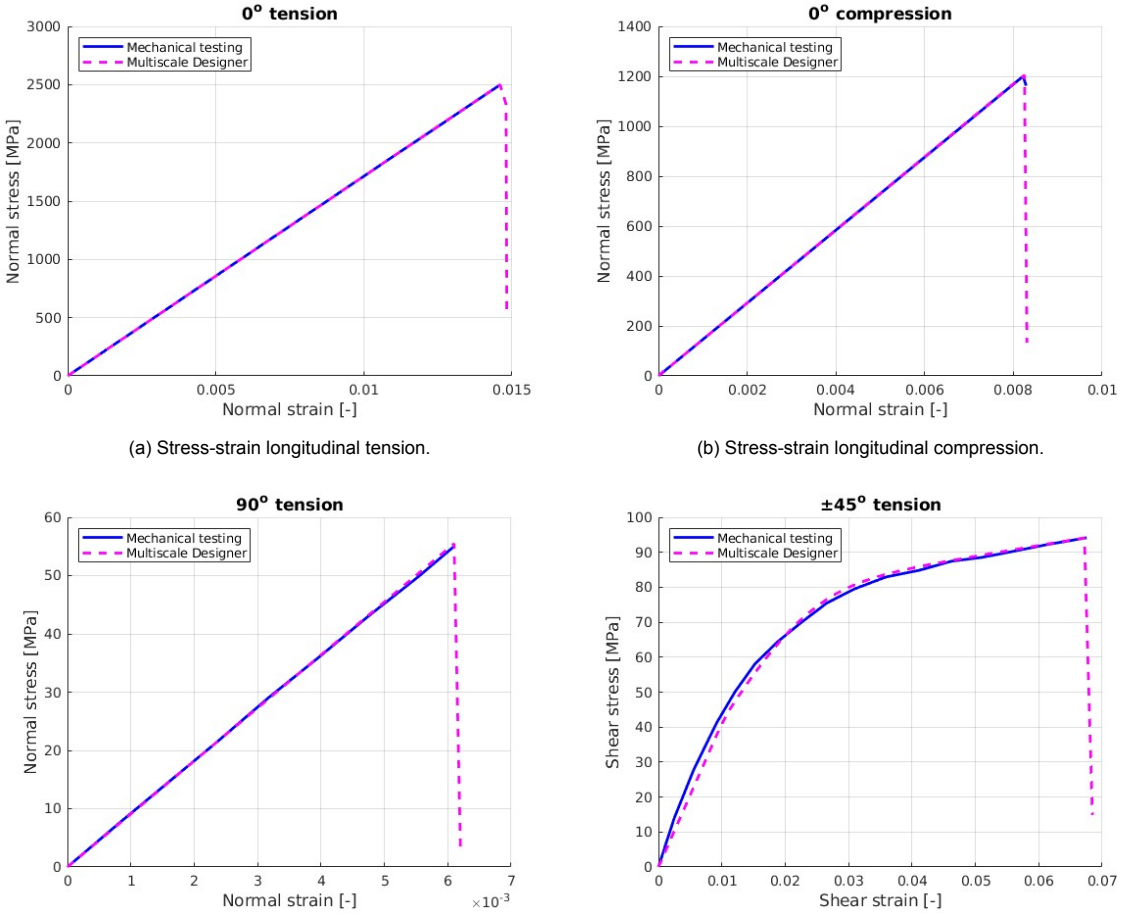

(a) Stress-strain longitudinal tension.

(b) Stress-strain longitudinal compression.

(c) Stress-strain transverse tension.

(d) Stress-strain in-plane shear curves.

Figure 4.10: Comparison of experimental and numerical stress-strain curves.

4.4. Validation and calibration of the material model

To analyse the effect of element size in the material characterisation process using RVE, three different meshes were created to conduct a convergence study with a 0.15, 0.10 and 0.05 element size. For the convergence study, values of simulated homogenised composite parameters with the same input values of the constituents parameters were analysed. The comparison between the simulated parameters and target values is presented in Figure 4.11, which shows a percentage difference between the simulated homogenised property and target value. It was decided to present such a graph because the stress-strain curves of coupons overlap, and no difference can be observed. No significant effect of the mesh size in the studied boundaries was seen on the values of the parameters and on the accuracy of the damage prediction. In all three meshes studied, the percentage difference between the simulated homogenised property and target value was under 1%. In Figure 4.11, a trend can be seen that with the decrease of the element size, the values of the simulated properties increase or stay on the same level. The independency of the homogenised value from the mesh size can be explained by using the mean stress values in the homogenisation approach proposed by Fish [68], which leads to uniform results independent of the mesh. This can also explain the fact that the boundaries of the element size

definition are defined by the real-time assistant, which doesn't allow the definition of a significantly low or high mesh size.

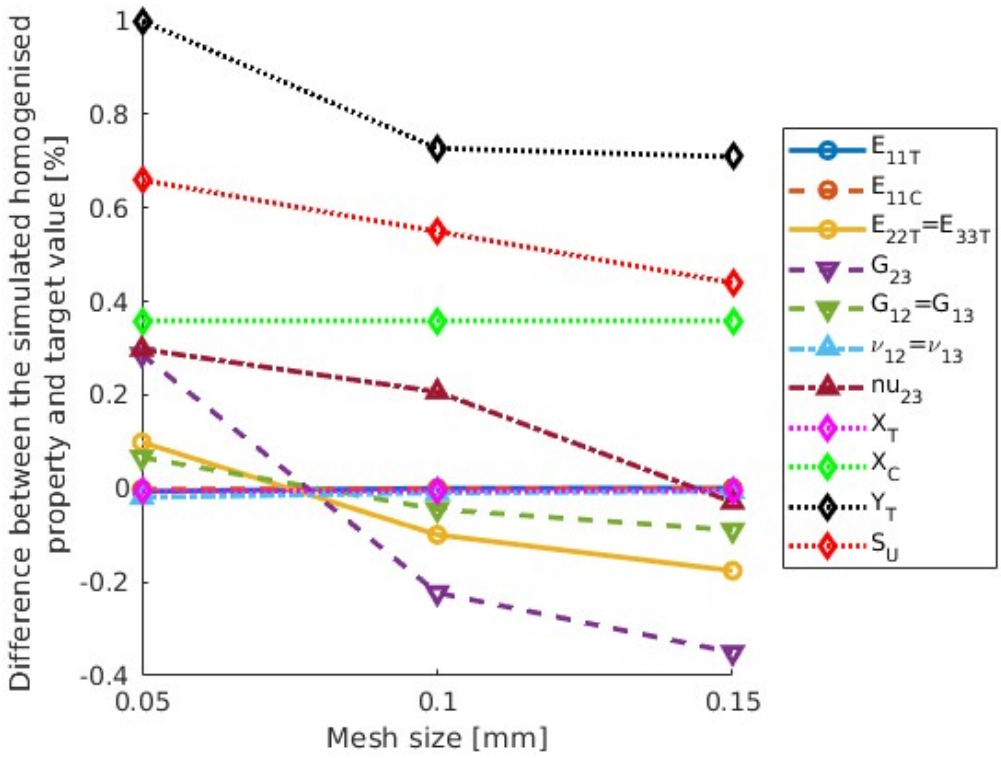

Figure 4.11: Difference between the simulated homogenised properties and target values for three meshes studied.

The next step of material model validation was to use the material model in a macro simulation of SLS0 and SLS45 coupons. In the first simulation, it was observed that the initial value of J1 taken with a factor of 1.25 as the multiplication in Equation 4.8 results in a preliminary failure of the SLS0 joint. As a reminder, the value of the volumetric strain to failure defines the distance in the strain domain between the damage initiation and full failure of the matrix constituent. It is possible that with lower values of the J1 parameter, the softening behaviour inside the matrix cannot be captured in detail in the macro-level simulation compared to the step size in the simulation. When a crack is initiated, the material's stiffness starts to decrease. Loads get redistributed around the cracked material, and the crack propagates further in the material with a further loss of the stiffness of the surrounding material. Another possible explanation is using the mean stress in the homogenisation and inverse characterisation approach. In contrast, the damage initiation and propagation are usually related to the peak stresses that allow for a crack opening and crack propagation.

The value of J1 was increased until the lower boundary of the standard deviation from the test was reached in the SLS0 specimen. Further increase of J1 above a multiplication factor of 2 in Equation 4.8 haven't increased the failure load. This can be observed in Figure 4.12. Similar effect presented in Figure 4.13 was seen on the SLS45 simulation. At the same time, the ultimate load value didn't change with the further increase of J1 above 0.0102. The possible reason for that could be that the region of the strain between the damage initiation and full damage state was stretched enough that the behaviour of the softening and load redistribution can be captured correctly, and further increase of the multiplication factor doesn't contribute to the more accurate capturing of the phenomena. It was decided that the value of J1=0.0102 is a convergence value that will be used in the final material characterisation. This value results in a multiplication factor of around 2 in Equation 4.8.

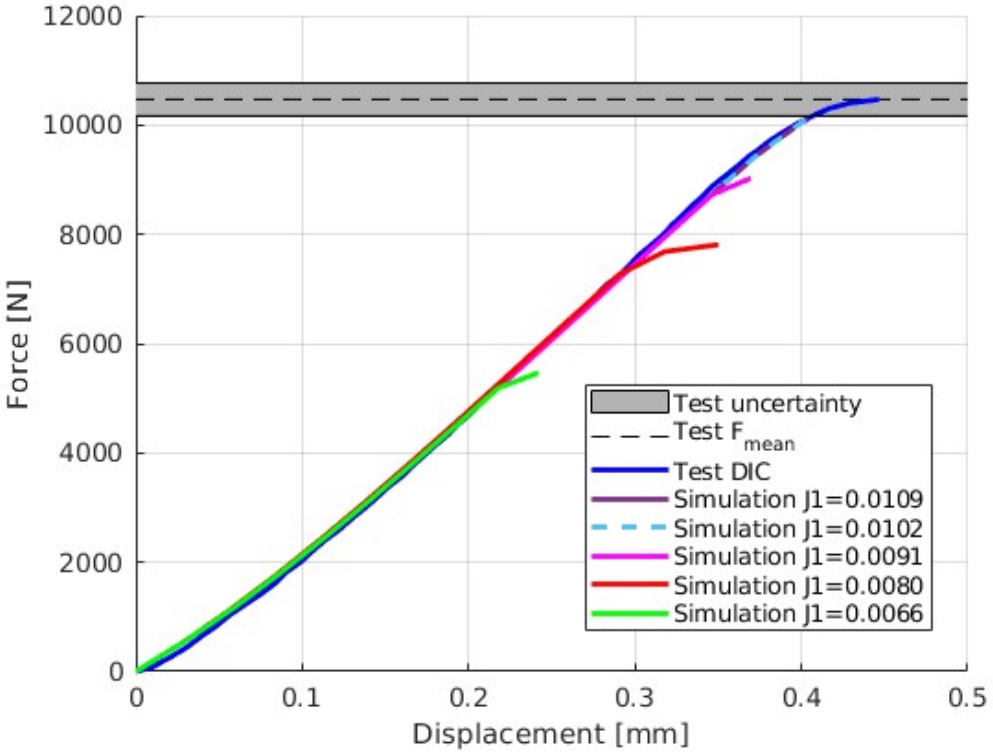

Figure 4.12: Effect of J1 on SLS0 simulation.

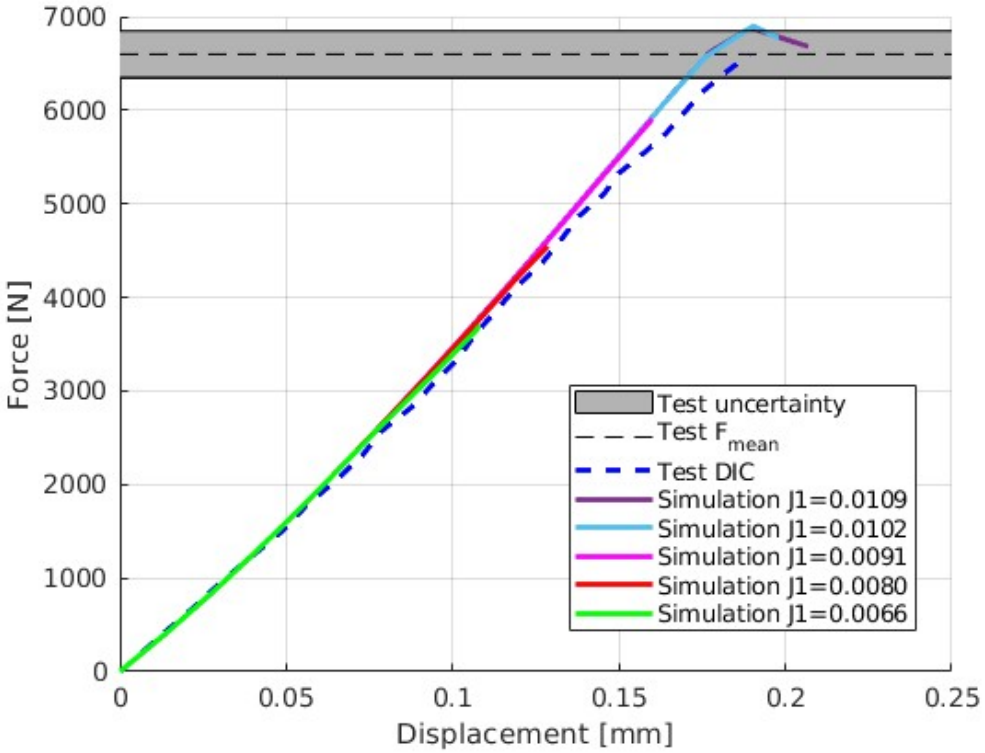

Figure 4.13: Effect of J1 on SLS45 simulation.

4.5. Summary of material characterisation

A multiscale material model for IM7-8552 was developed using the JoinDT material data set and four coupon tests: 0-tension, 90-tension, 0-compression and ± 45- tension. This model was validated in a macro-simulation of SLS0 and SLS45 specimens using an implicit solver.

To characterise the parameters of microphases, homogenisation and inverse characterisation were used. The fibre constituent was modelled using a transversely isotropic material model in the linear regime and an axial bi-linear damage model in the nonlinear region. Matrix was modelled as isotropic material in the linear regime with the orthotropic damage and rate-independent plasticity model describing the nonlinear region. It was identified that a link between the coupon tests and chosen laws can be obtained between (i) 0° tension, 0°compression and fibre damage properties, (ii) 90° tension and matrix damage properties and (iii) ±45° tension and matrix plasticity properties.

The usability of the generated model was confirmed in a convergence study. It showed that mesh influence in the studied range of 0.05 to 0.15 doesn't have an influence on the obtained results. However, the homogenisation time drastically increased from 5 to 30 min with the mesh size change from 0.1 to 0.05. Based on this, it is recommended in future studies to conduct optimisation on a coarser mesh and run a convergence study afterwards to check if the optimised constituent parameter set produces the same homogenised properties independently of the mesh. The mesh independency can be explained by using the mean stress in the homogenisation, which leads uniform results independently of the mesh.

The validation step allowed to calibrate the material model and change the guidelines for calculating the volumetric strain to failure with the application to the IM7/8552 material in implicit solver such as Optistruct. In this step, a simulation of detail utilising the generated multiscale material was conducted. This detail was independent of the conducted material characterisation. In this project, SLJ samples were used in the validation step. However, ideally a purely composite detail should be used to that the different material (adhesive) doesn't interfere with the calibration of the composite material model.

The calibration step was finalised with the conclusion that the multiplication factor of 2 should be used to define the volumetric strain to failure

$$J1 = 2\frac{\sigma_{mean}}{K}. \tag{4.11}$$

The possible reason for the higher value of volumetric strain to failure is the fact that the combination of the low strain between damage initiation and propagation in combination with the time-steps used in the implicit solver didn't allow to accurately capture the softening and redistribution of the load in the regions where damage in composite was observed which led to brittle failure of composite and underestimation of the ultimate load.

In the generic case, the guideline is to start with the lower boundary of 1.25 factor (the value recommended by Altair [33]) and increase the volumetric strain to failure up to the point that the correct softening and matrix failure can be observed in the simulation.

The calibrated matrix damage model is considered a more representative portrayal of the epoxy failure process, as the initial model was considered to describe a significantly brittler failure than what was expected, resulting in a preliminary failure of the matrix. This can also be related to the fact that an implicit solver is used in this work, meaning that when matrix failure occurs very brittle, the solver cannot decrease the time step accordingly within the set limits. On the other hand, this means that the failure process will be stretched in the time/displacement domain, and the final parts of the force-displacement curves between the experiment and simulation may differ.

In the scope of the thesis project, this material model is utilised in the FE models, specifically to the property of elements representing the composite laminate. The FE methodology for the simulation is explained in more detail in the following Chapter 5.

5

Numerical methodology and results

This chapter describes finite element modelling of bonded joint samples, with the modelling approach based on the researchers' observation of the failure of single lap joints. The modelling approach is presented for the composite adherend, adhesive, interlaminar behaviour, defects and damage resulting from impact. The chapter is divided into three main sections where modelling, simulation and results of simulation for (i) pristine in Section 5.1, (ii) artificially damaged in Section 5.2 and (iii) impacted samples in Section 5.3 are presented. The modelling and simulation of the samples were done utilising HyperWorks pre/post-processor with an Optistruct solver in the 2022.2 version. The simulation results are presented by comparing three main measures: ultimate load, stiffness and failure mode.

5.1. Pristine bonded joints

The modelling strategy is based on the conclusions of the work of Völkerink [16], Purimpat *et al.* [37], and Kupski *et al.* [38] and previous experience from the JoinDT project [10], [12]. The observed failure patterns in single lap configuration involve a cohesive failure in the adhesive and one or more of the laminate damage phenomena such as interlaminar damage (delaminations), intralaminar damage due to fibre failure and intralaminar damage due to interfiber failure or matrix damage. Thus damage models for both the adhesive and adherend have to be considered.

5.1.1. Modelling of adhesive

To model the behaviour of the adhesive, cohesive zone elements are used. The adhesive layer is meshed with the brick elements using the CIFHEX element type and PCOHE property card. The visualisation of the approach is presented in Figure 5.1.

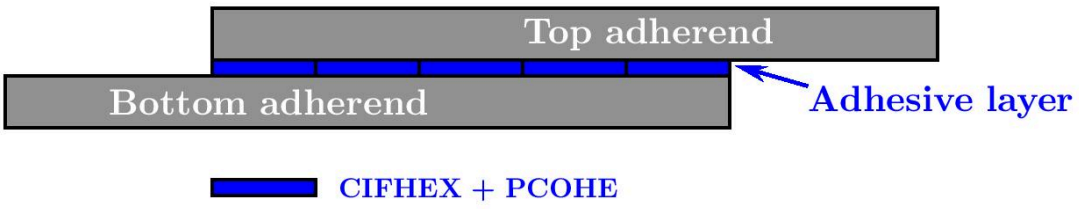

Figure 5.1: Schematics of the adhesive modelling.

Cohesive zone elements

Cohesive zone elements represent simple damage mechanics approach to model complex adhesive behaviour. With this approach, the entire adhesive layer is meshed with cohesive elements. In this modelling approach, the adherends are modelled as continua in joint models, and the cohesive zone's traction-separation response represents the adhesive layer. This type of modelling is considered attractive because only a limited number of parameters are needed, and mixed-mode loading can easily be incorporated. To characterise the numerical behaviour of the cohesive zone, the following parameters for three fracture modes are needed:

- K - Stiffness defines the slope of the traction-separation curve of undamaged material.
- T^0 - Maximum traction defines the damage initiation point.
- G_c - Critical strain energy release rate defines the area under the traction-separation curve.

However, the cohesive zone model also has many limitations. One of the disadvantages of the traction-separation law used to characterise the cohesive behaviour is the dependency on many factors, such as adhesive thickness or adherends layup. The adhesive thickness can significantly influence the parameters of the traction-separation law, especially in thick bondline [69]. The characterisation of the traction-separation law done by Völkerink [16] was conducted on the adhesive thickness of 0.2mm. However, in the JoinDT project, all single-lap joints studied have a thickness of 0.15mm. The calibration of the model based on the measured values has been conducted by both Volle [10] and Völkerink [16]. This was done assuming that the critical strain energy release rate wouldn't differ much between 0.15 and 0.2mm thickness.

The thickness of the bondline can have a significant effect on the stiffness of the traction-separation law. The chosen value was based on the literature as the typical value for this type of adhesive and its thickness [16]. For the dependency on the adherend's layup, the testing was conducted on the laminates with 0° plies that are standard for the adhesive characterisation because they guarantee that the crack will propagate inside the adhesive. In this scenario, the influence of the damage occurring in the composite that can influence the strain energy release rate in the experiment is significantly reduced.

Another limitation of the CZE is the element size needed to capture stress peaks at the overlap edge accurately and calibration of the model parameters (K and T^0). This limitation is discussed, and possible solutions are discussed in more detail on the topic of interlaminar CZE.

Damage initiation and propagation

To characterise the cohesive zone model, the damage initiation criterion is needed. In this work, the quadratic nominal stress criterion (QUADS) is used. This criterion was found by Ramalho *et al.* [19] to be best suited for mixed-mode loading in most joint configurations. The criterion of damage initiation is satisfied when the left-hand side of the equation reaches a value of one and can be defined as

$$\left(\frac{T_I}{T_I^0}\right)^2 + \left(\frac{T_{II}}{T_{II}^0}\right)^2 + \left(\frac{T_{III}}{T_{III}^0}\right)^2 = 1. \tag{5.1}$$

Once the damage is initiated, the material stiffness is gradually decreased. This takes place based on the damage propagation rule. The BK criterion was found by Ramalho *et al.* [19] to provide the best results for the damage propagation of brittle adhesives. The criterion is formulated as

$$G_c = G_{Ic} + (G_{IIc} - G_{Ic})MMR^{\eta_{BK}}. \tag{5.2}$$

The fracture toughness and fitting parameters values have been characterised in DCB, ENF and MMB tests during the work of Völkerink [16]. The curve fit of the η_{BK} parameter is presented in Figure 5.2.

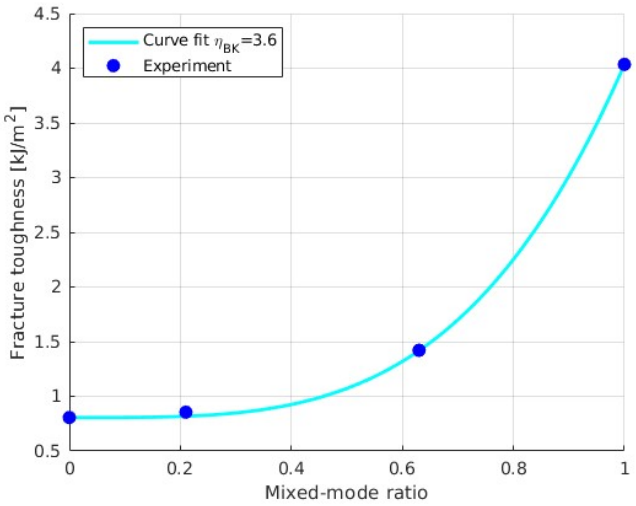

Figure 5.2: Curve fit of the η_{BK} parameter.

Table 5.1 summarises the parameters tested and calibrated by Völkerink [16] used for the adhesive modelling.

Table 5.1: Parameters of LOCTITE® EA 9695 AERO epoxy film adhesive used for CZM. From Völkerink [16]

Property	Value	Unit
$K_I = K_{II} = K_{III}$	10^5	N/mm^3
G_{Ic}	0.806	N/mm
$G_{IIc} = G_{IIIc}$	4.035	N/mm
T_I^0	51.94	MPa
$T_{II}^0 = T_{III}^0$	51.28	MPa
Damage Initiation Criterion	QUADS	
Damage Propagation Criterion	BK	
η_{BK}	3.6	-

5.1.2. Modelling of composite material

To model composite adherend, approaches reported by Bogenfeld *et al.* [41] and Sachse *et al.* [70] can be used. These range from models in a layered approach where few plies can be combined into one element to a more accurate stacked method where each ply is represented with one layer of elements in the thickness direction. Additionally, those approaches can use different element types: shell, continuum shell and solid. As summarised in the work of Bogenfeld *et al.* [41], the shell element was disregarded for the application in this project's high-fidelity simulation of damage initiation and propagation prediction. Considering previous work from the JoinDT project [10], [12], the choice of the modelling approach is stacked models using continuum shell and solid elements. The layered models studied showed a significant difference in ultimate load and stiffness up to ±20% compared to the stacked models. This was associated with the less accurate bending behaviour prediction, where combining a few plies to one element lead to the over-stiffened bending behaviour. Additionally, with the layered approach, one cannot model interlaminar CZE, which doesn't allow to model delamination failure mode, which was one of the observed damage types in the fracture surfaces of bonded joints. Based on this experience, this thesis compared two modelling approaches, one using a purely stacked method for modelling each ply with one through-thickness element and the second incorporating an additional layer of the elements modelling the interlaminar behaviour between the plies.

Modelling of damage in composite adherend

Similarly, for the material model to predict a failure of the bonded joint, the material model needs to consider the damage of the elements so that softening, cracking of matrix, fibre damage and delamination are taken into account. This thesis used a micromechanical approach for damage modelling using multiscale material. This allows modelling matrix and fibre damage. The general idea of the multiscale material model is to characterise composite material using the FE model of RVE and produce a reduced order model of a material characterised by stiffness matrices obtained in unitary strain simulation. The details of this procedure are described in Chapter 4.

Modelling of interlaminar behaviour

Similarly, as for adhesive modelling, cohesive zone elements or cohesive contacts can be used to model the interlaminar failure mode of composite adherends. The work of Volle [10] and Donelli [12] prompted the use of an interlaminar cohesive zone element, whereas the use of cohesive contact was found to be more unstable numerically. Those elements are created by splitting the original adherend mesh with a growth rate factor ranging between 0.01 to 0.05, meaning that the interlaminar layer will have a thickness from 1% to 5% of the original mesh thickness. In this thesis, a value of 0.03 was used. It is a known limitation of this approach which can reduce the strength of the original plies by the same percentage. Following conclusions from the work of Völkerink [16], Purimpat *et al.* [37], and Kupski *et al.* [38], the interlaminar behaviour is modelled until the first 0° ply in the adherend as shown in the Figure 5.3. This means the SLS0 sample with 0° ply at the bondline interface was modelled without interlaminar CZE. For SLS45 and SLTAI60, three interfaces were modelled, and for SLTAI30, one interface was modelled.

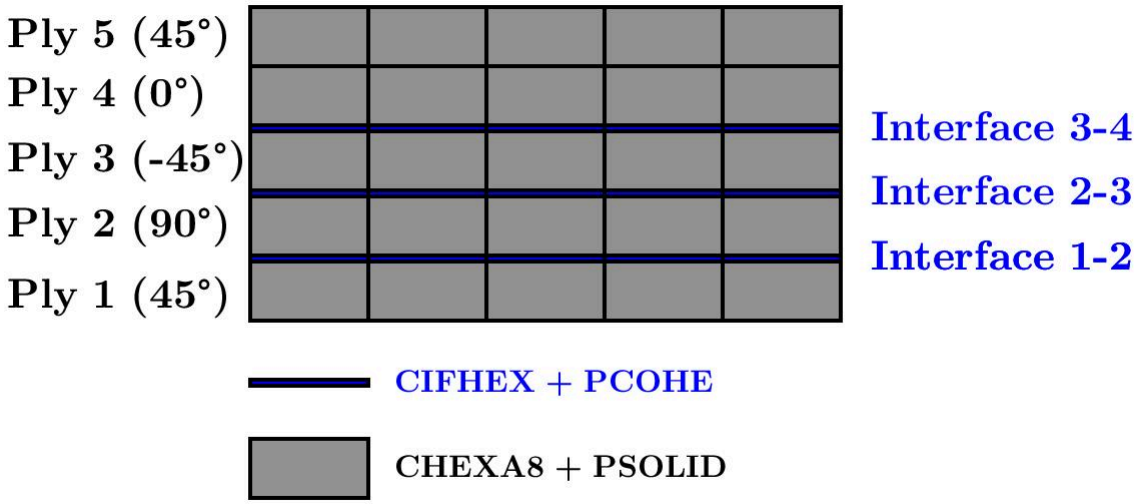

Figure 5.3: Schematics of the stacked mesh with interlaminar CZE approach for SLS45 and SLTAI60 samples.

Similarly, as for the adhesive, the quadratic nominal stress criterion is used for the damage initiation in the cohesive zone model, and the damage propagation is modelled using the BK model. Relevant parameters of the nominal interlaminar cohesive zone model are presented in Table 5.2.

Table 5.2: Interlaminar nominal material properties of IM7/8552 for cohesive zone model. Values from Völkerink [16].

Property	Value	Unit
$K_I = K_{II} = K_{III}$	10^5	N/mm^3
G_{Ic}	0.24	N/mm
$G_{IIc} = G_{IIIc}$	0.74	N/mm
T_I^0	62.3	MPa
$T_{II}^0 = T_{III}^0$	92.3	MPa
Damage Initiation Criterion	QUADS	
Damage Propagation Criterion	BK	
η_{BK}	2.07	-
VED	10^{-5}	-

Additionally, previous studies of Donelli [12] established that the factor of 2 can reduce the maximal traction to trigger the delamination failure mode in the joint models. This parameter configuration can be referred to as reduced material properties and was considered a more representative picture of the maximal traction required for crack propagation, typically lower than the one required for crack initiation. This calibration approach kept the same stiffness and critical strain energy release rate values as presented in Table 5.3. It originates from the fatigue simulations of Sachse [11], where the strain energy release rate at the crack tip is assessed to calculate the local crack growth rate based on the Paris law. In the static strength simulation, it was observed that the nominal traction values provide too conservative values to initiate a crack in the interlaminar layers and thus nominal values didn't allow to produce a realistic failure mode. Both material models are compared in a case study to see the effect of the chosen material parameters on the SLS45 simulation. This coupon was chosen for a case study due to the failure mode in the adherend in the form of inter- and intralaminar damage.

Table 5.3: Interlaminar reduced material properties of IM7/8552 for cohesive zone model.

Property	Value	Unit
$K_I = K_{II} = K_{III}$	10^5	N/mm^3
G_{Ic}	0.24	N/mm
$G_{IIc} = G_{IIIc}$	0.74	N/mm
T_I^0	31.15	MPa
$T_{II}^0 = T_{III}^0$	46.15	MPa
Damage Initiation Criterion	QUADS	
Damage Propagation Criterion	BK	
η_{BK}	2.07	-
VED	10^{-5}	-

Engineering solution for mesh size effects

The distance from the crack tip to the location where the greatest cohesive traction is reached is referred to as the cohesive zone's length, or l_{cz}. Different models have been proposed in the literature to estimate the length of the cohesive zone. Most of the models to predict the cohesive zone length have a form

$$l_{cz} = ME\frac{G_c}{(T_o)^2}, \tag{5.3}$$

where E is the Young modulus of the material, G_c is the critical energy release rate, T_0 is the maximum interfacial strength, and M is a parameter that depends on a specific cohesive zone model. For the case of orthotropic materials with transverse isotropy and assuming plane stress, the value of Young's modulus in the equation can be assumed to be the transverse modulus of the material $E2$. For one of the most popular models of Hillerborg *et al.* [71], the M is assumed to be equal to 1.

The tractions in the cohesive zone must be correctly represented by the finite element spatial discretization to produce appropriate FEM results when utilising CZM. The number of elements in the cohesive zone is calculated as

$$N_e = \frac{l_{cz}}{l_e}, \tag{5.4}$$

where l_e is the mesh size in the direction of crack propagation. Different authors have defined different recommendations for the number of elements that should be modelled in the cohesive zone to predict the fracture process correctly. Summarising the work done by the researchers, one can derive an optimal range of the elements in the cohesive zone from 2 to 5 [72]. However, the convergence study should still be conducted with a consideration of those guidelines as a good practice.

For the adhesive and interlaminar behaviour of the composite material used in this thesis, the cohesive zone length was calculated and is presented in Table 5.4. The obtained values confirm that small element sizes under 1mm size should be used while using CZE.

Table 5.4: Estimated cohesive zone length for adhesive and interlaminar material parameters.

Material	Cohesive zone length
Adhesive EA9695	0.94 mm
Interlaminar CFRP IM7/8552 nominal	0.56 mm
Interlaminar CFRP IM7/8552 reduced traction	2.24 mm

The cohesive zone length is one of the limiting factors for the mesh size in the finite element models. To accurately capture a fracture zone, a very dense mesh is needed. This factor limits the application of CZE on larger scale models as a simulation includes an enormous number of elements, which results in a very long simulation time.

To keep bigger elements and accurately capture a crack initiation and propagation behaviour, the procedure was proposed by Turon *et al.* [73]. This allows to account for the size of a cohesive element with regard to the length of the cohesive zone to ensure the correct energy dissipation.

Work of Donelli [12] tested the solution proposed by Turon *et al.* [73] with the Optistruct solver and assessed its usability in the simulation for the bonded joints. The answer is realised by reducing the maximum interfacial strength, critical strain energy release rate and/or stiffness, which results in an enlarged cohesive zone length, and the cohesive zone spans more elements. To adapt the interlaminar mesh, previous work at Airbus tested the reduction schemes with parameters presented in the traction-separation curves of the CZE to enlarge the cohesive zone length that can be approximated with equation 5.3. Based on the conclusions of the work of Donelli [12], it was decided to proceed with work without incorporation of the above schemes and test nominal versus reduced traction material parameters on SLJ models presented in Tables 5.2 and 5.3. This also has a direct influence on the cohesive zone length as presented in Table 5.4, however, it is rather origins from the model calibration than from the Turon *et al.* [73] approach.

5.1.3. Numerical methodology

The FE simulation of specimens was done in the non-linear implicit solver Optistruct version 2022.2. The Newton-Raphson scheme was used to solve the nonlinear FE problem. All results presented were realised on version 2022.2 due to the improved performance of the micromechanical solver compared to the previously used version 2021.2, in which the damage in the 90° composite layers wasn't predicted accurately. With version 2022.2, improved handling of mixed loading and compression handling was

introduced. The simulation ran on the Airbus cluster machines and each simulation utilised 28 CPU cores to speed up the simulation time by the parallelization of the numerical calculation.

Non-linear analysis settings

The analysis settings were set to the large displacement nonlinear static analysis using the nonlinear implicit solver. The large displacements were activated with the card LGDISP which is the analysis type suitable for the nonlinearities coming from the geometry and material. The large displacement is the only analysis type supported for the multiscale material model. Additionally, for the Newton-Raphson scheme, the analysis settings had to be set. The universal settings of the simulation established based on the previous work at Airbus [12] and the default values for this type of analysis in Optistrict are presented in Table 5.5.

Table 5.5: Nonlinear analysis settings.

Property	Keyword	Value
Total time	TTOT	1
Initial time increment	DT	0.03
Number of iterations to stiffness update	KSTEP	1
Maximum time increment allowed	DTMAX	0.03
Minimum time increment allowed	DTMIN	1E-05
Limit of iteration on each load increment	MAXITER	25
Number of cutbacks allowed to reduce the time increment	NCUTS	5
Number of intermediate results	NOUT	20

Boundary condition and load

To accurately reproduce the experiment, a test set-up has to be analysed. Numerical models of the samples were created from one clamp to another. Both edges of the joint were clamped in the machine, so also a model should be constrained on both ends. Within Optistruct, a particular element can be used to couple the displacement of the set of nodes (dependent nodes) to the displacement of one independent node. This element is called the rigid body element (RBE2). Such coupling was applied to both edges. Independent nodes of RBE2 are constrained in all six translational and rotational DOF (TX, TY, TZ, RX, RY, RZ) on one edge and in five DOF (TY, TZ, RX, RY, RZ) on the other edge. Loads are applied to the right edge of the sample in the form of enforced displacement in the x-direction. RBE2, boundary conditions and loads are visualised in Figure 5.4.

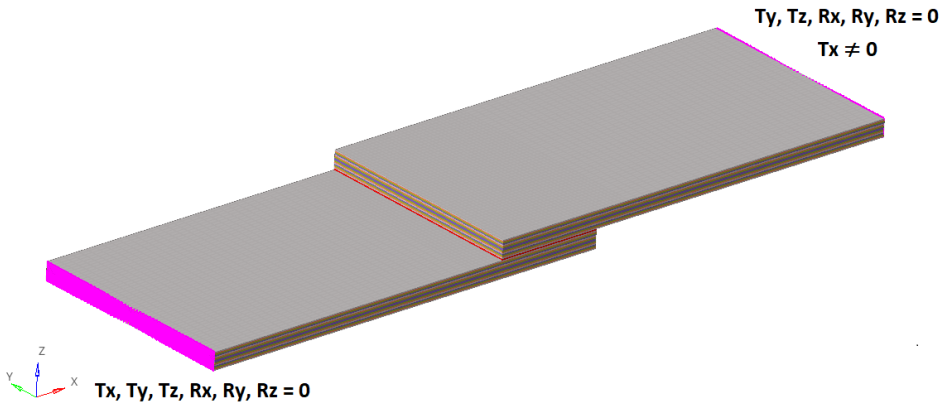

Figure 5.4: Boundary conditions and load.

Mesh size

Besides following the guidelines for the CZE set-up, a classical mesh convergence study was conducted to create a uniform meshing approach for all samples. A mesh study was conducted on the SLS0 sample characterised by the failure in the adhesive layer. Interestingly, the convergence issues dominate the ultimate load in the samples with a coarse mesh, leading to the underestimation of the ultimate strength. As visible in Figure 5.5 and 5.6, the decrease of element size from 1 mm to 0.75 significantly changed the resulting failure load. This can be related to the cohesive zone length of the adhesive material. With a size of 0.75, the fracture zone can be represented correctly, and what is interesting about this size is that one element is present in the cohesive zone. By changing the element size from 0.75mm to 0.5, an ultimate load increase of around 2.5% is visible. The simulation with an element size of 0.5 was the first one that could reach the state of the load drop visible at the end of the force-displacement curve, as presented in Figure 5.6. This load drop is related to the adhesive elements being deleted in the simulation and physically to a crack propagating through the bondline. Further refinement from 0.5mm to 0.25mm decreased the ultimate load by around 1%, which is considered a typical value for which mesh convergence can be assumed. The decrease can be related to more accurately capturing the peak stress at the adhesive edge. Thus the study confirmed the usability of the mesh of 0.5mm size in the adhesive area. Additionally, with the element size of 0.5mm, two elements are present in the cohesive zone, which confirms the guidelines for the cohesive zone element size concerning the cohesive length.

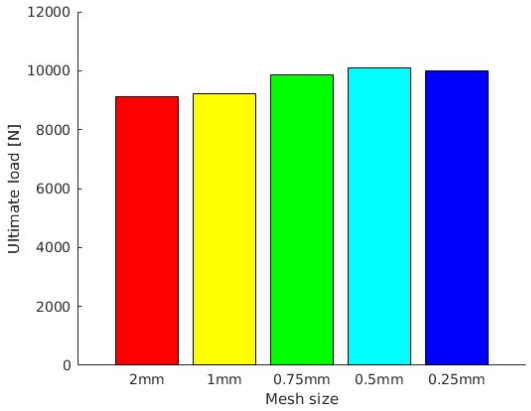

Figure 5.5: Effect of element size on the ultimate load of SLS0 specimen.

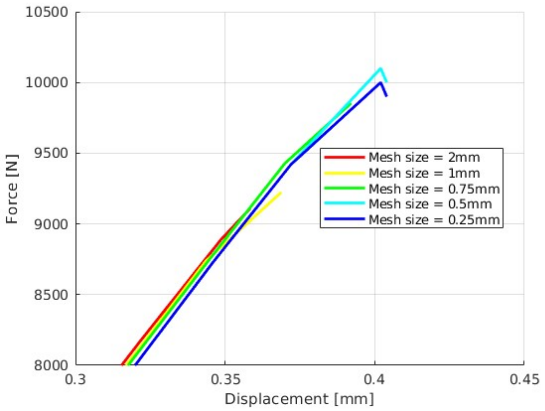

Figure 5.6: Effect of element size on the final part of the force-displacement graph of SLS0 specimen.

As the universal meshing approach for all the samples, it was decided to stick to the 0.5mm size in the zone of interest and enlarge the mesh length to 1mm in the field outside of the adhesion zone with a finer mesh left for the 50mm from the adhesive edge to capture damage in the composite that may occur in the areas around the adhesive edge. The example of this meshing approach is presented on the SLS45 specimen in Figure 5.7.

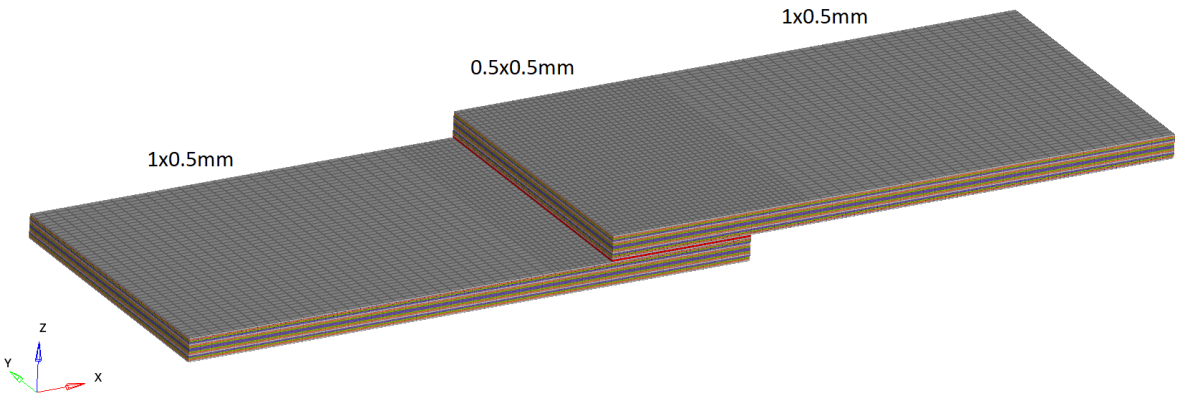

Figure 5.7: Universal meshing approach presented on SLS45 specimen.

Choice of element property card

After the mesh study, two elements types were investigated: continuum shell and solid. The element type in the Optistruct solver is defined with the specification of the property card. For the continuum shell, the property is PCOMPLS, and for the solid, it is PSOLID. These two are the elements supported that can be combined with the MDS material. Simulation on SLS0 and SLS45 was studied to assess the effect of element type on the simulation. It was quickly identified that the continuum shell element suffers from a convergence issue and excessive damage propagating in a specific time step, resulting in modes similar to hourglass patterns. This can be related to a simplification of parameters formulation in the thickness direction for the continuum shell. This resulted in disregarding a continuum shell in this study and was reported to Altair, meaning that for the representation of the composite laminate in this study, a CHEXA8 element with a property card PSOLID and material model MATMDS was used. Figure 5.8 presents an unexpected damage pattern observed with continuum shell elements.

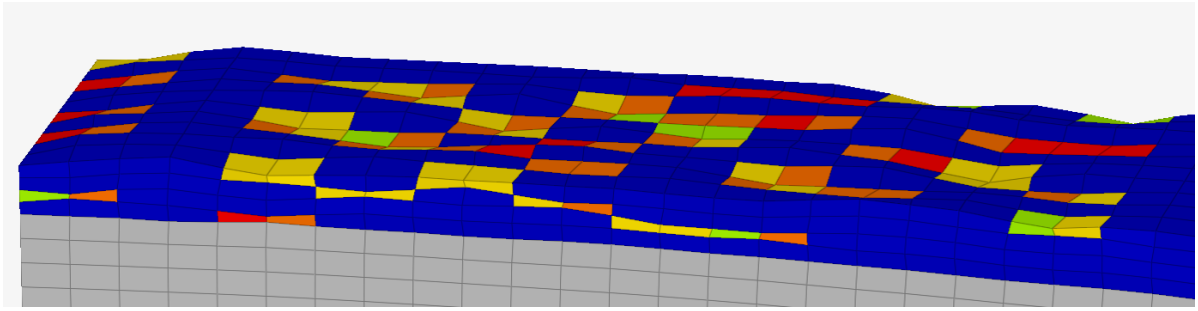

Figure 5.8: Preliminary damage pattern observed using continuum shell element.

Traction reduction for interlaminar CZE

The application of the methodology of maximal traction reduction to account for observed faster interlaminar crack initiation was verified on the SLS45 sample. A reduction was compared to the nominal maximum traction value and the base model without the interlaminar CZE. As visible in Figure 5.9, a base simulation and simulation utilising nominal traction value provide similar results. The failure is more ductile than the curve representing a reduction by a factor of 2. This is related to different failure modes observed in the simulation. The first two show mixed intralaminar failure with adhesive failure, and the model with reduced traction shows interlaminar damage initiating at the step region in the thickness direction up to the first 0° ply, where the delamination between the 90° (2nd) and 45° (3rd) layers is dominating damage type. As mentioned in the limitations of the multiscale material, the base models suffer from the stretched region of the damage propagation.

This study was summarised using the reduction factor 2 in the models, including interlaminar CZE, to trigger a brittle interlaminar failure and observe a delamination failure mode. The base model and model with interlaminar CZE utilising nominal values provided almost identical failure load with a smaller than 1 % difference, and the observed failure mode doesn't show interlaminar damage observed in the testing, which resulted in the usage of the reduced traction values in the models with interlaminar CZE. This offers an alternative to the base simulation with a reasonably underestimated failure load and more accurately predicted failure mode.

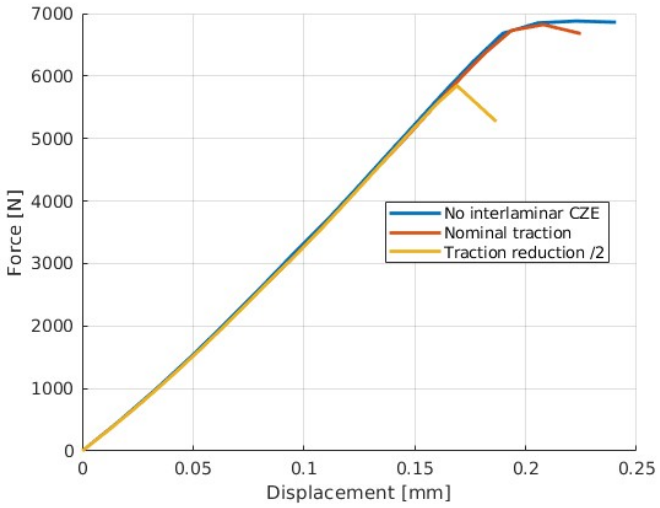

Figure 5.9: Effect of traction reduction on the force-displacement curves of SLS45 specimen.

Overconstrained edge

In the first simulations on the larger specimens, it is SLTAI60 and SLTAI30, it was observed that models suffer from early convergence issues due to the damage occurring on the specimen edge at clamps. It was identified that the reason for that might be the RBE2 with the combination of a pretty big application area. To encounter that issue, it was decided to apply an orthotropic material model with a card MAT9 which shows linear behaviour without damage or softening. Applying different material models on the boundaries is common in FE models, especially on the edges where different element types are used or where the boundaries for detailed models from a global model are defined. This is also considered for future application of such models where necessary details should be derived from global FE models. The material definition is presented in Figure 5.10.

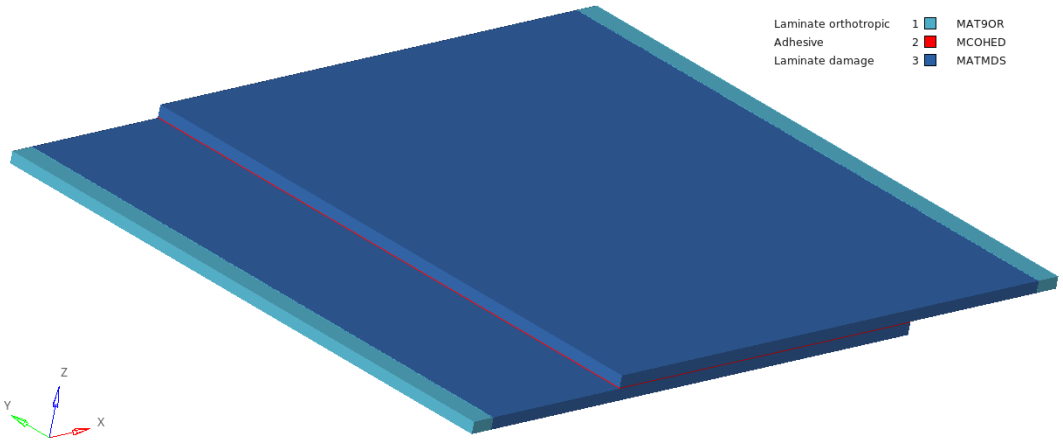

Figure 5.10: Definition of the laminate material to tackle the issue of overconstrained edge.

5.1.4. Results of simulation

The study of pristine bonded joints assessed the developed modelling base and compared two stacked models, one without and the second with interlaminar CZE, to determine the effect of this modelling feature on the results. For the SLS0, the second modelling approach wasn't tested due to a very good prediction of the base model and a purely cohesive failure. The comparison is based on three measures (i) ultimate load, (ii) stiffness and (iii) failure mode. The results are presented for SLS0, SLS45, SLTAI60 and SLTAI30 samples. Throughout the results subsection, the colour convention is applied, the magenta colour shows test results, the blue colour is for the simulation using the base modelling approach without the interlaminar CZE, and the cyan colour is for the simulation using the interlaminar CZE elements. The axis system in which the results are presented is the following: x-axis along the length, y-axis along the width and z-axis along the thickness of samples.

Remark about the confidentiality of the results

The results for the SLS0 and SLS45 samples are public when writing this thesis. They can be found in the PhD thesis of Völkerink [16]. However, for the SLTAI30 and SLTAI60 samples, they are part of the still ongoing investigation. Thus in consultation with JoinDT project partners, it was decided to present the results for those samples without exact numbers. This means that force-displacement results for the SLTAI samples are presented as relative numbers where 1 is the reference number related to the ultimate load and corresponding displacement from the mechanical testing. It was done this way to guarantee that it doesn't interfere with the interpretation of the results and conclusions drawn.

SLS0

The comparison between the force-displacement graphs from the mechanical testing and simulation with the base stacked modelling approach is presented in Figure 5.11 for SLS0. Simulated stiffness and ultimate load show very good predictions with an ultimate load under the standard deviation from the mechanical testing and overlap of the curves until the simulated ultimate load. The failure is more brittle in the simulation, where the load drop occurs at the end of the linear behaviour, and the test curve shows non-linear softening in the final part of the curve. This can be related to omitting the adhesive plastic effects with a simple bi-linear traction separation law.

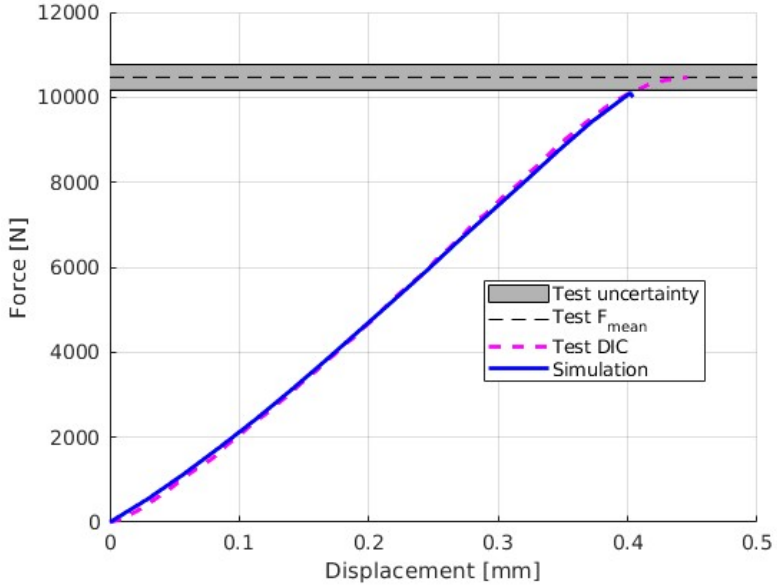

Figure 5.11: Comparison of experimental and simulated force-displacement curves for SLS0.

The simulated failure mode of the SLS0 specimen is presented in Figure 5.12, and the fracture surface observed in mechanical testing is presented in Figure 5.13. The failure mode from both the simulation and mechanical testing shows a cohesive failure in the adhesive as expected due to the interface layer being a 0° ply. In the simulation, due to the use of an implicit solver, it wasn't possible to propagate the crack up to the total fracture of an adhesive. However, a load drop observed in the force-displacement curve showcases that the state in which a few rows (3-4) show a full or almost full state of damage can be considered as a damaged state at a maximum load in SLJ configuration. The comparison between the damage state at ultimate load and the final simulation step shown in Figure 5.12, presents the deletion of the elements showcasing crack propagation from adhesive edges to the middle of the overlap.

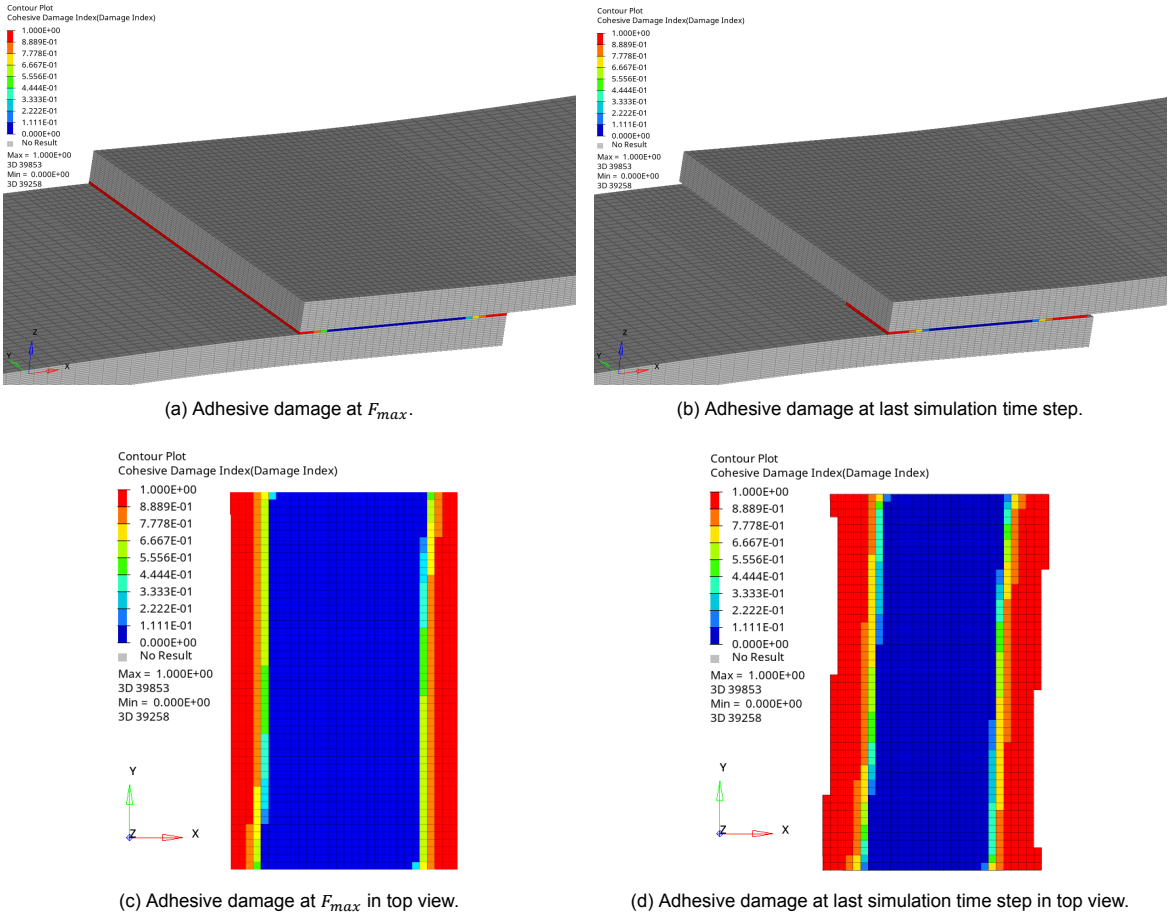

(a) Adhesive damage at F_{max}.

(b) Adhesive damage at last simulation time step.

(c) Adhesive damage at F_{max} in top view.

(d) Adhesive damage at last simulation time step in top view.

Figure 5.12: Simulated failure mode of SLS0.

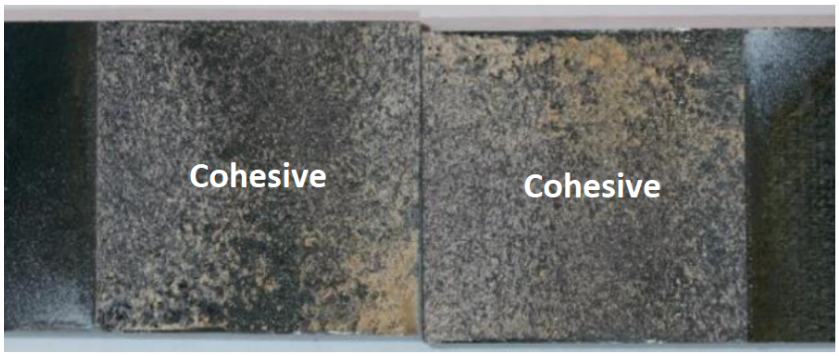

Figure 5.13: Experimental failure mode of SLS0.

SLS45

The comparison between the force-displacement graphs from the mechanical testing and simulation with two different modelling approaches are presented in Figure 5.14 for the SLS45 sample. For both simulation approaches, the stiffness prediction is very accurate with the overlap of the curve until the point where the failure occurs. The prediction of the ultimate load is also accurate, with an over-prediction just above the standard deviation from mechanical testing utilising a base model and an under-prediction of around -11 % with a model featuring interlaminar CZE.

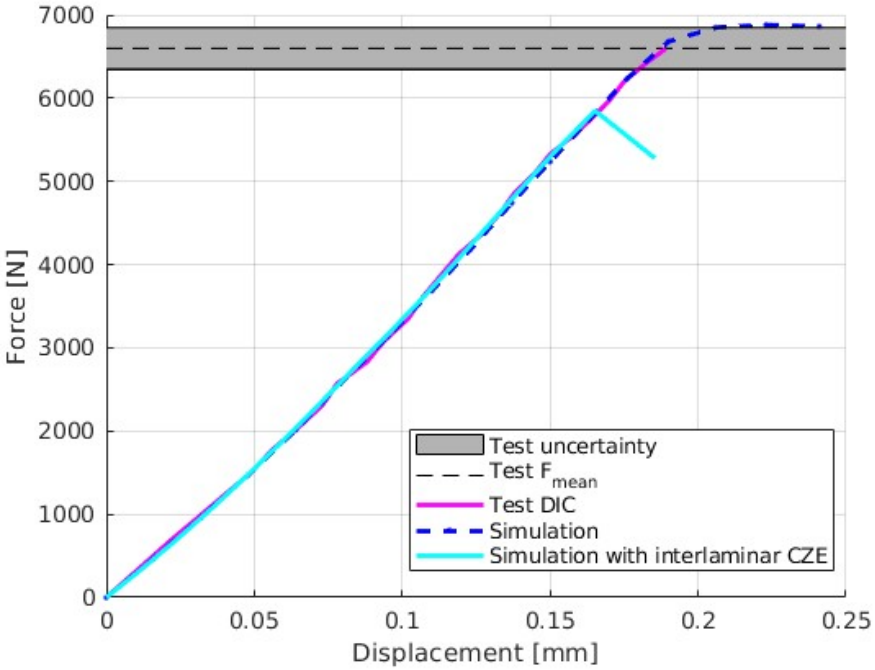

Figure 5.14: Comparison of experimental and simulated force-displacement curves for SLS45.

The failure mode from the simulation is presented in Figure 5.15 for the base simulation model, in Figure 5.16 for simulation model utilising interlaminar CZE and for mechanical testing in Figure 5.17. A base model offers a less accurate failure mode prediction where mixed adhesive and adherend failure is observed. The damage initiates on the adhesive edge and grows simultaneously in the length and thickness direction. The extension in thickness direction reaches around half of the adherend's thickness which wasn't observed in the test. The possible reason for that is the inability of the model to show the crack deflection on the interlaminar interface, which is possible with the model incorporating interlaminar CZE.

The more accurate portrait of the failure mode is considered to be obtained with the simulation utilising interlaminar CZE. The dominating cause of the failure is the interlaminar damage between the 90° (2nd) and -45° (3rd) layers. Together with the propagation of the interlaminar damage, the matrix damage is observed in the same area. The predicted triangular damage pattern is similar to the observed fracture pattern in Figure 5.17. The main difference comparing the simulation utilising interlaminar CZE and the test is between the multiple interlaminar layer damage in the mechanical testing and a dominating one interface in the simulation with minor damage in the other layer up to the first 0° (4th from bondline) ply.

It is essential to mention the damage propagation between the state at maximum load and at the last simulation step observed in the simulation utilising interlaminar CZE. The area of the damage extend is relatively small compared to the final simulation step and concentrated at the adhesive edge with the first four plies affected. In the state at the last simulation time step, the damage extend is much more significant in the length direction. The indication of the failure load is observed on the interlaminar layer,

which is affected by the damage on the whole width length at the adhesive edge. Following the growth of the damage, it first extends in the width direction at the adhesive edge. After the whole width is affected, the damage starts to grow in the length direction, which occurs very brittle and causes matrix damage in the adjacent plies. This indicator is used in the simulations on larger details like SLTAI samples, where the damage propagation to the same state as SLS45 was not possible.

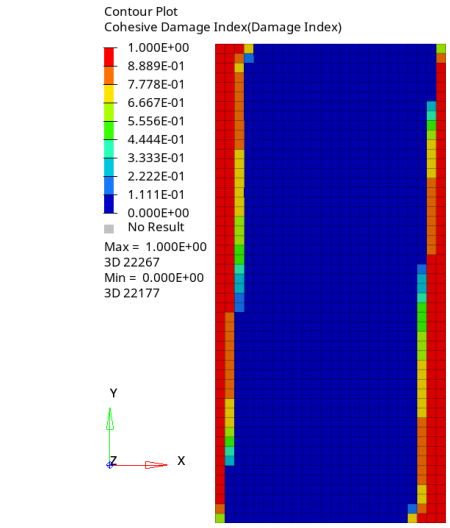

(a) Adhesive damage at $F = 6680N$.

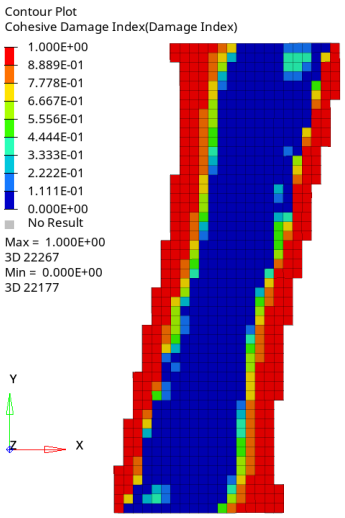

(b) Adhesive damage at last simulation time step.

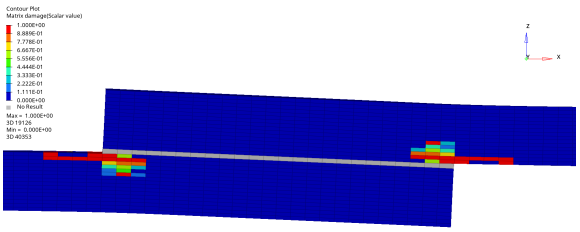

(c) Matrix damage at $F = 6680N$. Cross-sectional cut at the symmetry axis of the specimen.

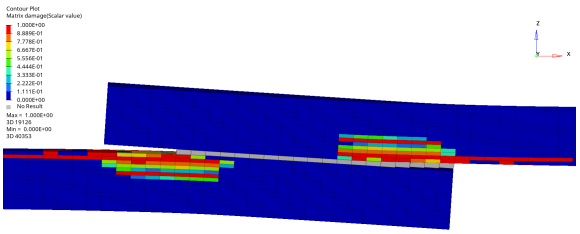

(d) Matrix damage at last simulation time step. Cross-sectional cut at the symmetry axis of the specimen.

Figure 5.15: Simulated failure mode of SLS45 with base model.

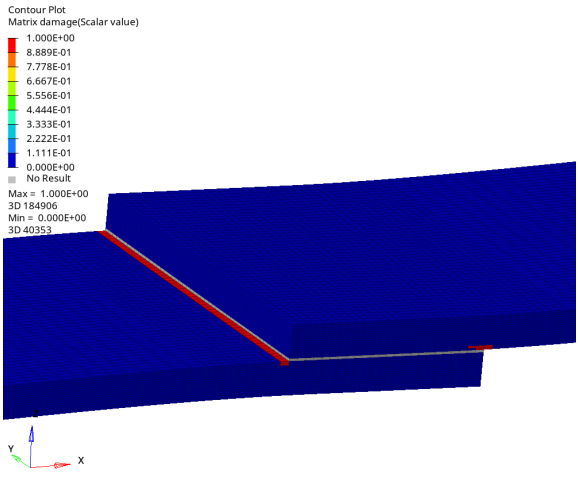

(a) Matrix damage at F_{max}.

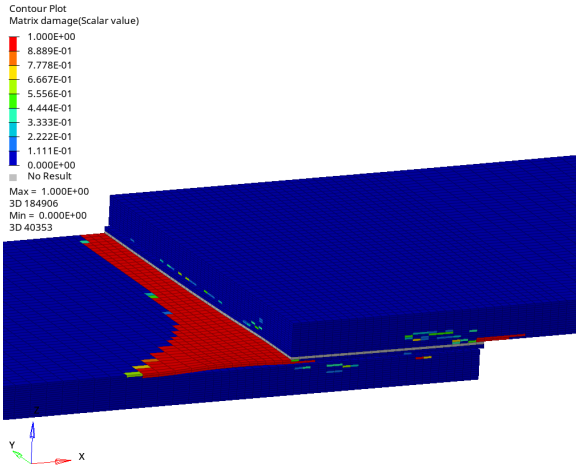

(b) Matrix damage at last simulation time step.

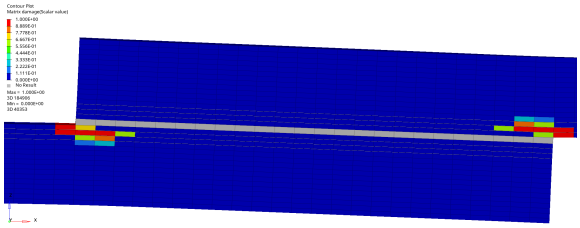

(c) Matrix damage at F_{max}. Cross-sectional cut at the symmetry axis of the specimen.

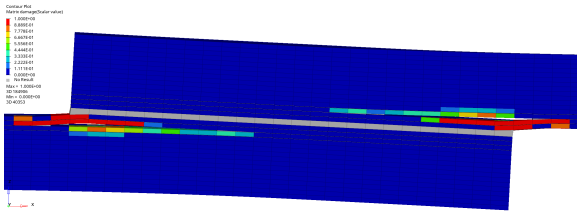

(d) Matrix damage at last simulation time step. Cross-sectional cut at the symmetry axis of the specimen.

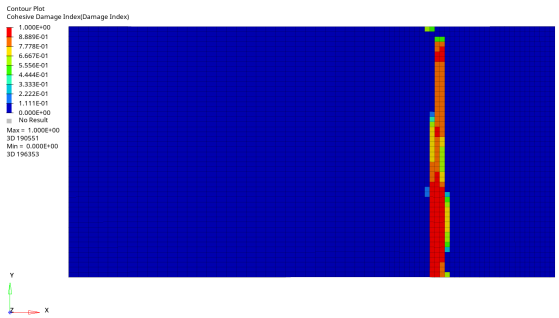

(e) Interlaminar damage between 90° (2nd) and -45° (3rd) layers at F_{max}.

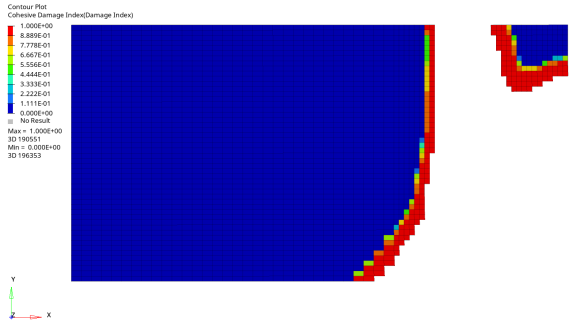

(f) Interlaminar damage between 90° (2nd) and -45° (3rd) layers at last simulation time step.

Figure 5.16: Simulated failure mode of SLS45 with interlaminar CZE model.

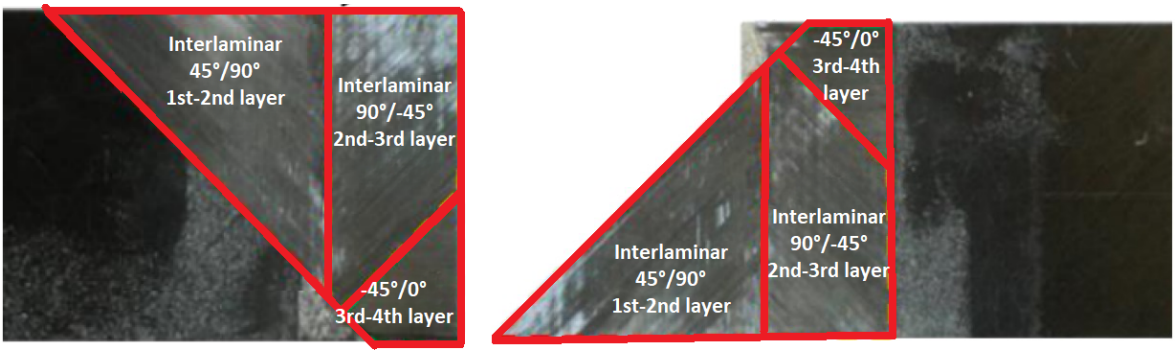

Figure 5.17: Experimental failure mode of SLS45.

SLTAI60

The comparison between the force-displacement graphs from the mechanical testing and simulation with two different modelling approaches are presented in Figure 5.18 for the pristine SLTAI60 sample. For both simulation approaches, the stiffness prediction is very accurate with the overlap of the curve until the point where the failure occurs. The prediction of the ultimate load is also accurate with a prediction between the standard deviation bands from mechanical testing utilising a base model and under-prediction of around -21 % with a model featuring interlaminar CZE. Similarly, as for the SLS45 sample which has the same layup, the force-displacement curve shows non-linear effects in the final part of the curve simulated with the base model and a sudden failure in the model utilising interlaminar CZE. In the case of this sample, it wasn't possible to simulate a load drop in the simulation with interlaminar CZE due to the large area being affected by damage which lead to convergence issues. However, a comparison between the damage state at failure load in the simulation can be used as the confirmation of the prediction of ultimate load as the final step of the SLTAI60 simulation.

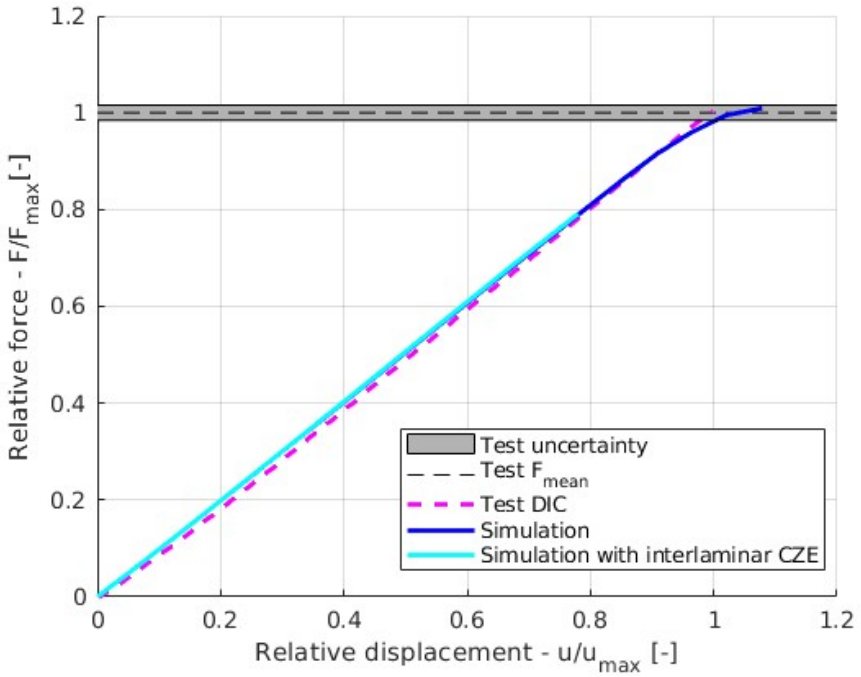

Figure 5.18: Comparison of experimental and simulated force-displacement curves for SLTAI60 pristine.

For the SLTAI60, the failure mode of the base model is presented in Figure 5.19. Two results steps are compared where the first one is the result indicating the kind in the force-displacement curve, and the second one is the final simulation step. The base model shows a mixed adhesive and adherend failure initiated at the adhesive edge. The failure mode prediction is accurate at the damage initiation. Still, the damage propagation shows much larger through-thickness than what is observed in a fracture surface presented in Figure 5.21. The fracture surface shows intra- and interlaminar damage in the first four layers. In the base simulation, the damage in the adherend extends up to half of the adherend, with the most critical damage in the 90° (2nd) and -45° (3rd) layers.

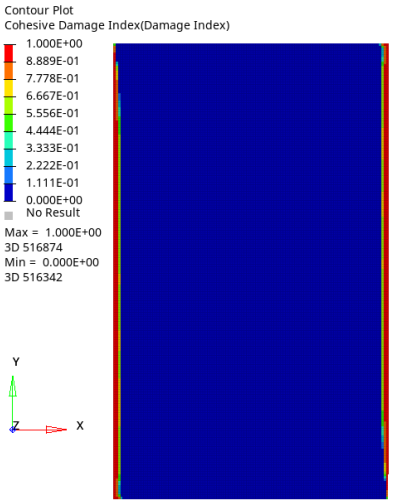

(a) Adhesive damage at $F/F_{max} = 0.93$.

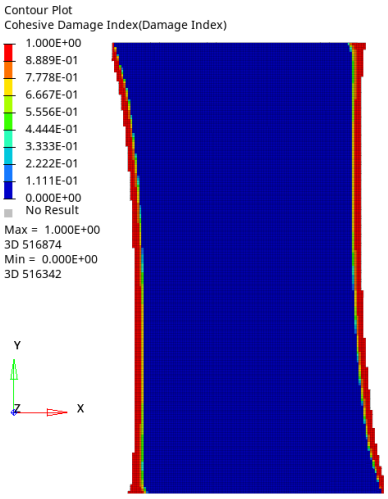

(b) Adhesive damage at last simulation time step.

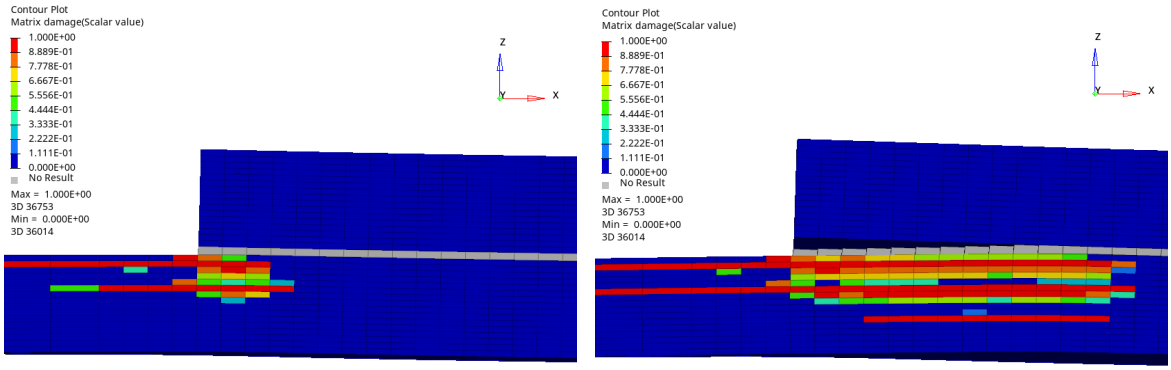

(c) Matrix damage at $F/F_{max} = 0.93$. Cross-sectional cut at the symmetry axis of the specimen.

(d) Matrix damage at last simulation time step. Cross-sectional cut at the symmetry axis of the specimen.

Figure 5.19: Simulated failure mode of SLTAI60 pristine with base model.

For the SLTAI60, the failure mode of the interlaminar CZE model is presented in Figure 5.20. The more accurate portrait of the failure mode is considered to be obtained with the simulation utilising interlaminar CZE. The dominating cause of the failure is the interlaminar damage between the 90° (2nd) and -45° (3rd) layers, which is also dominating failure mode observed in tests. In the last simulation time step, the elements started to be deleted on one edge of the laminate, and the damaged area extend is significant, but not until the other edge, as in the SLS45 sample. Together with the interlaminar damage, the matrix damage is observed in the same area of the adhesive edge. A similar difference between the base and interlaminar CZE model is observed for the SLS45 sample as samples have the same layup. The correlation between the observed interlaminar damage at the ultimate load in the SLS45 sample and at the last simulation time step in the SLTAI60 samples allows to consider this state as close to the ultimate load.

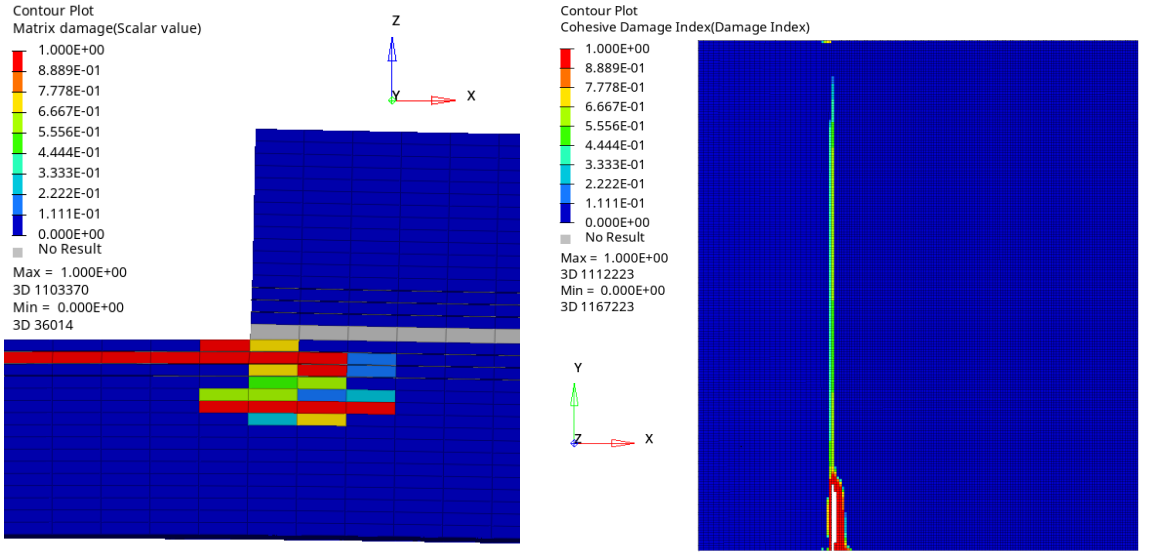

(a) Matrix damage at last simulation time step. Cross-sectional cut at the symmetry axis of the specimen.

(b) Interlaminar damage between 90° (2nd) and -45° (3rd) layers at last simulation time step.

Figure 5.20: Simulated failure mode of SLTAI60 pristine with interlaminar CZE model.

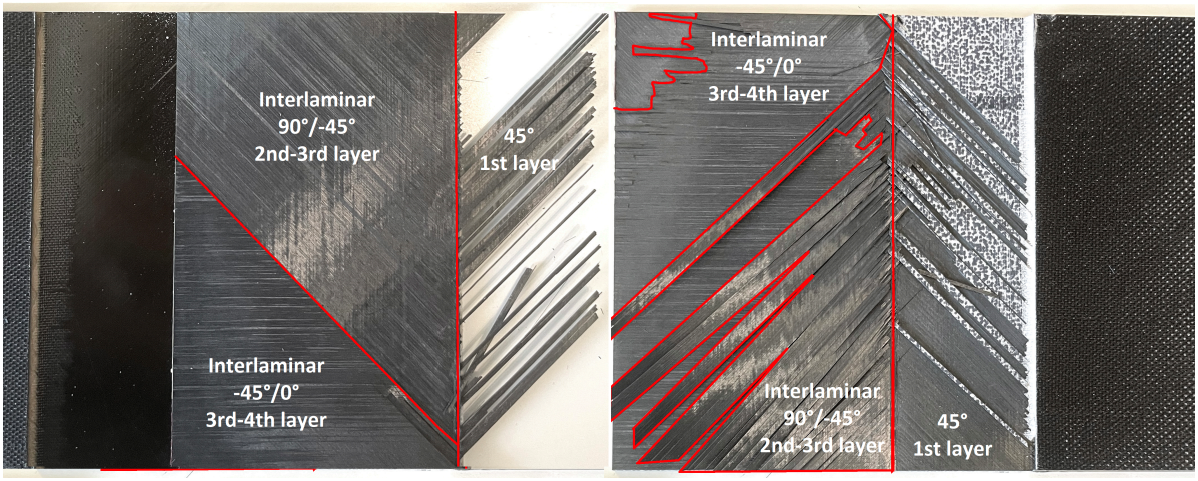

Figure 5.21: Experimental failure mode of SLTAI60 pristine.

SLTAI30

The comparison between the force-displacement graphs from the mechanical testing and simulation with two different modelling approaches are presented in Figure 5.22 for the pristine SLTAI30 sample. For both simulation approaches, the stiffness prediction is accurate. However, an overlap of the curves until the point where the failure occurs is not visible as for other samples. After the initial settling of the stiffness at around 0.25 of relative displacement, very similar stiffness values are obtained.

The prediction of the ultimate load is also quite accurate with an over-prediction of around 10 % utilising a base model and an under-prediction of around -11 % with a model featuring interlaminar CZE. In the case of this sample, just like for SLTAI60, it wasn't possible to simulate a load drop in the simulation with interlaminar CZE due to the large area being affected by damage, leading to convergence issues. However, a comparison between the damage state at failure load in the simulation can be used to confirm the prediction of the ultimate load as the final step of the SLTAI30 simulation.

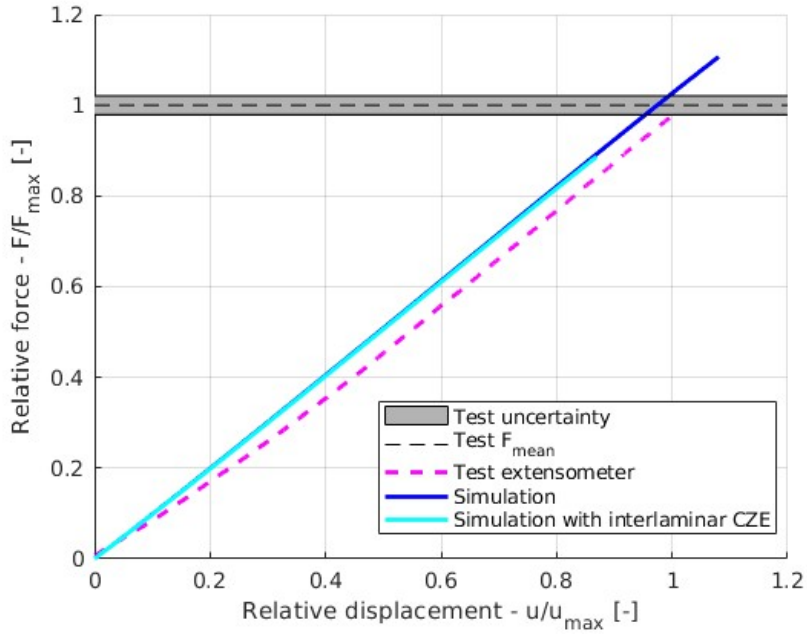

Figure 5.22: Comparison of experimental and simulated force-displacement curves for SLTAI30 pristine.

For the SLTAI30 base model, the simulated failure mode is presented in Figure 5.23. The model shows an area of damage at the adhesive edge with dominating adhesive damage and secondary intralaminar damage in the region up to the 5th ply, mostly in the 4th (90°) ply. The fracture surface presented in Figure 5.25 shows approximately half of the fracture surface failed in the adhesive damage, which is a domination failure mode in the base simulation. The other half shows clear interlaminar damage that cannot be predicted with a base model, which could lead to an over-prediction of the ultimate load.

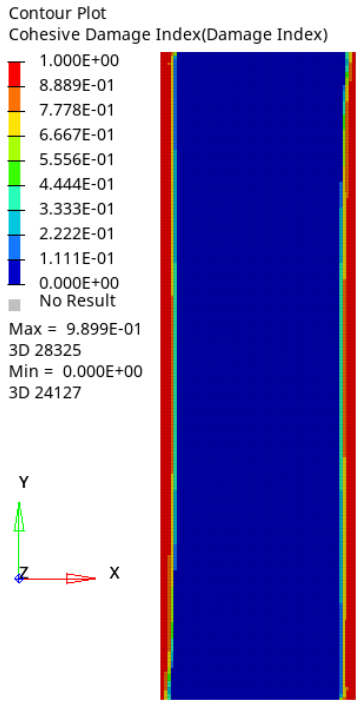

(a) Adhesive damage at last simulation time step.

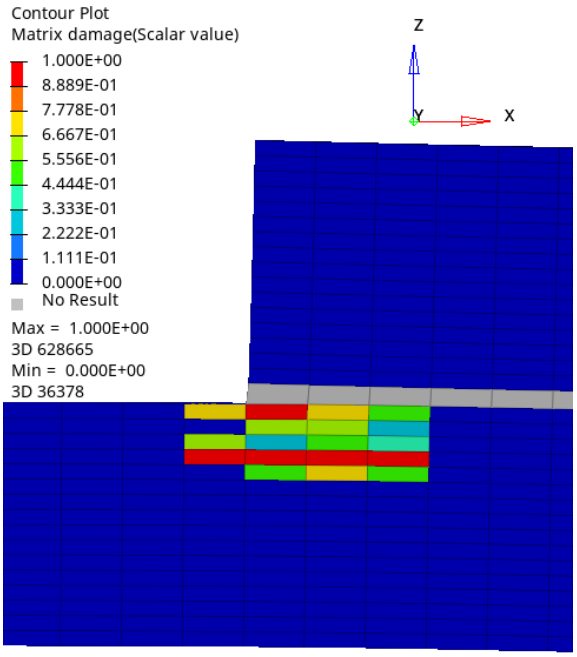

(b) Matrix damage at last simulation time step. Cross-sectional cut at the symmetry axis of the specimen.

Figure 5.23: Simulated failure mode of SLTAI30 pristine with base model.

For the SLTAI30 model with interlaminar CZE, the simulated failure mode is presented in Figure 5.24. The model shows an area of damage at the adhesive edge with dominating intra- and interlaminar damage in the region up to the 4th ply. The interlaminar damage between 45° (1st) and 0° (2nd) dominates the failure and reaches total damage in the whole width length at the adhesive edge. A very similar state was observed in the SLS45 sample at the ultimate load, which suggests a damage state of ultimate load at this time-step. Further very brittle propagation of damage in the interlaminar layer would occur in the following steps. The comparison between the two states creates an indication of the ultimate load of the sample. This offers a good prediction, as observed in the fracture surface presented in Figure 5.25. Approximately half of the fracture surface failed in the delamination between the 45° (1st) and 0° (2nd) layers, which is a domination failure mode in the simulation with interlaminar CZE.

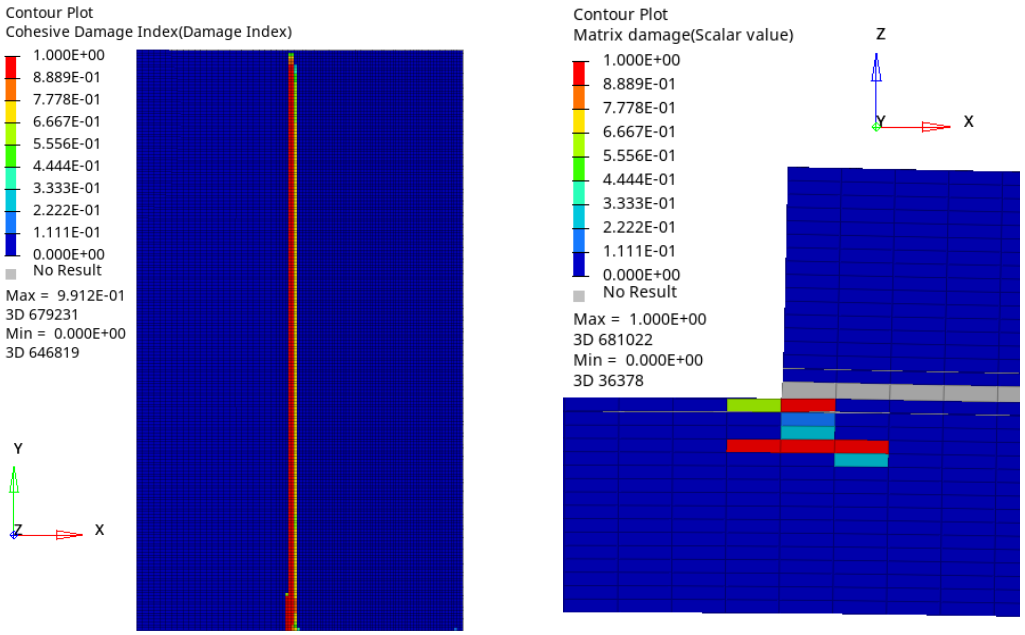

(a) Interlaminar damage between 45° (1st) and 0° (2nd) layers at last simulation time step.

(b) Matrix damage at last simulation time step. Cross-sectional cut at the symmetry axis of the specimen.

Figure 5.24: Simulated failure mode of SLTAI30 pristine with interlaminar CZE model.

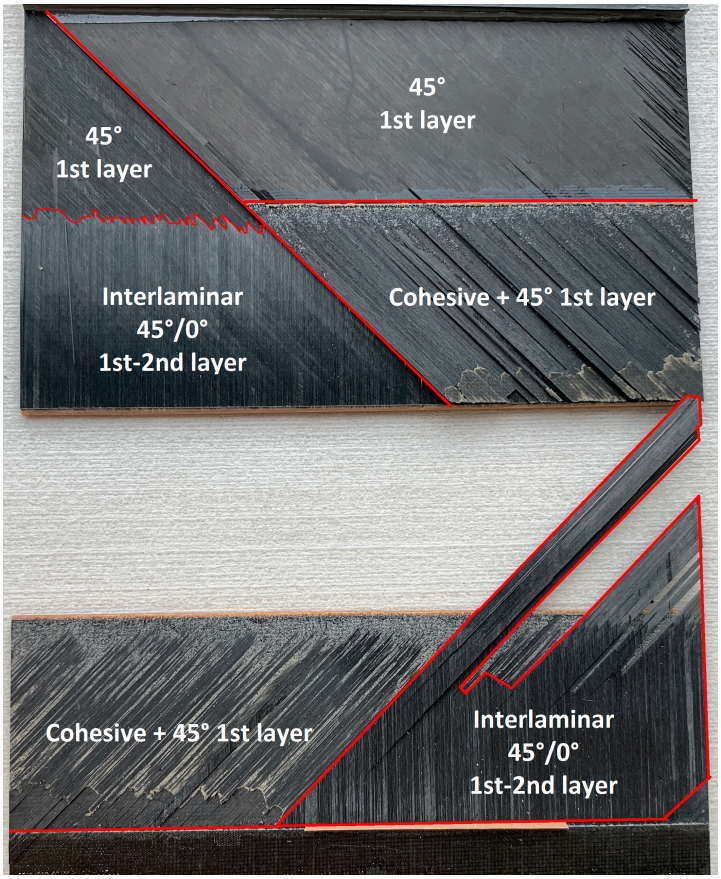

Figure 5.25: Experimental failure mode of SLTAI30 pristine.

5.1.5. Overview of the results

The developed approach for modelling the pristine samples showed a maximum over-prediction of the ultimate load of around 10 % for the base model and under-prediction of the ultimate load with a maximum error of around 20 % in the models with interlaminar CZE. The stiffness prediction is also very accurate for all models, with a good overlap for most of the curves. The predicted failure modes resemble the fracture patterns from the mechanical testing, which is especially visible in SLS0 and SLS45 samples where the simulation of the damage propagation till the significant state was possible.

The additional modelling feature of the interlaminar CZE allowed for a more accurate prediction of the failure mode in the samples that suffer from an adherend failure. As showcased in the single-lap configuration, due to the secondary bending induced by the geometry of the samples, delamination is an important mode to be considered. The modelling of interlaminar cohesive zone elements allows capturing a brittle behaviour of interlaminar failure, whereas, in the base model, the damage propagation was ductile and more distributed in the thickness and length direction, which showed slower building up to the damage in composite, stretched in the displacement/strain region. This can be related to the material model used where the volumetric strain to failure region was stretched for numerical reasons, which could lead to this behaviour. But also to the inability of capturing a deflection of damage building up at the adhesive edge region from the bondline in the thickness direction up to the critical interlaminar layer in which damage growth is deflected and propagates rapidly in the length direction. It is expected that to directly observe a crack deflection, a modelling feature of intralaminar CZE would be needed. However, matrix damage is already modelled at the microscale in the multiscale composite material model. Thus, it is also expected that it wouldn't contribute much to the more accurate simulation prediction.

The stiffness prediction is very good for the SLS0, SLS45 and SLTAI60 samples, with an overlap for most parts of the curves. For the SLTAI30 samples, one can see a difference which can be related to the test set-up or different measurement techniques. Laser extensometer results were used for the displacement measurement for SLTAI30 samples and DIC results for all other samples. Interestingly, the first part of the extensometer results provides a not expected measurement showing a curved shape and the settling of the stiffness in the first part of the curve. This can be related to some interference between the extensometer and test set-up. Other possibility is the surface treatment that differs between the samples. For SLTAI30, manual grinding was used, whereas for all other samples a plasma treatment was used to activate the surface before bonding.

A comparison of the curve shapes shows more ductile behaviour for the base models and brittle behaviour for the simulation utilising interlaminar CZE. The simulation on larger samples is finished without showing a significant load drop, as can be observed on SLS0 and SLS45 force-displacement curves. This is related to the convergence of the solution. In the presence of a large damaged area, converging the solution and propagating the damage in the simulation is harder. However, based on the observation of the simulated failure mode of SLS45, analogies can be made in the observed damaged areas in the SLTAI samples to showcase that the last simulation time-step can be considered a value very close to an ultimate load.

Comparison of the damage state in simulation at F_{max} between the SLS45 and larger samples (SLTAI30, SLTAI60) allows to interpret the final time step as the state close to the ultimate load. Both states show a through-width damaged area in the interlaminar layer that would propagate very brittle in the next time steps. In the larger samples, due to the much higher number of nodes/elements in the model, the simulation with interlaminar CZE was finished at this time step due to the convergence issues.

Based on the above, it was proceeded with incorporating damage into the pristine models with the methodology described in the following section 5.2.

5.2. Artificially damaged bonded joints

The modelling strategy for artificial damage is based on the experiences gained in the pristine joint simulation. The modelling of pristine samples provided two models in which the base model provided a more accurate prediction of ultimate load and the model with interlaminar CZE more accurate failure mode prediction. Those two models are used as the base to represent artificial damage. Two approaches are tested in the models: deletion and detaching of the elements. Two samples are modelled, one with an adhesive defect and the second one with an interlaminar defect.

For the model with a disbond, both the base model and interlaminar CZE model are compared to observe the influence of adhesive defect on a triggered failure mode. For the model with an interlaminar defect, in the model utilising deleting elements to represent defect, the interlaminar CZE are modelled only in the interface on which the release film was placed. This is based on a very accurate prediction of the ultimate load in the base model and preliminary failure of the model with interlaminar CZE modelled at the first three interfaces. For the model in which elements are detached, the incorporation is also based on the base pristine model to observe if the stress concentration around the inclusions modelled with the detachment can provide a similar effect as a release film in a real sample.

5.2.1. Modelling of defects and damage

Two different modelling techniques were explored to model different types of damage in bonded joints. The explored modelling techniques are deleting the interlaminar CZE and detaching the elements of adjacent plies. The idea behind the artificially damaged joints was to explore the applicability and limitations of methods on the samples with artificial damage before proceeding to model damage resulting from impact.

Due to the use of CZE to represent the adhesive material, elements were deleted to model defects in the adhesive. The detachment of the elements due to the nature of the traction-separation law wouldn't make sense in the case of adhesive defects as one of the surfaces wouldn't be connected to any other nodes resulting in free movement. To not increase the number of DOF and with the conservative assumption that the disbonded area results in the full loss of the adhesion, it was proceeded with the deletion of the elements in the adhesive to represent the disbond.

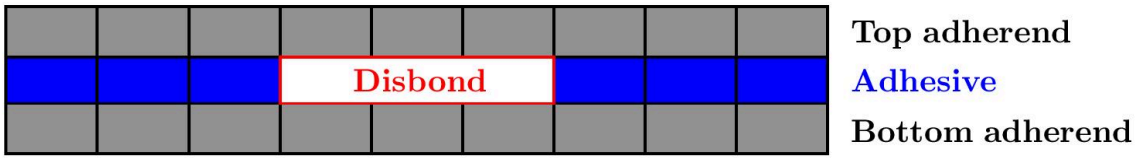

Figure 5.26: Schematics of deleting the cohesive elements to represent a disbond.

For the modelling of the delamination, both techniques were explored. To delete elements, an interface layer representing the boundary between two plies has to be modelled with CZE, which introduces an additional layer of nodes. This layer of elements can be deleted in the region where delamination is present or in the case of artificially damaged models where the release film was placed. The schematics of this modelling approach is presented in Figure 5.27.

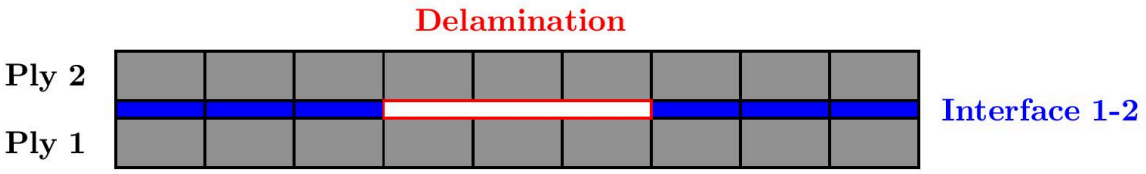

Figure 5.27: Schematics of the deletion of the interlaminar cohesive elements to represent delamination.

To detach elements, no additional interface layer is needed in the model. In the classical stacked mesh approach, elements representing composite plies share nodes between each layer. That means the top surface of the first ply shares nodes with the bottom surface of the second ply. To represent delamination, nodes between plies can be detached, meaning they won't share nodes between plies in a location where the delamination occurred. A very thin inclusion can be modelled by detaching nodes with an offset so that the thickness of initial elements is decreased by 3%, like in the case of interlaminar CZE. The schematics of this modelling approach are presented in Figure 5.27. In this case, no interlaminar CZE are implemented in the model. The inclusion resulting from a detachment of the nodes is expected to create a stress concentration around which intralaminar damage will build up within the plies elements. This is expected to show more ductile behaviour on the force-displacement curve compared to the deletion of the interlaminar CZE, where brittle behaviour is expected.

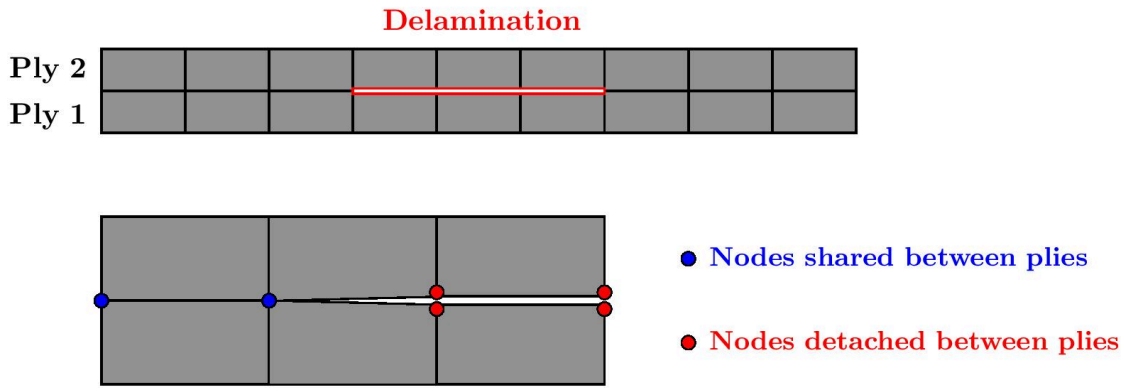

Figure 5.28: Schematics of the detachment of the nodes to represent delamination.

For both approaches, the delamination is incorporated into the model between the layers where the release film was placed. This is between every fourth layer. In the numerical model, the interlaminar layers are modelled only in the interfaces between which the release film was placed. This is based on the experience from the simulation of pristine SLTAI60, where the model with interlaminar layers modelled up to the first 0° ply from the interface showed a significantly under-predicted ultimate load.

A summary of the advantages and disadvantages of both options concerning the modelling of delamination is presented in Table 5.6. With additional interlaminar CZE, there is an increased number of nodes compared to the detachment approach, where the nodes are only doubled in the delamination area. The limitation of the detachment is that the delamination growth cannot be observed in the simulation, instead, it acts like a stress concentration inclusion. From the modelling point of view, the ease of implementing the deleting approach seems to be faster/easier to implement.

Table 5.6: Comparison of the modelling approaches.

Property	Deletion of elements	Detachment of elements
Number of nodes	-	+
Possibility of damage propagation	+	-
Ease of implementation	+	+/-

5.2.2. Results of simulation

The study of artificially damaged bonded joints assessed the developed modelling approaches and compared two models of modelling defect to assess the effect of this modelling feature on the results and its further usability to model existing impact damage. The comparison is based on three measures (i) ultimate load, (ii) stiffness and (iii) failure mode. The results are presented for SLTAI60 disbond and delamination samples. Similarly, as for the pristine SLTAI60 results, the numbers are presented as relative values, where 1 is the reference number related to the ultimate load and corresponding displacement from the mechanical testing.

SLTAI60 disbond

The prediction for the SLTAI60 disbond shows a similar trend as for the pristine sample, where the base model provides the over-prediction, and the model with interlaminar CZE shows an under-prediction of the ultimate load. In this case, the over-prediction is higher, and the under-prediction is smaller than for the pristine samples. The load decrease for the sample with disbond compared to the pristine sample is relatively high, around 25 %, with the disbond area representing 30% of the total bondline area.

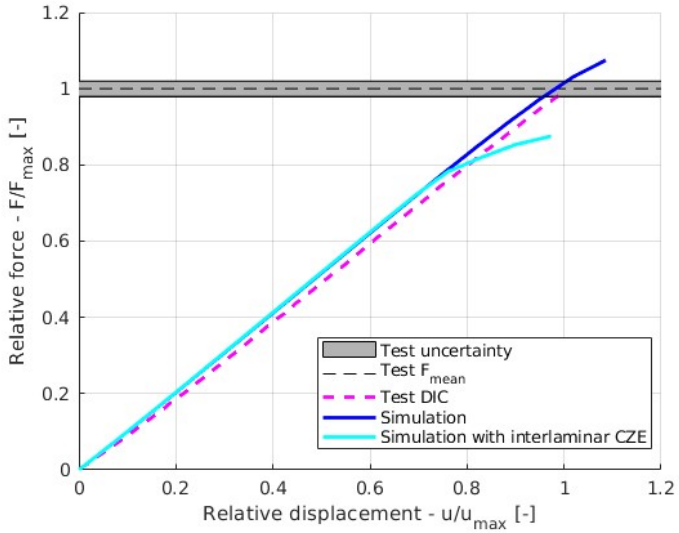

Figure 5.29: Comparison of experimental and simulated force-displacement curves for SLTAI60 disbond.

As observed in the simulation results for the base model in Figure 5.30 the crack initiation points are the corners of the adhesive bordering the disbond area. The crack grows in the adhesive forming a U-shaped feature and growing both in length and width direction. Additionally, intralaminar damage is observed with the strongest presence in the 90° (2nd) and -45° (3rd) layers. Similar behaviour is observed in the fracture surface in Figure 5.32. The same pattern of the u-shaped adhesive failure and combination of intra- and interlaminar damage up to the 4th layer is observed. However, in the case of the base simulation model, just like in the case of the pristine sample, the matrix damage extend is much more significant in the thickness direction than the one observed in the fracture surface.

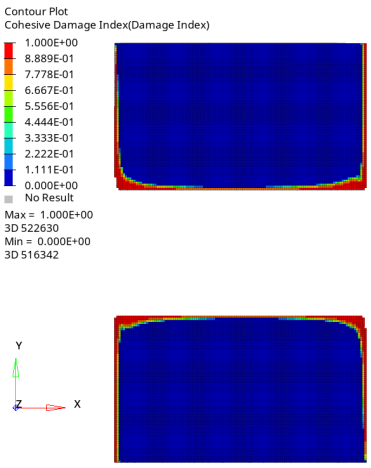

(a) Adhesive damage at $F/F_{max} = 0.85$.

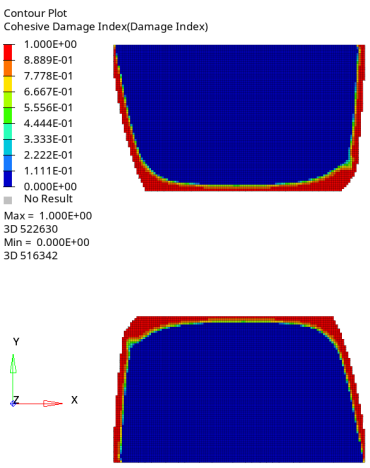

(b) Adhesive damage at last simulation time step.

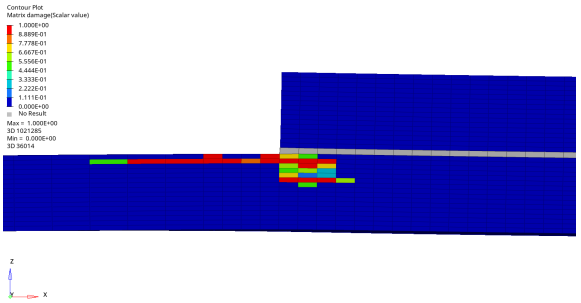

(c) Matrix damage at $F/F_{max} = 0.85$. The cross-section in the middle of the remaining adhesive.

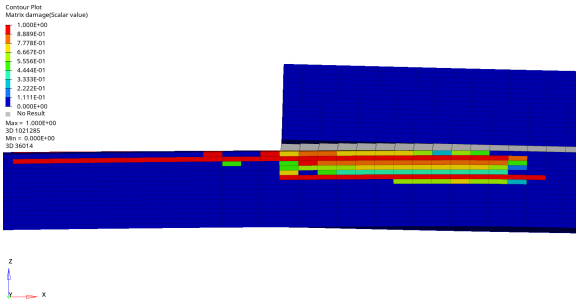

(d) Matrix damage at last simulation time step in top view. The cross-section in the middle of the remaining adhesive.

Figure 5.30: Simulated failure mode of SLTAI60 disbond with base model.

As observed in the simulation results for the interlaminar CZE model in Figure 5.31 the U-shaped damage pattern of the adhesive is predicted accurately. The most critical damage observed in the simulation is interlaminar damage between the 90° (2nd) and -45° (3rd) layers, like in a pristine sample. Similar behaviour of adhesive and interlaminar damage is observed in the fracture surface in Figure 5.32. However, comparing pristine simulation results and disbond simulation results, one can see that simulated failure is less brittle in the case of the disbond model This can be related to the fact that the intralaminar layers under the disbond stay intact due to load redistribution around it.

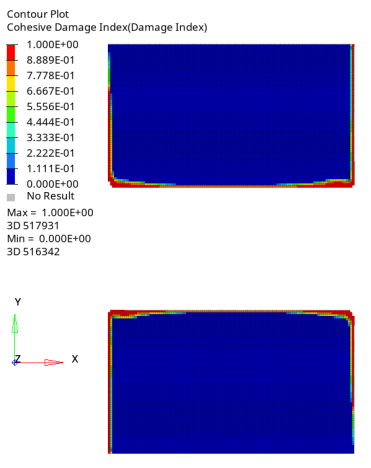

(a) Adhesive damage at $F/F_{max} = 0.79$.

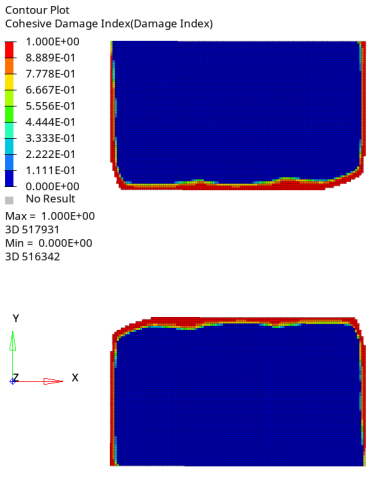

(b) Adhesive damage at last simulation time step.

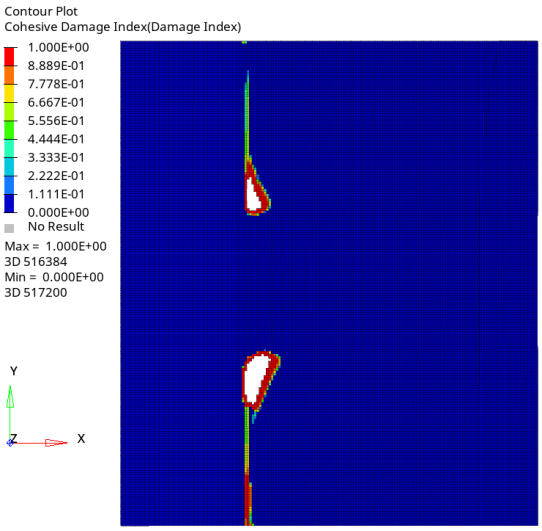

(c) Interlaminar damage between 90° (2nd) and -45° (3rd) layers at $F/F_{max} = 0.79$.

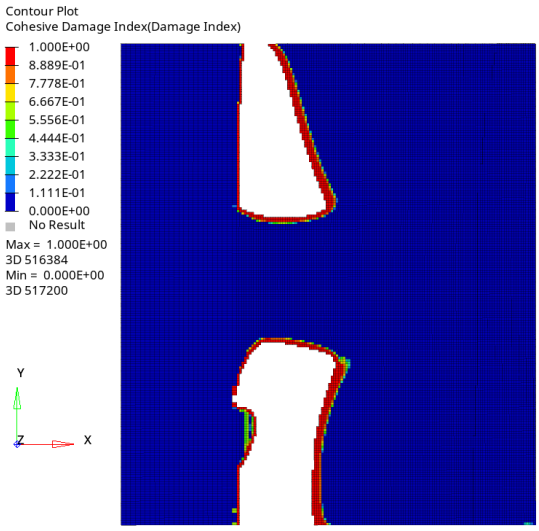

(d) Interlaminar damage between 90° (2nd) and -45° (3rd) layers at last simulation time step.

Figure 5.31: Simulated failure mode of SLTAI60 disbond with interlaminar CZE model.

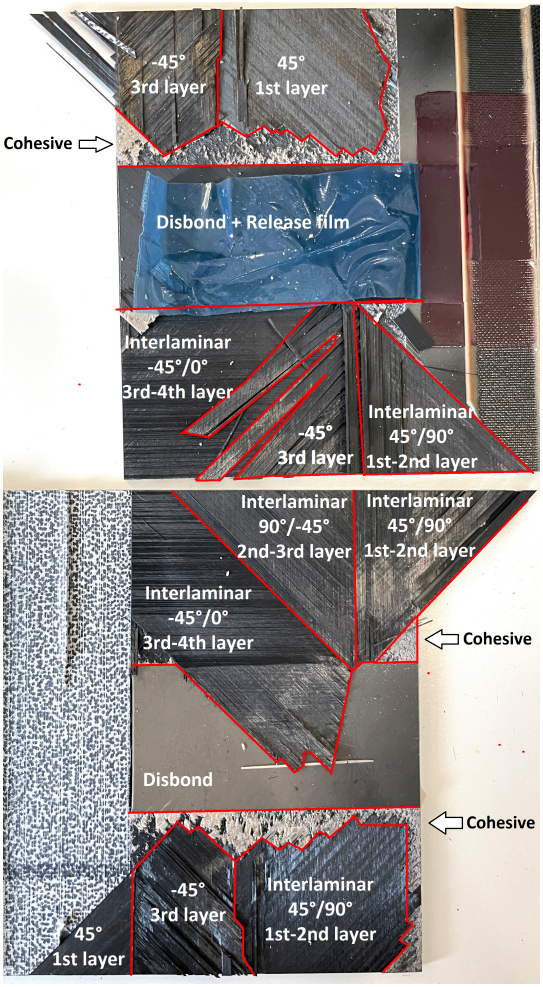

Figure 5.32: Experimental failure mode of SLTAI60 disbond.

SLTAI60 delamination

The comparison between the force-displacement graphs from the mechanical testing and simulation with two different modelling approaches are presented in Figure 5.33 for SLTAI60 delamination. Simulation over-predicts the stiffness slightly, similarly to the pristine samples. The prediction for the SLTAI60 delamination is within the standard deviation range for both models. The observed load decrease to the pristine samples is relatively small, around 2 %. Due to such a small difference and quite significant standard deviation, this can't really showcase the effect of the artificially introduced delamination. This is related to the chosen bad selection of the delamination position, especially the through-thickness location, which is showcased in more detail for the failure mode.

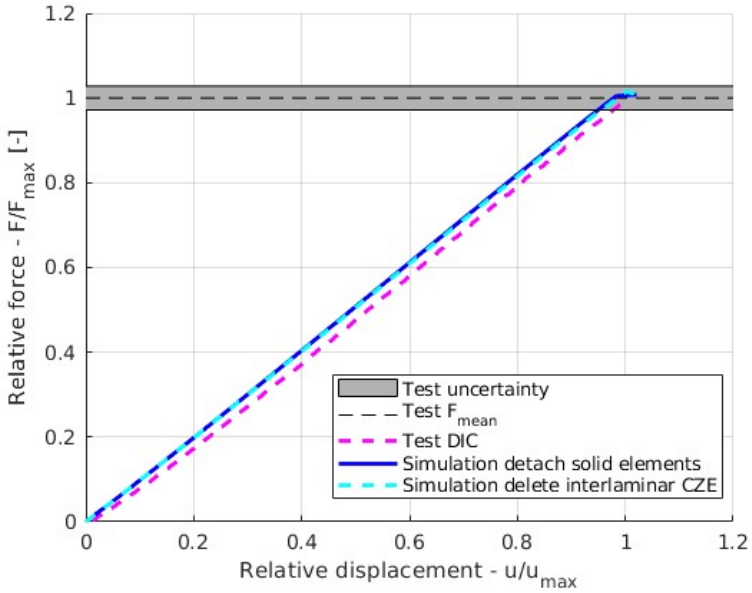

Figure 5.33: Comparison of experimental and simulated force-displacement curves for SLTAI60 delamination.

The comparison between the failure modes from the mechanical testing and simulation is presented in Figure 5.34 and 5.35 for SLTAI60 delamination. For the SLTAI60 delamination, a failure mode from the simulation with deleted interlaminar CZE is presented. For the model with detached elements, the observed element penetration is shown to explain why the results are considered not representative.

As observed in Figure 5.34 the damage initiates in the region of the adhesive edge in the simulation. The damage grows from the edge to the inside of the bondline. Additionally, intralaminar damage is observed with the strongest presence in the 90° (2nd) and -45° (3rd) layers growing together with the adhesive damage. Deleting the elements in the interlaminar layers shows a concentration around the square inclusion. However, due to the through-thickness position, this doesn't contribute to the failure mode. The concentration is clearly present on the first inclusion from the bondline between the 4th and 5th layers. The effect is minor for deeper layers, and the traction doesn't reach significant values. This contributed to the softening of the material and observed a load drop of around 2 %. A similar pattern is observed in Figure 5.35. The combination of intra- and interlaminar damage is shown on the fracture surface, with dominating damage in the first four layers. The same pattern was observed for pristine sample.

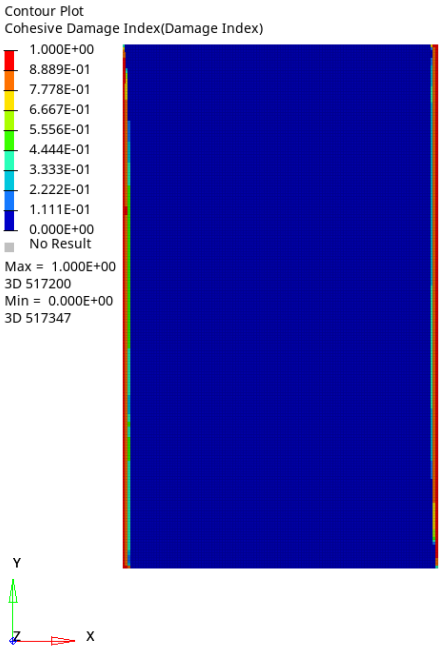

(a) Adhesive damage at $F/F_{max} = 0.88$.

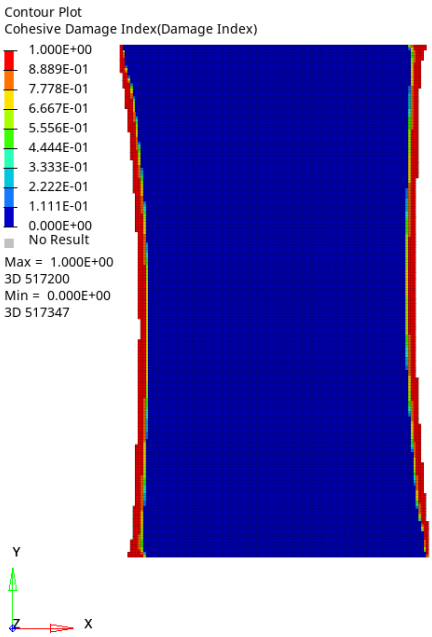

(b) Adhesive damage at last simulation time step.

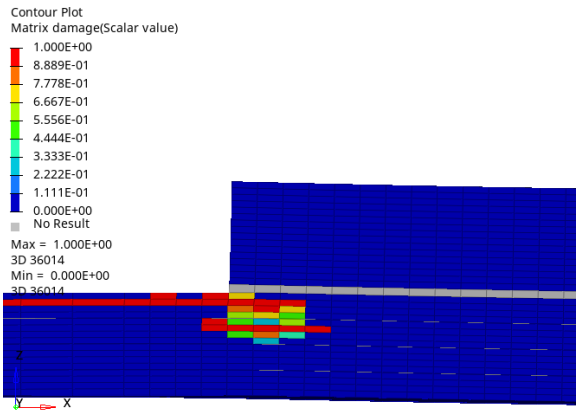

(c) Matrix damage at $F/F_{max} = 0.88kN$. Cross-section at the symmetry axis.

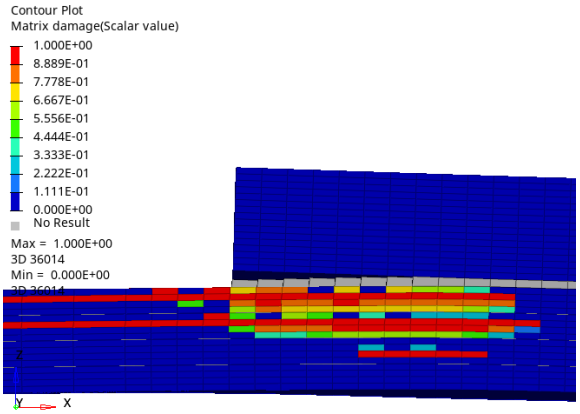

(d) Matrix damage at last simulation time step. Cross-section at the symmetry axis.

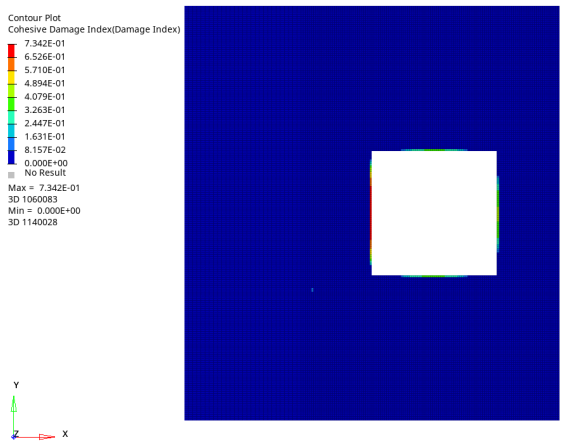

(e) Interlaminar damage between 0° (4th) and 45° (5th) layers at $F == 0.88kN$.

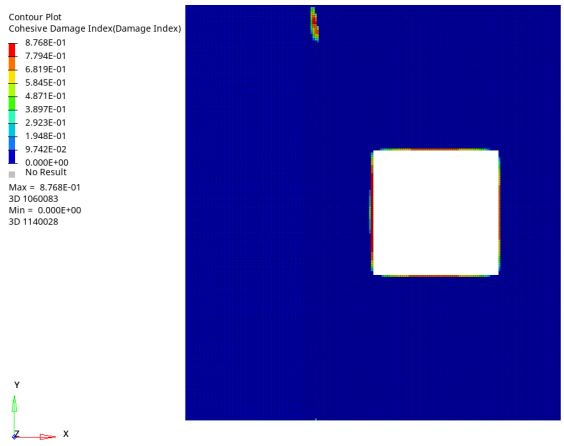

(f) Interlaminar damage at between 0° (4th) and 45° (5th) layers at last simulation time step.

Figure 5.34: Simulated failure mode of SLTAI60 delamination with deleted interlaminar CZE.

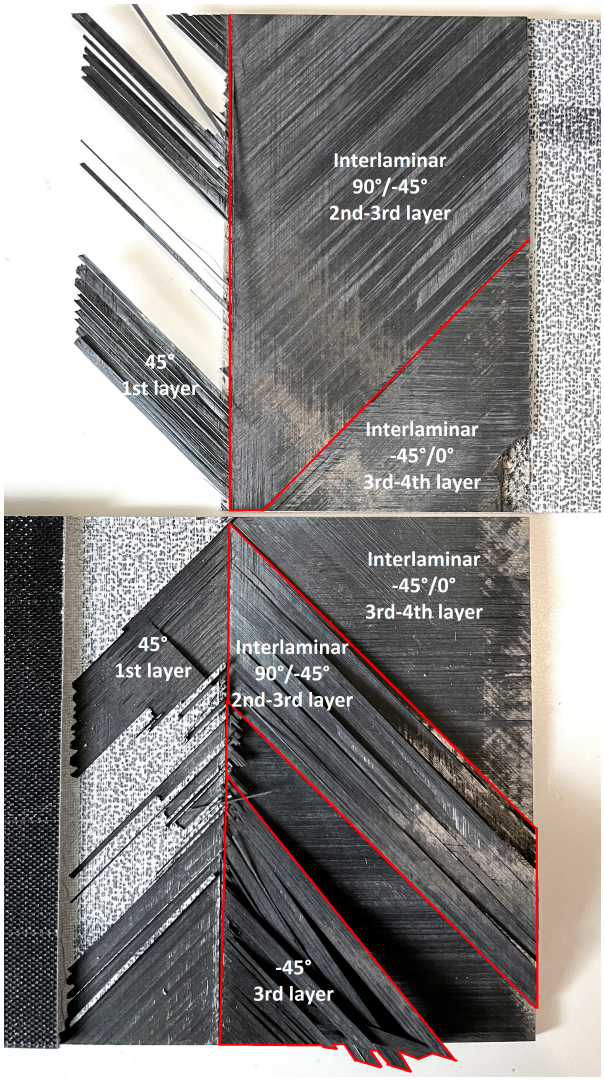

Figure 5.35: Experimental failure mode of SLTAI60 delamination.

As presented in Figure 5.36 the element penetration occurred between the laminate plies leading to a non-physical state where two plies are in the same position. In reality, the contact between the plies would produce a transverse force leading to the bending of the plies in the same direction, which can also be modelled in FE. However, the high computational cost related to this feature led to the abandonment of the detachment of the element to represent interlaminar damage in composite laminates.

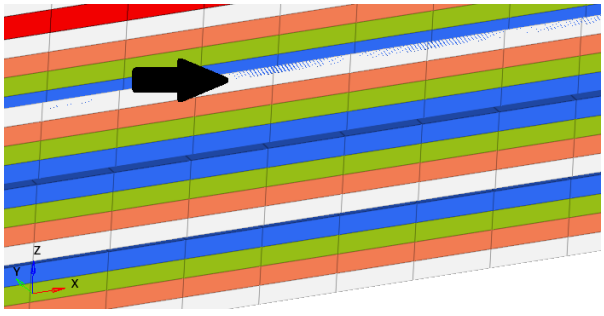

Figure 5.36: Observed element penetration in the simulation of SLTAI60 delamination with detached elements.

5.2.3. Overview of the results

In this section, a study was conducted regarding how the defects could be modelled based on the deletion of cohesive elements in the finite element models. For the study, joints with artificially introduced damage in the form of release film were tested and simulated using FEA. Results of the simulation showed that with the known size and shape of the damage, it is possible to include it in the simulation model, and accurately predict the failure load and mode of the specimen. This study is a link between the pristine and impacted samples, where in the impacted samples effects of randomness and variability come into play and damage is more distributed. Thus, artificial damage was used to confirm the approach in a fully known configuration.

Similarly, as for SLTAI60 pristine sample, the prediction of the ultimate load, stiffness and failure mode is replicated with the numerical simulation for SLTAI60 disbond and delamination samples. Interestingly the representation of the disbond in the base model over-predicts the ultimate load by around 8%, and the model with interlaminar CZE under-predicts an ultimate load by around 11 %. This indicates that even though the defect was localised in the bondline, the failure process involved the composite adherend in the region close to the bondline.

For the SLTAI60 delamination, the results are within the standard deviation bounds. Even though both models allow the prediction of the ultimate load, it was decided to proceed with the deletion of the interlaminar CZE, which allows for better tracking and simulation of initiation and propagation of the interlaminar cracks, which is not that obvious in the detached models, where non-psychical interpenetration between the plies can occur.

The simulation results for SLTAI60 with artificially introduced disbond and delamination showcased that deletion of the cohesive elements can be used to model defects in bonded joints and FE simulation. This study was conducted on samples with predefined defects before modelling impact damage with a lot of variability and randomness in the created damage pattern.

5.3. Impacted bonded joints

The modelling strategy for impact modelling is based on the experiences gained in the pristine and artificially damaged joint simulation. The lesson learned with the SLTAI60 delamination is about the criticality of the through-thickness position of the interlaminar damage in a single-lap configuration. Although quite prominent in the area, the chosen position showcased a load drop of only around 2 % compared to the pristine sample. This study is used as a base to create a critical position in which damage should be modelled in the impact cases.

The same approach and models are used, but to represent artificial damage, three approaches are tested, modelling of impact damage as a hole, multiple delaminations and single delamination utilising deletion of the elements as a modelling tool.

The modelling approach is also based on observation of the damage patterns from the impact testing campaigns. The results of ultrasonic scans and microsection are summarised in this section to explain observed patterns. A SLTAI30 sample with 8J offset impact is the main point of the study.

5.3.1. Experimental observation of damage resulting from impact

Before applying the modelling approaches for the impact damage proposed by Kassapoglou [43], the observation of the impacted samples from the JoinDT campaign is summarised. The campaign was focused on centred and offset impacts on SLTAI specimens, both SLTAI30 and SLTAI60 were impacted with variable impact energies. After the impact, the ultrasonic inspection was conducted, and samples were cut to inspect cross-sections around the impact point. The ultrasonic and microsection images taken with the microscope were analysed to identify the damage pattern in single-lap joints.

However, the indentation depth and impact energy were first post-processed to assess the low-energy impact boundary on the SLTAI30 and SLTAI60 specimens. A common way to determine the limit of the low-energy impact damage is to plot indentation versus impact energy and find a point where the indentation would be equal to 1mm by the curve fit of the existing data points [43]. For both samples, it was found that the boundary to classify impact as low-energy for those specific samples is around 30 J for SLTAI30 and 36 J for SLTAI60. The curve that fits the data points is presented in Figures 5.37 and 5.38.

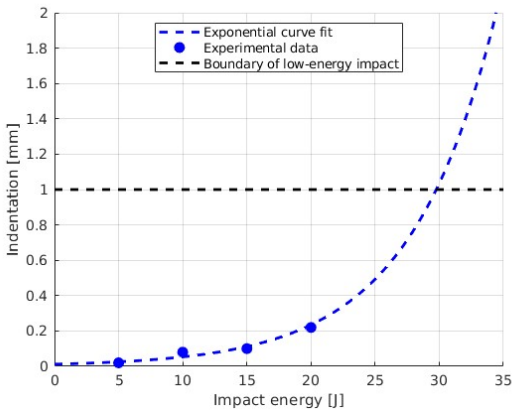

Figure 5.37: Indentation vs impact energy for SLTAI30.

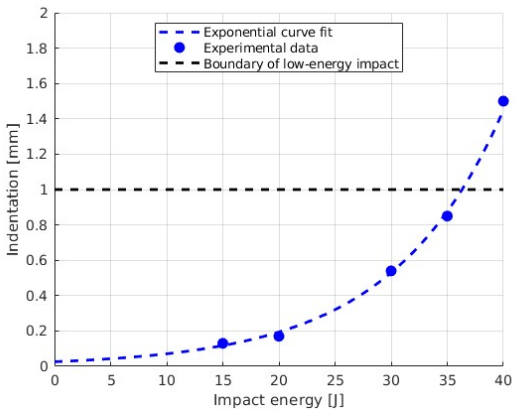

Figure 5.38: Indentation vs impact energy for SLTAI60.

Ultrasonic inspection

The first method to investigate the damage pattern was to perform ultrasonic scans of the specimens. Both B- and C-scans were used. C-scans show the position and extent of the damage, and B-scans give information about the through-thickness distribution of the damage.

For the centred impact in the middle of the width and length of the overlap, the shape of the damage resembles a circular zone concentrated in the impact point that resembles a double truncated cone pattern with the most oversized diameter in the adhesive area with single delamination in bottom adherend extending around this zone. The ultrasonic images are presented in Figure 5.39.

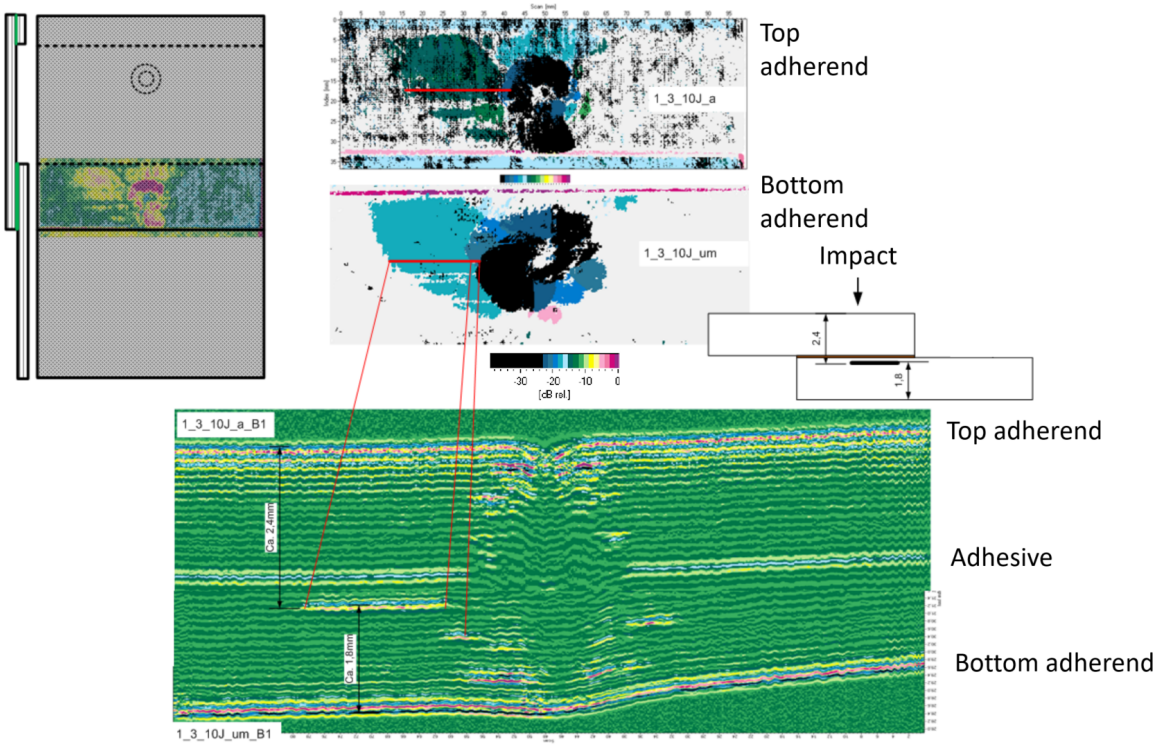

Figure 5.39: Ultrasonic images of damage after impact on SLTAI30 sample with 10J energy, centred impact position.

The damage pattern differs slightly for the offset impact in the step area. The circular zone concentrated in the impact point is relatively small and secondary compared to the larger single delaminations in the bottom composite adherend. The ultrasonic images are presented in Figure 5.40. Similar patterns were observed by Farrow *et al.* [60]. However, only C-scan images were studied. Thus, the through-thickness location of damage wasn't identified by the authors. As seen in the B-scan, the delaminations occur in the bottom composite adherend at the maximum distance of 0.30mm from the adhesive. As indicated in the C-scan image, they happen between different layers, which are indicated with different colours on the contours. The size of delamination ranges from 5 to 20mm in width and from 5 to 15mm in the length direction. As observed, ultrasonic inspection detects delamination easier compared to other damage types like matrix cracks and fibre breakage and can provide information about the location and area of the delamination [74].

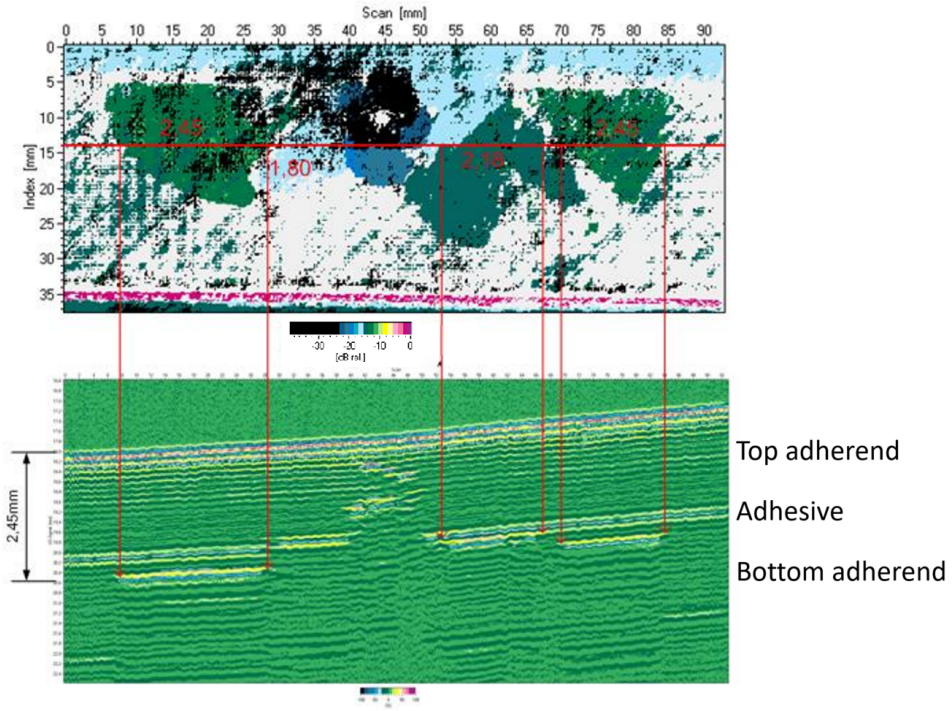

Figure 5.40: Ultrasonic images of damage after impact on SLTAI30 sample with 8J energy, offset impact position.

Microsections

Three different patterns were identified while assessing the multiple images and variety of impact energy. The first pattern identified is that in part of the samples, the damage is seen mainly in the impacted adherend and doesn't propagate to the adhesive or bottom composite adherend. The observed pattern is presented in Figure 5.41.

Figure 5.41: Damage in SLTAI30 after impact with 15J energy.

The second observation is made on the specimens with lower energy impacts (ranging from 5J to 15J). One can observe a characteristic pattern where delamination occurs mainly before the 0° layers. It can be observed in Figure 5.42 that matrix cracks initiate in the impact point but also on some micro defects and propagate through the thickness of composite adherend until they encounter a 0° ply, which changes the direction of the crack propagation to the interlaminar crack. It can be mainly observed with 10J impact energy on SLTAI 30 specimen. The pattern of delamination is presented in Figure 5.43.

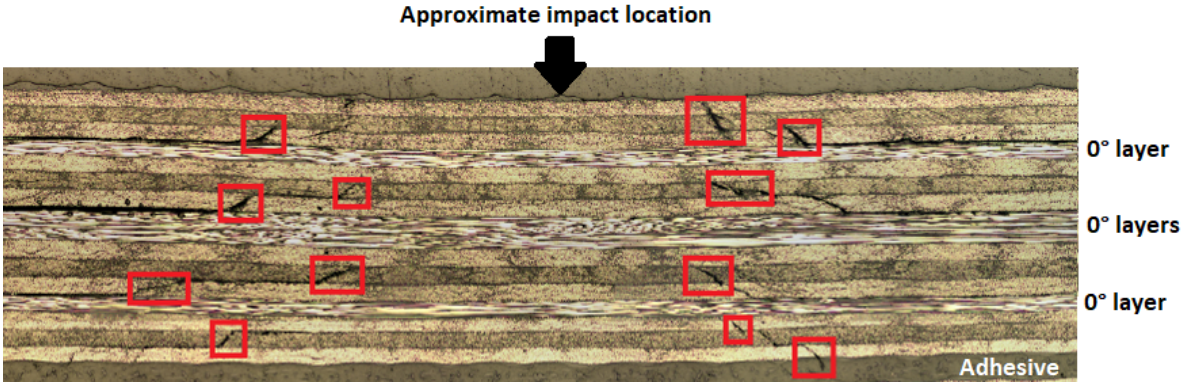

Figure 5.42: Matrix cracks after the impact with 10J energy in the top adherend of SLTAI30.

Figure 5.43: Delamination pattern in SLTAI30 specimen after impact with 10J energy.

The third observation is that the damage pattern is entirely random, and delamination occurs between most of the layers besides the stacked layers of the same orientation, like on the symmetry axis of each composite plate. No damage pattern could be found in some of the analysed cases, and a random mix of matrix cracks and delamination was observed. Additionally, it was reported by a technician that it was tough to produce a repetitive shape and pattern of the damage on the SLJ, especially with higher than 15J impact energy. Figure 5.44 presents an example of such a pattern.

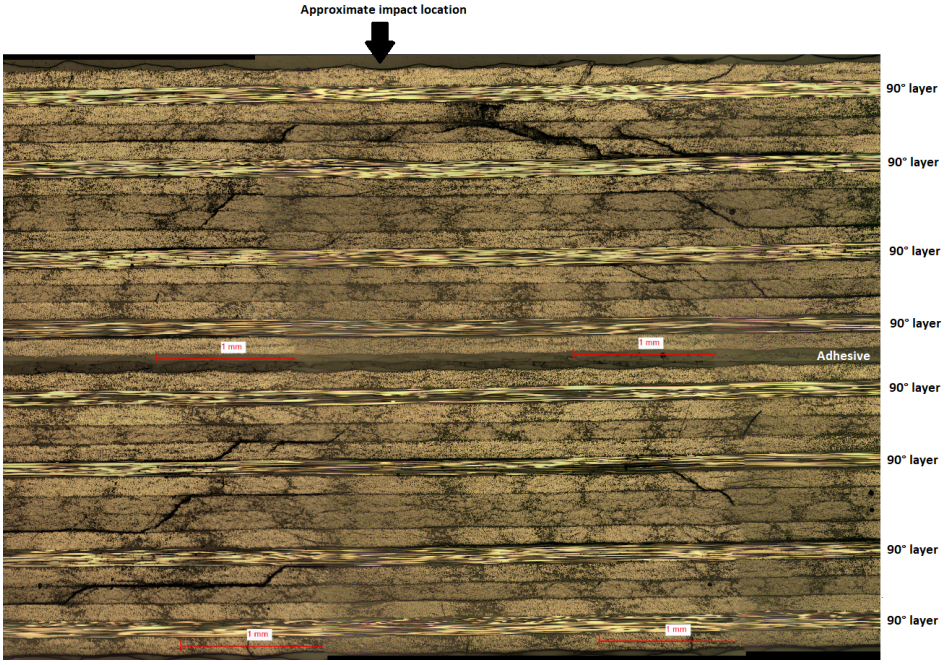

Figure 5.44: Random damage pattern in the SLTAI30 specimen after impact with 20J energy.

The limitation of this approach is that all images are two-dimensional, meaning that they are based on the direction of the cut and that different patterns are observed with varying lengths of overlap and impact energies. For example, the observed pattern with 0° layers is expected to be different if the microsection cut was made perpendicularly. The common observation is that damage resulting from impact occurs mainly through delamination and matrix cracks. This observation is used to define the modelling approach.

5.3.2. Modelling of damage resulting from impact

In this thesis, two approaches to represent impact damage are utilised. Implementing the idea for the third modelling approach as a reduced stiffness region was impossible for the Optistruct models. It was assessed that it was not possible to set the damage variable to any value between 0 and 1 for the initial state of the model, which made the research disregard this approach due to the lack of applicability of the approach.

The first approach studied takes a conservative approach to represent damage resulting from impact as a through-thickness hole in the bonded joint. The second approach models impact damage in the form of delamination. To assess the effect of such inclusions in the model, both approaches were compared in terms of the triggered failure mode of the specimen. For the modelling as delamination, two different approaches were studied on the representation as multiple and single delaminations. On top of that, the position of delamination was investigated. Models with delaminations between each layer were compared to models utilising a single delamination between the first (45°) and second (0°) ply. This choice of plies is based on the mechanical testing and simulation of the pristine sample, where one of the dominating damage types was interlaminar damage between the first (45°) and second (0°) ply. Generalising, this goes back to observing the fracture pattern of the SLJ, where the damage in adherend is observed up to the first 0° ply in a layup. To represent impact damage with a single delamination, a critical position should be chosen to collect the effects of all types of damage occurring during impact. This critical position should allow to vicariously represent the cumulative effect of spread damage in the bonded joint. Namely, three studies are conducted on (i) the modelling approach, (ii) the position of the damage and (iii) the size of the inclusion.

To model a hole, all elements are deleted in the cylindrical pattern as presented in Figure 5.45, and to model delamination, intralaminar CZE are deleted between the solid elements as presented in Figure 5.46. The important aspect to point out is that the inclusion of the damage should ideally be in a form that doesn't require an initial mesh to be changed. It was decided to delete the elements of the original mesh and the rule for deleting is that if more than 50 % of the top view (in the x-y plane) of the element is inside the assumed area of damage, the element is deleted. The mesh is not adjusted to create a perfect circular shape. As the initial size of the hole and delamination, a 10mm diameter was chosen as the average delamination size of the single delamination observed in the ultrasonic inspection.

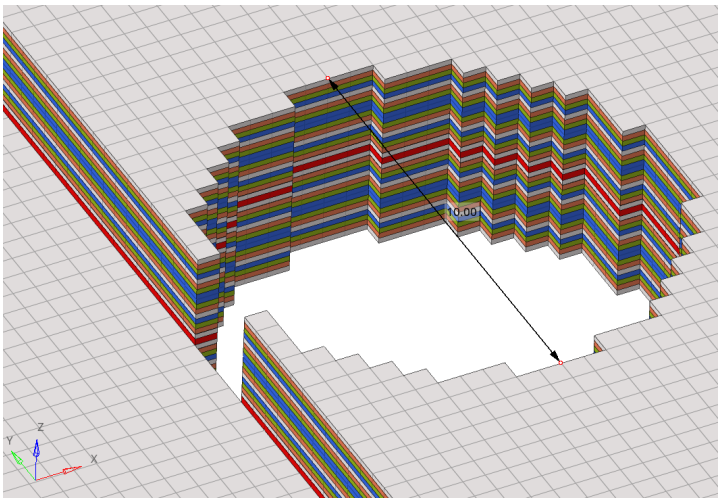

Figure 5.45: Modelling approach of impact damage as a hole in FE model.

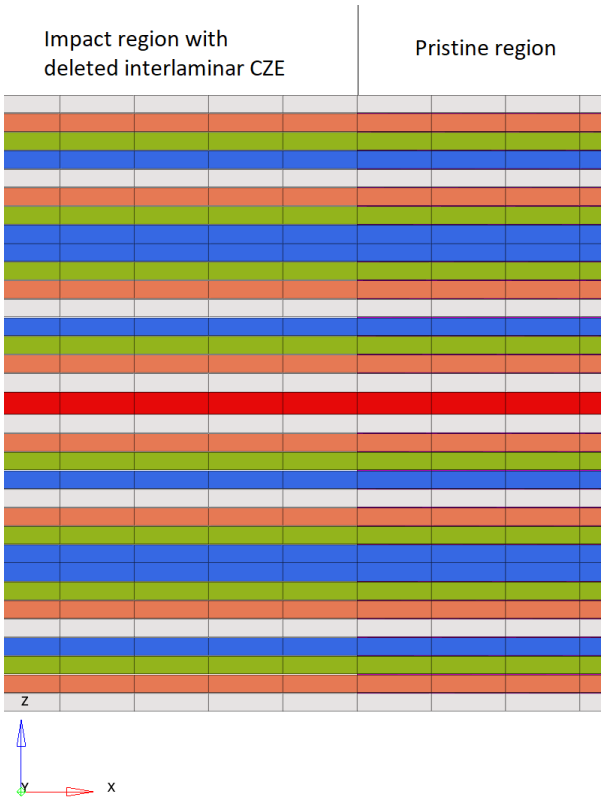

Figure 5.46: Modelling approach of impact damage as multiple delaminations in FE model.

The study following the representation of the impact damage investigated the size of the inclusion in the single delamination approach. It was proceeded with extending the size in the width direction as a general C-scan pattern observed on NDI. Due to this reason, a rectangular shape was chosen to extend the damage size in the width direction. Two different versions were tested, one with a width of 30mm and the second one with a width of 70mm, both with the same length of 10mm. The two widths are related to the patterns observed on the detailed ultrasonic inspection. A width of 30mm represents the width of the single delamination considering possible shade that could come from the impact point where the through-thickness pattern is observed. The width of 70 mm takes a conservative approach and contours all delamination between different layers observed on the images.

5.3.3. Results of simulation

The study of impacted bonded joints assessed the developed modelling approaches and compared three approaches of modelling defect to assess the effect of this modelling feature on the results. The comparison is based on three measures (i) ultimate load, (ii) stiffness and (iii) failure mode. The results are presented for the SLTAI30 sample impacted with 8J energy with an offset position. Similarly, as for the pristine SLTAI30 results, the numbers are presented as relative values, where 1 is the reference number related to the ultimate load and corresponding displacement from the mechanical testing.

SLTAI30 offset impact 8J

The comparison between the ultimate load from the mechanical testing and simulation with three different modelling approaches is presented in Figure 5.47 for the impacted SLTAI30 samples. To assess the drop of the ultimate load resulting from the impact, results are compared to the results for the pristine samples. The reduction of the ultimate load presented in Figure 5.47 is based on the mechanical testing results for the residual strength test results and on the simulation of the pristine ultimate load utilising model with interlaminar CZE for the simulation results. Such a comparison (test vs test and FEA vs FEA) allows for better quantification of the effect of the inclusion in the models on the ultimate load, taking into account the initial inaccuracy of the pristine model.

The representation as a hole decreased the ultimate load more compared to the delamination representation, which is expected due to the deletion of all elements compared to delamination, where the laminate elements can still carry some load. Both multiple and single delamination representations provide the same ultimate load with a smaller than 0.1 % difference. This showcases that more doesn't always mean better as a representation of just one delamination in a critical position between the 1st (45°) and 2nd (0°) ply allowed to obtain the same ultimate load. The delamination placed in a critical position between the first (45°) and second (0°) ply contributes to the fracture process of the bonded joint, and other represented delamination don't play a significant role in a simulation.

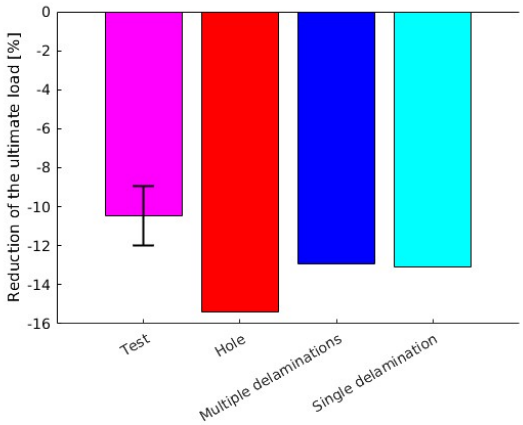

Figure 5.47: Reduction of the ultimate load in different representations of impact damage.

Three different sizes were tested for delamination in a single delamination approach. The comparison between the ultimate load from the mechanical testing and simulation with three different sizes/shapes is presented in Figure 5.48 for the impacted SLTAI30 samples. Similarly, as for the previous case study, the reduction of the ultimate load presented in Figure 5.48 is based on the pristine testing results for the impact test results and on the simulation of the pristine ultimate strength utilising model with interlaminar CZE (test vs test and FEA vs FEA). One can clearly see that with the bigger sizes of the inclusion, the reduction of the ultimate load is higher and can range up to 25 % with a 10x70mm rectangular inclusion. Interestingly the circular representation with a relatively small size of 10mm in diameter provides the most accurate results.

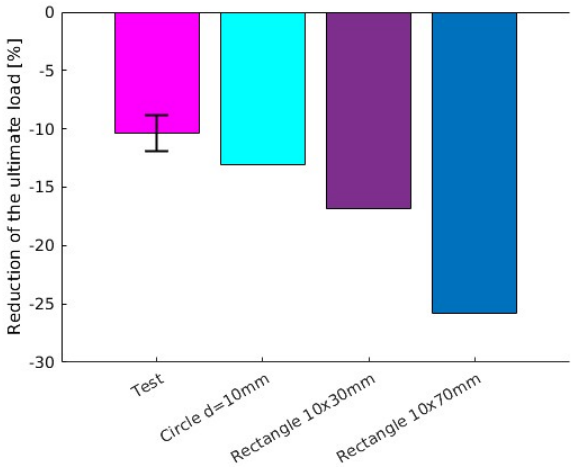

Figure 5.48: Reduction of the ultimate load in different shapes and sizes of impact damage represented as single delamination.

The comparison between the force-displacement graphs from the mechanical testing and simulation with three different modelling approaches are presented in Figure 5.49. The stiffness prediction is good for all curves. Interestingly the hole representation results in a smaller decrease in the stiffness compared to the multiple delaminations representation. This can be related to the redistribution of the load around the inclusion. For the hole, the redistribution is more equal between the adhesive and adhered, and in the multiple delamination representation, the redistribution is concentrated in the adherend leading to higher softening. For the comparison between different delamination sizes, the stiffness and ultimate load reduction are higher with the bigger size of the damage, as expected.

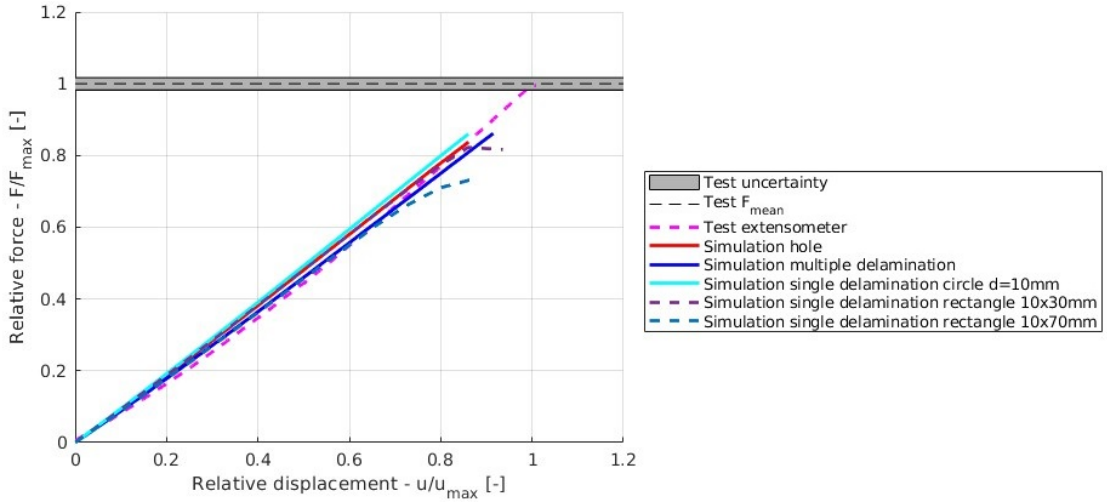

Figure 5.49: Comparison of experimental and simulated force-displacement curves for SLTAI30 impact.

The comparison between the failure modes from the mechanical testing and simulation is presented in Figure 5.50 for SLTAI30 impact hole representation and in Figures 5.51 for SLTAI30 delamination both multiple and single representations, where the same pattern was observed. A clear differentiation can be made between the hole and delamination. In contrast, the hole triggers a mixed failure in the adhesive and adherend and a delamination results in a clear damage initiation and propagation in the adherend. Observed fracture surface from a test shows damage dominating in the first two layers of the composite adherend (45° and 0°) with a cohesive failure in the corners of the overlapping area and minor damage in the third layer (-45°) and presented in Figure 5.54.

The effect of the increased size of a delamination representation on the damage initiation and propagation is presented in Figures 5.52 and 5.53. The damage starts to build up at the adhesive edge and at the edge of the rectangular inclusion because the damage is close to the bondline. The load transfer path between the two laminates has been altered. The load redistribution resulted in a stress concentration in the adhesive and laminate at the edge of the modelled rectangle.

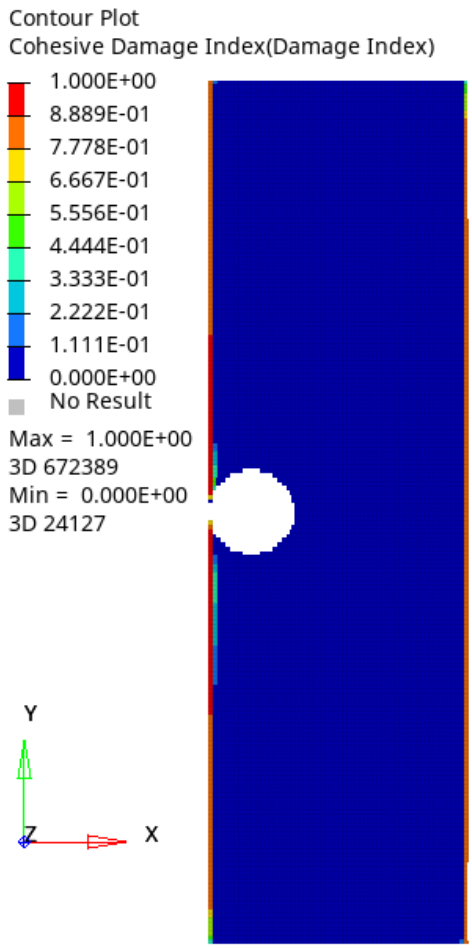

(a) Adhesive damage at $F/F_{max} = 0.7$.

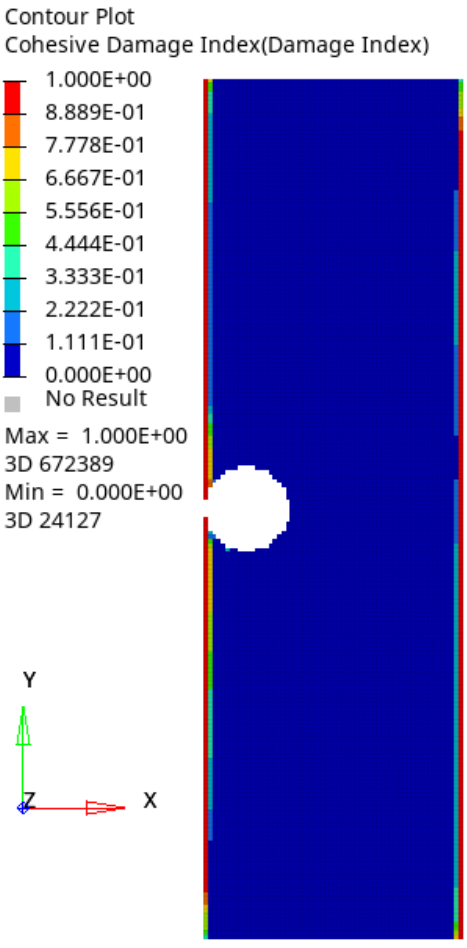

(b) Adhesive damage at last simulation time step.

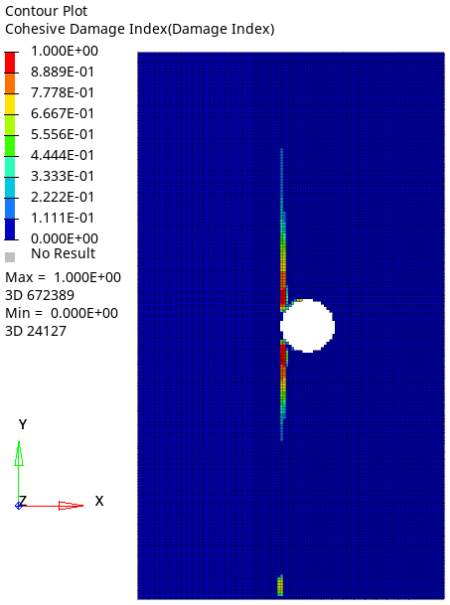

(c) Interlaminar damage between 45° (1st) and 0° (2nd) layers at $F/F_{max} = 0.7$.

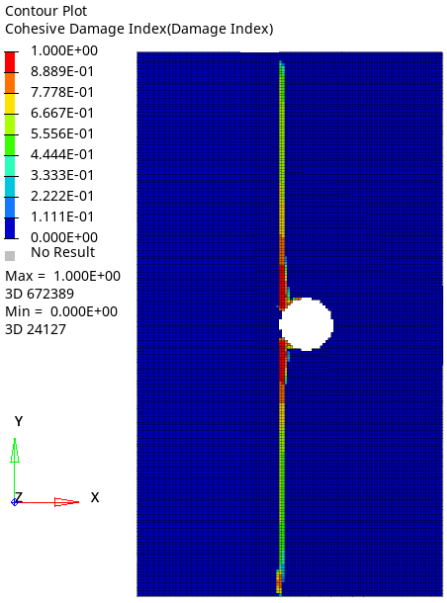

(d) Interlaminar damage at between 45° (1st) and 0° (2nd) layers at last simulation time step.

Figure 5.50: Simulated failure mode of SLTAI30 impact hole representation.

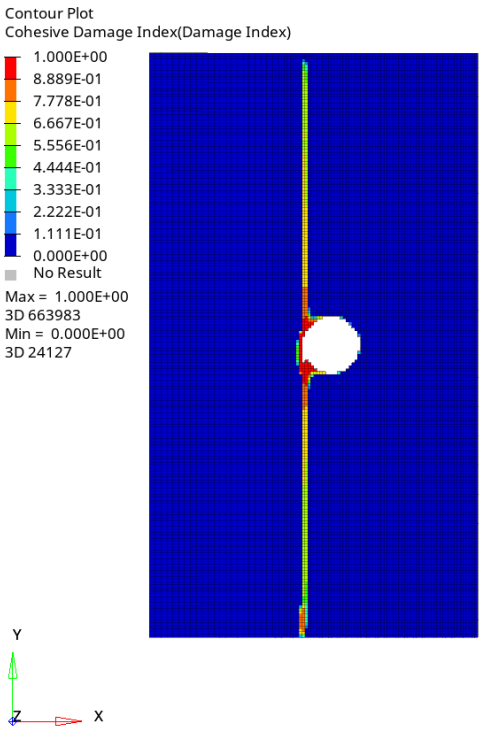

(a) Interlaminar damage between 45° (1st) and 0° (2nd) layers at $F/F_{max}0.8$.

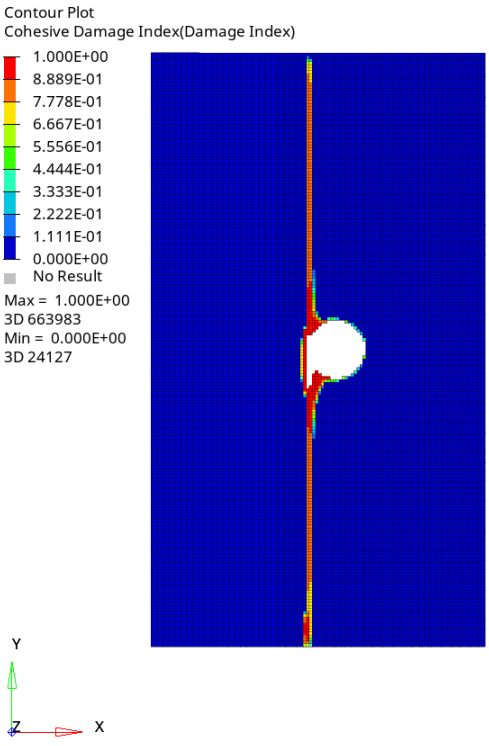

(b) Interlaminar damage at between 45° (1st) and 0° (2nd) layers at last simulation time step.

Figure 5.51: Simulated failure mode of SLTAI30 impact single delamination circle d=10mm representation.

5.3. Impacted bonded joints

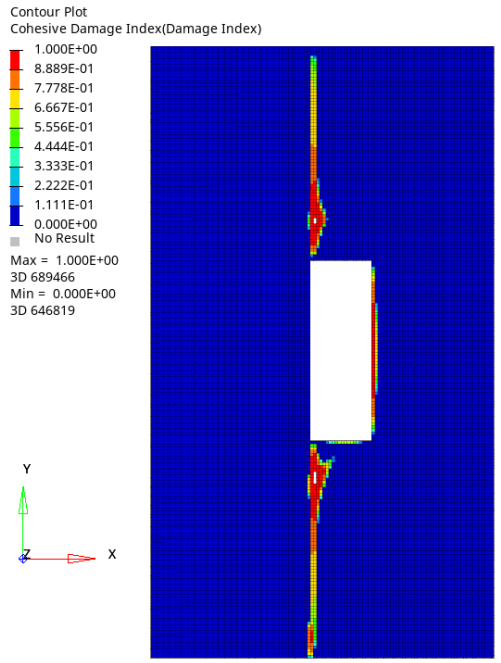

(a) Interlaminar damage between 45° (1st) and 0° (2nd) layers at $F/F_{max} = 0.8$.

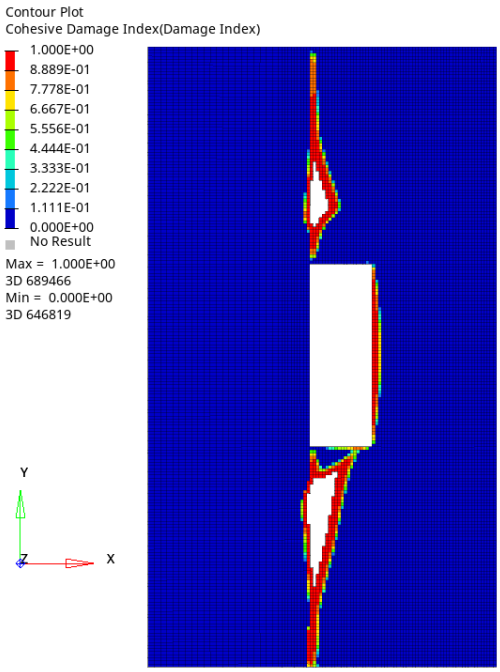

(b) Interlaminar damage at between 45° (1st) and 0° (2nd) layers at last simulation time step.

Figure 5.52: Simulated failure mode of SLTAI30 impact single delamination rectangle 10x30mm representation.

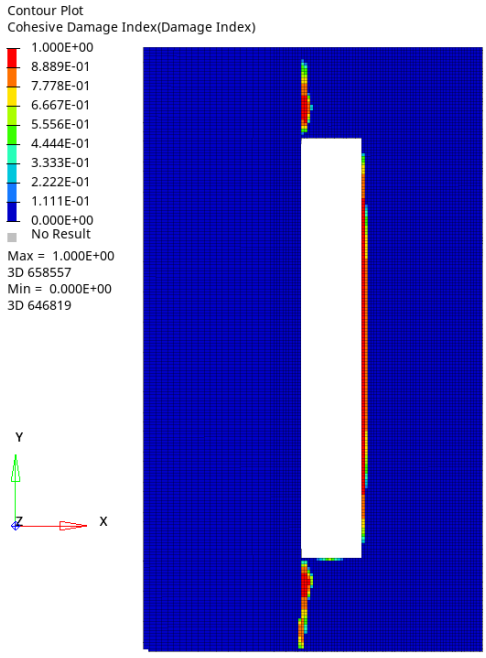

(a) Interlaminar damage between 45° (1st) and 0° (2nd) layers at $F/F_{max} = 0.61$.

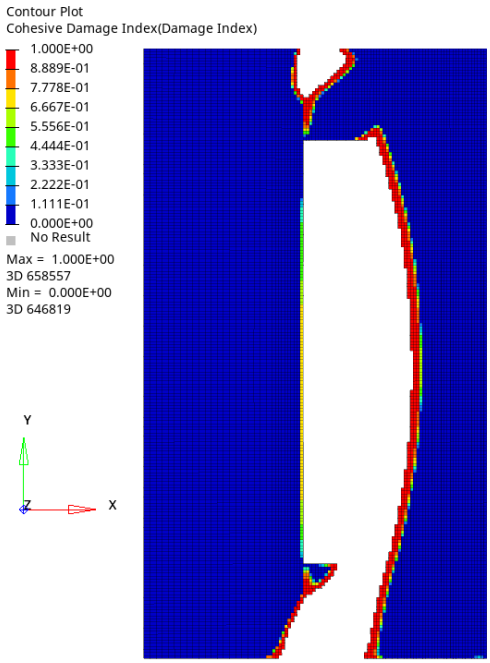

(b) Interlaminar damage at between 45° (1st) and 0° (2nd) layers at last simulation time step.

Figure 5.53: Simulated failure mode of SLTAI30 impact single delamination rectangle 10x70mm representation.

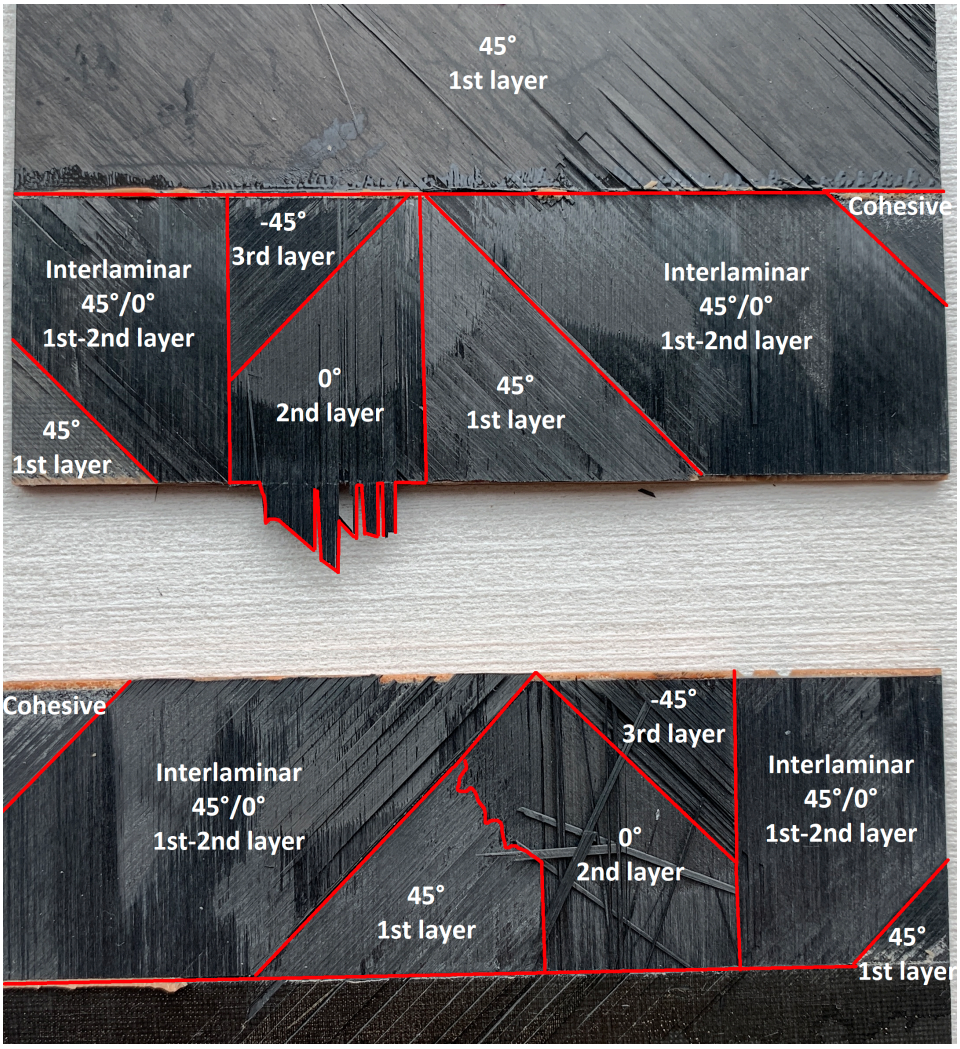

Figure 5.54: Experimental failure mode of SLTAI30 after impact.

5.3.4. Overview of the results

In this section, the simplified modelling approach was studied to represent impact damage in the single-lap joint numerical models. The modelling approach was proposed in which different types of damage occurring during impact showing a lot of variability are condensed into one modelling feature in which elements are deleted in the FE model. This was based on the ultrasonic scans, microsection images and critical position of the damage in the FE models.

Different representations of impact damage incorporated into the stacked model with interlaminar CZE provide a conservative prediction of the ultimate load. The representation of an impact as a hole through the complete thickness triggers a more adhesive-dominated failure mode, whereas the modelling as delamination results in a growth of the delamination and brittle failure. The more accurate comparison of the impact damage representation was based on the percentage reduction of the ultimate load compared to the pristine sample simulation. A similar percentage of the ultimate load reduction is obtained with different representations, where the most accurate is the representation as a delamination. In the topic of size, a representation as a circular inclusion of 10mm diameter, which is related to the maximum size of a double truncated cone damage pattern in impact point from the ultrasonic scans, provided the most accurate result and wider rectangular inclusions showed too conservative values.

6

Summary and discussion

In this project, a simulation approach was proposed and studied to efficiently and accurately predict the failure of composite bonded joints with manufacturing defects and damage from low-energy and low-velocity impact. The simulations were performed using finite elements with cohesive zone models for the adhesive and interlaminar regions with the multiscale material model generated and characterised in this thesis for carbon fibre-reinforced plastics laminate. The method was applied to various single-lap samples in different dimension configurations. This chapter summarises the simulation results with a discussion on the different modelling approaches studied.

6.1. Summary of the results

In Table 6.1, the summary of the simulation results is presented. Three measures are compared to the results from the mechanical testing (i) ultimate load, (ii) stiffness and (iii) failure mode. The summary of the results creates a base for the discussion and comparison between different approaches presented for the modelling of the samples in this thesis.

The percentage difference between the test and simulation is provided for the ultimate load. The stiffness was measured as a tangent between the closest points defining the linear part of force-displacement curves in the chosen range. For SLS0, it was measured between 0.05 and 0.3mm, for SLS45 between 0.05 and 0.15mm, for SLTAI60 between 0.05 and 0.3mm and for SLTAI30 between 0.05 and 0.2mm. The initial parts of the curves up to 0.05mm were not considered due to the effects of initial preload observed in mechanical testing. In the column of failure mode, a symbol + indicates if the predicted simulation failure mode was a dominating one observed in the fracture surface. For the +/-, the failure mode was observed in the test but wasn't a dominating one.

Table 6.1: Comparison of the simulation results with mechanical testing results.

Model	Ultimate load	Stiffness	Failure mode
Pristine			
SLS0	-3.5%	-1.7%	Cohesive +
SLS45	+4.7%	+0.8%	Intralaminar failure +/-
SLS45 interlaminar CZE	-11%	-0.6%	Delamination +
SLTAI60	+1.3%	+1.5%	Intralaminar failure +/-
SLTAI60 interlaminar CZE	-21%	-0.1%	Delamination +
SLTAI30	+10.5%	-7.9%	Intralaminar failure +/-
SLTAI30 interlaminar CZE	-11.3%	-8%	Delamination +
Artificially damaged			
SLTAI60 disbond	+8.6%	+0.5%	Mix adhesive and adherend +
SLTAI60 disbond interlaminar CZE	-11.6%	+0.4%	Mix adhesive and adherend +
SLTAI60 delamination delete	+1.5%	+0.1%	Intralaminar failure +/-
SLTAI60 delamination detach	+0.8%	+0.6%	Intralaminar failure +/-
Impacted			
SLTAI30 hole	-16.3%	-3.4%	Mix adhesive and adherend +/-
SLTAI30 multiple delaminations	-13.8%	-6.6%	Delamination +
SLTAI30 single delamination	-13.9%	-0.7%	Delamination +

Table 6.2 presents the summary of the simulation times. Because an implicit solver is used in this work, the simulation finished in a different damage state. Thus, the exact numbers should be rather treated as ballpark numbers. For the small coupons SLS0 and SLS45, a simulation run is quite short, and for the bigger samples SLTAI30 and SLTAI60, the simulation can run up to a few days. The critical thing to point out is that simulation of SLTAI30 with introduced impact damage runs faster than the pristine models incorporating interlaminar CZE used as a base for the impact damage modelling.

Table 6.2: Comparison of the simulation time.

Model	Simulation time
Pristine	
SLS0	57min
SLS45	4h 8min
SLS45 with interlaminar CZE	10h 14min
SLTAI60	9days 23h
SLTAI60 with interlaminar CZE	6days 18h
SLTAI30	1day 1h
SLTAI30 with interlaminar CZE	2days 11h
Artificially damaged	
SLTAI60 disbond	6days 23h
SLTAI60 disbond with interlaminar CZE	9days 16h
SLTAI60 delamination delete	4days 22h
SLTAI60 delamination detach	6days
Impacted	
SLTAI30 impact hole	15h
SLTAI30 impact multiple delamination	1day 21h
SLTAI30 impact one delamination	1day 13h

6.2. Discussion

Overall the results provide a good prediction of ultimate load with a maximum over-prediction of 10.5% and a maximum under-prediction of 21%. For the stiffness prediction, the differences are relatively small within the bounds of +1.5% to -8%. For the failure mode, the general prediction of the failure occurring either in the adhesive, adherend or mixed failure was correct in all simulations. The predicted failure mode in the simulation is highly dependent on the modelling approach. The difference is observed between the base model and the model incorporating interlaminar CZE, and the best example of this difference is the SLS45 sample. Samples with 45° ply on the interface show dominating relatively ductile intralaminar failure for the base stacked mesh approach. Delamination failure is predicted using a stacked mesh with interlaminar CZE, which shows brittle behaviour.

For both models, the most significant portion of the damage is expected up to the first 0° layer, which initiates at the edge of the overlap and propagates through the overlap length. For the models including interlaminar CZE, the failure is much more brittle than the matrix failure, which shows plastic effects. Both of the predicted failure modes are seen in the actual fracture surfaces of the samples, where the fracture shows a combination of intra- and interlaminar damage. For the pristine samples, the SLTAI30 sample shows a differentiation from the trend in predicted ultimate loads, whereas, in SLS45 and SLTAI60, the prediction with the base approach was closely in the standard deviation range of the ultimate load and for SLTAI30, the base model over-predicted the ultimate load by around 10 %.

For the SLTAI30, this difference is higher and can be related to the sample manufacturing process. Due to the different project partners manufacturing samples, the surface preparation was different. Surface treatment for SLTAI30 was done with a scotching procedure which involves manual grinding. On all other samples, the plasma treatment was used. Compared to the plasma treatment, manual grinding shows a higher scatter of the tested stiffness and ultimate load [16], [75]. The procedure can introduce micro-damage to the outer adherend ply. When damage is introduced to an outer ply, it effectively decreases its strength by creating micro-cracks, especially in the matrix. The cracks present in the material act like defects, and they grow under the loads applied to the joint. This, under relatively low loads, softens the ply material and redistributes the load to other plies. Additionally, when the stiffness of the outer ply decreases, it's possible that the mode I crack opening in the adhesive layer is more critical as lower stiffness would result in allowing for the adhesive layer opening between the two laminates. The micro-damage and reduced stiffness of the outer ply can also help trigger delamination under the first ply, especially in the layup configuration where the second from the bondline ply is oriented in 0° direction, which shows a stiff behaviour as it's oriented in a load direction.

6.2.1. Modelling approach with interlaminar CZE

The common factor between the simulation using the base approach and utilising interlaminar CZE is that the ultimate load in the base approach is over-predicted. With the interlaminar CZE layers, it's under-predicted. Both methods predict failure in the composite adherend in SLS45, SLTAI60 and SLTAI30 samples. However, the specifics differ. With the interlaminar CZE, the delamination failure mode is triggered between the second (90°) and third ply (-45°) in the layup or between the first (45°) and second (0°) ply in the layup depending on the stacking sequence. On the other hand, the damage dominates in the matrix for the base models due to the inability of capturing a brittle interlaminar crack propagation. For the two models, the areas of the damage initiation are the same at the edge of the adhesive in the composite adherend. First, the damage grows in the width direction up to the point when the whole width at the adhesive edge is damaged, and after that, it starts to propagate in the length direction. The state in which the whole width of the interlaminar is close to reaching total damage is considered the indicator of the ultimate load being reached. For the small coupon SLS45, it was possible to show what happens in the simulation after that state and simulate a very brittle propagation of the delamination in the length direction. However, for SLTAI samples, this state was the last simulation step that lead to the convergence issues due to the large number of elements being affected.

A more accurate failure mode prediction is obtained in models with interlaminar CZE, but a more precise prediction of the ultimate load is simulated with base models. It is possible that the traction reduction by a factor of two leads to a too-conservative prediction, whereas expected, it led to a faster crack initiation. However, a very brittle behaviour of damage propagation in interlaminar CZE resulted in a less accurate ultimate load prediction. From the design and analysis point of view, a simulation should provide conservative results obtained with interlaminar CZE models all over the simulated range of the samples. This under-prediction is simulated on various samples with different sizes and overlap lengths, highlighting its future applicability. The same stands for the base model, where all simulations showed a slight over-prediction of the ultimate load.

Another possible reason for result differences is that the use of implicit solver results in a fact that load drop is not observed at the last simulation time step. By comparing the damage state to the small samples like SLS45 for which the load drop was observed, it was assessed that the state at the last simulation time step can be treated as equivalent to the damage at the ultimate load. However, there is no 100% confidence in this approach as it is possible that the simulation can run further and the observed failure is not as brittle as expected. If the simulation can run further, that means that the under-prediction of failure load is not as significant as shown. However, this is the limitation that came into the developed methodology with the use of implicit simulation, and to assess the damage state with confidence, an explicit solver should be used, where convergence problems don't play such a significant issue.

Summarising, the biggest problem of the proposed modelling approach is associated to the interlaminar cohesive zone model, where the proposed reduction of the maximal traction resulted in too fast interlaminar crack initiation combined with a brittle growth. This goes back to the limitation of the cohesive zone models where the parameter measured in mechanical testing is a critical strain energy release rate, and two other parameters, stiffness and maximum traction, are fitted in the numerical model. This results in fitting the parameters based on a specific numerical model that influences fitting parameters, and thus a different model can provide less accurate results. The fracture modes were replicated by taking the material parameters with reduced traction values in the numerical models. However, the inaccuracy related to this modification is seen in the under-predicted ultimate load values. Additionally, the inaccuracy of the base model developed to the pristine samples is an inseparable part of the difference in the results propagating to the models with artificial and impact damage.

6.2.2. Modelling of damage

In this project, two approaches for representing the damage were studied, deletion and detachment of the elements. Deleting the elements allowed for representing two different defect types, a kissing bond and delamination. Both simulations showed the initiation and propagation of the damage in the cohesive layers, allowing for a simulation of the crack in the adhesive and interlaminar layers. However, for the sample with artificial interlaminar damage, the position of the artificial damage didn't allow to show the damage initiation around the release film due to the chosen position in the thickness direction. The sample showed the expected slight drop in the ultimate load, but this small value, in combination with a high standard deviation for the test, doesn't allow to confirm this study fully. The test design should be improved for future studies to observe the damage initiation at the edges of the area where elements are deleted and observe a significant drop in the ultimate load.

For the detachment of the elements, it was observed that besides acting like inclusion around which stress concentration occurs, the models show an interpenetration behaviour of the plies between the two ends of the initial delamination. This results in a non-physical behaviour of the different plies and can lead to very high peel-off stresses that haven't been observed in models with interlaminar CZE and tests. Very high peel stresses can lead to preliminary initiation and propagation of the damage in the composite material. In principle, this problem could be solved by applying a contact algorithm. However, in the first trials in was observed that the simulation time is significantly affected (2 times longer) by the multiple contact iteration, which resulted in disregard of this approach. Additionally, the lack of the possibility to simulate damage propagation resulted in disregarding this approach for further studies.

Modelling approaches for adhesive and adherend defects have been confirmed but without full confidence due to the test design that should be revisited. The choice of technique for the representation of the impact damage was the deletion of the interlaminar cohesive zone elements due to the problem with damage propagation and micro-buckling in the detachment of the element approach.

6.2.3. Representation of impact damage

Three different approaches were studied to represent the impact damage, modelling impact damage as a hole, as multiple delamination and a single delamination representation with the maximum diameter of a double-truncated cone observed in the ultrasonic inspection.

The first study was an impact damage representation by a through-thickness deletion of elements in a cylindrical shape. It was quickly disregarded due to the too-conservative load predicted and triggering different failure modes compared to the tested impacted samples. The significant difference in the failure mode between SLTAI30 pristine and impacted samples was that mixed failure in the adhesive and adherend occurred in the pristine sample. For the impacted joint, the adherend failure was dominating. In the numerical model, the hole inclusion triggered adhesive-dominated failure mode.

The following study was the simulation of the multiple delamination representation. It was observed that even though all interlaminar layers are modelled, the relevant damage occurs only in the layers up to the first 0° ply in the layup, which highlighted the critical position of impact damage representation for a single delamination representation. This resulted in the representation of impact damage as a single delamination between the first (45°) and second (0°) ply. This also reduced the model's size significantly, where all other interlaminar layers don't have to be modelled, resulting in a significantly lower number of nodes. Both models with multiple and single delaminations showed very similarly predicted ultimate load and slight differences in the stiffness prediction.

All results stay conservative because they are implemented on the model, including interlaminar CZE elements that predict a conservative ultimate load in the pristine samples. The study showed the predicted ultimate loads with a conservative under-prediction ranging from -11 to -20 %. As observed in the simulation and fracture surface analysis, the elements deleted in the interlaminar layers triggered a delamination failure mode between the first (45°) and second (0°) ply, which was a dominating failure mode in the fracture surface of the sample.

The final study explored the size of the single delamination representation, where a rectangular shape was chosen to extend the damage size in the width direction based on the damage extend observed in the ultrasonic scans. With the wider representation, the decrease of the ultimate load was very big and not comparable to the test results, which highlighted the use of the circular inclusion with the diameter size of the highly damaged conical area observed during the ultrasonic inspection in the future application.

One of the definite limitations of this representation is that delamination resulting from impact is usually created around the impact point, which is also known as the impact damage cone, which suffers from combined matrix cracks and delamination. In this approach, delamination was modelled directly in the impact point. This is related firstly to the width of the sample, where the effects of the different types of inclusion in the FE model were analysed. Going back to the longitudinal fuselage joint that was ideally to be studied, the impact of such delamination should be assessed in the global stress field in which the edge effect doesn't play a role. However, impacts can also occur at the edges in a real structure, highlighting the following research topic.

7

Conclusions and recommendation

This project aimed to develop a simulation approach for an efficient and accurate prediction of the failure of composite bonded joints with the defects resulting from manufacturing and damage from low-energy and low-velocity impact. The studied method was based on the finite element simulation models utilising state-of-the-art cohesive zone modelling of the adhesive and interlaminar composite layers and the multiscale material model generated and characterised in this thesis for the composite adherend. The method was applied to various single-lap joints in different dimensions and lay-up configurations.

There were two main investigative directions studied in this thesis. The first one is the generation and validation of a multiscale material model for the 8552/IM7 carbon fibre-reinforced plastic. Whereas in the second part, it was investigated if using pre-induced impact damages in a finite element model can allow for avoiding the explicit impact analysis step.

The first topic which was tackled was related to generating the multiscale material model utilising representative volume element. The constituent parameters were characterised by the linear, damage and plasticity laws and using a homogenisation and inverse characterisation in the optimisation scheme. The values of the constituent parameters were found based on the homogenised target values from the coupon testing. The material model was implemented as a reduced order model that links the homogenised and constituent strains. Finally, the model was validated on a higher scale single-lap joint detail, which allowed to adjust the value of matrix volumetric strain at full degradation and obtain an accurate prediction of stiffness and ultimate load in implicit solver.

The second topic investigated in the thesis was modelling the manufacturing defects and impact damage in the numerical models of single-lap joints. The base for the modelling was created with an adhesive modelled with cohesive zone elements and stacked adherend mesh utilising multiscale material and interlaminar cohesive zone elements modelled up to the first 0° ply in the layup. The defects/damage were incorporated into the models by deleting the elements in the damaged area. The application was in the same region where the release film was placed for the models with artificially damaged joints. For the impacted joints, the modelling was proposed based on the observations from the ultrasonic scans, microsection images and critical defect position in the simulation. The location between the first (45°) and second (0°) ply allowed to model a single delamination that provides a conservative ultimate load prediction with a quite low modelling effort needed to incorporate impact damage to models with interlaminar cohesive zone elements modelled up to the first 0° ply in the layup.

In the following sections, the main conclusions of the thesis work are discussed, and the answers to the studied research questions are provided and reflected upon. Finally, recommendations are provided for future testing, simulation and research on damage-tolerant design and composite bonded joint analysis.

7.1. Conclusions

In the conclusions, the answer to the set of research questions and subquestions is provided based on the research conducted. First, the answer to the main research subquestion is offered to create a base to answer the main questions.

Subquestion RQ1.1

How can the damage initiation and propagation be accurately modelled using the experimental data from coupon tests?

In this project, the bilinear model of the fibre and matrix damage combined with the rate-independent plasticity model of the matrix was used to model the initiation and propagation of the damage on the micro-scale in the composite material. It was identified that the data from the coupon tests, 0° tension, 0° compression, 90° tension, and ±45° tension, can be used to model initiation, and propagation of the damage in the composite by the identification of which parameters from the available material damage and plasticity models for the constituents can be linked to which of the coupon curves. For the composite material, the following links between the material models and coupon were used: 0° tension - fibre damage, 0° compression - fibre damage, 90° tension - matrix damage and ±45° tension - matrix plasticity. The damage model was based on the characterisation of the fibre and matrix parameters based on the homogenised material properties. Homogenisation and inverse characterisation incorporated in an optimisation loop were the link and solution to find the value of the constituent parameters. The optimisation loop was used to find matching parameters of the material models on the constituent scale based on the coupon results.

Subquestion RQ1.2

What is the applicability of the multiscale damage model generated with Multiscale Designer in the implicit Finite Element solver?

For the applicability of the material model, it was found that after an initial calibration, an additional step is needed to create a material model usable in the implicit solver. In this step, the value of the volumetric strain to failure (J1) should be adjusted based on element or detail level tests independently of the data used in the material characterisation. In the case of this study, SLS0 and SLS45 coupons were used. Even though the implicit solver was used during the study, it was possible to propagate damage in the composite adherend to a large size, which showcases the usability of this material model in the implicit solver after adjusting the J1 value.

Subquestion RQ1.3

How to model a bonded joint using RVE generated multiscale material model to consider all possible failure modes?

As identified during this thesis project, using a multiscale material model allows a model of a pure matrix and fibre failure. Without additional modelling features, it is limited to those failure modes. Different failure modes can be incorporated into the model using the interlaminar CZE, which allows the depiction of a failure mode of delamination. A multiscale material can also model a debonding between the fibre and matrix by modelling the third interphase. Even though identified, this wasn't tested in this thesis.

To depict the most accurate failure mode of the single-lap joint, the models utilising a stacked meshing approach with interlaminar cohesive zone elements (CZE) were used. Even though the pure stacking mesh approach was more accurate in predicting failure load, it failed to predict brittle delamination between the plies that are observed up to the first 0° ply in the layup.

Summarising, an additional modelling feature of interlaminar CZE is required to model all failure modes observed in the SLJ configuration.

Research Question RQ1

How can the multiscale material model be generated using the representative volume element and used on a macro level to predict damage in the composite material during static and residual strength simulations of bonded joints?

The answers to the subquestion RQ1.1, RQ1.2 and RQ1.3 create the base to answer the main research question. Based on the work conducted, a solution can be provided that the representative volume element (RVE) can be used to characterise the damage occurring in the composite material based on the plasticity and damage models on the scale of the constituent. The FE simulation can create a reduced order model that characterises the link between the homogenised and constituent strains to simulate the damage occurring in the constituents based on the strains from the macro-level simulation. This has to be combined with different modelling techniques, such as interlaminar CZE, to consider failure modes that appear on the macro-scale.

Subquestion RQ2.1

What is the applicability of the simplified modelling approaches, such as modelling impact damage as a hole, delamination and region of reduced stiffness in composite bonded joints?

This study investigated two approaches: modelling impact damage as a hole and delamination. For the modelling as a reduced stiffness region, the implementation of the idea was not possible for the Optistruct models, as it was assessed that it's not possible to set the damage variable to any value between 0 and 1 for the initial state of the model, which made the research disregard this approach due to the lack of possibility of application of the approach.

Deletion of the elements to represent a hole in a structure allowed for simple incorporation into the pristine model. However, the resulting drop of the ultimate load was very conservative, and on top of that, the hole triggered an adhesive-based failure mode. The test results of the failure mode between the pristine and impacted specimen showed the difference in the failure mode of samples. The pristine model was characterised by a mixed cohesive failure in the adhesive and delamination between the first and second layers. For the impacted sample, the damage in the adherend in the form of delamination and matrix damage dominated.

On the other hand, modelling of impact damage as delamination triggered the more accurate failure mode of delamination. The prediction was also conservative but closer to the actual ultimate load drop value.

It can be summarised that modelling impact damage as delamination provides the most accurate results regarding predicted load drop compared to the pristine samples and triggered failure mode.

Subquestion RQ2.2

What is the applicability of the modelling techniques, such as removing and detaching solid elements to represent impact damage in the form of delamination in composite bonded joints?

The study regarding modelling technique to represent damage was conducted on the SLTAI60 samples with artificially introduced damage in the form of release foil. The comparisons showed a similar drop in the ultimate load on the SLTAI60 delamination sample. Nevertheless, the model with detached nodes suffered from the interpenetration of the separate layers detached layers, resulting in disregarding this approach. To solve this issue, the contact should be defined between the plies, which significantly increases the simulation time. The existing crack can't propagate since no interlaminar CZE layers exist. It was assessed during this thesis that removing the elements in the delaminated zones allows for representing damaged zone and should be applied to the interlaminar CZE in the modified stacked mesh approach.

Subquestion RQ2.3

Which interlaminar layers are critical for the representation of impact damage?

During the analysis of the testing and simulation results, it was found that the critical layers for the representation are layers close to the bondline up to the first 0° ply in the layup. In numerical models, when modelling each interlaminar layer, the damage is initiated only in the layers in the through-thickness position close to the bondline up to the first 0° ply. For the specific impact position and energy studied, it was shown that the interlaminar layer between the first (45°) and the second ply (0°) is critical. Interestingly this goes back to the researchers' observation and the study conducted during this project about the failure modes of the different configurations of the single-lap joints, where the critical damage was observed in the same region for pristine samples.

Subquestion RQ2.4

How accurately and efficiently can ultimate load be predicted using the simplified impacted joint model?

The simplified impacted joint model allows for a conservative representation of the residual strength with the maximum error between the simulation and test of 13.8 % for the chosen impact representation as a single delamination. The observed difference comes mainly from the base model where the reduced traction in the interlaminar CZE material model resulted in under-predicted failure loads on variety of samples. The comparison in a different measure (test vs test and FEA vs FEA) allowed to compare the influence of this feature on the relative number. In this comparison, the reduction of ultimate load in the test was around 10% and in finite element simulation around 12%, which confirms the accuracy of the substitute impact representation, taking into account an initial error related to the interlaminar cohesive zone model.

For efficiency, interestingly, the simulation with the modelled impact damage runs faster compared to the simulation of the pristine sample. It can be associated with the more localised damage initiation compared to the pristine samples, where the damage was more distributed over the adhesive, interlaminar and interlaminar damage. This results in fewer iterations, especially of the micro-solver for the multiscale material model. The developed modelling approach doesn't increase the simulation time of the quasi-static simulation. Additionally, it doesn't include the step where the impact is modelled in an explicit impact simulation which shows a significant reduction of a workaround time compared to a traditional approach.

Research Question RQ2

How can damage resulting from low-velocity and low-energy impact be included in the Finite Element Model without running an explicit impact simulation?

Instead of running a traditional two-step simulation where in the first step, an impact event is simulated and in the second quasi-static step, a residual strength is tested, this project proposed a modelling approach for the impact damage based on the observation from a non-destructive and destructive testing and additionally a critical damage position based on the gathered simulation experience. The developed modelling approach includes impact damage in the form of circular delamination in the point of impact modelled by deleting the elements between the critical interlaminar layers. For the single-lap joint configuration, the critical position was found to lie in the adhesive edge region, through-thickness up to the first 0° ply in the layup. This modelling approach can be applied to the stacked mesh models with interlaminar CZE elements modelled only up to the first 0° ply in the layup.

Important takeaway points

Moreover, besides answering a set of research questions, the author wants to share the following takeaway points from the work:

- The damage resulting from impact in the composite bonded joints can be present both in the top and bottom adherend contradicting information from the literature that it is mostly present in the top adherend. The damage pattern highly depends on the location across the bondline, overlap length, layup, stacking sequence, and impact parameters that should be investigated in the future.
- The most critical location of the damage of any origin in single lap joint configuration is at the edge of the overlap in the length direction and up to the first 0° ply in the thickness direction. This area should be monitored during the structure's lifetime with particular emphasis and can be used to define the most critical damage and defects cases.
- In the finite element simulation, the occurrence of reaching the failure load is indicated by the damage observed at the adhesive edge, throughout the width of the specimen, depending on the layup that can be indicated either by the adhesive, intralaminar or interlaminar damage.

7.2. Recommendation

For the verification of the multiscale models, it was shown that the volumetric strain to failure (J1) should be adjusted independently of the material characterisation used data. For future studies, it is recommended to use tests of composite coupons with the layups showing a multiple-ply failure before the final fracture to analyse the accuracy of the created material model in more detail. The indicated ply failures on the force-displacement graph should be replicated with the simulation.

The material model of the interlaminar behaviour of IM7/8552 should be re-calibrated based on the results with nominal and reduced parameters. The re-calibration of the maximum traction and stiffness is expected to allow it to reach higher failure loads, like in the case of nominal parameters and show the accurate failure mode, like in the case of reduced parameters. With the value somewhere in-between the two models, a better balance between the accurate failure load and failure mode can be found. A sensitivity study should be performed first for the SLS45, and in the next step, it should be verified on a SLTAI60 sample.

In the topic of implicit FE simulation, finding an efficient approach to finish a simulation is recommended when an excessive amount of damage is present in the structure. The rule to finish the simulation depending on the damage size should be implemented to decrease the simulation time significantly. The damage propagation to capture a full failure mode of large samples is not preferred in the implicit solver due to the very in-time distributed damage propagation related to the time step size in the implicit simulation. The kinks on the force-displacement curves indicating the final portion of the curves can be used to indicate the significant damage present in the model. As observed on the base simulations, the ultimate load is over-predicted. Taking the first non-linearity shown on the force-displacement curve makes quantifying the lower load as an ultimate load possible. For the SLS45 and SLTAI60 samples, such a post-processing allows to predict a more accurate ultimate load.

To compare the performance of the solvers, it is recommended to apply the same methodology utilising the generated material model in an explicit solver. This can allow to verify how damage propagates after reaching the observed damage patterns indicating reaching ultimate loads. The limitation of the implicit solver is that it shows convergence issues when a large damage area is observed in the model, especially in wider samples like SLTAI60 and SLTAI30. The simulation times of the two solvers should be compared to assess if the developed implicit approach speeds up an overall analysis time.

The meshing approach should be revisited to reduce the simulation time on larger coupons such as WSLS. Due to the use of a pure stacked mesh with additional CZE between the ply elements, it is not

possible with current computational power to simulate the failure of large specimens. It is recommended to try different meshing approaches, such as a layered approach using a continuum shell outside of the region that was critical for the damage initiation and coarser meshes compared to the one used in this study. This can be combined with effective mesh transitions.

7.2.1. Proposition of future tests

Firstly, it is proposed to revisit the modelling of the delamination representation on the SLTAI60 test with a more critical position to observe a more significant drop in the ultimate load and assess the modelling technique more confidently. As the first step for this, it is recommended to move the location of the release foil from between every four layers to the critical through-thickness area close to the bondline up to the first 0° layer as presented in Figure 7.1. As the second step, it is recommended to change the location of the artificial damage in the length direction to the region of the step where the damage is initiated in the pristine single-lap configuration as presented in Figure 7.2. It is recommended to conduct separate actions, first to move the location in the thickness direction and second in the length direction to observe the influence of both changes independently.

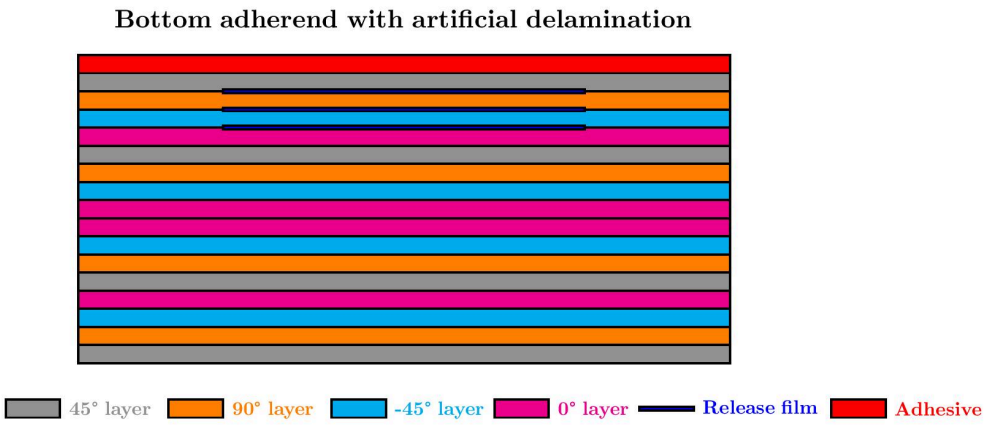

Figure 7.1: Proposition of the release foil through-thickness location in the new SLTAI60 test.

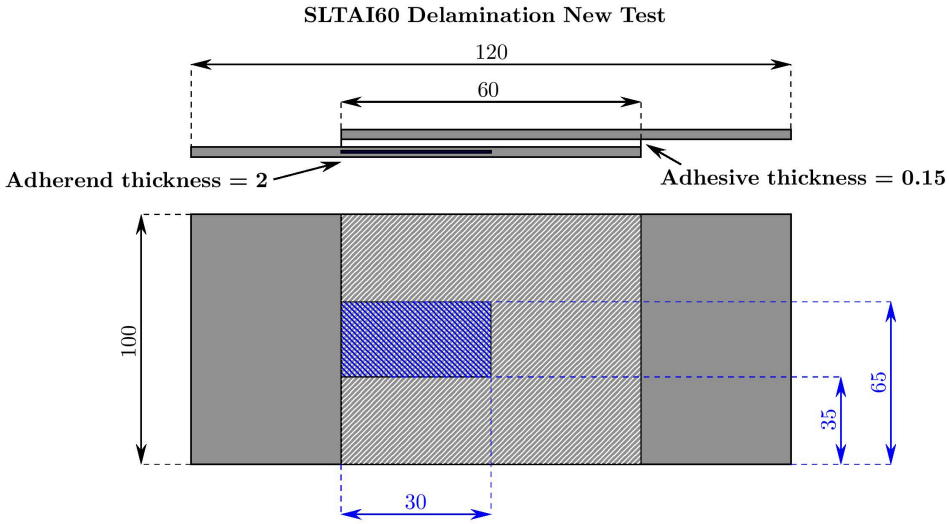

Figure 7.2: Proposition of the release foil position in the new SLTAI60 test.

Additionally, it is recommended to conduct future tests on a SLTAI60 specimen, not a SLTAI30 specimen, due to the more appropriate overlap length represented in the specimen. For sample manufacturing, using a unified manufacturing approach in the project is recommended, which results in comparable quality of the samples. As an outlier for the developed simulation method, a SLTAI30 specimen can be classified due to the different surface treatments applied to the sample. Ideally, the surface treatment should be done with a plasma treatment on all samples.

7.2.2. Future research directions

At the end of this thesis report, the author wants to present an overview of the possibility of future research on damage tolerance design and analysis of composite bonded joints and propositions based on the summary gained during the work in the JoinDT project.

The methodology to represent impact damage in composite bonded joints should be expanded to different impact cases and loading conditions to test the modelling approach's application on various samples. Additionally, extra layup stacking should be studied to confirm that modelling impact damage up to the first 0° ply is crucial in single-lap joint configuration.

The proposition for the future assessment of the static strength is that ideally, in the design and analysis phase, an expected damage size should be modelled in the critical impact point depending on a design configuration, and a remaining residual strength should be estimated. This can be used instead of the approach in which the static strength is simulated and a safety factor for BVID is applied to the value.

For the assesment of a fatigue crack growth after impact it is recommended to apply the methodology of Sachse [11] to assess the crack growth criteria of no-growth, slow-growth and arrested-growth in the developed numerical models.

For the mechanical testing, it is proposed to analyse the types of damage occurring during the impact and the residual strength testing with the help of acoustic emissions. This non-destructive technique detects and monitors the release of ultrasonic stress waves from specific sources when a material is under stress and deforms. This can help identify dominating damage types in different impact and joint configurations in more detail. Additionally, to assess the damage patterns, it is recommended to use computed tomography (CT) scan for the impacted bonded joints to confirm the damage pattern in the cone area where the ultrasonic scans suffer from the ultrasonic shadowing.

Future damage tolerant design should focus on enhancing properties and toughening the adhesives and develop concepts where the region up to the first 0° ply is toughened too. For example, the toughening mechanisms could be achieved by architecting the composite substrate layup or application of thin plies.

References

[1] R. Dilger, H. Hickethier, and M. D. Greenhalgh, “Eurofighter a safe life aircraft in the age of damage tolerance,” *International Journal of Fatigue*, vol. 31, no. 6, pp. 1017–1023, Jun. 2009. doi: 10.1016/j.ijfatigue.2008.05.014.

[2] A. Bautista, J. P. Casas-Rodriguez, M. Silva, and A. Porras, “A dynamic response analysis of adhesive - Bonded single lap joints used in military aircrafts made of glass fiber composite material undercyclic impact loading,” *International Journal of Adhesion and Adhesives*, vol. 102, p. 102 644, Oct. 2020. doi: 10.1016/j.ijadhadh.2020.102644.

[3] O. Memon, *Confusing Quantification: How Many Parts Does An Airliner Have?* Accessed on 13.01.2023. [Online]. Available: https://simpleflying.com/airliners-how-many-parts/?newsletter_popup=1.

[4] J. Kupski and S. Teixeira de Freitas, “Design of adhesively bonded lap joints with laminated CFRP adherends: Review, challenges and new opportunities for aerospace structures,” *Composite Structures*, vol. 268, p. 113 923, Jul. 2021. doi: 10.1016/j.compstruct.2021.113923.

[5] T. A. Schmid Fuertes, T. Kruse, T. Körwien, and M. Geistbeck, “Bonding of CFRP primary aerospace structures – discussion of the certification boundary conditions and related technology fields addressing the needs for development,” *Composite Interfaces*, vol. 22, no. 8, pp. 795–808, Sep. 2015. doi: 10.1080/09276440.2015.1077048.

[6] H. Cui, D. Thomson, S. Eskandari, and N. Petrinic, “A critical study on impact damage simulation of IM7/8552 composite laminate plate,” *International Journal of Impact Engineering*, vol. 127, pp. 100–109, 2019. doi: 10.1016/j.ijimpeng.2019.01.009.

[7] C. Kassapoglou, *Design and Analysis of Composite Structures: With Applications to Aerospace Structures*, Second Edition. New York: Wiley, 2013.

[8] O. Völkerink and C. Hühne, “Virtual testing for design and certification of (fusion) bonded longitudinal joints in a fibre composite fuselage: A proposal using FEM-based progressive damage analysis,” *Composites Part C: Open Access*, vol. 7, p. 100 236, Mar. 2022. doi: 10.1016/j.jcomc.2022.100236.

[9] Federal Aviation Administration, “Advisory circular 20-107B - Composite Aircraft Structure,” Tech. Rep., 2009.

[10] F. Volle, *Numerical Simulation of Damage Tolerant Bonding Methods for CFRP Aircraft Structures*, MSc thesis, University of Stuttgart, Oct. 2021.

[11] R. Sachse, “Untersuchungen zur Auslegung von schadenstoleranten Klebeverbindungen durch mechanische Riss-Stopper-Elemente,” Ph.D. dissertation, University of Stuttgart, 2020. doi: 10.18419/opus-10956.

[12] T. Donelli, *Numerical Simulations and Sizing Methods of Bonded Joints for CFRP Aircraft Structures*, MSc thesis, École Polytechnique Fédérale de Lausanne, Sep. 2022.

[13] Federal Aviation Administration, “Advisory circular 25.571-1D - Damage tolerance and fatigue evaluation of structure,” Tech. Rep., 2011.

[14] Federal Aviation Administration, *Lessons Learned - Transport Airplane - Accidents - De Havilland DH-106 Comet 1*, Accessed on 15.02.2023. [Online]. Available: https://www.faa.gov/lessons_learned/transport_airplane/accidents/G-ALYV.

[15] Federal Aviation Administration, *Lessons Learned - Transport Airplane - Accidents - Boeing 737-200*, Accessed on 15.02.2023. [Online]. Available: https://www.faa.gov/lessons_learned/transport_airplane/accidents/N73711.

[16] O. Völkerink, “Simulation-driven design of bonded joints in fibre composite aircraft structures using progressive damage analyses,” Ph.D. dissertation, Technische Universität Carolo-Wilhelmina zu Braunschweig, 2022. doi: 10.57676/hya4-2a09.

[17] C. S. Lopes, C. González, O. Falcó, F. Naya, J. LLorca, and B. Tijs, “Multiscale virtual testing: the roadmap to efficient design of composites for damage resistance and tolerance,” *CEAS Aeronautical Journal*, vol. 7, no. 4, pp. 607–619, Dec. 2016. doi: 10.1007/s13272-016-0210-7.

[18] J. Llorca, C. González, J. M. Molina-Aldareguía, *et al.*, “Multiscale Modeling of Composite Materials: a Roadmap Towards Virtual Testing,” *Advanced Materials*, vol. 23, no. 44, pp. 5130–5147, Nov. 2011. doi: 10.1002/adma.201101683.

[19] L. D. C. Ramalho, R. D. S. G. Campilho, J. Belinha, and L. F. M. da Silva, “Static strength prediction of adhesive joints: A review,” *International Journal of Adhesion and Adhesives*, vol. 96, p. 102 451, Jan. 2020. doi: 10.1016/j.ijadhadh.2019.102451.

[20] M. H. Kim, U. I. Ri, H. S. Hong, and Y. C. Kim, “Comparative study of failure models for prediction of mixed-mode failure characteristics in composite adhesively bonded joint with brittle/Quai-brittle adhesive using finite element analysis,” *International Journal of Adhesion and Adhesives*, vol. 109, p. 102 911, Sep. 2021. doi: 10.1016/j.ijadhadh.2021.102911.

[21] F. J. P. Chaves, L. F. M. Da Silva, M. F. S. F. De Moura, D. A. Dillard, and V. H. C. Esteves, “Fracture mechanics tests in adhesively bonded joints: A literature review,” *Journal of Adhesion*, vol. 90, no. 12, pp. 955–992, Nov. 2014. doi: 10.1080/00218464.2013.859075.

[22] J. Díaz, L. Romera, S. Hernández, and A. Baldomir, “Benchmarking of three-dimensional finite element models of CFRP single-lap bonded joints,” *International Journal of Adhesion and Adhesives*, vol. 30, no. 3, pp. 178–189, Apr. 2010. doi: 10.1016/j.ijadhadh.2009.12.005.

[23] F. M. F. Ribeiro, R. D. S. G. Campilho, R. J. C. Carbas, and L. F. M. da Silva, “Strength and damage growth in composite bonded joints with defects,” *Composites Part B: Engineering*, vol. 100, pp. 91–100, Sep. 2016. doi: 10.1016/j.compositesb.2016.06.060.

[24] R. Krueger, “1 - The virtual crack closure technique for modeling interlaminar failure and delamination in advanced composite materials,” in *Numerical Modelling of Failure in Advanced Composite Materials*, ser. Woodhead Publishing Series in Composites Science and Engineering, Woodhead Publishing, 2015, pp. 3–53. doi: https://doi.org/10.1016/B978-0-08-100332-9.00001-3.

[25] B. P. Justusson, M. J. Molitor, J. S. Iqbal, M. Rassaian, T. M. Ricks, and R. K. Goldberg, “Overview of Coupon Testing of an IM7/8552 Composite Required to Characterize High-Energy Impact Dynamic Material Models,” National Aeronautics and Space Administration, Glenn Research Center, Tech. Rep., 2020.

[26] M. Naghdinasab, A. Farrokhabadi, and H. Madadi, “A numerical method to evaluate the material properties degradation in composite RVEs due to fiber-matrix debonding and induced matrix cracking,” *Finite Elements in Analysis and Design*, vol. 146, pp. 84–95, Jul. 2018. doi: 10.1016/j.finel.2018.04.008.

[27] C. Hu, G. Huang, and C. Li, “Experimental and Numerical Study of Low-Velocity Impact and Tensile after Impact for CFRP Laminates Single-Lap Joints Adhesively Bonded Structure,” *Materials*, vol. 14, no. 4, p. 1016, Feb. 2021. doi: 10.3390/ma14041016.

[28] F. Dogan, H. Hadavinia, T. Donchev, and P. S. Bhonge, “Delamination of impacted composite structures by cohesive zone interface elements and tiebreak contact,” *Open Engineering*, vol. 2, no. 4, pp. 612–626, 2012. doi: 10.2478/s13531-012-0018-0.

[29] P. F. Liu and J. Y. Zheng, “Recent developments on damage modeling and finite element analysis for composite laminates: A review,” *Materials and Design*, vol. 31, no. 8, pp. 3825–3834, Sep. 2010. doi: 10.1016/j.matdes.2010.03.031.

[30] F. A. Leone, C. G. Dávila, and D. Girolamo, “Progressive damage analysis as a design tool for composite bonded joints,” *Composites Part B: Engineering*, vol. 77, pp. 474–483, Aug. 2015. doi: 10.1016/j.compositesb.2015.03.046.

[31] Y. Li, Y. Yang, J. Li, B. Wang, and Y. Liao, "Experimental-numerical analysis of failure of adhesively bonded lap joints under transverse impact and different temperatures," *International Journal of Impact Engineering*, vol. 140, p. 103 541, Jun. 2020. doi: 10.1016/j.ijimpeng.2020.103541.

[32] J. Fish and Q. Yu, "Multiscale damage modelling for composite materials: theory and computational framework," *International Journal for Numerical Methods in Engineering*, vol. 52, no. 1-2, pp. 161–191, Sep. 2001. doi: 10.1002/nme.276.

[33] Altair, *Multiscale Designer 2022.0 User Manual*. Troy, Michigan: Altair Engineering Inc., 2022.

[34] J. L. Thomason, "Glass fibre sizing: A review," *Composites Part A: Applied Science and Manufacturing*, vol. 127, p. 105 619, Dec. 2019. doi: 10.1016/J.COMPOSITESA.2019.105619.

[35] Z. M. Huang, "On micromechanics approach to stiffness and strength of unidirectional composites," *Journal of Reinforced Plastics and Composites*, vol. 38, no. 4, pp. 167–196, Feb. 2019. doi: 10.1177/0731684418811938.

[36] Z. Yuan, R. Crouch, J. Wollschlager, A. Shojaei, and J. Fish, "Assessment of Altair Multiscale Designer for damage tolerant design principles (DTDP) of advanced composite aircraft structures," *Journal of Composite Materials*, vol. 51, no. 10, pp. 1379–1391, May 2017. doi: 10.1177/0021998316651707.

[37] S. Purimpat, R. Jérôme, and A. Shahram, "Effect of fiber angle orientation on a laminated composite single-lap adhesive joint," *Advanced Composite Materials*, vol. 22, no. 3, pp. 139–149, 2013. doi: 10.1080/09243046.2013.782805.

[38] J. Kupski, S. Teixeira de Freitas, D. Zarouchas, P. Camanho, and R. Benedictus, "Composite layup effect on the failure mechanism of single lap bonded joints," *Composite Structures*, vol. 217, pp. 14–26, 2019. doi: https://doi.org/10.1016/j.compstruct.2019.02.093.

[39] C. Galliot, J. Rousseau, and G. Verchery, "Impact tension of composite single lap adhesive joints," in *Proceedings of ECCM 12 - 12th European Conference on Composite Materials*, Biarritz, France, Aug. 2006.

[40] R. Sachse, M. Jochens, M. Ross, A. K. Pickett, and P. Middendorf, "Low-velocity impact simulation with a special focus on thick composites," in *22nd International Conference on Composites Materials*, Melbourne, Sep. 2019.

[41] R. Bogenfeld, J. Kreikemeier, and T. Wille, "Review and benchmark study on the analysis of low-velocity impact on composite laminates," *Engineering Failure Analysis*, vol. 86, pp. 72–99, 2018. doi: https://doi.org/10.1016/j.engfailanal.2017.12.019.

[42] S. X. Wang, L. Z. Wu, and L. Ma, "Low-velocity impact and residual tensile strength analysis to carbon fiber composite laminates," *Materials and Design*, vol. 31, no. 1, pp. 118–125, Jan. 2010. doi: 10.1016/j.matdes.2009.07.003.

[43] C. Kassapoglou, *Modeling the Effect of Damage in Composite Structures: Simplified Approaches*. Hoboken: Wiley, 2015.

[44] A. S. Verma, N. P. Vedvik, Z. Gao, S. G. P. Castro, and J. J. E. Teuwen, "Bondline Thickness Effects on Damage Tolerance of Adhesive Joints Subjected to Localized Impact Damages: Application to Leading Edge of Wind Turbine Blades," *Materials*, vol. 14, no. 24, p. 7526, Dec. 2021. doi: 10.3390/ma14247526.

[45] A. Wronkowicz-Katunin, A. Katunin, and K. Dragan, "Reconstruction of Barely Visible Impact Damage in Composite Structures Based on Non-Destructive Evaluation Results," *Sensors*, vol. 19, no. 21, p. 4629, Nov. 2019. doi: 10.3390/s19214629.

[46] J. Bieniaś, P. Jakubczak, B. Surowska, and K. Dragan, "Low-energy impact behaviour and damage characterization of carbon fibre reinforced polymer and aluminium hybrid laminates," *Archives of Civil and Mechanical Engineering*, vol. 15, no. 4, pp. 925–932, Sep. 2015. doi: 10.1016/j.acme.2014.09.007.

[47] J. Zhou, P. Wen, and S. Wang, "Finite element analysis of a modified progressive damage model for composite laminates under low-velocity impact," *Composite Structures*, vol. 225, p. 111 113, Oct. 2019. doi: 10.1016/j.compstruct.2019.111113.

[48] A. Soto, E. V. González, P. Maimí, F. Martín de la Escalera, J. R. Sainz de Aja, and E. Alvarez, "Low velocity impact and compression after impact simulation of thin ply laminates," *Composites Part A: Applied Science and Manufacturing*, vol. 109, pp. 413–427, Jun. 2018. doi: 10.1016/j.compositesa.2018.03.017.

[49] S. Hoseinlaghab, M. Farahani, M. Safarabadi, and M. Nikkhah, "Tension-after-impact analysis and damage mechanism evaluation in laminated composites using AE monitoring," *Mechanical Systems and Signal Processing*, vol. 186, p. 109 844, 2023. doi: 10.1016/j.ymssp.2022.109844.

[50] A. P. Sharma, S. H. Khan, and R. Velmurugan, "Effect of through thickness separation of fiber orientation on low velocity impact response of thin composite laminates," *Heliyon*, vol. 5, no. 10, 2019. doi: 10.1016/j.heliyon.2019.e02706.

[51] N. Rajic, "13 - Non-destructive evaluation (NDE) of aerospace composites: flaw characterisation," in *Non-Destructive Evaluation (NDE) of Polymer Matrix Composites*, ser. Woodhead Publishing Series in Composites Science and Engineering, Woodhead Publishing, 2013, pp. 335–366. doi: 10.1533/9780857093554.3.335.

[52] ASTM, *ASTM D7136/D7136M-15: Standard Test Method for Measuring the Damage Resistance of a Fiber-Reinforced Polymer Matrix Composite to a Drop-Weight Impact Event*. West Conshohocken, Pennsylvania: ASTM International, 2020.

[53] W. Huang, L. Sun, Y. Liu, Y. Chu, and J. Wang, "Effects of low-energy impact at different temperatures on residual properties of adhesively bonded single-lap joints with composites substrates," *Composite Structures*, vol. 267, p. 113 860, Jul. 2021. doi: 10.1016/j.compstruct.2021.113860.

[54] Y. Shi and C. Soutis, "A finite element analysis of impact damage in composite laminates," *Aeronautical Journal*, vol. 116, no. 1186, pp. 1331–1347, Dec. 2012. doi: 10.1017/S0001924000007661.

[55] O. Sayman, V. Arikan, A. Dogan, I. F. Soykok, and T. Dogan, "Failure analysis of adhesively bonded composite joints under transverse impact and different temperatures," *Composites Part B: Engineering*, vol. 54, no. 1, pp. 409–414, 2013. doi: 10.1016/j.compositesb.2013.06.017.

[56] W. A. de Morais, S. N. Monteiro, and J. R. M. d'Almeida, "Effect of the laminate thickness on the composite strength to repeated low energy impacts," *Composite Structures*, vol. 70, no. 2, pp. 223–228, Sep. 2005. doi: 10.1016/j.compstruct.2004.08.024.

[57] B. Y. Chen, S. T. Pinho, N. V. De Carvalho, P. M. Baiz, and T. E. Tay, "A floating node method for the modelling of discontinuities in composites," *Engineering Fracture Mechanics*, vol. 127, pp. 104–134, 2014. doi: 10.1016/j.engfracmech.2014.05.018.

[58] ASTM, *ASTM D7137/D7137M-17: Standard Test Method for Compressive Residual Strength Properties of Damaged Polymer Matrix Composite Plates*. West Conshohocken, Pennsylvania: ASTM International, 2017.

[59] F. Chen, W. Yao, and W. Jiang, "Experimental and simulation investigation on BVID and CAI behaviors of CFRP laminates manufactured by RTM technology," *Engineering Computations*, vol. 38, no. 5, pp. 2252–2273, Oct. 2020. doi: 10.1108/EC-01-2020-0008.

[60] I. R. Farrow, K. Potter, A. Fisher, and M. Kelly, "Impact of Adhesively Bonded Composite Joints with Edge Effect," *Advanced Composites Letters*, vol. 9, no. 6, 2000. doi: 10.1177/096369350000900603.

[61] L. Llopart, K. I. Tserpes, and G. N. Labeas, "Experimental and numerical investigation of the influence of imperfect bonding on the strength of NCF double-lap shear joints," *Composite Structures*, vol. 92, no. 7, pp. 1673–1682, Jun. 2010. doi: 10.1016/j.compstruct.2009.12.001.

[62] Y. Liu, S. Lemanski, and X. Zhang, "Parametric study of size, curvature and free edge effects on the predicted strength of bonded composite joints," *Composite Structures*, vol. 202, pp. 364–373, 2018. doi: https://doi.org/10.1016/j.compstruct.2018.02.017.

[63] H. Kim and K. Kedward, “Stress Analysis of In-Plane, Shear-Loaded, Adhesively Bonded Composite Joints and Assemblies,” University of California Santa Barbara, Tech. Rep. DOT/FAA/AR-01/7, 2001.

[64] T. Körwien, T. Kruse, A. Callés, *et al.*, *BOPACS Review*, BOPACS Consortium, Germany, 2016.

[65] ASTM, *ASTM D5868-01: Standard Test Method for Lap Shear Adhesion for Fiber Reinforced Plastic (FRP) Bonding*. West Conshohocken, Pennsylvania: ASTM International, 2014.

[66] Airbus S.A.S, *AITM1-0010: Determination of Compression Strength After Impact*. Blagnac, France, 2005.

[67] JoinDT Consortium, *JoinDT project data*, Germany, 2023.

[68] J. Fish, *Practical Multiscaling*. Chichester, West Sussex, United Kingdom: John Wiley & Sons, 2013.

[69] G. Ji, Z. Ouyang, G. Li, S. Ibekwe, and S.-S. Pang, “Effects of adhesive thickness on global and local Mode-I interfacial fracture of bonded joints,” *International Journal of Solids and Structures*, vol. 47, no. 18, pp. 2445–2458, 2010. doi: https://doi.org/10.1016/j.ijsolstr.2010.05.006.

[70] R. Sachse, A. K. Pickett, and P. Middendorf, “Simulation of impact and residual strength of thick laminate composites,” *Composites Part B: Engineering*, vol. 195, p. 108 070, Aug. 2020. doi: 10.1016/J.COMPOSITESB.2020.108070.

[71] A. Hillerborg, M. Modéer, and P.-E. Petersson, “Analysis of crack formation and crack growth in concrete by means of fracture mechanics and finite elements,” *Cement and Concrete Research*, vol. 6, no. 6, pp. 773–781, 1976. doi: 10.1016/0008-8846(76)90007-7.

[72] J. A. Pascoe, S. Pimenta, and S. T. Pinho, “How to set up a cohesive zone model for an LEFM dominated problem,” 2020.

[73] A. Turon, C. Dávila, P. Camanho, and J. Costa, “An engineering solution for mesh size effects in the simulation of delamination using cohesive zone models,” *Engineering Fracture Mechanics*, vol. 74, no. 10, pp. 1665–1682, 2007. doi: https://doi.org/10.1016/j.engfracmech.2006.08.025.

[74] D. Biagini, J. A. Pascoe, and R. Alderliesten, “Experimental investigation of fatigue after impact damage growth in CFRP,” *Procedia Structural Integrity*, vol. 42, pp. 343–350, Jan. 2022. doi: 10.1016/j.prostr.2022.12.042.

[75] L. Wen, X. Xu, and L. Qin, “Effect of Low-Temperature Plasma Surface Treatment on Bonding Properties of Single-Lap Joint of Thermosetting Composites,” *Polymers*, vol. 15, no. 7, p. 1631, 2023. doi: 10.3390/polym15071631.

Appendix

In the appendix, the observed role and influence of the parameters of the constituent material models on the homogenised properties and stress-strain coupon curves used in Chapter 4 is briefly discussed.

Linear isotropic model of matrix

- Young's Modulus in tension (E_T) is a dominating parameter influencing composite material stiffness in the transverse direction. The increase of the value of the E_T increases the value of the homogenised E_{22} and E_{33}.

- Poisson ratio (ν) is a parameter that influences in-plane and out-of-plane Poisson's ratio of the composite material. The increase of the value of the ν increases the value of the homogenised ν_{12}, ν_{13}, and ν_{23}.

- Young's modulus in compression (E_C) is a secondary parameter influencing composite material stiffness in compression in the longitudinal direction. Increasing the value of the E_C increases the value of the homogenised E_{11C}.

Linear transversely isotropic model of fibre

- Longitudinal Young's modulus in tension (E_{11}) is a dominating parameter influencing composite material stiffness in the fibre direction. The increase of the value of the fibre E_{11} increases the value of the homogenised E_{11}.

- Transverse Young's modulus (E_{22}) is one of the parameters contributing to the stiffness in the transverse direction. Together with the matrix Young's modulus, these parameters should be adjusted to match the homogenised stiffness in the transverse direction.

- In-plane Poisson ratio (ν_{12}) is a parameter that has an influence on the in-plane Poisson's ratio of the composite material. Together with a matrix Poisson's ratio, the values were calibrated to obtain the target value of the homogenised ν_{12}.

- Transverse Poisson ratio (ν_{23}) is a parameter that has a influence on out-of-plane Poisson's ration of the composite material. Together with a matrix Poisson's ratio, the values were calibrated to obtain the target value of the homogenised ν_{23}.

- Longitudinal Young's modulus in compression (E_{11C}) is a dominating parameter influencing composite material stiffness in the fibre direction. The increase of the value of the fibre E_{11C} increases the value of the homogenised E_{11C}.

Orthotropic damage and rate-independent plasticity model of matrix

- Yield stress (σ_y) denotes the end of elastic behaviour and the start of plastic material behaviour. Under the yield stress, a material will deform elastically and revert to its original shape once the applied force is removed. The value of σ_y affects an observed behaviour in a ±45 tension test. The increase of the σ_y value increases the point at which plastic behaviour is observed in a ±45 tension test.

- Ultimate stress (σ_1) - defines the stress at which the plastic behaviour reaches the hardening. The value of σ_1 affects an observed behaviour in a ±45 tension test. The increase of the σ_1 value increases the point at which hardening behaviour is observed in a ±45 tension test.

- Exponent for the evolution law (δ) defines the shape of the stress-strain curve between yield and ultimate stress. The increase in the value of δ lead to a bigger curvature off this part of the curve. The value was optimised to match the shape of the ±45 tension stress-strain curve in the plastic region.

- Linear term for the hardening law (H) defines the tangent of the hardening part of the stress-strain curve between ultimate stress and equivalent plastic strain at which damage begins. Material's strength continues to grow but with a smaller slope. A linear function approximates the hardening part of plasticity. The value was optimised to match the final part of the ±45 tension stress-strain curve.

- Equivalent plastic strain at which damage begins (ϵ_{p0}) - defines the value of the plastic strain at which the maximum matrix stress is present in the final part of the ±45 tension curve. The value was optimised to match the final point of this coupon curve.

- Equivalent plastic strain at zero stress (ϵ_{p1}) defines the distance between the damage initiation and full damage state in the matrix. The value is defined for numerical reasons. To have a significant enough distance for a solver to be able to capture accurately softening of the material.

- Mean stress at damage initiation (σ_{mean}) defines the maximum volumetric stress at which the damage initiation begins. The value of the mean stress at damage initiation directly influences the ultimate transverse strength in tension (Y_T) of the composite material.

- Volumetric strain to failure ($J1$) defines the volumetric strain at which full damage state is reached. The increase of the value of $J1$ has an influence on the distance between the damage initiation and full damage state, and for numerical reasons, this region should be stretched enough. The calibration of this parameter should be done on a macro-simulation of the sample independent of material characterisation.

- Compression factor (C) is introduced to account for differences between tension and compression. The value of 0 was introduced to differentiate tensile and compressive loading scenarios fully. For comparison, the value of 1 describes the state where tensile and compressive loading results in the same material behaviour.

- Maximum allowed damage (w_{max}). The influence of this parameter can be explained in a simulation of a single composite element as presented in Figure A1, where the load is applied in the direction perpendicular to the fibre orientation. When the element reaches the damaged state, it undergoes softening, which reduces its stiffness. Maximum allowed damage defines the maximum reduction applied to the stiffness matrix, meaning that the residual stiffness of the element will be equal to (1-w_{max})K. This parameter set to $w_{max} = 0.99$ helped with the encountered convergence issues in the older version of the solver (2021.2), where the sudden reduction of the out-of-plane stiffness led to the collapse of the elements.

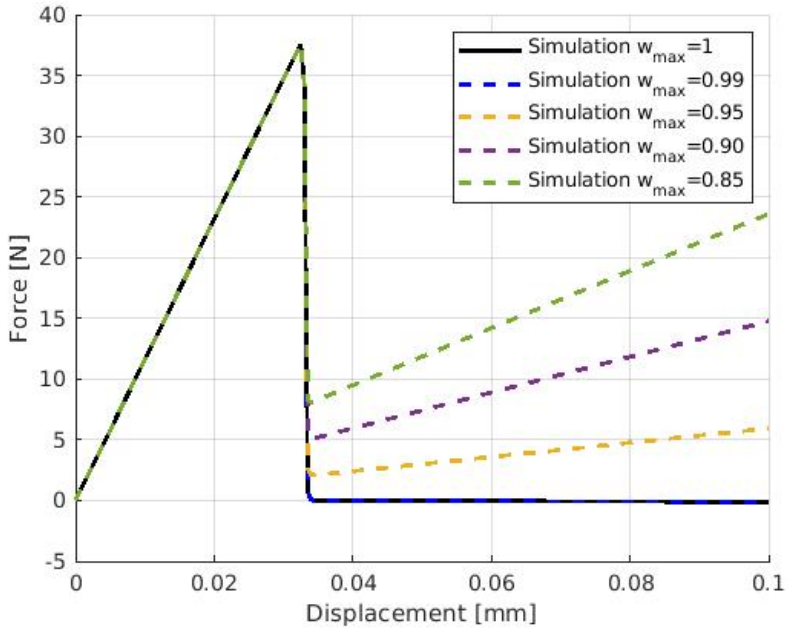

Figure A1: Influence of w_{max} on the simulation of single element loaded in the transverse direction (90°).

Axial bi-linear isotropic damage model of fibre

- Failure stress in tension (σ_0). The value of the failure stress of fibre in tension directly influences the ultimate longitudinal strength in tension (X_T) of the composite material. The increase of the value of σ_0 directly influences the increase of X_T.
- Strain at zero stress in tension (ϵ_1). The value of the ϵ_1 defines the strain value between the damage initiation and full damage state in tensile loading for the fibre. This value doesn't directly influence the homogenised stress-strain curves of the coupons. However, for numerical reasons, should be set as a 1.1 time the strain at damage initiation ϵ_0.
- Failure stress in compression (σ_{0C}). The value of the failure stress of fibre in tension directly influences the ultimate longitudinal strength in compression (X_C) of the composite material. The increase of the value of σ_{0C} has a direct influence on the increase of X_C.
- Strain at zero stress in compression (ϵ_{1C}). The ϵ_{1C} value defines the strain value between the damage initiation and full damage state in compressive loading for the fibre. This value doesn't directly influence the homogenised stress-strain curves of the coupons, however, should be set as a 1.1 time the strain at damage initiation ϵ_{0C} for numerical reasons.